Cohesive laws for assessment of materials failure: Theory, experimental methods and application

Sørensen, Bent F.

Publication date:
2010

Document Version
Publisher's PDF, also known as Version of record

Cohesive laws for assessment of materials failure: Theory, experimental methods and application

Bent F. Sørensen

Doctor of Technices thesis

Risø-R-1736 (EN)

Risø DTU
National Laboratory for Sustainable Energy

ISBN 978-87-550-3827-1
ISSN 0106-2840

Risø DTU
National Laboratory for Sustainable Energy
Technical University of Denmark

Frederiksborgvej 399
PO Box 49
DK-4000 Roskilde
Denmark
Phone +45 4677 4677
Fax +45 4677 5688

www.risoe.dtu.dk

Risø-R-1736 (EN)

Centertryk A/S - 4300 Holbæk

Risø-R-1736 (EN)

Cohesive laws for assessment of materials failure: Theory, experimental methods and application

Cohesive laws for assessment of materials failure: Theory, experimental methods and application

Bent F. Sørensen

Materials Research Division
Risø National Laboratory for Sustainable Energy
The Technical University of Denmark
DK-4000 Roskilde, Denmark

Doctor of Technices thesis

2010

Denne afhandling er af Danmarks Tekniske Universitet antaget til forsvar for den tekniske doktorgrad. Antagelsen er sket efter bedømmelse af den foreliggende afhandling.

Kgs. Lyngby, den 26. maj 2010

Lars Pallesen
Rektor

/Martin P. Bendsøe
Dean

This thesis has been accepted by the Technical University of Denmark for public defence in fulfilment of the requirements for the degree of Doctor Technices. The acceptance is based on an evaluation of the present dissertation.

Kgs. Lyngby, den 26. maj 2010

Lars Pallesen
Rector

/Martin P. Bendsøe
Dean

Table of contents

Preface

"Wisdom begins in wonder"
Socrates

"Do just once what others say you can't do, and you will never pay attention to their limitations again"
James Cook

Simulation of crack propagation by cohesive zone modelling has recently become an active research area in the field of fracture mechanics. In cohesive zone modelling, the mechanical behaviour of the fracture process zone is represented by a traction-separation relation called a cohesive law. Cohesive zone modelling is a paradigm shift: A cohesive law includes both a peak stress and a work of separation, and it is likely to replace strength and fracture toughness as strength-controlling parameters. Until now, cohesive zone modelling has almost entirely been done by the use of simplified, idealised cohesive laws. However, for engineering purposes, reliable predictions using cohesive zone modelling must be based on cohesive laws that characterise the specific material under investigation. Thus, there is a general need for the development of theoretical and experimental methods for the determination of cohesive laws. This thesis is an attempt to establish such methods for cases that involve a large-scale fracture process zone. The methods are applied in areas of scientific and industrial importance, such as adhesive joints and fibre composites experiencing delamination.

The thesis comprises an eight-chapter overview and an appendix of ten papers published by the author during the last decade. The overview is intended to provide a comprehensive description of the work with the focus on the new tools as well as presenting cohesive laws to solve practical engineering problems. Details concerning the methods, their limitations and the results obtained are given in the individual papers.

Chapter 1 gives an introduction to the field of fracture mechanics from the early considerations of material strength and crack resistance to bridging laws and cohesive laws. Chapter 2 gives the theoretical framework for the J integral-based methods used first by the author for determination of Mode I cohesive laws under large-scale bridging in fibre composites using a DCB (double cantilever beam) specimen loaded with pure bending moments. Chapter 3 covers the development of experimental methods that enables the study of micromechanics of fracture as well as the analysis of a new generation of fracture mechanics test specimens that are well suited for the determination of cohesive laws. The author was the first to use these specimens for the determination of Mixed-Mode cohesive laws. Some of these test specimens are now used by a leading wind turbine blade manufacturer [1]. Chapter 4 and Chapter 5 cover (i) experimental results (characterisation of microstructural toughening mechanisms and measurements of cohesive laws), (ii) micromechanical modelling (prediction of cohesive laws based on microscale toughening

mechanisms), and (iii) modelling of structures (prediction of structural strength from cohesive laws). These chapters are presented as four Case Studies that connect at least two length scales each (microscale, macroscale, structural scale). The topics of the four Case Studies are chosen to elucidate various important aspects of cohesive laws and to verify the approaches developed. Chapter 6 contains ideas regarding future developments, while Chapter 7 summarises the major results and Chapter 8 presents the conclusions of this thesis. An appendix contains the ten journal publications that form the basis of this thesis. These publications are (in the order of appearance in the thesis):

[A1] Sørensen, B. F., Gamstedt, E. K., and Jacobsen. T. K., 2000, "Equivalence of J integral and stress intensity factor approach for large scale bridging problems", *International Journal of Fracture*, Vol. 104, pp. L31-6.

[A2] Sørensen, B. F., and Kirkegaard, P., 2006, "Determination of mixed-mode cohesive laws", *Engineering Fracture Mechanics*, Vol. 73, pp. 2642-61.

[A3] Sørensen, B. F., Jørgensen, K., Jacobsen, T. K., and Østergaard, R. C., 2006, "DCB-specimen loaded with uneven bending moments", *International Journal of Fracture*, Vol. 141, pp. 163-176.

[A4] Sørensen, B. F., and Jacobsen, T. K., 2009, "Characterising delamination of fibre composites by mixed-mode cohesive laws", *Composite Science and Technology*, Vol. 69, pp. 445-456.

[A5] Sørensen, B. F., Gamstedt, E. K., Østergaard, R. C., and Goutianos, S., 2008, "Micromechanical model of cross-over fibre bridging - prediction of mixed-mode bridging laws", *Mechanics of Materials*, Vol. 40, pp. 220-34.

[A6] Sørensen, B. F., Horsewell, A., Jørgensen, O., Kumar, A. N., and Engbæk, P., 1998, "Fracture resistance measurement method for *in-situ* observation of crack mechanisms", *Journal of the American Ceramic Society*, Vol. 81, pp. 661-9.

[A7] Sørensen, B. F., 2002, "Cohesive law and notch sensitivity of adhesive joints", *Acta Materialia*, Vol. 50, pp. 1053-61.

[A8] Sørensen, B. F. and Jacobsen, T. K., 1998, "Large scale bridging in composites: R-curve and bridging laws", *Composites part A*, Vol. 29A, pp. 1443-51.

[A9] Jacobsen, T. K., and Sørensen, B. F., 2001, "Mode I Intra-laminar crack growth in composites - modelling of R-curves from measured bridging laws", *Composites part A*, Vol. 32, pp. 1-11.

[A10] Sørensen, B. F., Goutianos, S., and Jacobsen, T. K., 2009, "Strength scaling of adhesive joints in polymer-matrix composites", *International Journal of Solids and Structures*, Vol. 46, pp. 741-761.

Terminology, abbreviations and symbols

"*I think; therefore I am*"
Rene Descartes

"*Integrity has no need of rules*"
Albert Camus

Definitions of key concepts

Bridging/cohesive laws: The term "bridging/cohesive laws" is used to describe features that are the same for both bridging laws and cohesive laws.

Bridging law: A bridging law is a traction-separation relation that represents the stress transmitted between crack faces in a bridging zone.

Bridging zone: A bridging zone is a fracture process zone in which the mechanical response can be described in terms of a bridging law. A bridging zone has a well-defined crack tip that has a stress singularity. A bridging zone is said to be fully developed when the end-opening exceeds the critical opening corresponding to breakage of all bridging ligaments (and zero bridging tractions) in the crack wake.

Cohesive law: A cohesive law is a traction-separation relation that represents the stress transmitted between crack faces in a cohesive zone.

Cohesive zone: A cohesive zone is a mathematical representation of a fracture process zone in which the mechanical response can be described in terms of a cohesive law. In contrast to a bridging zone, a cohesive zone does not possess a crack tip stress singularity. A cohesive zone can be specified along an anticipated path. A part of the cohesive zone can be active, i.e., giving a crack opening (crack face separation) while other parts of the cohesive zone can remain closed (inactive). A cohesive zone is said to be fully developed when the end-opening exceeds the critical separation, so that the cohesive tractions are zero in the wake of the crack.

Crack bridging: Crack bridging is used for describing a crack with ligaments that connect the crack faces within a fracture process zone.

Critical opening: The critical opening of a bridging/cohesive law is the crack separation where the bridging/cohesive tractions have decreased to zero during a monotonic opening.

End-opening: The end-opening is defined as the opening at the location where the crack initiated, i.e. the position at which the fracture process zone forms in the first stages of loading (the notch, crack starter foil or pre-crack cut).

Fracture: Fracture is a term used for failure types that occur predominantly by the formation or propagation of a single crack.

Fracture energy: The energy consumed per unit area by the crack tip fracture process as the crack advances.

Fracture process zone: A fracture process zone is the zone near a notch or a macroscopic crack tip where the material develops damage due to the high stress in the vicinity of the crack tip. The fracture process zone can be modelled by a cohesive zone or a bridging zone.

Fracture resistance: Fracture resistance is defined as the value of the J integral during crack growth. A fracture resistance curve (R-curve) is the J integral as a function of the crack extension.

J integral: A path-independent contour integral.

K-dominant region: The region near a crack tip (in a linear-elastic material), where the stress field approaches the stress field (the K-field) predicted by linear elastic fracture mechanics. Far away from the crack tip the stress state is controlled by the applied load and the specimen geometry. Within the fracture process zone, the stress is controlled by a cohesive law. Typically, the size of the K-dominant region is a few percent of the smallest relevant length of the specimen.

K- field: An universal, singular crack tip stress field predicted by linear elastic fracture mechanics.

Large-scale bridging: Large-scale bridging indicates that the bridging zone is larger than the K-dominant region.

Macroscale: The length scale where materials are treated as a continuum; typically the scale ranging from fractions of a millimetre to several metres.

Material laws: Mathematical descriptions of material behaviours that are independent of specimen size, geometry and load. Examples are constitutive laws such as stress-strain and traction-separation relations.

Microscale: The length scale where material microstructures (e.g. fibre diameters and spacing) are characterised and modelled; typically in the range from 1 μm to 1 mm.

Mixed-Mode: Mixed-Mode is used to describe a combination of Mode I and Mode II.

Mode I, Mode II, Mode III: The crack opening displacements can be considered being a combination of the 3 modes: pure opening normal to the crack tip (Mode I), sliding, tangential crack face displacements (Mode II) and tearing, out-of plane crack face displacements (Mode III).

Mode mixity: The phase angle of stress intensity factors of a crack subjected to Mixed-Mode crack opening displacements. For a homogenous specimen, a phase angle of 0° corresponds to pure Mode I while a phase angle of 90° is equivalent to Mode II.

R-curve: A resistance curve (R-curve) is the (rising) fracture resistance expressed in terms of the J integral as a function of the crack extension.

Separation: Opening (displacement difference) between the two surfaces of a crack in a cohesive zone.

Stress intensity factor: The stress intensity factor is a parameter that scales the magnitude of the singular stress field in the K-dominant region near a crack tip.

Structural scale: The length scale of typical engineering structures or products; typically in the range from decimetres to decametres.

Traction: The stress vector at a point associated with a plane with a normal vector (in cohesive zone modelling, the vector normal to the crack plane).

Work of separation: The work per unit cross section area of the cohesive tractions in a cohesive zone.

Abbreviations

DCB	double cantilever beam
DCB-UBM	DCB specimen loaded with uneven bending moments
ESEM	environmental scanning electron microscope
FPZ	fracture process zone
LEFM	linear elastic fracture mechanics
LVDT	linear variable differential transducer
SEM	scanning electron microscope

Symbols

Roman symbols (section where they are introduced)

a crack length (Section 1.4)
b width of bridging ligament (Section 4.2)
h height of bridging ligament (Section 4.2)
h_1 beam thickness of a thin beam of a medium size specimen (Section 5.1)
h_2 beam thickness of a thick beam of a medium size specimen (Section 5.1)
ℓ moment arm of forces applied to a medium size specimen (Section 5.1)
ℓ_1 moment arm for moment M_1 (Section 3.3)
ℓ_2 moment arm for moment M_2 (Section 3.3)
x_1 coordinate axis parallel to the crack propagation direction (Section 1.2)
x_2 coordinate axis perpendicular to the cracking plane (Section 1.2)
w width of plate (Section 4.1)

B specimen width (Section 2.3)
D offset distance for a force (Section 3.2)
D_K size of the K-dominant region (Section 1.4)
E Young's modulus (Section 1.4)
F applied shear force (Section 5.1)
F_{ss} applied shear force during steady-state cracking (Section 5.1)
$\mathcal{G}_c$ fracture energy of fibre/matrix interface (Section 4.2)
H specimen thickness (Section 2.3)
J_0 crack tip fracture energy (Section 1.8)
J_c work of separation (Section 1.4)
J_{ext} J integral evaluated along external boundaries of specimen (Section 1.8)
J_{loc} J integral evaluated locally around the fracture process zone (Section 1.8)
J_R fracture resistance (Section 1.8)
J_{ss} steady-state fracture resistance (Section 1.8)
K stress intensity factor (Section 1.1)
K_a stress intensity factor from applied loads (Section 1.7)
K_b stress intensity factor from bridging tractions (Section 1.7)
L size of fracture process zone (Section 1.2)
M applied moment for a DCB specimen (Section 2.3)
M^* resultant moment for a DCB specimen (Section 2.3)
M_1 applied moment for beam #1 of a DCB-UBM specimen (Section 2.3)
M_2 applied moment for beam #2 of a DCB-UBM specimen (Section 2.3)
P applied axial force (Section 2.3)
W width of a medium size specimen (Section 5.1)

Greek symbols (section where they are introduced)

α	crack/notch sensitivity parameter (Section 1.4)
δ_n	separation (opening) in the direction normal to the crack plane (Section 1.2)
δ_n^*	end-opening in the direction normal to the crack plane (Section 1.2)
δ_n^0	critical end-opening in the direction normal to the crack plane (Section 1.2)
$\dot{\delta}_n$	end-opening rate (Section 4.1)
δ_t	separation (crack sliding) parallel to the crack plane (Section 1.5)
δ_t^*	end-opening (end-sliding) parallel to the crack plane (Section 2.2)
δ_t^0	critical end-opening (end-sliding) parallel to the crack plane (Section 5.1)
δ^*	magnitude of the end-opening (Section 2.2)
φ^*	phase angle of the end-opening (Section 2.2)
η	number of bridging ligaments per unit cracked area (Section 4.2)
ν	Poisson's ratio (Section 2.3)
$\overline{\sigma}$	applied uniform stress (Section 4.1)
$\overline{\sigma}_{\max}$	maximum applied stress (Section 4.1)
σ_{fu}	fibre strength (Section 5.2)
σ_n	bridging/cohesive traction component normal to the cracking plane (Sect. 1.2)
$\hat{\sigma}_n$	maximum value of σ_n (Section 1.2)
σ_t	bridging/cohesive (shear) traction parallel to the cracking plane (Section 1.5)
$\hat{\sigma}_t$	maximum value of σ_t (Section 5.1)
ψ_{nom}	nominal mode mixity (Section 5.1)
Δa	crack extension (Section 1.8)
Δu_2	crack opening displacement normal to the crack plane (Section 1.6)
ΔJ_{ss}	increase in fracture resistance from initiation to steady-state (Section 4.2)
Φ	potential function (Section 2.2)
Γ_{ext}	integration path around the external boundaries of a specimen (Section 1.8)
Γ_{loc}	integration path locally around the fracture process zone (Section 1.8)

1. Introduction

"What is a scientist after all? It is a curious man looking through a keyhole, the keyhole of nature, trying to know what's going on"
Jacques Yves Cousteau

"If you wish to make an apple pie from scratch, you must first create the universe"
Carl Sagan

Modern society relies on the utilisation of a wide range of materials with distinctively different properties. For structural applications, a crucial material property is the mechanical strength. Therefore, a more accurate description of strength properties of materials and interfaces between dissimilar materials will allow for a safer and more cost-efficient use of materials.

This thesis focuses on polymer-matrix composites, such as carbon fibre/epoxy or glass fibre/polyester composites, which are used in many light-weight structures including aerospace structures, ships, aircraft and wind turbine blades. Usually, polymer-matrix composites are used in the form of multi-directional laminates that are bonded together by adhesive joints, since thermosetting polymers, unlike metals, cannot be welded together. The structure can therefore fail by:

- delamination (cracking along interfaces between layers inside the laminates)
- adhesive joint failure (cracking along the laminate/adhesive interfaces)

Such failures often involve crack bridging by intact fibres behind the damage front. An example of this is shown in Fig. 1.1. The length of the fracture process zone can be of the order of several centimetres. The present study is motivated by a desire to be able to determine cohesive laws for such large-scale fracture processes, allowing delamination and adhesive joint failure to be accurately characterised in terms of a material model, the cohesive law, which is then the source for accurate prediction of the load-carrying capability of structures through cohesive zone models that accounts for the large-scale fracture process zone.

1.1. Historical background

Analysis of the strength of materials goes back to Galileo, who reasoned that the strength of a bar subjected to an uniaxial stress should be proportional to its cross-sectional area and independent of its length, thus, introducing a stress-based criterion [2]. A stress criterion works well for ductile materials that fail as a result of plasticity. However, brittle materials such as ceramics and glass possess a large scatter in strength values since they fail from flaws and cracks which vary in size from specimen to specimen. In 1921 Griffith formulated an energy-based criterion for crack growth [3]: Crack growth will occur when the potential energy release per cracked area just equals the energy consumed by the fracture process (the fracture energy). In the 1950's and 1960's Irwin, Williams, Paris and co-workers developed the fundamentals of linear elastic fracture mechanics (LEFM) [4, 5]: When the crack tip fracture process zone and the plastic zone are small (small scale yielding), an universal singular stress field will dominate near the crack tip (the so-called K-

dominant region). The magnitude of the stress field scales with a constant called the stress intensity factor, *K*. A crack growth criterion based on a critical value of the stress intensity was shown mathematically to be equivalent to the Griffith energy release rate criterion [6]. Three pure modes of cracking were defined for a plane crack problem: Mode I (opening of the crack faces only in the direction normal to the cracking plane), Mode II (sliding, tangential crack opening displacements) and Mode III (tearing, out-of-plane crack opening displacements). Cyclic crack growth in metals was shown to be controlled by the range (difference between maximum and minimum) of the stress intensity factor [7]. Now, a large number of practical crack problems have been analysed by LEFM; many solutions can be found in fracture mechanics hand books [8, 9].

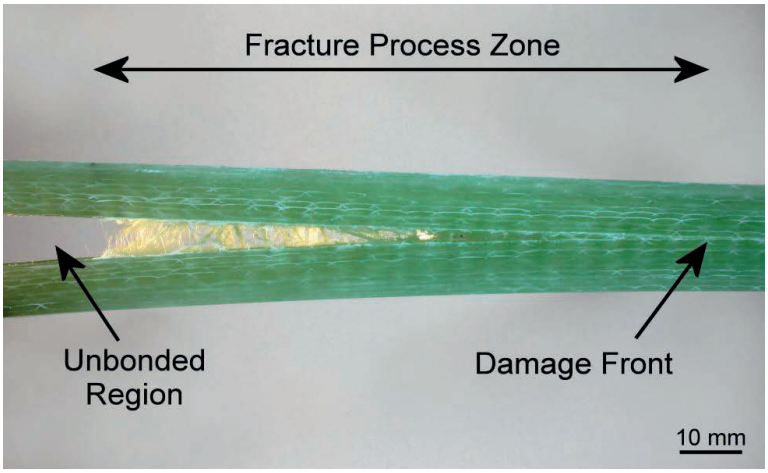

a)

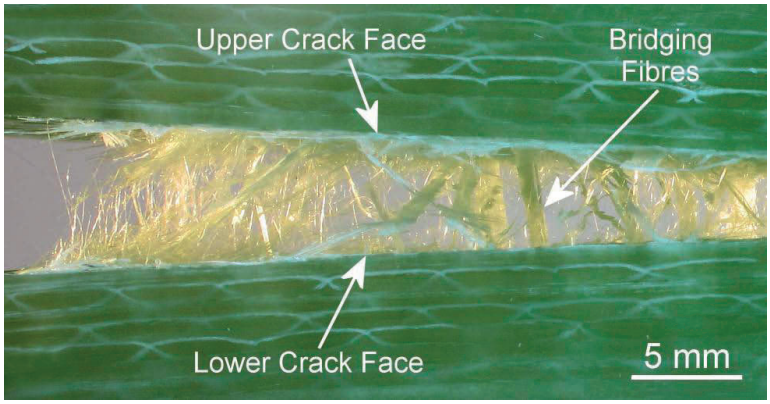

b)

Fig. 1.1 Photographs of a large-scale fracture process zone developing during delamination of a glass fibre polymer-matrix composite - a fracture mode encountered e.g. in load-carrying structures in boats and wind turbine blades. (a) The fracture process zone spans from the unbonded region (flaw) to the damage front. (b) A close view of the fracture process zone reveals crack bridging by fibres.

Cracking in homogenous, isotropic materials usually occurs under pure Mode I [10]. In contrast, cracking along weak planes or along interfaces between different materials occurs under a combination of modes, called Mixed-Mode cracking [11, 12]. The universal crack tip stress field for a crack along the interface between two dissimilar materials possesses a singularity that depends on the elastic properties of the two materials [13]. For many interfaces, the fracture energy has been found to increase significantly with an increasing amount of tangential crack opening displacement, usually expressed in terms of the mode mixity, ψ, which is the phase angle of the complex stress intensity factor in combination with a reference length [14-17].

Dugdale and Barenblatt, although from quite different perspectives, introduced the modelling of cohesive stresses of the fracture process zone. Dugdale [18] modelled a yield zone ahead of a physical crack. Barenblatt [19] introduced cohesive stresses to model the fracture process zone. These approaches remove the singular crack tip stress field that predicts an infinitely high stress at the crack tip, which was considered physically unrealistic. The path-independent J integral, introduced by Rice [20], extends fracture mechanics to non-linear elastic materials and unifies the classic LEFM stress intensity factor approach, the Griffith-Irwin energy release rate and the cohesive stress theory of Barenblatt. For small cohesive zones, the work of separation of the cohesive stress theory equals the Griffith fracture energy [20].

Micromechanical models were used for the prediction of bridging/cohesive laws for fibre bridging of cracks in ceramic-matrix composites, e.g. for the prediction of steady-state multiple matrix cracking in ceramic-matrix composites [21-23] and toughness due to fibre-pull-out [24-26].

Cohesive laws were used in numerical models (cohesive zone models) as a convenient way to simulate crack propagation in fundamental studies of the interplay between the fracture process zone and plasticity in metals [27, 28]. Mixed-Mode cohesive laws were used to study the effect of plasticity on the Mixed-Mode fracture toughness of bimaterial interfaces [29] and adhesive joints [30].

Cohesive laws were used for strength prediction of plates with holes and notches [31, 32], establishing a link between cohesive laws and notch sensitivity. The competition between crack propagation and splitting by shear bands was modelled by cohesive laws [33]. Cohesive laws were also used in modelling the fracture process zone in concrete [34], which can be of the order of several millimetres [35].

More recently, cohesive laws were used in numerical models of more engineering problems, such as the strength prediction of adhesive joints [36-39]. This involves a determination of the appropriate Mixed-Mode cohesive law parameters for the actual problem. These studies show that cohesive zone modelling can potentially be used in strength prediction of engineering structures. Therefore, the use of cohesive laws forms a paradigm shift; a cohesive law is a new material model that encompasses strength and work of separation. As such, cohesive laws need to be measured for materials and interfaces between dissimilar materials. It is thus necessary to develop approaches for accurate determination of cohesive laws. This is the theme of this thesis; reaching from theory to applications.

1.2 The concepts of fracture process zone and cohesive laws

The thesis focuses on the use of cohesive laws in polymer-matrix composites and adhesive joint problems where plasticity plays a negligible role (small-scale yielding). Therefore, crack tip plasticity is disregarded. Nevertheless, non-linear fracture mechanics is required, since the description of the fracture process zone can be strongly non-linear. Important problems that require cohesive zone modelling are for example delamination and adhesive joint failure of large structures such as wind turbine blades.

A fracture process zone (FPZ) is defined as the zone near a crack tip (or a notch) where the material strength is locally reduced due to damage caused by the stress field around the crack tip, see Fig. 1.2. The macroscopic crack tip is defined as the position where there is no physical connection between the crack faces, i.e., position $x_1 = -L$ in Fig. 1.2a. Assume that the material possesses a finite tensile strength, $\hat{\sigma}_n$. This is physically realistic since, far ahead of the crack where the stress is below $\hat{\sigma}_n$, the material should remain undamaged. At a certain distance, L, from the macroscopic crack tip, the stress has increased to $\hat{\sigma}_n$. Then, at this location the material develops damage. This position can be considered being the tip of a fictitious crack. In the zone given by $-L < x_1 < 0$, the material weakens and its ability to transfer stress decreases, while an opening, δ_n, develops. When loaded sufficient highly, the material will weaken completely at $x_1 = -L$, so that its ability to transfer stresses at the end-opening of the FPZ vanishes. The associated critical value of the end-opening, δ_n^* (the opening at $x_1 = -L$), is denoted δ_n^0. The stress ahead of the macroscopic crack tip is shown schematically in Fig. 1.2b. Fig. 1.2c shows a fictitious crack model [34] in which two crack tips can be considered: the damage front at $x_1 = 0$ and the macroscopic crack tip at $x_1 = -L$. The FPZ is now replaced by a cohesive zone in which the stress transfer between the two fictitious crack faces are described in terms of a cohesive law, which represents the traction-separation response of the FPZ. The cohesive law is assumed to be the same at any position along the cohesive zone (i.e., assuming homogenous material properties); the local traction, σ_n, is assumed only to be a function of the local separation, δ_n [40]. The cohesive law definition, $\sigma_n = \sigma_n(\delta_n)$, implies that during a monotonic opening, the traction at a given x_1-position depends only on the current separation at that position.

Since the material will not develop non-reversible deformation (damage) before the stress reaches $\hat{\sigma}_n$, the cohesive law should be formulated such that the cohesive traction can increase to $\hat{\sigma}_n$ without separation. However, once $\hat{\sigma}_n$ is reached, the cohesive traction decreases with increasing separation, as shown schematically in Fig. 1.2d.

The cohesive zone as described above has zero initial thickness. However, a cohesive law can also represent material having an initially finite thickness, h, such as an entire adhesive layer in adhesive joints. Then, the traction-separation curve also contains an initially rising part, representing the bulk deformation of the layer prior to damage ($\sigma_n < \hat{\sigma}_n$), as shown in Fig. 1.3. A comprehensive description of the concepts for modelling of a FPZ is given by Broberg [41].

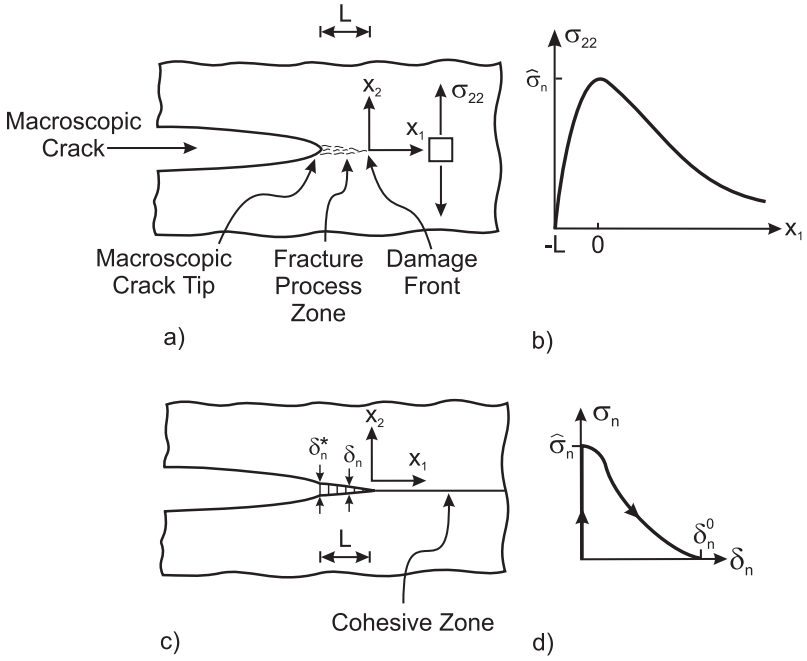

Fig. 1.2 Illustration of a cohesive law representing a fracture process zone (FPZ) that initially has zero thickness. (a) The physical problem: the development of a FPZ ahead of the macroscopic crack ($x_1 = 0$ corresponds to the damage front), (b) schematic of the stress ahead of the main crack tip, (c) the model: illustration of a cohesive zone, the mathematical representation of the FPZ, which is specified along the anticipated cracking path, from the macroscopic crack tip ($x_1 = -L$) to far ahead of the crack tip. Only a part of the cohesive zone is open (active), $-L < x_1 < 0$. (d) A cohesive law provides the relationship between the normal stress (traction), σ_n, and separation, δ_n, across the FPZ.

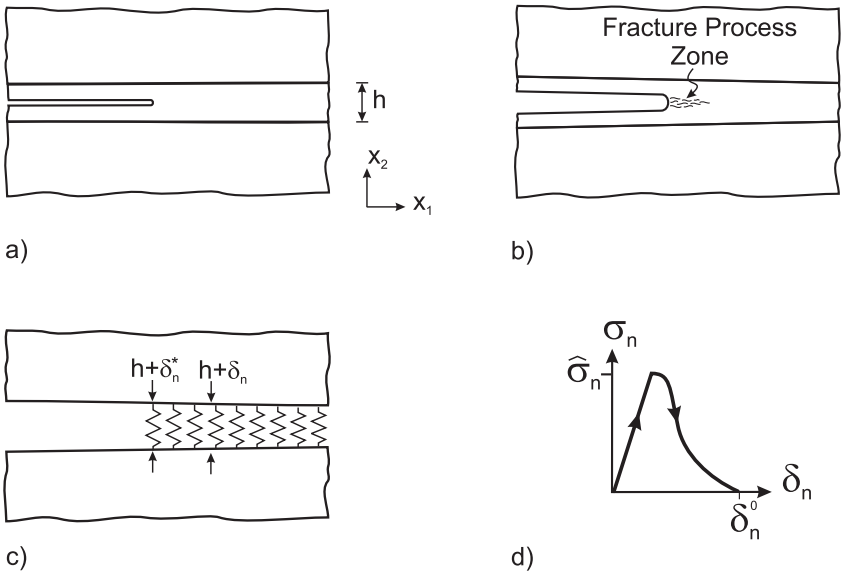

Fig. 1.3 The deformation of a finite thickness, *h*, e.g. the adhesive layer of an adhesive joint. (a) the stress free-state, (b) loaded, (c) the model, where the entire layer is represented by the cohesive law and (d) schematic illustration of a cohesive law representing the entire layer thickness. After Sørensen [A7].

1.3 Difference between cohesive zone and bridging zone

In some materials, the FPZ includes two distinct phenomena in two distinct regions: a sharp crack tip at the front of the FPZ and crack bridging in the wake region, see Fig. 1.4. In this case it can be convenient to treat the two phenomena independently. The criterion for propagation of the crack tip at the front of the FPZ is that the J integral evaluated around the crack tip equals a critical value, the crack tip fracture energy. The mechanical response of a bridging zone is a stress-separation law called the bridging law. The zone in which the bridging law is active is called the bridging zone. The difference between a bridging zone and a cohesive zone is that the bridging zone retains a stress singularity at the crack front; the cohesive zone does not. Therefore, in cohesive zone modelling, the cohesive zone should extend far ahead of the point where the cohesive zone opens, so that the model does not give a stress singularity in front of the cohesive zone [42]. The part of the cohesive zone where the crack is open ($-L < x_1 < 0$ in Fig. 1.2) is called the active cohesive zone.

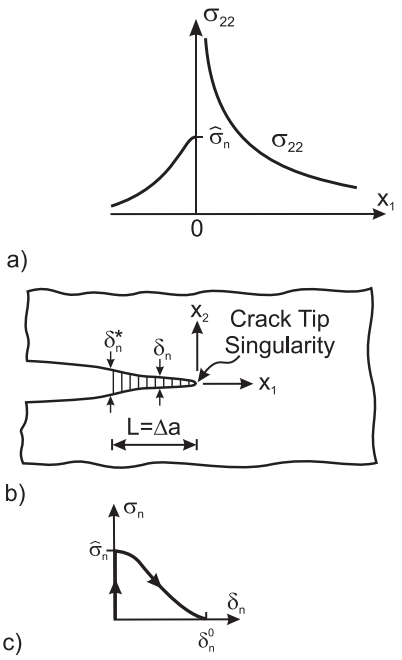

Fig. 1.4 Illustration of a bridging zone problem. (a) The damage front retains a crack tip fracture energy, J_0, and a singular stress field, (b) the bridging zone extends only to the crack tip, and (c) schematic of a bridging law.

1.4 Size of the fracture process zone

In modelling of structures with cracks, the size of the FPZ relative to the size of the structure controls whether or not it is necessary to model the FPZ by a cohesive zone. In order to illustrate this, consider a large structure with a crack. Denoting the work of separation of the cohesive law by J_c, a LEFM estimate of the order of magnitude of the FPZ size is [4, 43]:

$$L = \frac{J_c E}{\hat{\sigma}_n^2} \ , \qquad (1\text{-}1)$$

where E is the Young's modulus of the material. If the size of the FPZ is very small in comparison with the crack size, the surrounding stress field will approach the universal crack tip stress field of LEFM in the vicinity of the crack tip. However, within the FPZ, the stress field will be bounded by the peak tractions of the cohesive laws. Also, remote from the FPZ, the stress field depends on the external dimensions and geometry of the specimen. A so-called "K-dominant" region can exist in the intermediate distance. The K-dominant region is defined as the region near the crack tip where the stress field closely approaches that of the singular stress field of LEFM. The versatility of LEFM is that the stress and strain fields within the K-dominant region are the same regardless of the specimen size, geometry and load configuration [44]. Thus, two specimens of different sizes, geometries and loadings will have identical stress fields in the K-dominant region if their stress intensity factors are

identical. Then, all information regarding the specimen size, geometry and load is fed to the crack tip fracture process through the *K*-field. The fracture process will thus evolve in the same manner in the two specimens, regardless of their size, geometry and loading. Details of the cohesive law are then unimportant since a critical value of the stress intensity factor can be used as a criterion for crack growth.

Typically, the size of the K-dominant region, D_K, is a few percent of the crack length (or other relevant specimen dimensions such as the beam thickness, *H*, of DCB specimens [45]), say $D_K \approx 0.05\, a$, [46] where *a* is the crack length. LEFM is then applicable only when $L/a < 0.05$. A non-dimensional parameter, α, can be constructed as the ratio between the crack length and the approximate FPZ size given by eq. (1-1) [31]:

$$\alpha = \frac{a}{L} = \frac{a\hat{\sigma}_n^2}{J_c E} \ . \qquad (1\text{-}2)$$

A large value of α (e.g. $\alpha > 20$) implies that the FPZ is small and may be confined in the K-dominant region, so that LEFM is applicable. A small value of α indicates that the FPZ is large in comparison with the size of the K-dominant region so that the K-field alone does not control the loading in the FPZ; then the facture behaviour depends on specimen geometry [47]. For many modern materials and structures α is small so that the criterion for a small scale FPZ is not fulfilled. Examples are delamination of polymer-matrix composites and ceramic-matrix composites [48]. Then, the appropriate material property is the cohesive law and cohesive zone modelling should be used.

The parameter α also illustrates the interaction between cohesive law parameters and the structural parameters (crack size and Young's modulus). For a given material, having specific fracture properties, a sufficiently large structure with a large crack length will contain a small-scale FPZ since α becomes large. Conversely, a geometrically similar, but sufficiently small, specimen with a smaller crack will possess a large-scale FPZ since α is smaller.

The concept of a large-scale fracture process zone also applies for bridging problems. If the size of a bridging zone is large in comparison with the size of the K-dominant region around the crack tip, the material is said to experience large-scale bridging.

1.5 Mixed-Mode bridging/cohesive laws

Under Mixed-Mode opening, both normal and shear stresses are transferred between the crack planes within the FPZ. Denote σ_n and σ_t as the normal and the tangential (shear) components of the traction vector along the plane of the FPZ. It is reasonable to assume that both σ_n and σ_t depend on both the normal and tangential opening displacements (crack face separations), δ_n and δ_t,

$$\sigma_n = \sigma_n(\delta_n, \delta_t) \quad \wedge \quad \sigma_t = \sigma_t(\delta_n, \delta_t) \ . \qquad (1\text{-}3)$$

The notation used in eq. (1-3) implies that the bridging/cohesive stresses at a given point within the FPZ depend only on the current openings, not the opening history.

Mixed-Mode cohesive laws for the normal and shear tractions can be taken to be completely independent (viz., the normal traction depends only on the normal opening displacement, but not the tangential opening displacement and visa versa for the shear traction) [38, 29]. In other cases, a specific coupling is assumed between the cohesive tractions and separations [29, 49]. Usually, Mixed-Mode cohesive laws are taken to be derived from a potential function [27, 29, 50], but sometimes not [51]. Some Mixed-Mode cohesive laws possess the same work of separation (fracture energy) for all opening modes [27, 29]. Other models have a larger Mode II fracture energy than the Mode I fracture energy [38, 39].

1.6 Experimental approaches for determination of bridging/cohesive laws

As discussed above (Section 1.4), many engineering problems involve large-scale bridging, which requires the use of non-linear fracture mechanics, e.g., the use of the J integral. However, most fracture mechanics test methods for composite materials have been developed within the context of LEFM [52, 53]. No analytical J integral solutions are available for these LEFMs specimens. Therefore, new experimental methods for the accurate determination of bridging/cohesive laws are needed. A brief overview will be given in the following of experimental approaches that have been proposed for the determination of Mode I bridging/cohesive laws, and their advantages and limitations will be highlighted. A requirement for all approaches is that, for all points within the bridging/cohesive zone, the opening should increase in a monotonic, stable manner, such that it is possible to measure the entire bridging/cohesive law. It is thus mandatory to use experiments that give stable crack growth.

The most straightforward experimental method is the direct tension method. The applied stress and the displacement difference between two sides of a localized zone are recorded [54]. In practice, however, it is difficult to obtain stable and uniform separation across the specimen width [35] (the x_1-direction in Fig. 1.5a).

Another method involves the calculation of bridging tractions from measurements of the crack opening profile. The principle behind this approach is that the bridging tractions reduce the crack opening, Δu_2, as indicated in Fig. 1.5b. The crack opening profile depends on the specimen geometry, the applied load and the distribution and magnitude of the bridging traction along the bridging zone. The measured crack opening profile can be recreated in models, using superposition of stress intensity factors, by adjusting the bridging tractions [55, 56]. In principle, if the bridging zone is fully developed (i.e., $\delta_n^* \geq \delta_n^0$), the entire bridging law can be determined from a single measurement of the crack opening profile. However, in practice, it is preferable to use data from several cracks having different bridging zone lengths (and different values of the end-opening, δ_n^*) to reduce the sensitivity to noise in the data [55]. Since the bridging tractions are likely to change if the crack opening is reduced, the crack opening profile should be measured for a stationary crack at a load level corresponding to cracking. However, it is difficult to avoid crack growth during the measurement.

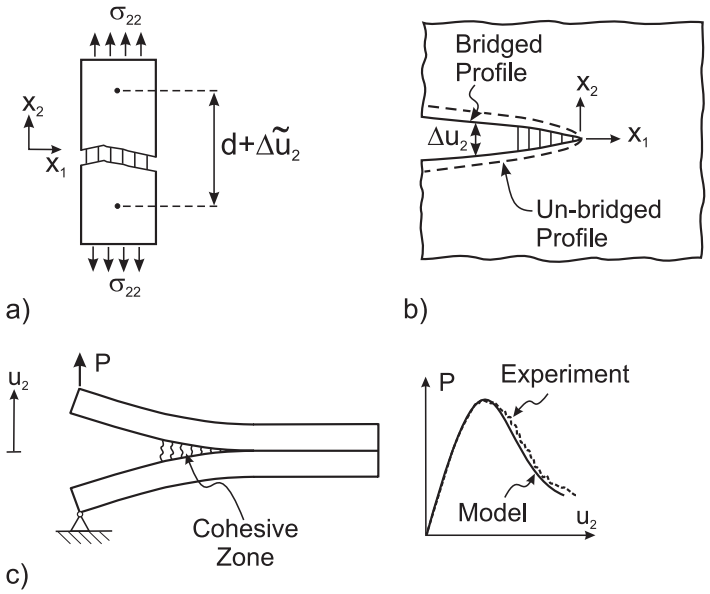

Fig. 1.5 Commonly used approaches for experimental determination of macroscale bridging/cohesive laws: (a) measurement of localised deformation during direct tension, (b) measurement and modelling of the crack opening profile and (c) measurement and modelling of load-displacement relationship.

Another method to obtain cohesive laws from experiments is to perform numerical simulations of tested specimens. A number of incremental finite element simulations are made, each using a different trial cohesive law. The trial cohesive law that gives the best agreement with the overall experimental data, e.g. the load-displacement curve [39] or the near-tip displacement field [38], is then takes to be the "true" cohesive law, as indicated in Fig. 1.5c. A drawback of such approaches is that the cohesive laws cannot be identified better than the assumed trial cohesive laws allow. For instance, for Mixed-Mode cohesive laws, if uncoupled cohesive laws are assumed, the parameter identification process cannot reveal if the cohesive laws of the experiments in reality were coupled. If a specific coupling has been assumed, the approach cannot uncover if the coupling in the experiment was different. Finally, if opening path history-independent cohesive laws were assumed, the approach cannot reveal if the true cohesive laws were opening-path dependent or not.

A J integral based approach for the determination of Mode I bridging/cohesive laws has been suggested by Li and Ward [57]. The approach includes the simultaneous measurement of the end-opening of the bridging zone, δ_n^*, and the J integral value during crack growth. The bridging/cohesive law is then determined by differentiation. Li and Ward [57] determined the J integral from tests of two specimens having different crack lengths, using a graphical method devised for the J integral determination of non-linear, elastic materials [58]. The J integral approach is described in more detail in Section 1.8.

1.7 Analysis of large-scale bridging by a stress intensity approach

A major complication for a crack problem with large-scale bridging is that the assumptions of LEFM are not fulfilled, since the FPZ is larger than the size of the K-dominant region. If the material outside the FPZ behaves linearly elastic, calculation methods, such as superposition of stress intensity factors, can be used for large-scale bridging problems, e.g. [47, 59]

$$K = K_a + K_b, \tag{1-4}$$

where K is the crack tip stress intensity factor, K_a is the stress intensity factor for the applied load and K_b is the stress intensity factor of the bridging stresses (K_b is negative when the bridging stresses retard the crack opening). The stresses in the fracture process zone are regarded as surface tractions like any other external stresses.

1.8 J integral analysis of a Mode I crack with large-scale bridging

The use of the J integral is valid for large-scale bridging problems [40]. Consider a Mode I crack where the FPZ is modelled by a Mode I bridging law, $\sigma_n = \sigma_n(\delta_n)$ and with a crack tip fracture energy, J_0. Assume that the crack is initially free from bridging. The unbridged crack will start propagating when J_{loc}, the J integral evaluated along a local path, Γ_{loc}, around the FPZ gives:

$$J_{loc} = J_0. \tag{1-5}$$

Due to the integration-path independence of the J integral [20], the J integral evaluated around the FPZ and around the external boundaries (Γ_{ext} in Fig. 1.6) are identical,

$$J_{ext} = J_{loc}. \tag{1-6}$$

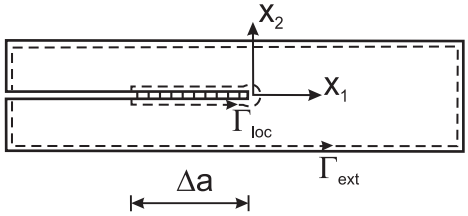

Fig. 1.6 Integration paths for the J integral when analysing a DCB specimen along a path, Γ_{loc}, locally around the FPZ and along a path, Γ_{ext}, along the external boundaries of the specimen.

The J integral value during cracking is labelled J_R. When the crack tip has propagated a distance Δa from the initial position of the crack tip, a bridging zone has formed between the original and present crack tip, such that the bridging stress operates along the entire bridging zone, $L = \Delta a$. Then an application of the J integral gives [20, 40]

$$J_R = \int_0^{\delta_n^*} \sigma_n(\delta_n)\, d\delta_n + J_0 \,. \qquad (1\text{-}7)$$

In eq. (1-7), δ_n^* is the end-opening, i.e., the crack face separation at the initial crack tip position (x_1 = -Δa in Fig. 1.6). Equation (1-7) can be given a physical interpretation as the work per unit cross section area of the bridging stress at the end of the bridging zone, i.e., at the position of the initial crack tip, as shown in Fig. 1.7.

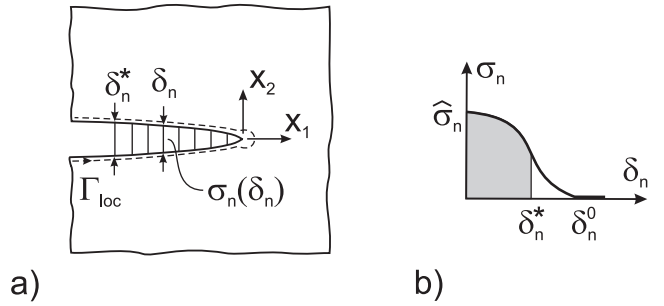

Fig. 1.7 J integral analysis around the FPZ. (a) The integration path, and (b) the contribution to the J integral from a bridging zone equals the area under the stress-separation curve from zero to the end-opening. After Sørensen *et al.* [A1].

If the end-opening increases monotonically with $\sigma_n > 0$, it follows from eq. (1-7) that the J integral value increases as the crack extends. As shown in Fig. 1.8, J_R rises, eventually attaining a steady-state value, J_{ss}, as the end-opening reaches the critical separation where the bridging stress has decreased to zero, δ_n^0. The bridging zone is then said to be fully developed. With further crack extension, the fracture resistance remains at the steady-state value

$$J_{ss} = \int_0^{\delta_n^0} \sigma_n(\delta_n)\, d\delta_n + J_0 \,, \qquad (1\text{-}8)$$

which is the work of separation per unit fracture surface area.

Equations (1-6) and (1-7) provide a way to connect the bridging law in the FPZ to the external load.

From (1-7) it follows [40, 57, 60]

$$\sigma_n(\delta_n^*) = \frac{dJ_R}{d\delta_n^*} \,. \qquad (1\text{-}9)$$

Thus, the bridging law can be determined by recording the J integral value and the end-opening during an experiment and performing the differentiation (1-9). In order to use the J integral approach, all that is needed is a J integral solution for the test

specimen. Furthermore, it is fairly easy to evaluate the accuracy of an idealised bridging law by performing the integration (1-7) and comparing the $J_R - \delta_n^*$ relationship obtained with the measured $J_R - \delta_n^*$ data.

When analysing a cohesive zone, the same results ((1-7) with J_0 = 0 and (1-9)) will be obtained when Γ_{loc} is chosen such that the integration path extends so far ahead of the crack that the cohesive zone remains closed where the integration path crosses the cohesive zone.

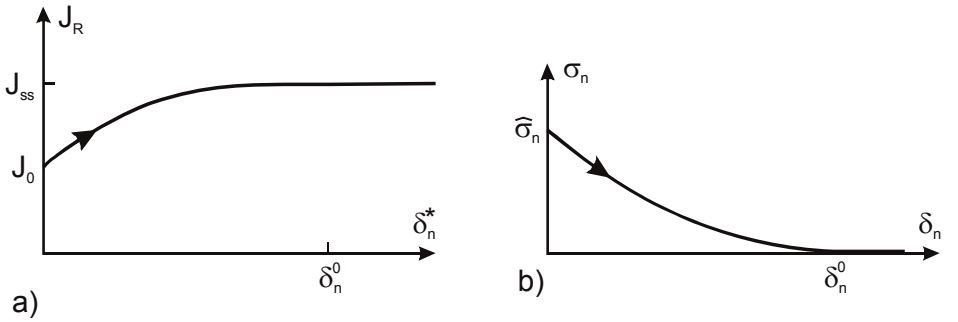

Fig. 1.8 Schematic of (a) the fracture resistance, J_R, as a function of the end-opening, δ_n^*, and (b) the associated bridging law.

1.9 Unresolved issues regarding bridging/cohesive laws

As discussed in Section 1.5, a number of model approaches and couplings between tractions and separations are possible for Mixed-Mode cohesive laws. A Mixed-Mode cohesive law (i.e. incorporating a specific coupling) that works well for one material may not be suitable for another material. An important theoretical issue is whether a Mixed-Mode cohesive law can be derived from a potential function or whether the Mixed-Mode cohesive law of a given material is opening-path history dependent. Therefore, it is relevant to consider which Mixed-Mode cohesive model is the most appropriate for a given material. In order to clarify these issues, better experimental approaches are required for the determination of cohesive laws under Mode I and Mixed-Mode (Mode I and Mode II).

A common view in the literature is that the most important cohesive law parameters for strength predictions are the work of separation (the area under the traction-separation curve) and the peak traction value. While this has indeed been shown to be true for a small-scale fracture process zone [28], there are cases where the shape of the cohesive law is not insignificant [32]. Although the shape of bridging/cohesive laws may be of minor importance for strength predictions at the structural scale, the shape of a cohesive law contains information about the fracture behaviour of a material at a small scale (microscale toughening mechanisms). Micromechanical models and experimental results have shown that different crack bridging mechanisms have a very different bridging law shape. For instance, crack bridging by weakly bonded, frictionally restrained long fibres, oriented perpendicular to the crack plane, gives a bridging stress that increases with the opening [21, 61, 62]. In contrast, crack bridging by long fibres, oriented parallel to the crack plane gives a

bridging stress that decreases with increasing crack opening displacement [48, 63]. This demonstrates that the shape of the bridging/cohesive law contains valuable information regarding the underlying crack bridging mechanisms, and thereby serves as a tool to guide microstructural optimisation. The establishment of connections between microscale mechanisms and macroscale bridging/cohesive laws through micromechanical modelling is a necessity for optimisation of macroscopic properties based on microscale parameters (microscale optimisation).

Another common view in the literature is that bridging/cohesive laws are material laws, i.e., independent of specimen size, geometry and loading. This presumption can be examined (i) by comparing cohesive laws, measured from specimens having different size, geometry and loading and/or (ii) by ascertain whether a cohesive law found for one specimen size, geometry and loading can be used for the accurate strength prediction of other specimens of different size, geometry and loading.

1.10 Aims of the thesis

The objectives of the thesis fall into two groups:

(A) To develop theoretical analyses, measurement methods and data analysis tools for determination of cohesive laws under large-scale bridging.

(B) To relate microscale toughening mechanisms to macroscale bridging/cohesive laws for delamination of fibre composites and for adhesive joint failure.

Under topic (A), the aims are to:

A1. Develop a theoretical approach for the determination of Mixed-Mode cohesive laws

A2. Develop fracture mechanics test configurations that are suitable for Mode I, Mode II and Mixed-Mode cohesive laws determination

Under topic (B), the aims are to:

B1. Investigate whether the shape of bridging/cohesive laws can be used for extracting information regarding the dominating microscale toughening mechanism

B2. Investigate whether bridging/cohesive laws can be regarded as material laws

B3. Investigate whether it is realistic to use bridging/cohesive laws that are based on a potential function

B4. Investigate whether real Mixed-Mode cohesive laws are coupled or uncoupled

1.11 Overview of methods and results

In order to meet the objective stated above, new analysis methods and new experimental methods are developed. These include:

- Generalisation of the J integral method to determine Mixed-Mode cohesive laws, (i.e., both the normal and shear tractions) (Chapter 2)

- Analytical J integral solutions for large-scale bridging problems for Mode I, Mode II and Mixed-Mode test specimens (Chapter 2)

- Three fracture mechanics test devices for J integral testing. Two of these are for microscale observation of toughening mechanisms and one is for Mixed-Mode testing of macroscale specimens (Chapter 3).

The thesis covers three length scales: microscale, macroscale and structural scale, establishing connections between these length scales. The multi-scale approach is illustrated in Fig. 1.9.

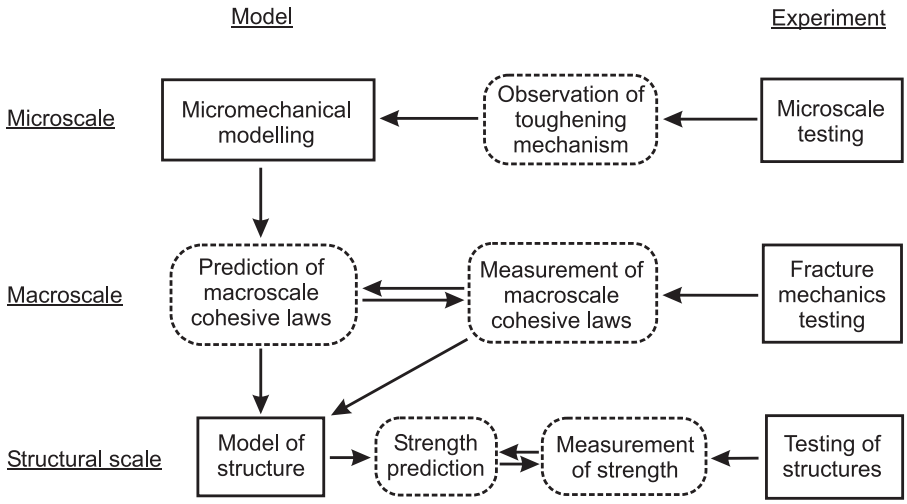

Fig 1.9 Illustration of the multi-scale approach used in this thesis. Micromechanical models are used for prediction of macroscale cohesive laws. Macroscale cohesive laws are measured and compared with cohesive laws predicted by micromechanical modelling and are used for strength prediction of generic structures (representative for components).

Microscale toughening mechanisms operating in the FPZ are identified by in situ observations as a basis for the development of micromechanical models for prediction of macroscale bridging/cohesive laws of fibre composites with a polymer-matrix. Macroscale bridging/cohesive laws are measured in an attempt to verify the laws predicted by the micromechanical models. Macroscale bridging/cohesive laws are used for the prediction of the strength (load-carrying capability) of real

structures. The accuracy of such predictions is assessed by comparing predicted and experimentally measured strength values (see Fig. 1.9).

Four Case Studies (Chapter 4 and Chapter 5) have been chosen for verification of the approaches developed and for meeting the objectives. The case studies cover investigations related to toughening mechanisms in adhesive joints and delamination of polymer-matrix composites:

- In order to investigate whether measured Mode I cohesive laws are material laws, i.e. independent of specimen size, geometry and loading, the cohesive law of an adhesive joint is measured and used for predicting the strength of bonded panels. The strength of such panels are measured and compared with the strength predictions Furthermore, the Mode I cohesive law of a unidirectional polymer-matrix composite is determined for DCB specimens having different beam thickness (Case Studies I and II, Sections 4.1 and 4.2)

- In order to investigate whether there is a connection between a microscale toughening mechanism and the shape of the resulting cohesive law, the Mode I toughening mechanism in an unidirectional polymer-matrix composite is characterised. The shape of the bridging law is predicted by a micromechanical model and compared with the measured macroscale bridging law (Case Study II, Section 4.2)

- In order to investigate whether measured Mixed-Mode cohesive laws are material laws, Mixed-Mode cohesive laws, obtained from fracture mechanics testing of adhesive joint test specimens of a polymer-matrix composite, are used to predict the strength of large specimens at the structural scale. The strength of large specimens is determined experimentally and compared with predictions (Case Study III, Section 5.1)

- In order to investigate whether it is realistic to use cohesive laws derived from a potential function, a micromechanical model is developed, based on an experimentally-observed Mixed-Mode toughening mechanism in polymer-matrix composites. It is investigated whether a potential function exists for the cohesive tractions (Case Study IV, Section 5.2)

- In order to investigate whether Mixed-Mode cohesive laws of real materials are coupled or uncoupled, Mixed-Mode cohesive laws are determined for the delamination of a polymer-matrix composite (Case Study IV, Section 5.3)

2. Theoretical framework

"For our remote ancestors, a specific ability to do sophisticated mathematics can hardly have been a selective advantage but a general ability to understand could well have"
Roger Penrose

"It doesn't matter how beautiful your theory is, it doesn't matter how smart you are. If it doesn't agree with experiment, it's wrong. That's all there is to it"
Richard Feynman

This chapter summarises the theoretical development regarding the use of the J integral approach for determination of Mode I [A1] and Mixed-Mode cohesive laws [A2]. Analytical solutions for several fracture mechanics test specimens suitable for cohesive law determination are presented.

2.1 J integral analysis under large-scale bridging

As discussed in Section 1.7, cracking problems involving large-scale bridging can be analysed by the superposition of stress intensity factors of the applied load and of the bridging stress, eq. (1-4). Sørensen *et al*. [A1] showed that for two Mode I DCB specimen configurations there is consistency between analyses of large-scale bridging problems by the stress intensity approach and the J integral approach. However, the LEFM relation

$$J_{ext} = \frac{K_a^2}{E} \qquad (2\text{-}1)$$

does not hold true under large-scale bridging [A1]. In eq. (2-1), J_{ext} is the J integral evaluated along the external boundaries of the fracture specimen where the loads are applied and E is the Young's modulus of the material. Since the relation (2-1) is not valid under large-scale bridging, text book solutions for stress intensity factors cannot be used for calculation of J_{ext} for large-scale bridging problems [A11]. Consequently, most well-known LEFM fracture mechanics test specimens used for composite materials (see e.g. [52, 53]) are not well suited for the determination of J_{ext}, since J_{ext} depends on details of the yet unknown cohesive law, as also discussed by Bao and Suo [64].

A new generation of fracture mechanics test specimens, which consists of configurations that have analytical solutions for J_{ext} even for large-scale bridging, has been developed [40, A3, A4]. Some of these specimens are shown in Fig. 2.1. These specimens are analysed in Section 2.3.

With J_{ext} determined, the next step is to utilise the path-independence of the J integral for a determination of bridging/cohesive laws. This is the theme of the next section.

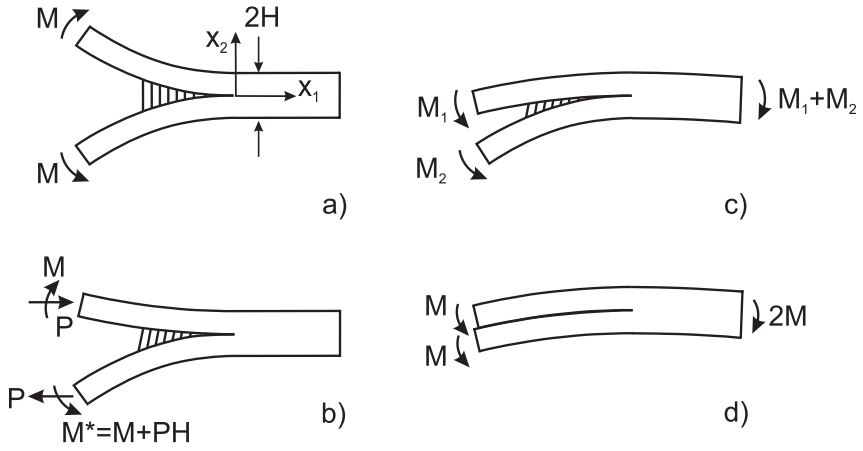

Fig. 2.1 Examples of test specimen configurations having analytical J integral solutions that are independent of details of the bridging/cohesive laws: (a) A DCB specimen loaded with pure bending moments for pure Mode I, (b) a DCB specimen loaded with a combination of axial forces and bending moments and (c) a DCB specimen loaded with uneven bending moments (DCB-UBM) for Mixed-Mode and (d) DCB specimen loaded with pure, equal moments for pure Mode II testing. From Sørensen and Jacobsen [A4].

2.2 J integral analysis of Mixed-Mode cohesive laws

The Mode I approach described above was generalised to Mixed-Mode bridging/cohesive laws by Sørensen and Kirkegaard [A2]. No restrictions are made regarding the shape of the cohesive laws and the manner in which the tractions depend on δ_n and δ_t - the cohesive law shape and possible coupling will come out of the analysis.

Applying the J integral around the FPZ during cracking gives:

$$J_R = J_{loc} = \int_0^{\delta_n^*} \sigma_n(\delta_n, \delta_t)\, d\delta + \int_0^{\delta_t^*} \sigma_t(\delta_t, \delta_t)\, d\delta_t + J_0, \qquad (2\text{-}2)$$

where δ_t^* is the end-sliding, see Fig. 2.2, and J_0 is the crack tip fracture energy. The physical interpretation of eq. (2-2) is similar to the one given for pure Mode I: The J integral equals the sum of the work per unit area of the bridging/cohesive tractions and the crack tip fracture energy.

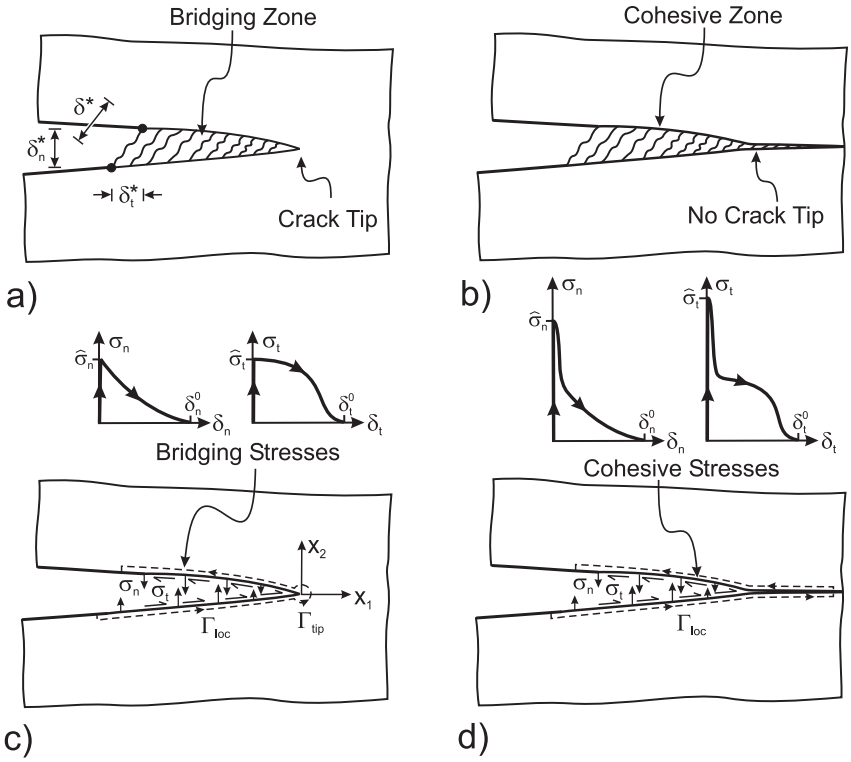

Fig. 2.2 Schematic illustration of Mixed-Mode bridging/cohesive laws. A long failure process zone can be modelled (a) as a crack tip and bridging zone or (b) as a long cohesive zone with no crack tip. (c) The bridging laws represent the stresses transmitted between the crack faces behind the crack tip while (d) a cohesive zone is prescribed along the anticipated cracking path until far ahead of the crack. From Sørensen and Jacobsen [A4].

Assume that the bridging/cohesive tractions can be derived from a potential function $\Phi = \Phi(\delta_n, \delta_t)$ with $\Phi(0;0) = 0$:

$$\sigma_n(\delta_n,\delta_t) = \frac{\partial \Phi(\delta_n,\delta_t)}{\partial \delta_n} \qquad \sigma_t(\delta_n,\delta_t) = \frac{\partial \Phi(\delta_n,\delta_t)}{\partial \delta_t}. \tag{2-3}$$

This is not a strong assumption, since it is already assumed that the bridging/cohesive tractions are opening-path history-independent (see Section 1.5). Inserting eq. (2-3) into eq. (2-2) gives

$$J_R = \Phi(\delta_n^*, \delta_t^*) + J_0 \tag{2-4}$$

and

$$\sigma_n(\delta_n^*,\delta_t^*) = \frac{\partial J_R(\delta_n^*,\delta_t^*)}{\partial \delta_n^*} \qquad \sigma_t(\delta_n^*,\delta_t^*) = \frac{\partial J_R(\delta_n^*,\delta_t^*)}{\partial \delta_t^*} \tag{2-5}$$

The fracture resistance, J_R, should thus be considered as being a function of δ_n^* and δ_t^* or alternatively a function of the magnitude

$$\delta^* = \sqrt{\delta_n^{*2} + \delta_t^{*2}} \tag{2-6}$$

and the phase angle

$$\varphi^* = \tan^{-1}\left(\frac{\delta_t^*}{\delta_n^*}\right) \tag{2-7}$$

of the end-openings.

Mixed-Mode bridging/cohesive laws can be derived by simultaneous measurements of J_R, δ_n^* and δ_t^* and performing partial differentiation of the J_R data according to (2-5). This can be done by numerical differentiation and by fitting a function to the $J_R = J_R(\delta_n^*, \delta_t^*)$ data. Sørensen and Kirkegaard [A2] proposed fitting the J_R-δ_n^*-δ_t^* data with a sum of orthogonal polynomials (Chebyshev polynomials). The approach was tested against artificial data, without and with random noise [A2]. It was found that that (a) the number of experiments having different phase angles of openings should be eight or more, (b) the maximum polynomial degree should be 3 or higher to obtain a reasonably accurate bridging law shape, and (c) the standard deviation of the noise in the data should be less than 1% of the maximum value of the data.

2.3 J integral analysis of test specimens

As mentioned in Section 2.1, for most fracture mechanics test specimens experiencing large-scale bridging, the J integral evaluated along the external boundaries depends on the bridging/cohesive law. This complicates the cohesive law determination.

Fig. 2.1 shows some of the new fracture mechanics tests configurations that allow the calculation of the J integral along the external boundaries in closed analytical form [A4]. They share the common feature that they are slender beam specimens loaded with moments and axial forces. Then, the only contributions to J_{ext} come from the loaded edges. Providing that the beams are sufficiently long, the J integral can be evaluated long a path where the beams are subjected to a combination of uniform axial strain and pure bending, independent of the details of the bridging/cohesive law operating in the FPZ.

A symmetric double cantilever beam (DCB) specimen loaded by pure moments (Fig. 2.1a) is a pure Mode I specimen. The J integral evaluated around the external boundaries gives under plane strain conditions [40]

$$J_{ext} = \left(1-\nu^2\right)\frac{12M^2}{B^2H^3E}\ , \tag{2-8}$$

where M is the applied bending moment, B is the specimen width (in the x_3-direction), H is the beam thickness, E is the Young's modulus and ν is the Poisson's ratio, respectively. For plane stress, the term $1-\nu^2$ is replaced by unity. This specimen configuration was first suggested for large-scale bridging studies by Suo *et al*. [40].

A DCB specimen loaded with a combination of axial force, P, and a bending moment, M, shown in Fig. 2.1b, is a Mixed-Mode specimen [65]. The reaction moment, M^*, is given by moment equilibrium, $M^* = M + PH$, where H is the beam height. The J integral for this specimen configuration is (plane strain) [A5]:

$$J_{ext} = \left(1-\nu^2\right)\frac{7P^2H^2 + 12M^2 + 12PHM}{B^2H^3E}. \qquad (2\text{-}9)$$

Mode I is recovered for $P = 0$ and Mode II is obtained for $M/PH = -1/2$. The specimen is subjected to Mixed-Mode for $-1/2 < M/PH < \infty$.

The combined axial force and moment loading can be created by applying a single force (see Section 3.2). Unfortunately, for Mode II dominated loading, the magnitude of the resulting moment is influenced by the beam deflection. Therefore, Sørensen *et al*. [A3] proposed another Mixed-Mode specimen, the DCB specimen loaded with uneven bending moments (DCB-UBM). The two bending moments, M_1 and M_2, are taken positive in the directions shown in Fig. 2.1c. The J integral evaluated around the external boundaries gives (plane strain):

$$J_{ext} = \left(1-\nu^2\right)\frac{21\left(M_1^2 + M_2^2\right) - 6M_1M_2}{4B^2H^3E} \quad for \quad \left|M_1\right| \le M_2. \qquad (2\text{-}10)$$

Pure Mode I is obtained for $M_1/M_2 = -1$. For $-1 < M_1/M_2 < 1$, the specimen is subjected to Mixed-Mode. Setting $M_1/M_2 = 1$ gives pure Mode II (Fig. 2.1d). Then, the J integral can be expressed as (plane strain):

$$J_{ext} = \left(1-\nu^2\right)\frac{9M^2}{B^2H^3E}. \qquad (2\text{-}11)$$

For all the test specimens described above, the J integral is independent of the crack length. Fracture tests using these specimens are anticipated to be stable under displacement (rotation) control, since the forces and moments decrease when crack growth takes place under "fixed grip" conditions. Another prominent feature of these test specimens is that they are "steady-state" specimens [A4]; when the bridging/cohesive zone is fully developed, cracking will occur in a steady-state fashion, in the sense that the FPZ retains its size but translates along with the crack tip in a self-similar manner. For other specimen configurations, e.g. the force loaded DCB, the FPZ changes in size even after J_{ss} has been attained [40, A11]. The test specimen configurations described here form the basis for development of the test devices described in the next Chapter.

3. Development of experimental methods

"*If you can dream it, you can do it*"
Walt Disney

"*It is the weight, not numbers of experiments that is to be regarded*"
Isaac Newton

As illustrated in Fig. 1.9, fracture mechanics testing at the microscale and macroscale are central in the study of cohesive laws. This chapter describes the three new testing devices that were developed for the microscale study of toughening mechanisms and for the determination of macroscale bridging/cohesive laws. Two dedicated fracture mechanics test devices were designed with the aim of enabling high-magnification in-situ observations of toughening mechanisms in test specimens under pure Mode I and Mixed-Mode crack opening, respectively [A5, A6]. The third device is a laboratory test device developed for determination of macroscale Mixed-Mode bridging/cohesive laws [A3]. During the design phase, particular attention was given to ensure that the test devices are statically determinant, so that the stresses at the surfaces of the specimens are also well-defined in the deformed state.

3.1 ESEM test device for in-situ observation of microscale toughening mechanisms under Mode I cracking (DCB specimen loaded with pure bending moments)
A test device was developed for Mode I fracture mechanics testing in an environmental scanning electron microscope (ESEM). Scanning electron microscopes (SEMs) allow a much higher magnification and depth of focus than light microscopes. In conventional SEMs, the surfaces to be investigated must be electronically conductive. A polymer-matrix composite will therefore require a thin coating of a conducting layer to prevent charging-up. Upon cracking, new coating-free fracture surfaces will charge-up, preventing imaging of the new cracked surfaces, which typically would be the most interesting thing to investigate. In contrast, the ESEM has the advantage that the surface to be imaged does not need to be conductive. Therefore, it is attractive to perform mechanical testing in an ESEM; damage and fracture mechanisms can be observed in-situ at large magnifications without the charging-up of newly-created fracture surfaces. Therefore, the fracture mechanics test devices were developed for use in an ESEM.

The loading device for Mode I fracture mechanics testing has to be placed inside the vacuum chamber of the ESEM, and mounted on a base that is attached to a moveable *x-y-z* stage. Due to the relatively small size of the ESEM vacuum chamber, the loading device must be compact. The test specimen is therefore smaller than those used in standard materials testing. The Mode I test configuration is a DCB specimen loaded by pure bending moments (Section 2.3). Since this test configuration gives stable cracking, it is possible to grow cracks in small increments and thus observe in-situ how toughening mechanisms evolve.

The loading device is shown in Fig. 3.1. Nearly all parts are made of non-magnetic materials (primarily stainless steel) to minimize disturbance of the magnetic lenses of the microscope. The design is made such that the grips, which lie on a platform and

transfer the pure moments to the DCB specimen, are loaded by the use of a metallic band that tightens as the base fixture is opened, being driven by an electric motor. The magnitude of the moment is measured by strain gauges that act as a load cell (see Fig. 3.1). An acoustic emission sensor can be mounted on the test specimen for the purpose of detecting the onset of damage.

Stable crack growth has been demonstrated using the loading device [A6]. It is possible to measure the crack opening displacements with an accuracy better than 30 nm [A6]. The loading device is thus well suited for the study of fracture processes in materials.

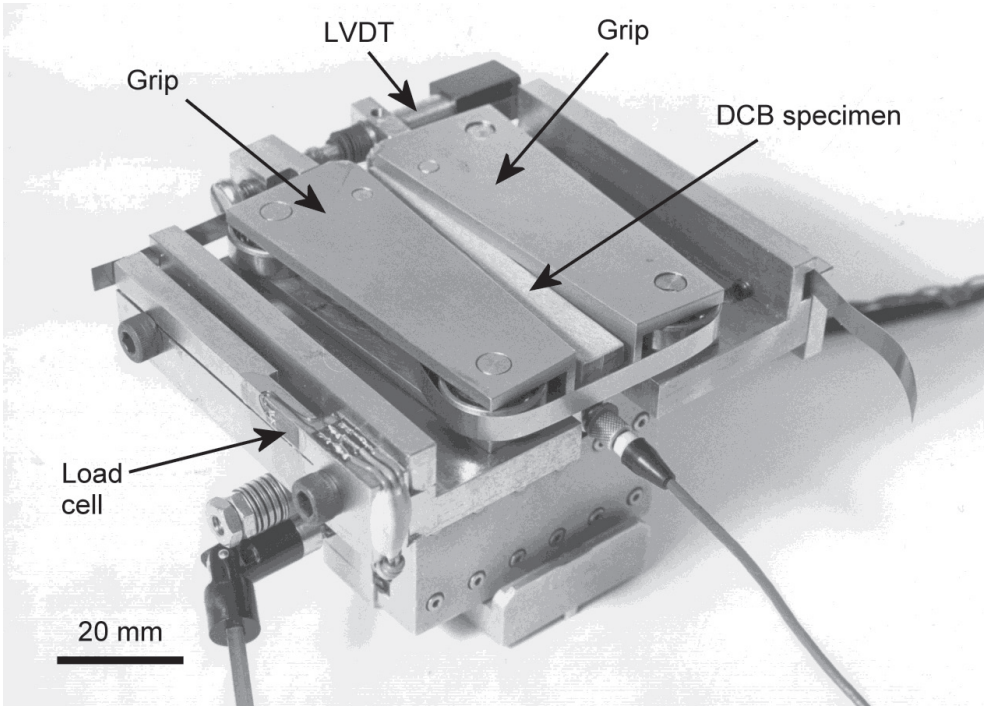

Fig. 3.1 Photograph of the ESEM test device for Mode I DCB specimens loaded with pure bending moments. After Sørensen *et al.* [A6].

3.2 ESEM test device for in-situ observation of microscale toughening mechanisms under Mixed-Mode cracking (DCB specimen loaded with an axial force and moment)

A test device for Mixed-Mode cracking was also developed for testing in the ESEM by Sørensen *et al*. [A5]. The testing method utilises a DCB specimen loaded with a combination of an axial force and a bending moment (see Fig. 2.1b); the specimen configuration is described in Section 2.3. This load combination can be created by applying an axial force that is offset from the neutral axis of the beam, as shown in Fig. 3.2. Denoting D as the distance from the crack plane to the x_2-position of the force (see Fig. 3.2), Mode I is obtained for $D/H >> 1$, where H is the beam height. Mode II is obtained for $D = 0$ [A5]. The practical design was made such that the parts are fitted to the base fixture that is attached to the x-y-z stage of the microscope, see Fig. 3.3. As for the Mode I test device (Section 3.1), nearly all parts of the loading device are made of non-magnetic materials. In order to avoid a frictional force at the contact point as the beams deflect, the point of attack of the force follows the beam. This is accomplished by the use of a V-notch in the loading beam and two blade springs made of thin metallic foils that have a low bending stiffness, so that they deflect sideways, inducing only a very low transverse force. The applied load is measured by a load cell based on strain gauges.

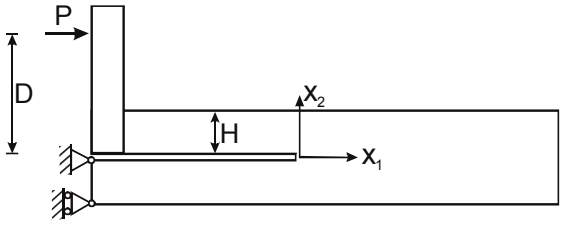

Fig. 3.2 Loading principle for the creation of a combination of a bending moment and an axial force in a DCB specimen by a single force, P, acting at a distance D from the crack plane. From Sørensen *et al.* [A5].

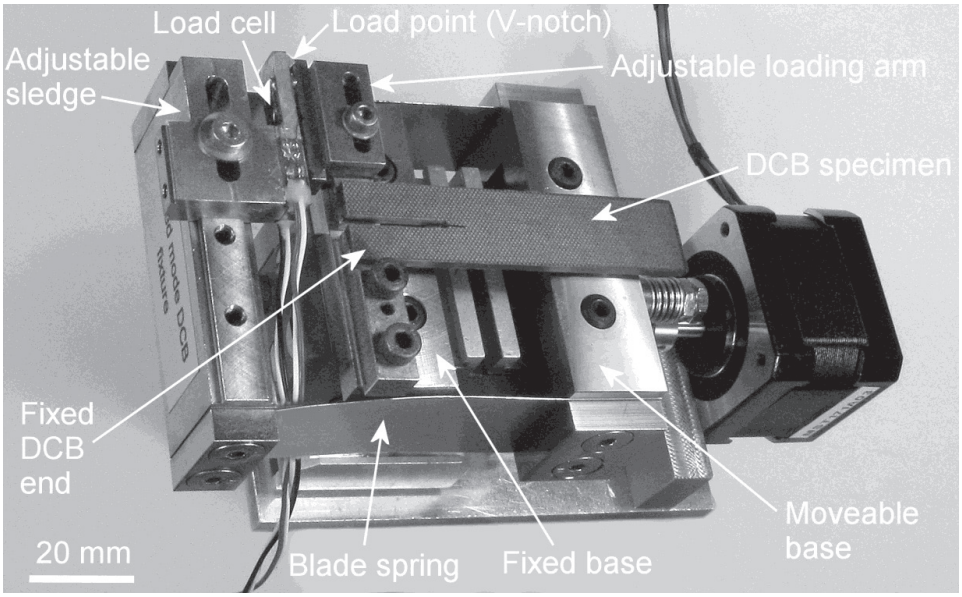

Fig. 3.3 Photograph of the ESEM loading device for Mixed-Mode cracking of a DCB-specimen.

Tests showed that crack growth was stable [A5], as expected (see Section 2.3). One drawback of the design is that quite a high load is required for Mode II dominated experiments. Furthermore, for Mode II dominated experiments, the applied J value depends strongly on the distance D. This induces some uncertainties when the beams flex and thus changes the effective distance, D. Nevertheless, the test device is useful for obtaining in-situ observations of microscale toughening mechanisms, where precise loading is of less importance.

3.3 Loading device (DCB-UBM) for macroscale fracture mechanics characterisation

As mentioned in the Introduction (Chapter 1), the determination of cohesive laws requires data from stable crack growth experiments. The test methods commonly used for LEFM characterisation of the macroscale fracture energy of composite materials give unstable crack growth under Mode II dominated experiments [52, 53, 66] and are therefore unsuited for experiments to characterise cohesive laws. The DCB-UBM is a promising specimen configuration for Mixed-Mode cohesive law determination, since, under displacement control, it gives stable crack growth in the entire range from pure Mode I to pure Mode II [A3]. Moreover, the J integral solution under large-scale bridging is given in closed analytical form (Section 2.3).

Fig. 3.4 shows a schematic illustration of how uneven bending moments are created. Transverse arms are attached to the two free beam ends. Identical forces are made at the transverse arms by the use of a wire/roller arrangement that ensures that the same force exists everywhere in the wire. The moments are then controlled by the moment arms, i.e., the distances between the forces, ℓ_1 and ℓ_2, see Fig. 3.4. The force in the wires is measured by two load cells. The un-cracked end of the DCB specimen

is mounted on a central support that allows translation in the x_2 direction but restricts rotation; this induces a restraining moment equal to $M_1 + M_2$, but no axial force.

An extensometer and two LVDT's (linear variable differential transducers) are used for the measurement of the end-opening, δ_n^*, and the end-sliding, δ_l^* (see Sørensen and Jacobsen [A4] for more details). A photograph of the set-up developed is shown in Fig. 3.5.

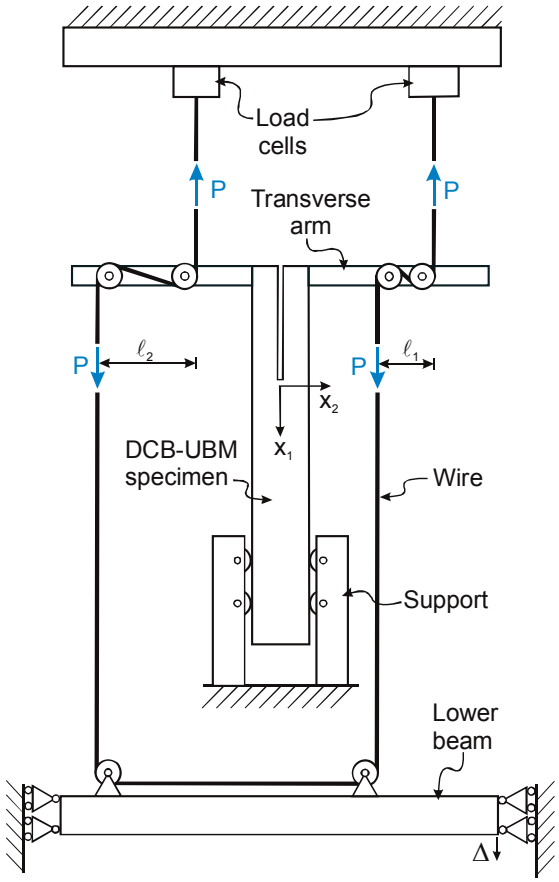

Fig. 3.4 Schematic of the loading device used to generate pure, but uneven, bending moments in a DCB specimen by the use of a wire and rollers. The wire force increases as the lower beam moves in the x_1-direction. From Sørensen and Jacobsen [A4].

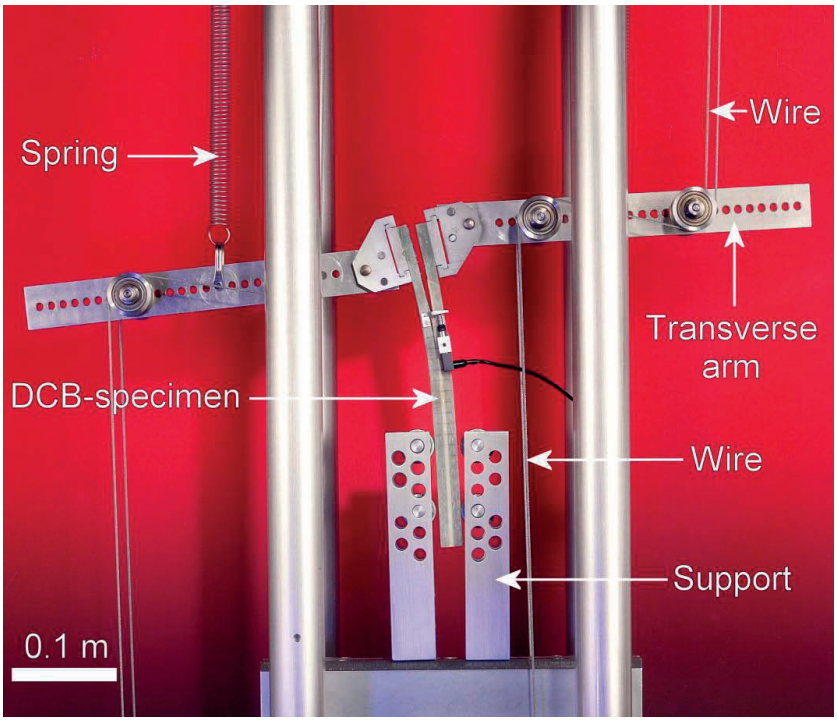

Fig. 3.5 Photograph of the DCB-UBM set-up. Springs are used to balance the forces due to gravity.

Experiments show that crack growth is stable for all moment ratios [A3]. Unlike other fracture mechanics specimens, it is not necessary to measure the crack length for the determination of J, see eq. (2-10).

4. Mode I case studies

"*Good tests kill flawed theories; we remain alive to guess again*"
Karl Popper

"*Everything should be made as simple as possible, but not simpler*"
Albert Einstein

In order to investigate (i) whether there is a connection between a microscale toughening mechanism and the resulting cohesive law and (ii) to investigate whether a measured cohesive law can be used for accurate strength prediction of structures as outlined in Fig. 1.9, this chapter addresses the use of the J integral approach for Mode I cohesive law determination. Two large-scale fracture process zone problems are studied. Case Study I concerns steel parts joined by an adhesive layer. Here, a cohesive law, determined from data using DCB specimens loaded with pure bending moments is used to predict the strength of bonded panels [A7]. The predictions are compared with experimental strength measurements. Case Study II addresses intralaminar cracking of an unidirectional fibre composite material [A8]. Microscale bridging mechanisms are identified and an appropriate micromechanical model is used to predict the macroscale bridging law. The predicted bridging law is compared with the bridging law determined from fracture resistance data using the J integral approach.

4.1 Case Study I: Strength of adhesive joints (steel/polyurethane adhesive)
Sørensen [A7] studied interfacial cracking of steel specimens joined by an elastomer adhesive (Sikaflex 228). The steel has a high yield stress so that plastic deformation does not occur in the steel and the adhesive has a large strain to failure. The use of the J integral is assumed valid since the adhesive is taken to behave non-linearly but elastically. Fig. 4.1 outlines the problem. First, fracture tests are conducted using DCB specimens loaded with pure bending moments. The Mode I cohesive law is obtained by differentiation of the $J - \delta_n^*$ data according to the J integral approach, eq. (1-9). On the basis of the cohesive law parameters, the notch sensitivity parameter, α, eq. (1-2), is determined for a generic structure (bonded panels having a width, $2w$ = 200 mm, and a central crack of length $2a$). Next, the tensile strength of the bonded panels is predicted as a function of the crack size. Bonded panels are manufactured and their strength determined. Finally, the predicted strength values are compared with the experimental results.

4.1.1 Experimental measurement of macroscale cohesive laws
Testing of the DCB specimens was conducted at two different loading rates [A7]. The associated end-openings rates were approximately constant, at 0.5 mm/s and 0.005 mm/s, respectively. A photograph of the test is shown in Fig. 4.2. The end-opening was measured as the displacement between pins in the neutral axis of the steel beams. Therefore, the measured end-opening represents the elongation over the entire adhesive layer thickness, not only the fracture process zone along the steel/adhesive interface.

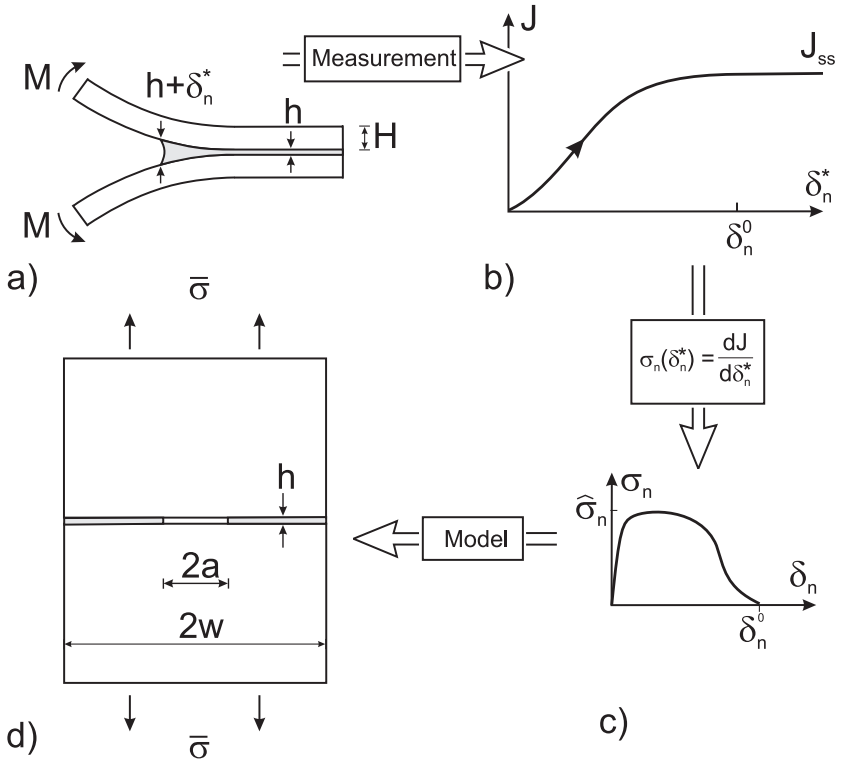

Fig. 4.1 Case Study I involves measurement of the Mode I cohesive law of a polyurethane/steel interface. The J integral approach is applied to DCB sandwich specimens loaded with pure bending moments (a) to determine the fracture resistance (b) and the cohesive law (c). The cohesive law is used for strength prediction of bonded panels having a central notch and loaded with an uniform stress, $\bar{\sigma}$, along the remote edges (d) and finally experimental strength determination. After Sørensen [A7].

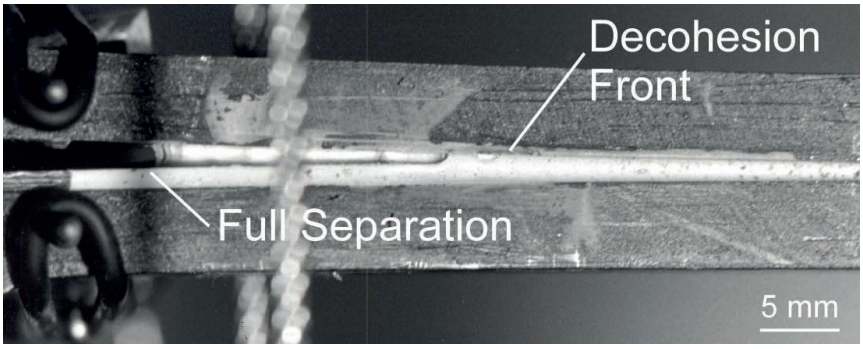

Fig. 4.2 Fracture process zone of the polyurethane/steel interface (h = 1 mm), δ_n^* = 1.5 mm. From Sørensen [A7].

Fig. 4.3 shows measured $J-\delta_n^*$ curves for the two opening rates. *J* increases with increasing δ_n^*, reaching a steady-state value. The fact that *J* remains at the steady-state value as the crack propagates along the specimen suggests that the cohesive law parameters are the same along the length of the FPZ, i.e. independent of position.

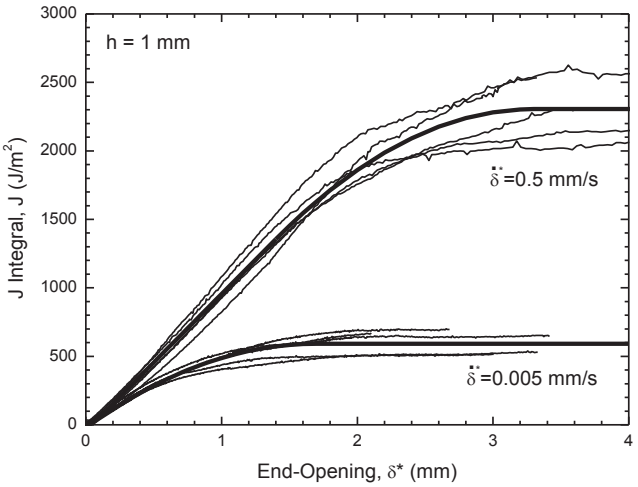

Fig. 4.3 Measured *J*-δ_n^* curves for two opening rates are shown as thin lines. The approximate end-opening rates, $\dot{\delta}_n^*$, are indicated. The thick lines are *J*-$\dot{\delta}_n^*$ relationships obtained by integration of a multi-linear function fitted to the $\sigma_n-\delta_n^*$ data of Fig. 4.4 according to eq. (1-7). From Sørensen [A7].

Cohesive laws, obtained by numerical differentiation of the $J-\delta_n^*$ data, are shown in Fig. 4.4. The results also demonstrate that the fracture process is sensitive to the opening rate; the higher opening rate gives significantly higher cohesive tractions. Thus, the cohesive law should be written as a function of the opening, δ_n, and the opening rate, $\dot{\delta}_n$, i.e., $\sigma_n=\sigma_n\left(\delta_n,\dot{\delta}_n\right)$. In view of this, only results for the slowest opening rate will be discussed in the following. The cohesive law shows opening at a small value of the traction; the traction increases to a maximum value, $\hat{\sigma}_n$, of about 0.6 MPa, remains at the maximum value until the opening is about 0.2 mm, beyond which the traction decreases (nearly proportional to the opening) to zero at an opening of approximately 2 mm.

Recently, Zhu *et al*. [67] measured the cohesive law of a steel/polyurea interface using a DCB specimen and the J integral approach, eq. (1-9). They obtained a Mode I cohesive law that has a shape rather similar to the cohesive law shown in Fig. 4.4.

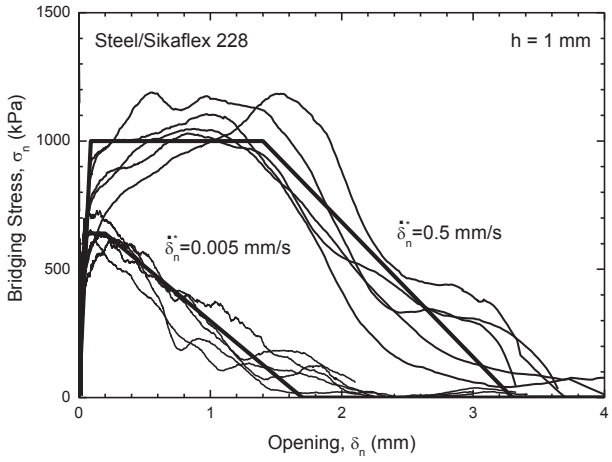

Fig. 4.4 Measured macroscale Mode I traction-separation laws for two opening rates of a polyurethane/steel interface. The approximate end-opening rates, $\dot{\delta}_n^*$, are indicated. The thin lines were obtained by numerical differentiation; the thick lines represent multi-linear curve fitted to the $\sigma_n - \delta_n^*$ data. From Sørensen [A7].

4.1.2 Prediction of notch sensitivity and strength of bonded panels

With the cohesive law determined, predictions are made for the strength of bonded panels having a central crack. The notch sensitivity parameter, α, calculated by eq. (1-2), is 0.01 or smaller for the range of a in the present experiments. Then, according to the discussion in Section 1.4, the specimen experiences a large-scale FPZ.

Fig. 4.5 shows the predicted joint strength as a function of a/w and α, using the data corresponding to the slow opening rate and the analytical model of Suo *et al*. [31]. A structure having $\alpha \approx 0$ is notch insensitive, such that the effect of the size of the central crack of the joint is simply the reduction of the cross section of the bonded area. The strength, $\overline{\sigma}_{\max}$, is thus predicted by:

$$\frac{\overline{\sigma}_{\max}}{\hat{\sigma}_n} = 1 - \frac{a}{w}. \qquad (4\text{-}1)$$

The predicted strength is depicted as the thick solid line in Fig. 4.5. The dashed lines indicate predictions based on the upper and lower values of $\hat{\sigma}_n$.

The experimental strength data of the bonded panels are superimposed in Fig. 4.5 (the opening rate was about 0.01 mm/s). It is seen that the experimental strength data of the bonded panels are close to the prediction. The experimental variation (error bars) is quite similar to that predicted by the upper and lower values of $\hat{\sigma}_n$. Thus, there is an excellent agreement between the strength found experimentally and predictions based on cohesive law parameters determined independently by the DCB tests.

Tensile testing of bonded panels without a central notch ($a/w = 0$) corresponds to testing by the direct tension method, Fig. 1.5a (Section 1.6). Since $\bar{\sigma}_{\max}/\hat{\sigma}_n \approx 1$ for $a/w = 0$, Fig, 4.5, the two methods give similar values for the peak traction, $\hat{\sigma}_n$.

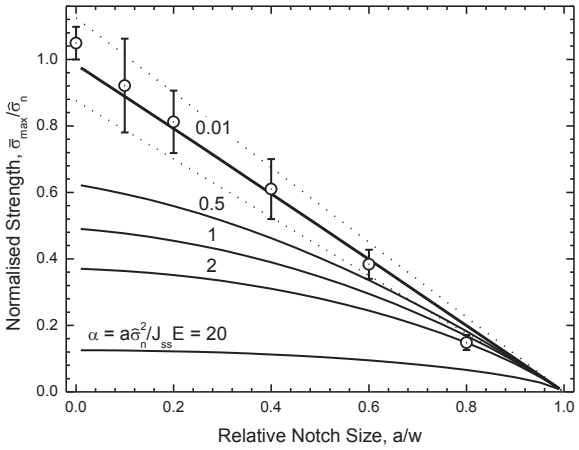

Fig. 4.5 Predicted strength, $\bar{\sigma}_{\max}$, of bonded panels (polyurethane/steel) normalised by peak cohesive traction, $\hat{\sigma}_n$, as a function of the notch sensitivity parameter α and the notch size normalised by the panel width. The actual value of α is 0.01 (thick line). Dotted lines are predictions based on upper and lower values for $\hat{\sigma}_n$. Measured strength values are superimposed as points (average of 3 or more experimental results); error bars indicate the standard deviation. After Sørensen [A7].

4.2 Case Study II: Intralaminar cracking in a carbon/epoxy composite

Following Fig. 1.9, the overall idea of Case Study II is to investigate crack bridging on two length scales: the microscale and the macroscale [A8], see Fig. 4.6. The microscale study focusses on observing the bridging mechanisms, so that an appropriate micromechanical bridging law model can be used for the prediction of the macroscale bridging law. The macroscale study concerns the determination of the macroscale bridging law from tests using DCB specimens.

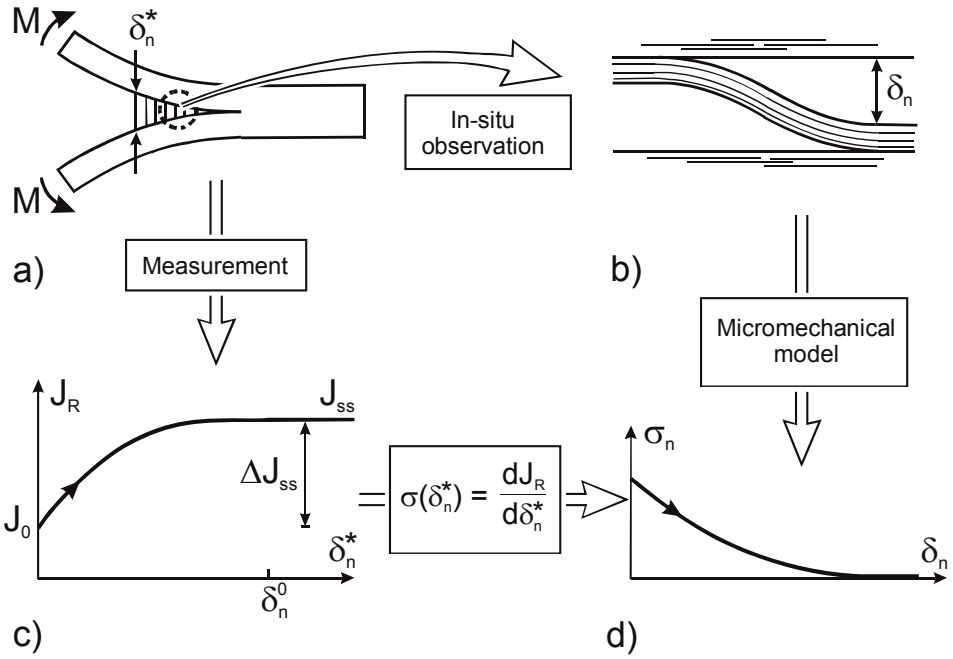

Fig. 4.6 Case Study II, Mode I intra-laminar cracking of an unidirectional carbon fibre/epoxy composite, comprises the observation of microscale toughening mechanism (a), the use of a micromechanical model for prediction of a macroscale Mode I bridging law (b), simultaneous measurements of the fracture resistance, J_R, and the end-opening, δ_n^* (c), deriving the bridging law via differentiation (d) and comparing the measured bridging law with the predicted bridging law.

4.2.1 The microscale toughening mechanism

Sørensen and Jacobsen [A8] performed fracture mechanics tests on an unidirectional carbon fibre/epoxy composite material in the vacuum chamber of an ESEM using the Mode I DCB testing device described in Section 3.1. The primary toughening mechanism is crack bridging by single fibres and ligaments consisting of multiple fibres. Fig. 4.7 shows sequences of the evolution of a bridging ligament during increasing crack opening (and extension of the crack). The bridging mechanism evolves by splitting along the interface, increasing the length of the ligament with increasing opening. This type of crack bridging is denoted cross-over fibre bridging. For this composite material, the bridging terminates by fibre failure (see Fig. 4.7), suggesting that the bridging fibres carry a high stress comparable to their strength.

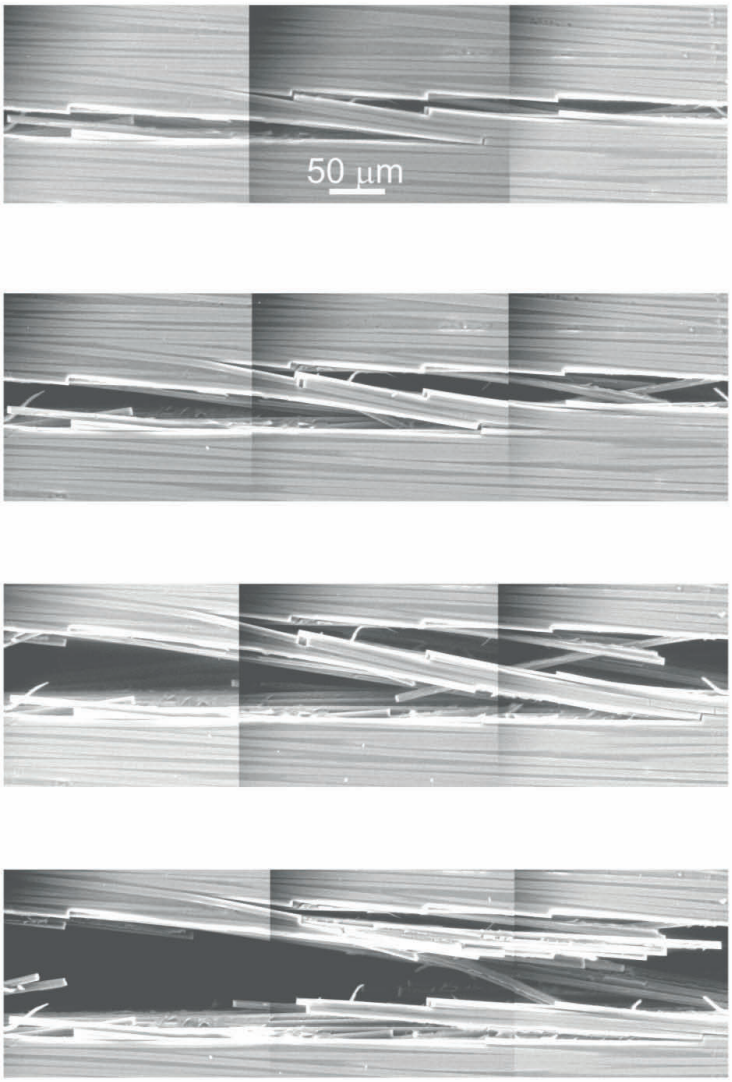

Fig. 4.7 Sequential series of ESEM micrographs showing details of cross-over bridging during Mode I intra-laminar cracking of an unidirectional carbon fibre/epoxy composite during increasing crack opening displacement. The crack tip is far to the right. After Sørensen and Jacobsen [A8].

4.2.2 Micromechanical model for prediction of a macroscale bridging law

Disregarding fibre failure, the beam-type micromechanical model of Spearing and Evans [48] seems appropriate for cross-over bridging. When the bridging ligament is long in comparison to its thickness, the shear deformation can be neglected. Then, the model predicts the bridging law as [A8]:

$$\sigma_n(\delta_n) = \left(\frac{2}{3}\right)^{3/4} \eta \frac{(\mathcal{G}_c h)^{3/4} E^{1/4} b}{\sqrt{\delta_n}}, \qquad (4\text{-}2)$$

where η is the number of bridging ligaments per unit cracked area, $\mathcal{G}_c$ is the interfacial fracture energy and h and b are the ligament height and width, respectively. With other parameters held fixed, the model thus predicts that the bridging stress decreases with increasing opening as $\sigma_n \propto \delta_n^{-1/2}$. Since this result comes from a model based on classical Bernoulli-Euler beam theory, it is not accurate for very short ligaments and the singular stress predicted for $\delta_n \to 0$ should not be taken literally.

4.2.3 Measurement of macroscale R-curves and bridging law

Sørensen and Jacobsen [A8] also performed macroscale fracture mechanics testing of an unidirectional carbon fibre/epoxy composite material using DCB specimens loaded with pure bending moments. Specimens having different beam thickness, H, were tested.

Classical R-curves, J_R as a function of the crack extension, Δa, are shown in Fig. 4.8. No crack growth occurred until J had reached a certain value, denoted J_0. J_0 can be understood as the fracture energy of the crack tip when no bridging is present. J_R increases with increasing crack length, eventually reaching a steady-state level, J_{ss}. Both J_0 and J_{ss} were found to be approximately the same for all specimens. However, the rising part of the J_R - Δa relationship depends significantly on H.

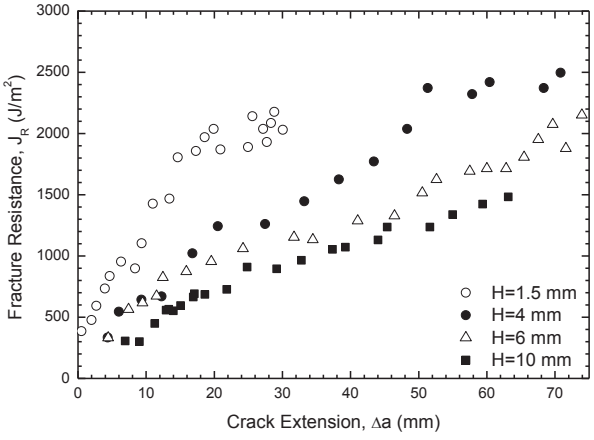

Fig. 4.8 Typical macroscale R-curves. The Mode I fracture resistance, J_R, is shown as a function of crack extension, Δa, and beam thickness, H, for intra-laminar cracking in an unidirectional carbon fibre/epoxy composite. After Sørensen and Jacobsen [A8].

Other results from the same experiments, J_R as a function of the end-opening, δ_n^*, are shown in Fig. 4.9. Unlike the J_R - Δa relationship, there is no significant difference between the $J_R - \delta_n^*$ data for specimens having different beam thicknesses. The function

$$J_R\left(\delta_n^*\right) = J_0 + \Delta J_{ss}\sqrt{\frac{\delta_n^*}{\delta_n^0}} \qquad (4\text{-}3)$$

fits the data well. In eq. (4-3), ΔJ_{ss} is the increase in fracture resistance, i.e., $\Delta J_{ss} = J_{ss} - J_0$. Differentiating the curve fit to the $J_R - \delta_n^*$ data, eq. (4-3), according to eq. (1-9) gives the bridging laws (see Fig. 4.10) as:

$$\sigma_n\left(\delta_n\right) = \frac{\Delta J_{ss}}{2\sqrt{\delta_n^0 \delta_n}}. \qquad (4\text{-}4)$$

This bridging law is obtained from $J_R - \delta_n^*$ data that were found to be independent of the specimen thickness. Thus, the bridging law can be considered as being specimen size independent, i.e. a material property. Furthermore, the bridging law, eq. (4-4), has the same shape as predicted by the micromechanical model, i.e., $\sigma_n \propto \delta_n^{-1/2}$, eq. (4-2). The fact that the shape of the cohesive law predicted by the micromechanical model is identical to that found from the macroscale tests verifies that the cross-over bridging mechanism is the primary toughening mechanism in the unidirectional carbon fibre/epoxy composite material during intralaminar cracking.

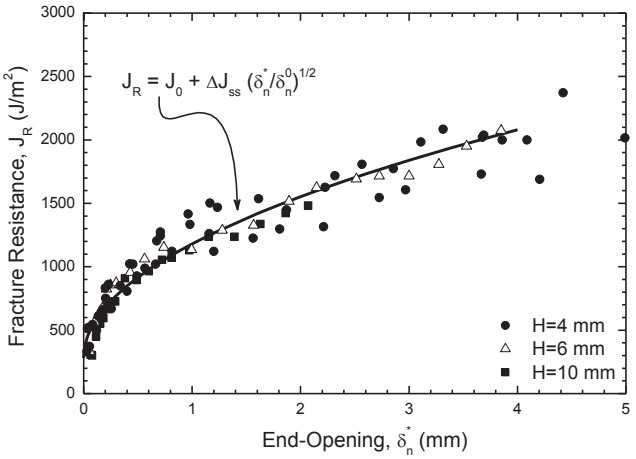

Fig. 4.9 Mode I fracture resistance, J_R, of an unidirectional carbon fibre/epoxy composite as a function of the end-opening, δ_n^*, for various specimens having different beam thicknesses. After Sørensen and Jacobsen [A8].

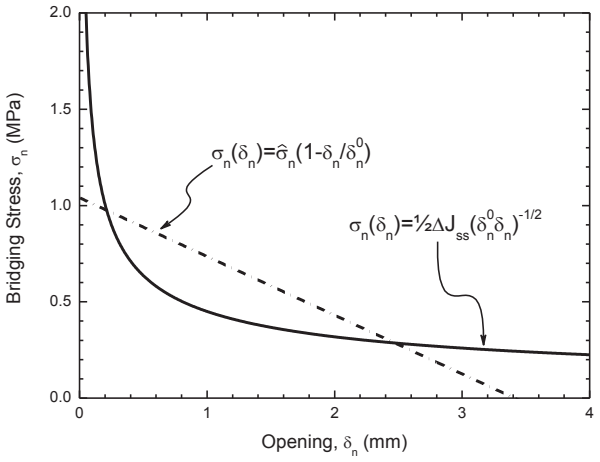

Fig. 4.10 Non-linear Mode I bridging law for intra-laminar cracking of an unidirectional carbon fibre/epoxy composite, obtained by differentiation of the curve shown in Fig. 4.9. A linear softening cohesive law, having the same steady-state fracture resistance, is also shown (dashed line). After Sørensen and Jacobsen [A8].

The non-linear shape of the bridging law for cross-over bridging was later confirmed by other studies [63, 68]; the latter study also used DCB specimens and derived the bridging law by the J integral approach, eq. (1-9).

The experimental bridging law data leading to Fig. 4.10 starts at an initial opening of about 50 μm [A8]. No bridging law data is available for an opening smaller than this value, since this is the opening encountered just after crack initiation. Thus, the bridging law behaviour for openings smaller than 50 μm is unknown. A pragmatic approach is to take the peak stress of the bridging law as the stress value at an opening of 50 μm, i.e. $\hat{\sigma}_n \approx 2$ MPa. With H as the relevant structural length scale (see Section 1.4), the notch sensitivity parameter α, eq. (1-2), is found to be less than 10^{-3}, confirming that the problem is a large-scale bridging problem.

Fig. 4.10 also includes a more approximate bridging law that has a linear softening relationship between σ_n and δ_n; the bridging law parameters were determined using an approach suggested by Suo *et al.* [40]. The areas under the two bridging law curves are the same, so that the fracture toughness increase, ΔJ_{ss}, of the two bridging laws are identical.

4.2.4 Model prediction of fracture resistance (R-curve)

Fig. 4.11 shows simulated R-curves made by a finite element model that includes a bridging zone [A9]. Predictions made using the two bridging laws in Fig. 4.10 are shown as curves in Fig. 4.11 together with the experimental results which are shown as points. Both bridging laws predict the overall trend well: a specimen having thicker beams requires a longer crack extension before a steady-state is attained. This can be understood as follows: The R-curve reaches the steady-state when the end-opening reaches the critical value, δ_n^0; since the thicker beam has a higher bending stiffness it opens less for the same crack extension. Consequently, a thicker beam requires a longer FPZ for the end-opening to reach the critical opening where the

bridging stress vanishes. There is some difference between the curves obtained by the use of the two different bridging laws. The curves based on the non-linear cohesive law, eq. (4-4), are closer to the experimental data than the curves made assuming linear softening. This suggests that the non-linear bridging law, eq. (4-4), represents the bridging law of the experiment better than one with linear softening.

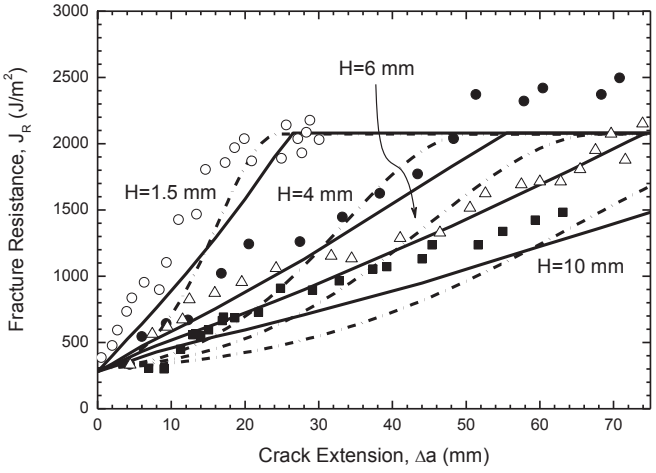

Fig. 4.11 Simulated Mode I R-curves (curves) for an unidirectional carbon/epoxy composite material obtained using the two bridging laws shown in Fig. 4.10; dashed lines show predictions based on linear softening and solid lines indicate predictions obtained using the non-linear Mode I bridging law. The experimental measurements from Fig. 4.8 are superimposed as points. After Sørensen and Jacobsen [A8].

5. Mixed-Mode case studies

"*Measure what is measurable, and make measurable what is not so*"
Galileo Galilei

"*Computers are useless. They can only give you answers*"
Pablo Picasso

Delamination of polymer-matrix composites and cracking of adhesive joints often occur under Mixed-Mode conditions. Analysis of Mixed-Mode large-scale bridging problems requires the determination of Mixed-Mode bridging/cohesive laws. In the following, bridging laws for Mixed-Mode cross-over bridging will be investigated. The motivation for the subsequent investigations is to investigate (i) whether measured Mixed-Mode cohesive laws are material laws, i.e., independent of specimen size, geometry and loading (ii) whether a potential function exists for the cohesive tractions of a toughening mechanism in a composite material, and (iii) whether real Mixed-Mode cohesive laws are coupled or uncoupled. Two Case studies involving large-scale bridging are examined: Case Study III covers Mixed-Mode cracking of adhesive joints [A10] and Case Study IV concerns Mixed-Mode cracking of polymer-matrix composites [A4]. Cohesive laws will be determined using the testing methods described in the Sections 3.2 and 3.3 and the J integral/potential function approach developed in Section 2.2.

5.1. Case Study III: Mixed-Mode cracking of adhesive joints
The problem studied in this section is Mixed-Mode cracking along an adhesive/laminate interface in an adhesive joint between two beams made of a glass fibre composite material [A10]. The specimens used are 30 cm long DCB specimens and 2 metre long "medium size" adhesive joint specimens, as indicated in Fig. 5.1. The aims of this study are (a) to determine Mixed-Mode fracture energy and cohesive laws for pure Mode I and Mode II, (b) to use the cohesive laws in a finite element model for predicting the load-carrying capacity of the medium size specimens, (c) to perform independent strength measurements of the medium size specimens and (d) to compare the predicted and measured strength values of the medium size specimens [A10]. The medium size specimen can be considered as being a model experiment for cracking of adhesive joints in large structures such as wind turbine blades.

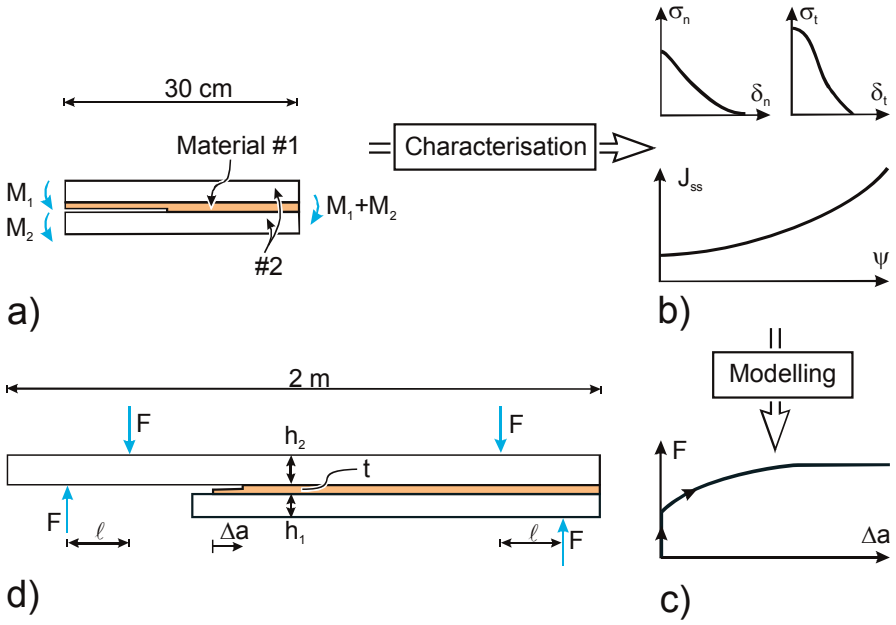

Fig. 5.1 Case Study III, the study of Mixed-Mode cracking of adhesive joints between glass fibre laminates. DCB specimens loaded with uneven bending moments (a) are used for the measurement of Mode I and Mode II cohesive laws and Mixed-Mode values of J_{ss} (b). These measurements are used to predict the load-carrying capacity of medium size specimens (c), which are compared with experimental measurements (d). After Sørensen *et al*. [A10].

5.1.1 Determination of fracture resistance and macroscale cohesive laws

The Mixed-Mode fracture energy was determined as a function of the nominal mode mixity (see Sørensen *et al*. [A10] for more details) by the use of the DCB-UBM (DCB loaded with uneven bending moments) specimen described in Section 3.3. Experiments were conducted for a variety of moment ratios. The moment ratio was kept constant during each experiment.

Typically, no crack growth occurred until the J integral had reached a characteristic value, denoted, $J_0(\psi_{nom})$, which should be understood as J_0 being a function of ψ_{nom}, where ψ_{nom} is the nominal mode mixity. After the onset of cracking, the fracture resistance, J_R, increases with increasing crack opening, eventually reaching a steady-state level, $J_{ss}(\psi_{nom})$, which also depends on the load combination, here expressed in terms of the nominal mode mixity. Fig. 5.2 shows a typical fracture process.

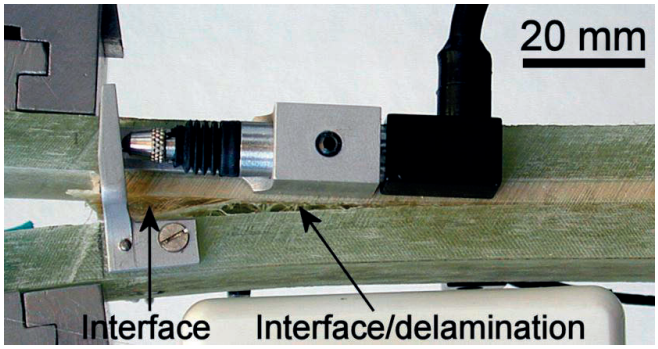

Fig. 5.2 Photograph of a DCB-UBM specimen subjected to Mixed-Mode cracking (M_1/M_2 = -0.45). From Sørensen *et al*. [A10].

Fig. 5.3 summarises the observed J_0 and J_{ss} values as a function of ψ_{nom}. It is seen that both J_0 and J_{ss} increase with ψ_{nom}. Curves representing fits to the average and the lower and upper bounds of the steady-state fracture resistance are superimposed.

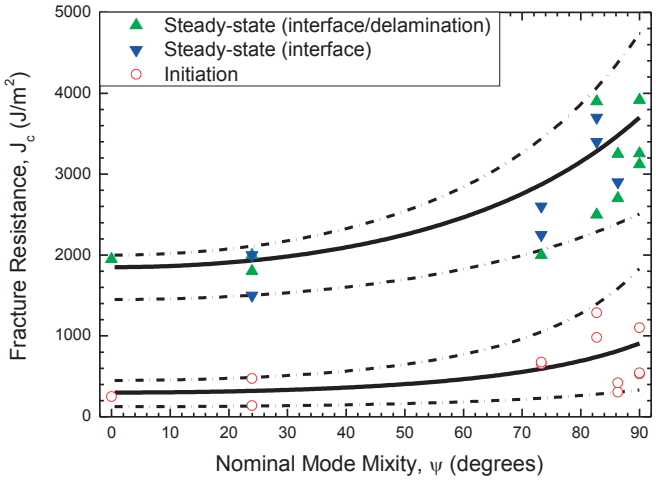

Fig. 5.3 Measured Mixed-Mode fracture resistance of an adhesive joints between glass fibre laminates as a function of nominal mode mixity. After Sørensen *et al*. [A10].

Pure Mode I and Mode II cohesive laws, obtained by the J integral approach outlined in Section 2.2, are shown in Fig. 5.4. Both the Mode I and the Mode II cohesive laws are highly non-linear. The Mode I cohesive law has a peak traction, $\hat{\sigma}_n\left(\psi_{nom}=0^\circ\right)$ = 12 MPa and critical opening, δ_n^0, of about 1.4 mm. The Mode II cohesive law has an initial rising part, reaching a maximum value, denoted $\hat{\sigma}_t$, of 17 - 26 MPa and decreases to zero at a critical tangential opening, δ_t^0, of approximately 0.3 - 0.5 mm.

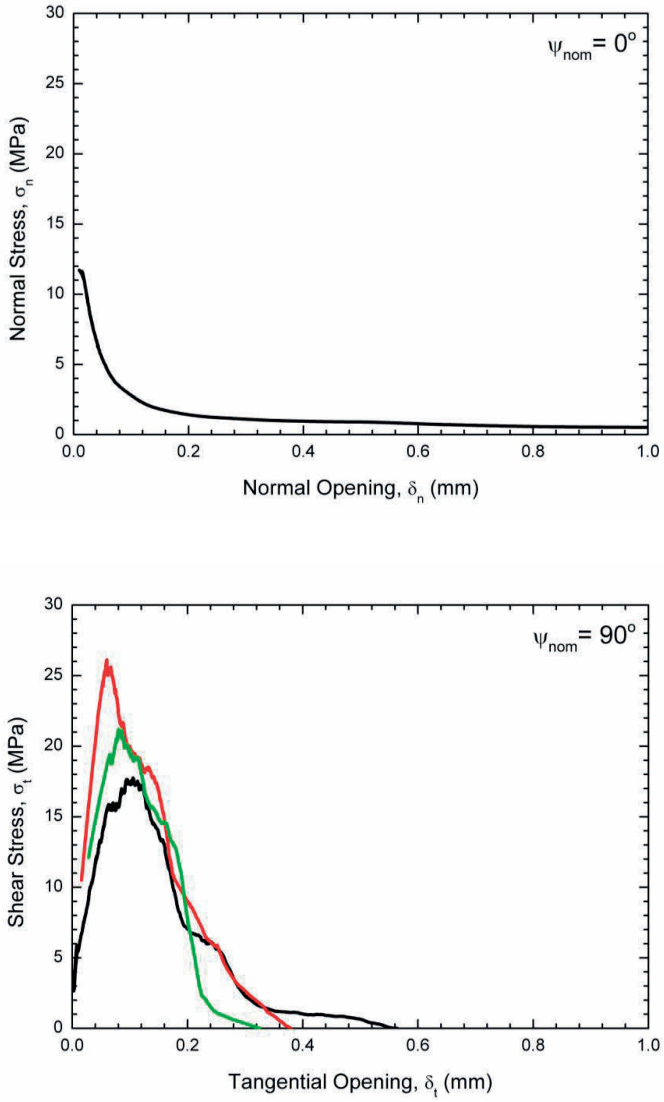

Fig. 5.4 (a) Pure Mode I (1 series) and (b) pure Mode II (3 series) cohesive laws of adhesive joints between glass fibre laminates obtained using the J integral approach. From Sørensen *et al*. [A10].

5.1.2 Model prediction of structural strength from cohesive laws

The cohesive laws were modelled in the commercial finite element program Abaqus [A10]. The cohesive laws in Abaqus are bi-linear and are coupled in a pre-determined manner so that the resulting local cohesive tractions have the same phase angle as the local crack opening displacements. In order to ensure that the cohesive laws attain the same $J_{ss}(\psi_{nom})$ as found experimentally for that mode mixity, the peak traction values and the critical openings of the Mixed-Mode cohesive law are adjusted so that the sum of the areas under the traction-separation curves (eq. (2-2) with $J_0 = 0$) equals $J_{ss}(\psi_{nom})$.

As an example, Fig. 5.5 shows the predicted relationship between moment (force, F, multiplied by moment arm, ℓ) and crack extension computed for the thickness ratio $h_1/h_2 = 1$. Results based on different cohesive law parameters, corresponding to average, lower and upper steady-state fracture resistance values are also shown. The predicted curves show similar trends: The predicted moment increases to a constant, steady-state value after some crack extension. Experimental data are superimposed as points in Fig. 5.5. Most experimental points fall within the predicted bounds. Thus, the agreement between model predictions and experimental results are satisfactory. This validates the cohesive law determination and the model predictions.

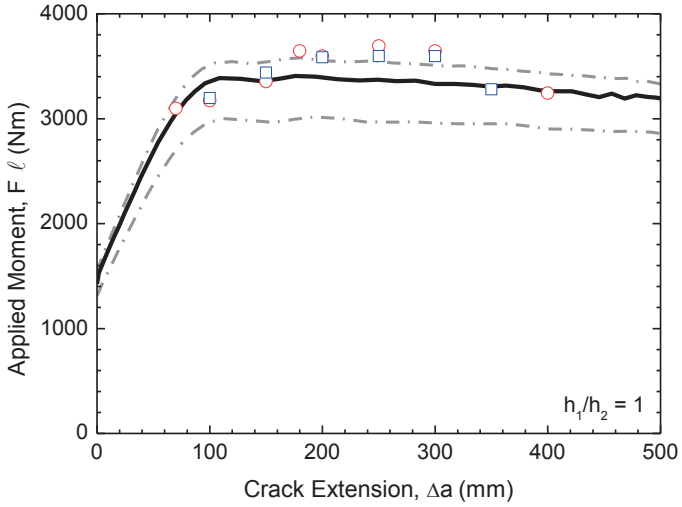

Fig. 5.5. Predicted moment-crack extension data for medium size specimens are shown as curves for $h_1/h_2 = 1$. The solid line is based on best fit (average J_{ss}) cohesive law parameters, dashed curves are based on cohesive law parameters that correspond to lower and upper bound values of J_{ss}. Experimental data are superimposed as points. From Sørensen *et al*. [A10].

The load level at steady-state cracking, F_{ss}, can be predicted from analytical results obtained by a J integral analysis of the medium size specimen. The result is thus valid under large-scale bridging [A10]:

$$\frac{F_{ss}\ell}{W\sqrt{J_{ss}h_2^3E}} = \frac{1}{\sqrt{6}\sqrt{1-\frac{1}{\left(1+\frac{h_1}{h_2}\right)^3}}} \qquad (5\text{-}1)$$

where ℓ is the moment arm, W is the specimen width, J_{ss} is the appropriate steady-state fracture resistance, E is the Young's modulus of the beam material and h_1 and h_2 are the thicknesses of the short and long beam respectively (see Fig. 5.1).

For the present specimen geometry and loading, ψ_{nom} is between 41° and 49° for 0.1 < h_1/h_2 < 1 [A10]. Taking the minimum, average and maximum values of $J_{ss}(\psi)$ from Fig. 5.3 at the average phase angle, ψ_{nom} = 45°, the load-carrying capability under steady-state cracking can be predicted from eq. (5-1). Predictions are shown in Fig. 5.6. It is seen from the Figure that the analytical model predicts that the strength decreases with increasing h_1/h_2 ratio. The average experimental strength values are superimposed as points; highest and lowest values are shown as error bars. The experimental strength values lie close to or within the band between upper and lower bound predictions. Furthermore, the trend of the model prediction (decreasing strength with increasing h_1/h_2) agrees with the experimental findings. The scatter of the experimental strength values is similar to the variation predicted by the upper and lower bound values of J_{ss}. It is thus concluded that both the numerical and the analytical model give satisfactory predictions. This validates the cohesive law measurement method, the models and the testing of the medium scale specimens and suggests that mixed mode cohesive laws are independent of specimen size and geometry.

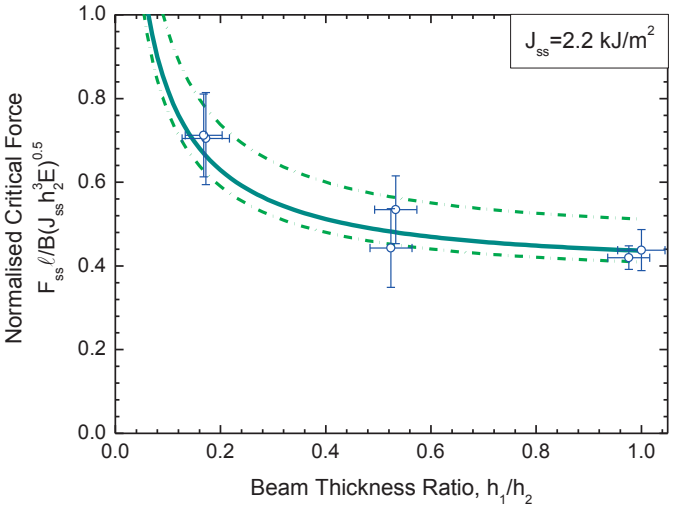

Fig. 5.6 Load-carrying capacity of medium size specimens predicted from an analytical model (eq. 5-1). Dashed curves are predictions based on upper and lower values of J_{ss}. Experimental results are shown as points; error bars represent the maximum and minimum values of the measured steady-state force, F_{ss} and of h_1/h_2. From Sørensen *et al.* [A10].

5.2 Case Study IV: Mixed-Mode cracking of polymer-matrix composites

This section studies Mixed-Mode cracking of unidirectional fibre composites. The aim is to uncover the possible coupling and shape of Mixed-Mode cohesive laws for the bridging problem encountered during cracking. Mixed-Mode bridging is investigated at two length scales that are related via cohesive laws, see Fig. 5.7: The microscale [A5] and the macroscale [A4].

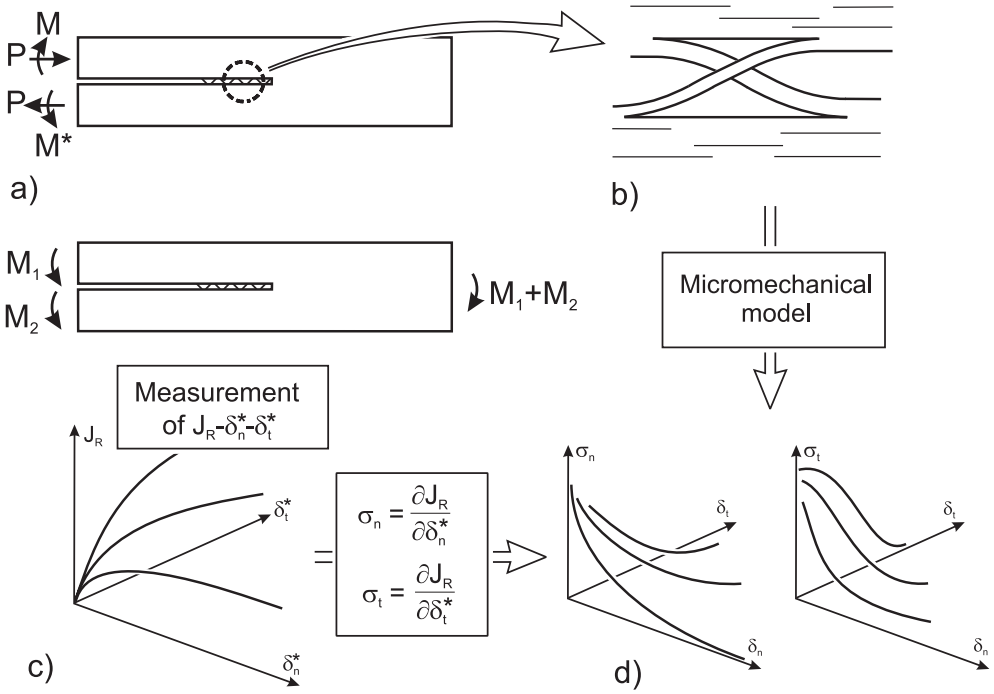

Fig. 5.7 Case Study IV: Study of Mixed-Mode crack bridging in unidirectional fibre composites. (a) In situ observation of microscale bridging mechanisms, (b) micromechanical model for prediction of Mixed-Mode bridging laws, (c) measurement of Mixed-Mode fracture resistance as a function of the end-opening and end sliding gives Mixed-Mode cohesive laws (d).

5.2.1 In situ observation of microscale toughening mechanisms

Sørensen *et al*. [A5] made in-situ observations in the ESEM of toughening mechanisms during Mixed-Mode intralaminar cracking in an unidirectional carbon fibre/epoxy composite using the test device that loads DCB specimens with a combination of an axial force and a bending moment (see Fig. 3.2), as described in Section 3.2. The dominant toughening mechanism is cross-over bridging by single fibres and by ligaments consisting of several fibres, see Fig. 5.8, as for the pure Mode I cracking (Section 4.3). However, under Mixed-Mode opening, bridging ligaments behave differently when loaded in compression or in tension. Ligaments loaded in compression can undergo buckling, whereas ligaments loaded in tension are likely to straighten like a string. When buckled, ligaments loaded in compression are therefore anticipated to transmit much less stress than ligaments loaded in tension.

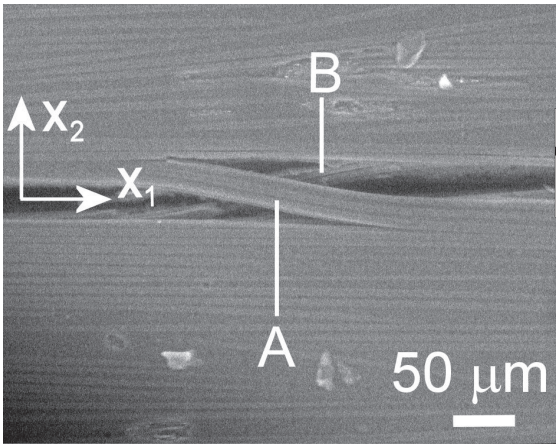

Fig. 5.8 In-situ observation of Mixed-Mode bridging mechanisms in an unidirectional carbon fibre/epoxy composite during Mixed-Mode testing of a DCB specimen loaded with a combination of axial forces and bending moments. The crack tip is far to the right. The upper beam of the DCB-specimen is loaded a combination of axial compression and bending while the lower beam is loaded in axial tension and bending, as shown in Fig. 5.7a. Therefore the upper crack face moves in the positive x_1-direction relative to the lower crack face. Ligament (A) is loaded partially in compression while ligament (B) is loaded primarily in tension. From Sørensen *et al*. [A5].

5.2.2 Predictions of Mixed-Mode cohesive laws by micromechanical modelling

A micromechanical model of Mixed-Mode cross-over bridging, disregarding ligaments loaded in compression, was developed using the Bernoulli-Euler beam theory and the compliance method [A5]. The model is shown schematically in Fig. 5.9.

The model predicts the following bridging tractions:

$$\frac{\sigma_n}{\eta bhE} = \frac{\dfrac{\delta_n}{h}\left[\dfrac{\mathcal{G}_c}{Eh}\right]^{3/2}}{\left[\left(\dfrac{\delta_t}{2h}\right)^2 + \sqrt{\left(\dfrac{\delta_t}{2h}\right)^4 + 6\dfrac{\mathcal{G}_c}{Eh}\left(\dfrac{\delta_n}{2h}\right)^2}\right]^{3/2}} \qquad (5\text{-}2)$$

and

$$\frac{\sigma_t}{\eta bhE} = \frac{\dfrac{\delta_t}{h}\left[\dfrac{\mathcal{G}_c}{Eh}\right]^{1/2}}{\left[\left(\dfrac{\delta_t}{2h}\right)^2 + \sqrt{\left(\dfrac{\delta_t}{2h}\right)^4 + 6\dfrac{\mathcal{G}_c}{Eh}\left(\dfrac{\delta_n}{2h}\right)^2}\right]^{1/2}}, \qquad (5\text{-}3)$$

where η is the number of bridging ligaments per unit cracked area (assumed to be constant, i.e., the same for all opening paths), h and b denote the height and width of the ligament, respectively, $\mathcal{G}_c$ is the fracture energy of the interface and E is the Young's modulus of the ligament. It is clear from eq. (5-2) and (5-3) that both the normal and the shear tractions depend on both the normal and tangential crack opening displacements. In other words, the bridging laws are coupled.

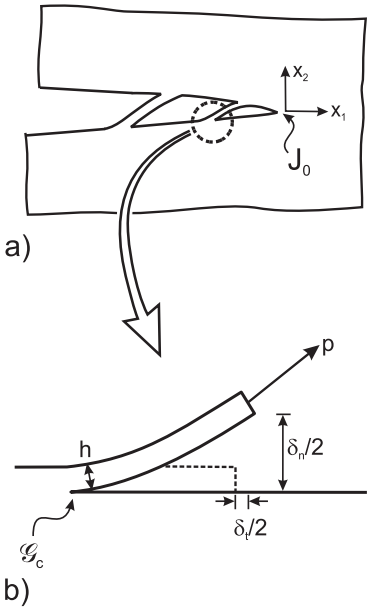

Fig. 5.9 Schematic of the Mixed-Mode model of a bridging ligament loaded in tension (a). Due to point symmetry, only half the ligament is modelled (b). From Sørensen *et al*. [A5].

Fig. 5.10 plots the bridging tractions as a function of δ_n and δ_t. The functions for σ_n and σ_t are clearly different. The normal traction, σ_n, decreases from a high value at zero opening, and approaches zero stress asymptotically with increasing δ_n and δ_t. Again the singularity should not to be taken literarily, given the assumption of the model. Under Mixed-Mode opening, the shear traction, σ_t, increases to a near-constant value, similar to the bridging traction obtained under pure Mode II.

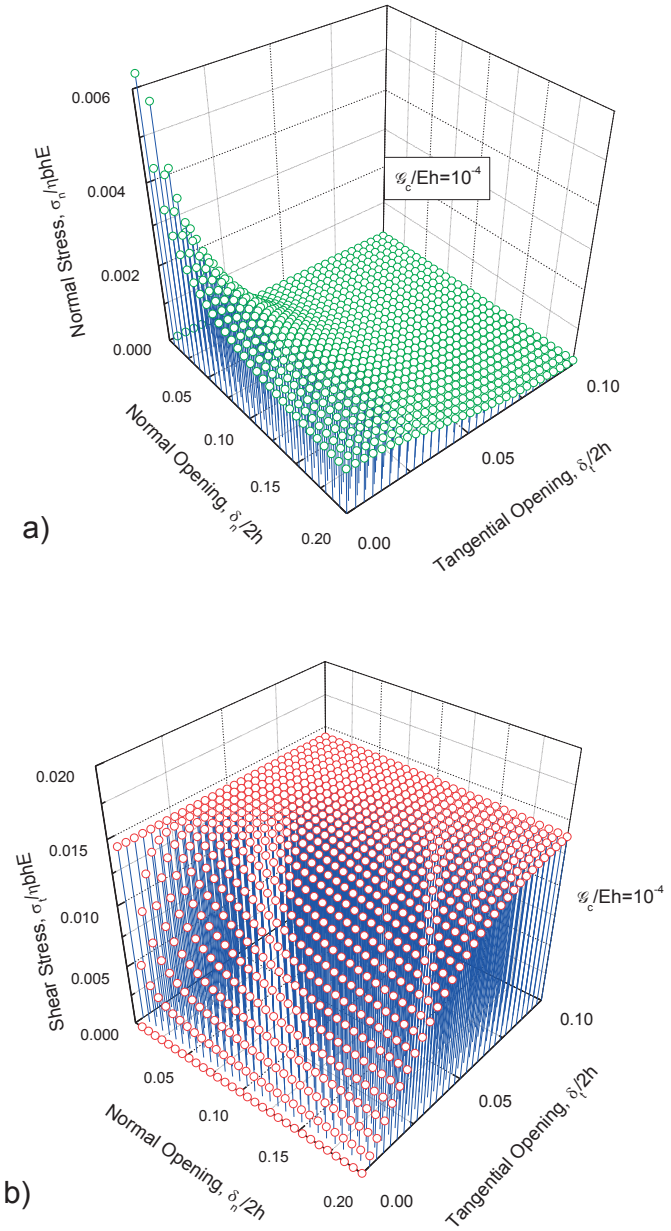

Fig. 5.10 Predicted Mixed-Mode bridging laws. (a) The normal traction, σ_n, as a function of the normal opening, δ_n, and the tangential opening, δ_t, and (b) the shear traction, σ_t, as a function of δ_n and δ_t. From Sørensen *et al*. [A5].

It was proven [A5] that a potential function $\Phi(\delta_n, \delta_t)$ exists for the bridging tractions given by eq. (5-2) and eq. (5-3). During cracking, the J integral, eq. (2-2), will be equal to the potential function evaluated at the end-openings (eq. (2-4)), so that

$$J_R = \Phi\left(\delta_n^*, \delta_t^*\right) + J_0 . \qquad (5\text{-}4)$$

A plot of the potential function as a function of the total end-opening, δ^*, is shown in Fig. 5.11 for various constant values of the phase angle of the end-opening, φ^*. For pure Mode I (pure normal opening, $\varphi^* = 0°$), Φ increases as $\sqrt{\delta_n^*}$ in agreement with the earlier Mode I model (eq. (4-2)). With increasing φ^*, the potential function exhibits a near-linear dependence on δ^*. For pure Mode II (pure tangential opening, $\varphi^* = 90°$) Φ increases linearly with δ^*. With all other parameters held constant, the value of the potential function increases with increasing φ^*, except for small openings. Thus, with all other parameters constant, cross-over bridging appears to be a much more effective toughening mechanism under Mode II than under Mode I.

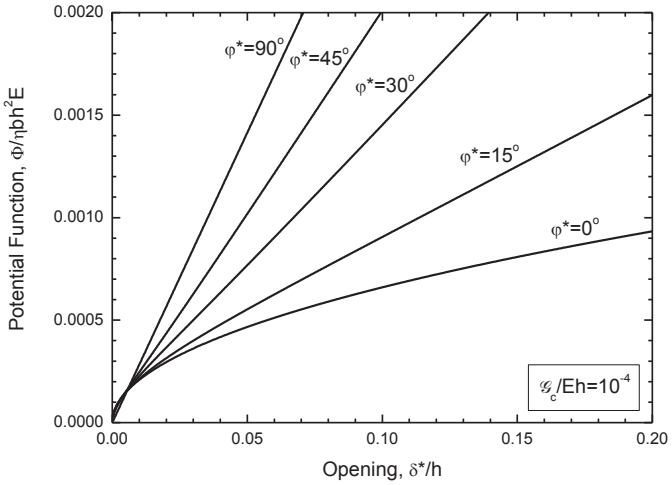

Fig. 5.11 Predicted potential function as a function of the magnitude of the end-opening, δ^*, for various constant values of the phase angle of the end-opening, φ^*. From Sørensen *et al*. [A5].

Toughening by the cross-over bridging mechanism loses efficiency when the bridging ligaments fail. A criterion for prediction of fibre failure under Mixed-Mode conditions was developed by Sørensen *et al*. [A5]. Under pure normal opening (Mode I), fibre failure occurs when

$$\frac{\mathcal{G}_c E}{\sigma_{fu}^2 h} \geq \frac{1}{6}, \qquad (5\text{-}5)$$

where σ_{fu} is the fibre strength. Equation (5-5) reveals the role of the interfacial fracture energy. For a sufficiently low value of $\mathcal{G}_c$, the left hand side, which can be considered as being a non-dimensional cracking parameter, will be lower than the

right hand side, so that the fibre failure criterion is not fulfilled. A sufficiently high $\mathcal{G}_c$ increases the cracking parameter to the critical value, so that the inequality is fulfilled and fibre failure is predicted.

For pure Mode II, fibre failure occurs when

$$\frac{\mathcal{G}_c E}{\sigma_{fu}^2 h} \geq \frac{1}{2}, \tag{5-6}$$

viz., the critical value of the cracking parameter is three times that of the Mode I criterion. Thus, for ligaments of the same thickness, fibre failure is predicted to occur at a lower $\mathcal{G}_c$ for Mode I than for pure Mode II. Predictions of the critical $\mathcal{G}_c$, based on (5-5), for unidirectional glass/epoxy and carbon fibre/epoxy matrix composites are in close agreement with predictions made using an advanced finite element model using Mixed-Mode cohesive laws for the interfacial separation [69].

5.2.3 Measurement of macroscale Mixed-Mode cohesive laws

Sørensen and Jacobsen [A4] measured Mixed-Mode as well as pure Mode I and pure Mode II bridging laws and cohesive laws for delamination of a (near) unidirectional glass fibre/polyester composite material processed by vacuum assisted resin transfer moulding. DCB specimens were loaded with uneven bending moments, M_1 and M_2 using the DCB-UBM loading device described earlier (Section 3.3). The end-opening δ_n^* and the end-sliding δ_t^* of the fracture process zone were calculated from measurements obtained from an extensometer and two LVDTs (see [A4] for more details).

The fracture resistance, J_R, is shown as a function of the magnitude of the end-opening δ^* in Fig. 5.12. For $M_1/M_2 \leq 0.5$, the curves are relatively smooth; J_R increases with increasing end-opening, approaching a steady-state value. The curves for $M_1/M_2 \geq 0.7$ are far less smooth. Moreover, they do not flatten out, but take a near-constant slope. The curves are qualitatively not very different from the predictions of the micromechanical model (Fig. 5.11).

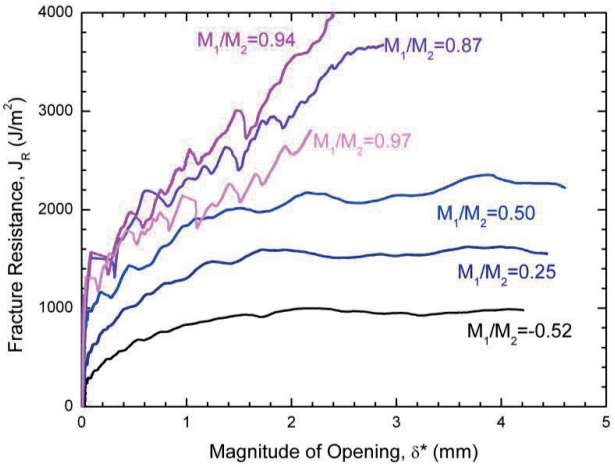

Fig. 5.12 Measured Mixed-Mode fracture resistance, J_R, of an unidirectional glass fibre/polyester composite as a function of the end-opening, δ^*, for various moment ratios. From Sørensen and Jacobsen [A4].

Fig. 5.13 shows the associated end-opening/sliding histories. The opening paths are nearly-proportional. It appears, however, that it is not possible to obtain a pure tangential opening (i.e., $\delta_n^* = 0$ $\delta_t^* \neq 0$) even for M_1/M_2 very close to unity. Similar observations have been found for Mode II tests of metal/adhesive joints [70]. A possible reason for this behaviour is the formation of multiple shear cracks leading to roughening of the fracture surface. Roughness would wedge the crack faces open, i.e. creating a normal opening, which will cause interfacial dilatation [A12].

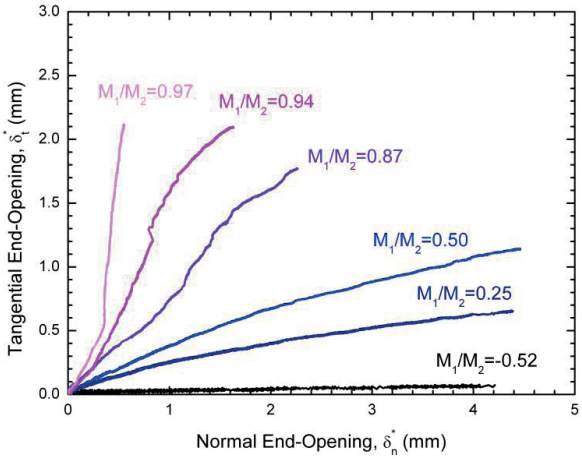

Fig. 5.13 Relationship between the normal end-opening, δ_n^*, and the tangential end-opening (end-sliding), δ_t^*, measured in an unidirectional glass fibre/polyester composite for various Mixed-Mode fracture mechanics experiments having a constant moment ratio. From Sørensen and Jacobsen [A4].

Mixed-Mode cohesive laws, obtained from the $J_R - \delta_n^* - \delta_t^*$ data by the use of the J integral/potential function approach described in Section 2.2, are shown in Fig. 5.14. Both the normal and shear tractions are found to depend on both δ_n and δ_t. Thus, the measured cohesive laws are coupled. The normal traction, σ_n, plotted in Fig. 5.14a, is found to start from a peak traction value, $\hat{\sigma}_n$, of about 8 MPa at zero separation but decreases rapidly with increasing δ_n and δ_t. In the near-pure Mode II region ($\delta_n^* \approx 0$ - 0.5 mm) σ_n is negative (compressive). Although there is no conclusive evidence, this is consistent with the hypothesis that crack face roughness causes contact; this leads to compressive contact stresses that tend to wedge the crack faces open in the normal direction. The cohesive shear traction, σ_t, shown in Fig. 5.14b, has a much higher peak value, $\hat{\sigma}_t$, than the normal traction. With increasing opening the cohesive shear traction decreases to a near constant value, consistent with the predictions of the Mixed-Mode micromechanical models, eq. (5-3) and Fig. 5.10.

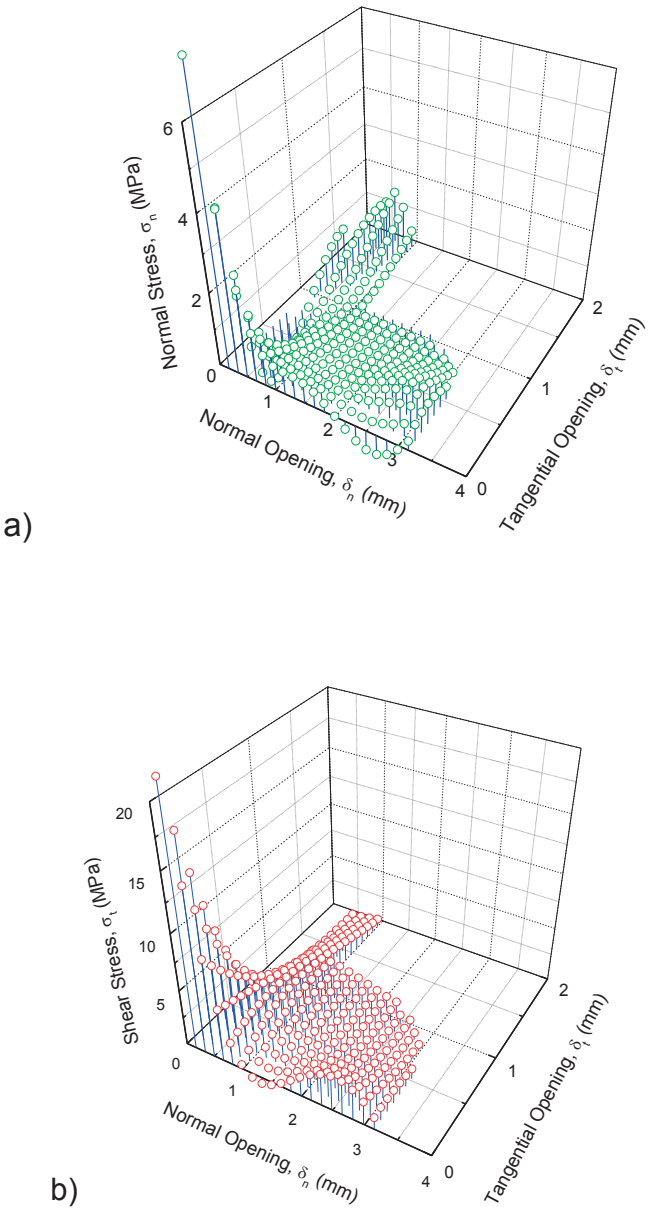

Fig. 5.14 Mixed-Mode cohesive laws for an unidirectional glass fibre/polyester composite determined experimentally by the J integral/potential function approach. (a) The normal traction, σ_n, as a function of the normal opening, δ_n, and the tangential opening, δ_t, and (b) the shear traction, σ_t, as a function of δ_n and δ_t. From Sørensen and Jacobsen [A4].

6. Future developments

"*The human mind is our fundamental resource*"
John F. Kennedy

"*Science is what you know, philosophy is what you don't know*"
Bertrand Russell

6.1 Limitations of the approaches

A fundamental assumption for the application of cohesive laws, as opposed to the modelling of discrete crack bridging ligaments, is that there are enough bridging ligaments so that their collective mechanical response can be "smeared out" in a continuum-mechanics sense. This is assumed in nearly all model studies in the literature; however, it would be useful to establish a general criterion ensuring this. Östlund *et al*. [71] studied crack bridging by discrete, intact fibres oriented perpendicular to the crack plane. They concluded that the bridging zone should extend over 5-10 bridging fibres before the smeared-out continuum approach gives similar results to a model based on discrete ligaments. It may be anticipated that very narrow specimens - that possess a low number of bridging ligaments - may show a different and more jagged fracture resistance behaviour than wider specimens that exhibit a sufficiently high number of bridging ligaments.

Another fundamental assumption is that the cohesive traction at a given location in the cohesive zone depends only on the local opening at that position and is independent of the crack-opening history. Cohesive laws derived from a potential function are independent of the opening history. The existence of a potential function for the cohesive tractions is a pre-requisite for use of the J integral approach (Section 2.2). This requirement was fulfilled for the micromechanical model of Mixed-Mode cross-over bridging described in Section 5.2. The requirement could also be fulfilled for other bridging mechanisms that do not involve history-dependent phenomena such as plasticity and/or friction. Obviously, opening-path history-dependent cohesive laws are more difficult to characterise and formulate. It is therefore proposed to use cohesive laws derived from a potential function unless there is clear experimental evidence that suggests otherwise.

Another advantage of using cohesive laws derived from a potential function is that the work of the cohesive tractions (per unit cross section area) within a cohesive zone can be calculated from the end-opening and end-sliding of the cohesive zone (eq. (2-4)), independent of the opening-path history. If the cohesive tractions are not derived from a potential function, the work of the cohesive tractions can only be calculated by recording the traction-separation history of each point along the cohesive zone and performing the integration corresponding to eq. (2-2) numerically [72]. Thus, there are still unresolved issues concerning the use of bridging/cohesive laws, although the major theoretical and experimental tools are now established.

6.2 Further possibilities and future tasks

Having established micromechanical models, they can be used for microstructural optimisation. The thesis has shown (Section 5.2) that the toughening due to fibre cross-over bridging can be increased by increasing the fracture energy of the fibre/matrix interface. The maximum toughening is anticipated for the maximum value of the fibre/matrix interfacial fracture energy that does not cause fibre failure as assessed by eq. (5-5). Experimental studies could be directed towards tailoring of the fibre/matrix interface towards this target value, such that the macroscale fracture resistance and structural strength can be maximised.

The tools developed in the thesis can be applied to other important topics such as the determination of rate dependent cohesive laws and the characterisation of fibre/matrix interfaces by microscale cohesive laws rather than just fracture energy. This would enable a more accurate micromechanical modelling of fibre cross-over bridging and thus enable microscale optimisation. The basic concepts and analysis procedures developed for cohesive law determination established in this thesis are directly applicable.

Few papers address the influence of crack bridging on cyclic crack growth and the influence on cyclic loading on bridging/cohesive laws. McMeeking and Evans [73] and Cox [74] showed that for a certain type of bridging laws, the formulation of the change in crack tip stress intensity factors takes the same mathematical form as the calculation of the stress intensity factor for a monotonic loading problem. However, whether or not real bridging laws belong to this type is uncertain. Under cyclic loading, the J integral approach may not be useful, since the traction-separation response of a given bridging ligament does not only depend on the local opening but also on the number of opening cycles the ligament has experienced. Furthermore, while cyclic crack growth in metallic materials depends of the difference between the maximum and minimum stress intensity factor [7], the situation may be different under large-scale bridging. For instance, it can be anticipated that bridging ligaments can be damaged more if the minimum crack opening is small than if the minimum crack opening is large. This is likely to result in different bridging stresses and thus different crack growth rates, even though the stress intensity range is the same. Thus, much more research is needed in the area of cyclic crack growth involving large-scale bridging.

7. Summary

"Strength does not come from physical capacity. It comes from an indomitable will"
Mohandas Gandhi

"Difficulties are just things to overcome, after all"
Ernest Shackleton

This Chapter summarises the major results of this thesis. The summary follows the aims listed in Section 1.10.

A.1. Develop a theoretical approach for the determination of Mixed-Mode cohesive laws

- A theoretical J integral/potential function approach can be used for extracting Mixed-Mode bridging/cohesive laws (Chapter 2)

A.2. Develop fracture mechanics test configurations that are suitable for Mode I, Mode II and Mixed-Mode cohesive laws determination

- A new generation of fracture mechanics test specimens allows the J integral approach under large-scale bridging (Chapter 2)

- Dedicated test devices, used in the vacuum chamber of an ESEM, enable in-situ observations of microscale toughening mechanisms (Chapter 3)

- The J integral approach can be used for identifying opening rate effects on cohesive laws, as exemplified by the polyurethane/steel interface, since tests can be done without interruptions at near-constant opening rates (Chapter 4)

B.1. Investigate whether the shape of bridging/cohesive laws can be used for extracting information regarding the dominating microscale toughening mechanism

- Fracture mechanics testing in the ESEM revealed that for crack growth in unidirectional polymer-matrix composites the major toughening mechanism for crack growth parallel to the fibre direction is single fibre and ligament bridging, in brief called fibre cross-over bridging. The macroscale bridging law, predicted from a micromechanical model of Mode I cross-over bridging, shows that the bridging normal stress, σ_n, depends on the normal opening, δ_n, as $\sigma_n \propto \delta_n^{-1/2}$ (Case Study II, Section 4.2)

- The macroscale Mode I bridging law, obtained by a J integral approach, is found to have the same functional dependence on the normal opening as predicted by the micromechanical model, i.e., as $\sigma_n \propto \delta_n^{-1/2}$ (Case Study II, Section 4.2)

- Modelling using the non-linear bridging law, $\sigma_n \propto \delta_n^{-1/2}$, gives a better agreement with experimental measurements of R-curve behaviour of a polymer-matrix composite than modelling assuming a linear softening bridging law (Case Study II, Section 4.2)

- The agreement between the model predictions and experimental measurements underpins the combined approach of the in-situ observations, the micromechanical modelling and the cohesive zone modelling (Case Study II, Section 4.2)

B.2. Investigate whether bridging/cohesive laws can be regarded as material laws

- The cohesive law for a polyurethane/steel interface is used for the prediction of the notch sensitivity and the strength of bonded panels having a central notch. There is excellent agreement between the strength found experimentally and the strength predictions based on cohesive law parameters determined independently by the DCB tests (Case Study I, Section 4.1)

- For the intralaminar cross-over bridging mechanism identified in an unidirectional carbon fibre/epoxy composite, the Mode I bridging law is found to be the same for DCB specimens having different thicknesses, and thus different bridging zone sizes (Case Study II, Section 4.2)

- The successful strength prediction of the medium size adhesive joint/glass fibre composite specimens by cohesive zone modelling shows that it is feasible to use cohesive laws, determined independently by DCB-UBM specimens, for strength predictions of significantly larger specimens (Case Study III, Section 5.1)

B.3. Investigate whether it is realistic to use bridging/cohesive laws that are based on a potential function

- A micromechanical model of cross-over bridging, formulated on the basis of bridging mechanisms identified by in-situ observations, shows that Mixed-Mode bridging laws for cross-over bridging can be derived from a potential function (Case Study IV, Section 5.2)

B.4. Investigate whether real Mixed-Mode cohesive laws are coupled or uncoupled

- The micromechanical Mixed-Mode model predicts that both the normal stress, σ_n, and the shear stress, σ_t, depend on the normal opening, δ_n and tangential opening displacement, δ_t (Case Study III, Section 5.1)

- The results from DCB-UBM tests of an unidirectional glass fibre/polyester composite show that the macroscale Mixed-Mode cohesive laws, obtained from the J integral/potential function approach, are coupled (Case Study IV, Section 5.2)

8. Conclusions

"*All truths are easy to understand once they are discovered; the point is to discover them*"
Galileo Galilei

"*People have a way of coming to a very rational conclusion in a very irrational manner*"
Caldwell Johnson

1. Theoretical and experimental methods are established for the determination of Mode I and Mixed-Mode cohesive laws

2. The shape of a cohesive law is shown to be important for an analysis of the bridging mechanisms as it allows an experimental verification of micromechanical models of toughening mechanisms

3. Cohesive laws are shown to be material laws, by being independent of specimen size, geometry and load configuration

4. The potential function assumption is physically realistic for toughening mechanisms that are not significantly influenced by history-dependent phenomena such as plasticity and friction

5. Mixed-Mode cohesive laws are coupled in a manner which reflects the underlying toughening mechanism

Acknowledgements

"A rich man is nothing but a poor man with money"
W. C. Fields

""Buy, buy!", says the sign in the shop window. "Why, why?", says the junk in the yard"
Paul McCartney

There are many people to thank for helping me in this endeavour. First, I would like to thank the former heads of the Materials Research Division at Risø DTU, Niels Hansen, Robert Feidenhans'l and Allan Schrøder Pedersen as well as the current head of Division Dorte Juul Jensen for creating excellent laboratory facilities and maintaining an inspiring working environment that allows cross-disciplinary collaboration and free-thinking. I have benefited from fruitful discussions with my former and present colleagues from the Composite and Material Mechanics Group and members of other research programmes at Risø DTU. Those that I have interacted most with (besides, of course, my co-authors) are Kristoffer Almdal, Svend Ib Andersen, Tom L. Andersen, Jørgen B. Bilde-Sørensen, Kim Branner, Povl Brøndsted, Stefanie Feih, Hans Lilholt, Lars P. Mikkelsen and Helmuth Toftegaard. I also wish to express my gratitude to and admiration for our technicians for their enthusiasm and for always performing highly skilled work. In particularly, I wish to thank Erik Hansen, Jan Larsen, Christian H. Madsen, Claus Mikkelsen, Jens Olsson, Erling Sørensen and Erik Vogeley for their constructive approach for finding practical solutions for my sometimes wild, academic ideas.

My interest in crack bridging and cohesive laws really took off when I was working at the Engineering Science Centre at Risø for Structural Characterisation and Modelling of Materials. I thank the centre head Torben Leffers for allowing me to pursue new, unplanned research ideas.

I wish to acknowledge that it was Ramesh Talreja who taught me always to think about failure mechanisms, and Jes Christoffersen who taught me to think in equations. Povl Brøndsted and John W. Holmes tried to teach me to be a good experimentalist and always relate experiments to models. I am grateful that they have shared their knowledge with me. This has lead me to the viewpoint that it is better to perform experiments that are difficult to make but are easy to model and interpret, instead of making experiments that are easy to perform but difficult to interpret.

I acknowledge good, inspiring discussions and enjoyable collaboration with my co-authors of the attached papers: Preben Engbæk, E. Kristofer Gamstedt, Stergios Goutianos, Andy Horsewell, Torben K. Jacobsen, Kenneth Jørgensen, Peter Kirkegaard, Amar N. Kumar, Ole Jørgensen and Rasmus C. Østergaard.

It was Povl Brøndsted, Niels Hansen and Ramesh Talreja who constantly encouraged me to write a Doctoral Thesis. I am grateful for their belief in me. Thanks to Prof. Brian Ralph and others for proof-reading drafts of this manuscript and for providing many useful suggestions.

Most of the research of the thesis was made in projects with external funding, such as EFP-projects (partly funded by the Danish Energy Agency) and the Frame Work Programme "Interface design of Composite Materials" partly funded by STVF. I am grateful to the funding agencies for the support for my projects, which, although it might not have been visible from the outside, has enabled my mind to follow a reasonably steady course throughout the years. These projects have all had industrial collaboration. It is a pleasure to see that the industry is now in the process of employing cohesive zone modelling, e.g. in the analysis of wind turbine blades. The Mixed-Mode fracture mechanics test (the double-cantilever beam specimen loaded with uneven bending moments) that was developed from my idea is now being used by LM Glasfiber A/S, the world largest manufacture of wind turbine blades. I am proud to think that I may have made a small difference and that my work has been of benefit for the society.

Finally, but not the least, I wish to thank my wife, Birgit, and our two sons, Morten and Mathias, for their love and for reminding me of the important sides in life (away from research), such as being a family, including going shopping, barbecuing, discovering the fun of playing with a boomerang, designing sophisticated Pokémon card decks and strategies, and uncovering tiny but significant details in the Harry Potter books.

Dansk resumé

"*In the end, it's got to come right*"
Gordon Murray

"*There is no terror in a bang, only in the anticipation of it*"
Alfred Hitchcock

Modellering med kohæsiv zone er inden for det seneste årti blevet udviklet fra at være en avanceret numerisk metode ved modellering af revnevækst til at blive et værktøj som kan bruges til styrkeberegning af industrielle komponenter.

Modellering med kohæsiv zone er baseret på de såkaldte kohæsive love, som beskriver sammenhængen mellem spænding og separation over en brudzone (populært kaldet "sammenhængskraften"). En kohæsiv zone beskriver udviklingen af en brudzone i et materiale eller i en grænseflade under belastning. Det er en ny materialebeskrivelse, der i moderne design kan erstatte styrke og brudsejhed, men som ikke kan bestemmes med de samme metoder. Dette paradigmeskift skaber et behov for metoder til bestemmelse af kohæsive love. Denne afhandling præsenterer nye metoder til bestemmelse af sådanne love for lange brudzoner, hvori fibre eller ligamenter danner "bro" mellem revnefladerne, som det ses f.eks. ved delaminering af laminater fremstillet af polymer-matrix kompositter.

Makroskopiske kohæsive love kan bestemmes på to principielt forskellige måder: ved eksperimentelle målinger og ved mikromekanisk modellering. Eksperimentel bestemmelse af makroskopiske kohæsive love kompliceres af (1) at de matematiske modeller af brudmekaniske prøveemner, der er udviklet inden for rammerne af den lineært-elastisk brudmekanik, ikke er anvendelige når emnerne udviser stor-skala brodannelse og (2) at der kun er få analytiske J integral løsninger for prøveemnekonfigurationer der udviser stor-skala brodannelse.

Mikromekaniske modeller til forudsigelse af kohæsive love bør baseres på brudmekanismer observeret på mikroskala i materialerne. Det kræver at man udfører stabile revnevækstforsøg, dvs. revnen må ikke vokse i spring, og at man udfører sådanne forsøg i et mikroskop, hvor mikrostrukturen kan studeres under stor forstørrelse.

Den foreliggende afhandling kan opdeles i fem dele. I den først del opstilles en teori for J-integral-analyse af kohæsive love og der gennemføres en J-integral-analyse af en ny generation af brudmekaniske prøveemner, som først benyttedes af forfatteren.

Den anden del beskriver udviklingen af brudmekanisk prøvningsudstyr til anvendelse i vakuumkammeret i et ESEM elektronmikroskop. Disse prøvningskonfigurationer er udviklet for at kunne opnå stabil revnevækst; desuden har de en analytisk J-integralløsning som også er gyldig under stor-skala "brodannelseszone". Ved udførelse af forsøg i ESEM er brodannelsesmekanismer blevet karakteriseret under stabil revnevækst.

Den tredje del består af udvikling af mikromekaniske modeller. De mikromekaniske modeller forudsiger makroskopiske kohæsive love, deres størrelse og form, ud fra mikrosmekaniske parametre. En mikromekanisk Mixed-Mode model er blevet udviklet for brodannelse ved fiber-overkrydsning.

Den fjerde del består af måling af makroskopiske kohæsive love for limsamlinger og delaminering af fiberkompositer. En J-integral-baseret metode er anvendt til bestemmelse af en kohæsiv lov under normal åbning (Mode I) til karakterisering af revnevækst i ensrettede fiberkompositter med fiber-overkrydsning. Den fundne brodannelseslov har samme form som forudsagt af en mikromekaniske model. Kohæsive love er også målt for en limsamling under Mode I.

Detaljerede Mixed-Mode kohæsive love er bestemt for delaminering af et laminat med polymer-matrix ved hjælp af et nyudviklet prøveemne, et såkaldt double cantilever beam (DCB) emne belastet med uens bøje momenter (DCB-UBM). Mixed-Mode kohæsive love er fundet ved en fremgangsmåde baseret på anvendelsen af J-integralet og en potentialfunktion. De målte og forudsagte Mixed-Mode kohæsive love er i god kvalitativ overensstemmelse.

Den femte del omfatter styrkeberegning af strukturelle, komponentlignende dele ved anvendelse af målte kohæsive love. To problemer, der udviser stor-skala brudzone, er undersøgt. En Mode I kohæsiv lov, bestemt ved J-integral-metoden på DCB emner, er anvendt til forudsigelse af styrken af limsamlinger med en central kærv; der er opnået en meget god overensstemmelse mellem de forudsagte og målte styrker. Lastbæreevnen af 2-meter lange mellemskala-emner er forudsagt ved simuleringer, hvori der er anvendt Mode I og Mode II kohæsive love bestemt ved DCB-UBM emnerne ved J-integral fremgangsmåden. Mellemskala-emner er fremstillet og testet. Der er fundet god kvantitativ overensstemmelse mellem de forudsagte og målte styrker af mellemskala-emnerne.

Afhandlingen beskriver metoder og kohæsive- og brodannelseslove med henblik på anvendelser ved styrkeberegning af industrielle komponenter af fiberkompositter og limsamlinger, f.eks. i forbindelse med design af vindmøllevinger. En af de brudmekaniske testmetoder (DCB-UBM), som er udviklet af forfatteren, anvendes nu af en af verdens førende vindmøllevingefabrikanter i forbindelse med forbedrede designmetoder til limsamlinger.

De vigtigste konklusioner der kan uddrages af det foreliggende arbejde er følgende: (1) de udviklede teoretiske og eksperimentelle metoder muliggør bestemmelse af kohæsive love under Mode I, Mode II og Mixed-Mode, (2) formen af kohæsive love repræsenterer vigtig information om de underliggende sejhedsforøgende mekanismer, som kan verificeres gennem mikromekaniske modeller, (3) kohæsive love er materiale egenskaber, dvs. uafhængig af belastning og emnegeometri, (4) det er realistisk at anvende kohæsive love der er udledt fra en potentialfunktion, så længe den sejhedsøgende mekanisme ikke i betragtelig grad er påvirket af historieafhængige fænomener så som friktion og plasticitet og (5) Mixed-Mode kohæsive love er koblede på en måde der afhænger af den underliggende sejhedsforøgende mekanisme.

References

"I don't care to belong to any club that will have me as a member"
Groucho Marx

"It is our choices that show what we truly are, far more than our abilities"
J. K. Rowling

Author's selected references that are attached in the Appendix

[A1] Sørensen, B. F., Gamstedt, E. K., and Jacobsen. T. K., 2000, "Equivalence of J integral and stress intensity factor approach for large scale bridging problems", *International Journal of Fracture*, Vol. 104, pp. L31-6.

[A2] Sørensen, B. F., and Kirkegaard, P., 2006, "Determination of mixed-mode cohesive laws", *Engineering Fracture Mechanics*, Vol. 73, pp. 2642-61.

[A3] Sørensen, B. F., Jørgensen, K., Jacobsen, T. K., and Østergaard, R. C., 2006, "DCB-specimen loaded with uneven bending moments", *International Journal of Fracture*, Vol. 141, pp. 163-176.

[A4] Sørensen, B. F., and Jacobsen, T. K., 2009, "Characterising delamination of fibre composites by mixed-mode cohesive laws", *Composite Science and Technology*, Vol. 69, pp. 445-456.

[A5] Sørensen, B. F., Gamstedt, E. K., Østergaard, R. C., and Goutianos, S., 2008, "Micromechanical model of cross-over fibre bridging - prediction of mixed-mode bridging laws", *Mechanics of Materials*, Vol. 40, pp. 220-34.

[A6] Sørensen, B. F., Horsewell, A., Jørgensen, O., Kumar, A. N., and Engbæk, P., 1998, "Fracture resistance measurement method for *in-situ* observation of crack mechanisms", *Journal of the American Ceramic Society*, Vol. 81, pp. 661-9.

[A7] Sørensen, B. F., 2002, "Cohesive law and notch sensitivity of adhesive joints", *Acta Materialia*, Vol. 50, pp. 1053-61.

[A8] Sørensen, B. F. and Jacobsen, T. K., 1998, "Large scale bridging in composites: R-curve and bridging laws", *Composites part A*, Vol. 29A, pp. 1443-51.

[A9] Jacobsen, T. K., and Sørensen, B. F., 2001, "Mode I Intra-laminar crack growth in composites - modelling of R-curves from measured bridging laws", *Composites part A*, Vol. 32, pp. 1-11.

[A10] Sørensen, B. F., Goutianos, S., and Jacobsen, T. K., 2009, "Strength scaling of adhesive joints in polymer-matrix composites", *International Journal of Solids and Structures*, Vol. 46, pp. 741-761.

Other references by the author (not included in the thesis)

[A11] Sørensen, B. F. and Jacobsen, T. K., 2000, "Crack growth in composites: Applicability of R-curves and bridging laws", *Plastic Rubber and Composites, Processing and Application*, Vol. 29, pp. 119-33.

[A12] Sørensen, B. F., 1993, "Effect of fibre roughness on the overall stress-transverse strain response of ceramic composites", *Scripta Metallurgica et Materialia*, Vol. 28, pp. 435-9.

Other references

[1] "New approaches to testing of design details", *LM Newsletter*, February 2005, p. 3.

[2] Timoshenko, S. P., 1953, History of strength of materials, Dover Publishing, Inc. New York.

[3] Griffith, A. A., 1921, "The phenomena of rupture and flow in solids", *Proceedings of the Royal Society A - Mathematics, Physics and Engineering Sciences,* Vol. A221, pp. 163-98.

[4] Irwin, G. R., Kies, J. A., and Smith, H. L., 1958, "Fracture strength relative to onset and arrest of crack propagation", *Proceedings of the American Society for Testing Materials*, Vol. 58, pp. 640-57.

[5] Williams, M. L., 1957, "On the stress distribution at the base of a stationary crack", *Journal of Applied Mechanics*, Vol. 24, pp. 109-14.

[6] Irwin, G. R., 1957, "Analysis of stress and strains near the end of a crack traversing a plate", *Journal of Applied Mechanics*, Vol. 24, pp. 361-4.

[7] Paris, P., and Erdogan, F., 1963, "A critical analysis of crack propagation laws", *Journal of Basic Engineering, Series D*, Vol. 85, pp. 528-34.

[8] Sih, G. C., 1973, Handbook of stress-intensity factors, Lehigh University, Bethlehem, Pennsylvania.

[9] Tada, H., Paris, P. C., and Irwin, G. R., 2000, The stress analysis of cracks handbook, American Society of Mechanical Engineers.

[10] Thouless, M. D., and Evans, A. G., 1990, "Comment on the spalling and edge-cracking of plates", *Scripta Metallurgical et Materialia*, Vol. 24, pp. 1507-10.

[11] Rice, J. R., 1988, "Elastic fracture mechanics concepts for interfacial cracks", *Journal of Applied Mechanics*, Vol. 55, pp. 98-103.

[12] Hutchinson, J. W., and Suo, Z., 1992, "Mixed mode cracking in layered materials", in Advanced in Applied Mechanics, Vol. 29 (Ed. J. W. Hutchinson and T. Y. Wu), Academic Press, Inc., Boston, pp. 63-191.

[13] Williams, M. L., 1959, "The stresses around a fault or crack in dissimilar media", *Bulletin of the Seismological Society of America*, Vol. 49, pp. 199-204.

[14] Cao, H. C., and Evans, A. G., 1989, "An experimental study of the fracture resistance of bimaterial interfaces", *Mechanics of Materials*, Vol. 7, pp. 295-304.

[15] Thouless, M. D., 1990, "Fracture of a model interface under mixed-mode loading", *Acta Metallurgica*, Vol. 38, pp. 1135-40.

[16] Jensen, H. M., 1990, "Mixed-mode interface fracture criteria", *Acta Metallurgica et Materialia*, Vol. 38, pp. 2637-44.

[17] Liechti, K. M., and Chai, Y. -S., 1992, "Asymmetric shielding in interfacial fracture under in-plane shear", *Journal of Applied Mechanics*, Vol. 59, pp. 295-304.

[18] Dugdale, D. S., 1960, "Yielding of steel sheets containing slits", *Journal of the Mechanics and Physics of Solids*, Vol. 8, pp. 100-4.

[19] Barenblatt, G. I., 1962, "The mathematical theory of equilibrium cracks in brittle fracture" *Advances in Applied Mechanics*, Vol. 7, pp. 55-129.

[20] Rice, J. R., 1968, "A path independent integral and the approximate analysis of strain concentrations by notches and cracks", *Journal of Applied Mechanics*, Vol. 35, pp. 379-86.

[21] Marshall, D. B., Cox, B. N. and Evans, A. G., 1985, "The mechanics of matrix cracking in brittle-matrix fiber composite", *Acta Metallurgica*, Vol. 33, pp. 2013-21.

[22] Budiansky, B., Hutchinson, J. W., and Evans, A. G., 1986, "Matrix fracture in fiber-reinforced ceramics", *Journal of the Mechanics and Physics of Solids*, Vol. 34, pp. 167-78.

[23] McCartney, L. N., 1987, "Mechanics of matrix cracking in brittle-matrix fiber-reinforced composites", *Proceedings of the Royal Society A - Mathematics, Physics and Engineering Sciences*, Vol. A409, pp. 329-50.

[24] Curtin, W. A., 1991, "Theory of mechanical properties of ceramic matrix composites", *Journal of the American Ceramic Society*, Vol. 74, pp. 2837-45.

[25] Thouless, M. D., and Evans, A. G., 1988, "Effects of pull-out on the mechanical properties of ceramic-matrix composites", *Acta Metallurgica*, Vol. 36, pp. 517-22.

[26] Hutchinson, J. W., and Jensen, H. M., 1990, "Models of fiber debonding and pullout in brittle composites with friction", *Mechanics of Materials*, Vol. 9, pp. 139-63.

[27] Needleman, A., 1987, "A continuum model for void nucleation by inclusion debonding", *Journal of Applied Mechanics*, Vol. 54, pp. 525-531.

[28] Tvergaard, V., and Hutchinson, J. W., 1992, "The relation between crack growth resistance and fracture process parameters in elastic-plastic solids" *Journal of the Mechanics and Physics of Solids*, Vol. 40. pp. 1377-97.

[29] Tvergaard, V., and Hutchinson, J. W., 1993, "The influence of plasticity on mixed-mode interface toughness", *Journal of the Mechanics and Physics of Solids*, Vol. 41, pp. 1119-35.

[30] Tvergaard, V., and Hutchinson, J. W., 1994, "Toughness of an interface along a thin ductile layer joining elastic solids", *Philosophical Magazine A*, Vol. 70, pp. 641-56.

[31] Suo, Z., Ho, S., and Gong, X., 1993, "Notch ductile-to-brittle transition due to localized inelastic band", *Journal of Engineering Materials and Technology*, Vol. 115, pp. 319-26.

[32] Gu, P., 1995, "Notch sensitivity of fiber-reinforced ceramics", *International Journal of Fracture*, Vol. 70, pp. 253-66.

[33] He, M.-Y., Wu, B., and Suo, Z., 1994, "Notch sensitivity and shear bands in brittle matrix composites", *Acta Metallurgica et Materialia*, Vol. 42, pp. 3065-70.

[34] Hillerborg, A., 1991, "Application of the fictitious crack model to different types of materials", *International Journal of Fracture*, Vol. 51, pp. 95-102.

[35] Cotterell, B., and Mai, Y.W., 1996, Fracture mechanics of cementitious materials, Blackie Academic & Professional, an Imprint of Chapman and Hall, London, UK.

[36] Serrano, E., Gustafsson, P. J., 1999, "Influence of bondline brittleness and defects on the strength of timber finger-joints", *International Journal of Adhesion and Adhesives*, Vol. 19, pp. 9-17.

[37] Yang, Q. D., Thouless, M. D., and Ward, S. M, 1999, "Numerical simulations of adhesively-bonded beams failing with extensive plastic deformation", *Journal of the Mechanics and Physics of Solids*, Vol. 47, pp. 1337-53.

[38] Mohammad, I., and Liechti, K. M., 2000, "Cohesive zone modelling of crack nucleation at bimaterial corner", *Journal of the Mechanics and Physics of Solids*, Vol. 48, pp. 735-64.

[39] Yang, Q. D. and Thouless, M. D., 2001, "Mixed-mode fracture analysis of plastically-deforming adhesive joints", *International Journal of Fracture*, Vol. 110, pp. 175-87.

[40] Suo, Z., Bao, G., and Fan, B., 1992, "Delamination R-curve phenomena due to damage", *Journal of the Mechanics and Physics of Solids*, Vol. 40, pp. 1-16.

[41] Broberg, K. B., 1999, Cracks and fracture, Academic Press, San Diego, pp. 15-26.

[42] Jin, Z.-H., and Sun, C. T., 2006, "Cohesive zone modelling of interface fracture in elastic bi-materials", *Engineering Fracture Mechanics*, Vol. 72, pp. 1805-17.

[43] Cottrell, A. H., 1963, "Mechanics of fracture", The 1963 Tewksbury Symposium on Fracture, University of Melbourne, pp. 1-27.

[44] Kanninen, M. F., and Popelar, C. H., 1985, Advanced fracture mechanics, Oxford University Press, New York.

[45] Wang, S. S., Mandell, J. F., and McGarry, F. J., 1978, "An analysis of the crack tip stress field in DCB adhesive fracture specimen", *International Journal of Fracture*, Vol. 14, pp. 39-58.

[46] Charalambides, M., Kinloch, A. J., Wang, Y., and Williams, J. G., 1992, "On the analysis of mixed-mode failure", *International Journal of Fracture*, Vol. 54, pp. 269-91.

[47] Cox, B. N., 1991, "Extrinsic factors in the mechanics of bridged cracks", *Acta Metallurgica et Materialia*, Vol. 39, pp. 1189-201.

[48] Spearing, S. M., and Evans, A. G., 1992, "The role of fiber bridging in the delamination resistance of fiber-reinforced composites", *Acta Metallurgica et Materialia*, Vol. 40, pp. 2191-9.

[49] Camanho, P. P., Davilia, C. G., and de Moura, M. F., 2003, "Numerical simulation of mixed-mode progressive delamination in composite materials", *Journal of Composite Materials*, Vol. 37, pp. 1415-1438.

[50] Xu, X.-P., and Needleman, A., (1993), "Void neucleation by inclusion debonding in a crystal matrix", *Modelling and Simulation in Materials Science and Engineering.*, Vol. 1, pp. 111-132.

[51] Tvergaard, V., 1990, "Effect of fibre debonding in a whisker-reinforced metal", *Materials Science and Engineering*, Vol. A125, pp. 203-13.

[52] Hashemi, S., Kinloch, A. J., and Williams, J. G., 1990, "The analysis of interlaminar fracture in unidirectional fibre-polymer composites", *Proceedings of the Royal Society A - Mathematics, Physics and Engineering Sciences*, Vol. A 427, pp. 173-90.

[53] Reeder, J. R., and Crews Jr, J. H., 1992, "Redesign of the mixed-mode bending delamination testing", *Journal of Composites Technology & Research*, Vol. 14, pp. 12-19.

[54] Brenet, P. Conchin, F., Fantozzo, G., Reynaud, P., Rouby, D., and Tallaron, C., 1996, "Direct measurement of the crack bridging tractions: A new approach of the fracture behavior of ceramic-matrix composites", *Composite Science and Technology*, Vol. 56, pp. 817-23.

[55] Cox, B. N., and Marshall, D. B., 1991, "The determination of crack bridging forces", *International Journal of Fracture*, Vol. 49, pp. 159-76.

[56] Fett, T., 1995, "Evaluation of the bridging relation from crack-opening-displacement measurements by use of the weight function", *Journal of the American Ceramic Society*, Vol. 78, pp. 945-8.

[57] Li, V. C., and Ward, R. J., 1989, "A novel testing technique for post-peak tensile behaviour of cementitious materials", in Fracture toughness and fracture energy - testing methods for concrete and rocks (eds. H. Mihashi, H. Takahashi and F. H. Wittmann), A. A. Balkema Publishers, Rotterdam, pp. 183-95.

[58] Rice, J. R., 1968, "Mathematical analysis in the mechanics of fracture", in Fracture, An Advanced Treatice, Vol. II (ed. H. Liebowitz), Academic Press, New York and London, pp. 191-311.

[59] Fett, T., and Munz, D., 1993, "Evaluation of R-curve effects in ceramics", *Journal of Mater Science*, Vol. 28, pp. 742-752.

[60] Olsson, P. and Stigh, U., 1989, "On the determination of the constitutive properties of thin interphase layers - an exact solution", *International Journal of Fracture*, Vol. 41, pp. R71-6.

[61] Marshall, D. B., Shaw, M. C., and Morris, W. L., 1992, "Measurement of interfacial debonding and sliding resistance in fiber reinforced intermetallics", *Acta Metallurgica et Materialia*, Vol. 40, pp. 443-54.

[62] Budiansky, B., Evans, A. G., and Hutchinson, J. W., 1995, "Fiber-matix debonding effects on cracking in aligned fiber ceramic composites", *International Journal of Solids and Structures*, Vol. 32, pp. 315-28.

[63] Sorensen, L., Botsis, J., Gmür, T., and Cugnoni, 2007, "Delamination detection and characterisation of bridging tractions using long FBG optical sensors", *Composites part A*, Vol. 38, pp. 2087-96.

[64] Bao, G. and Suo, Z., 1992, "Remarks on crack-bridging concepts", *Applied Mechanics Review*, Vol. 45, pp. 355-61.

[65] Suo, Z., and Hutchinson, J. W., 1990, "Interface crack between two elastic layers", *International Journal of Fracture*, Vol. 43, pp. 1-18.

[66] Carlsson, L. A., Gillespie, J. W. Jr., and Pipes, R. B., 1986, "On the analysis and design of the end notch flexure (ENF) specimen for mode II testing", *Journal of Composite Materials*, Vol. 20, pp. 594-604.

[67] Zhu, Y., Liechti, K. M., and Ravi-Chandor, K., 2009, "Direct extraction of rate-dependent traction-separation laws for polyurea/steel interfaces", *International Journal of Solids and Structures*, Vol. 46, pp. 31-51.

[68] Tamuzs, V., Tarasovs, S., and Vilk, U., 2001, "Progressive delamination and fiber bridging modelling in DCB composite specimens", *Engineering Fracture Mechanics*, Vol. 68, pp. 513-25.

[69] Østergaard, R. C., 2007, Interface fracture in composite materials and structures, Ph.D.-thesis, DCAMM Special Report No. S102, Department of Mechanical Engineering, The Technical University of Denmark, Lyngby, Denmark, p. 61.

[70] Leffler, K., Alfredsson, K. S., and Stigh, U., 2007, "Shear behaviour of adhesive layers", *International Journal of Solids and Structures*, Vol. 44, pp. 530-45.

[71] Östlund, S., 1995, "Fracture modelling of brittle-matrix composites with spatially dependent crack bridging", *Fatigue & Fracture of Engineering Materials & Structures*, Vol. 18, pp. 1213-30.

[72] Van den Bosch, M. J., Schreurs, P. J. G., and Geers, M. G. D., 2006, "An improved description of the exponential Xu and Needleman cohesive zone law for mixed-mode decohesion", *Engineering Fracture Mechanics*, Vol. 73, pp. 1220-34.

[73] McMeeking, R. M., and Evans, A. G., 1990, "Matrix fatigue cracking in fiber composites", *Mechanics of Materials*, Vol. 9, pp. 217-27.

[74] Cox, B. N., 1993, "Scaling for bridged cracks", *Mechanics of Materials*, Vol. 15, pp. 87-98.

APPENDIX: Published papers

[A1] Sørensen, B. F., Gamstedt, E. K., and Jacobsen. T. K., 2000, "Equivalence of J integral and stress intensity factor approach for large scale bridging problems", *International Journal of Fracture,* Vol. 104, pp. L31-6.

[A2] Sørensen, B. F., and Kirkegaard, P., 2006, "Determination of mixed-mode cohesive laws", *Engineering Fracture Mechanics,* Vol. 73, pp. 2642-61.

[A3] Sørensen, B. F., Jørgensen, K., Jacobsen, T. K., and Østergaard, R. C., 2006, "DCB-specimen loaded with uneven bending moments", *International Journal of Fracture,* Vol. 141, pp. 163-176.

[A4] Sørensen, B. F., and Jacobsen, T. K., 2009, "Characterising delamination of fibre composites by mixed-mode cohesive laws", *Composite Science and Technology,* Vol. 69, pp. 445-456.

[A5] Sørensen, B. F., Gamstedt, E. K., Østergaard, R. C., and Goutianos, S., 2008, "Micromechanical model of cross-over fibre bridging - prediction of mixed-mode bridging laws", *Mechanics of Materials,* Vol. 40, pp. 220-34.

[A6] Sørensen, B. F., Horsewell, A., Jørgensen, O., Kumar, A. N., and Engbæk, P., 1998, "Fracture resistance measurement method for in-situ observation of crack mechanisms", *Journal of the American Ceramic Society,* Vol. 81, pp. 661-9.

[A7] Sørensen, B. F., 2002, "Cohesive law and notch sensitivity of adhesive joints", *Acta Materialia,* Vol. 50, pp. 1053-61.

[A8] Sørensen, B. F. and Jacobsen, T. K., 1998, "Large scale bridging in composites: R-curve and bridging laws", *Composites part A,* Vol. 29A, pp. 1443-51.

[A9] Jacobsen, T. K., and Sørensen, B. F., 2001, "Mode I Intra-laminar crack growth in composites - modelling of R-curves from measured bridging laws", *Composites part A,* Vol. 32, pp. 1-11.

[A10] Sørensen, B. F., Goutianos, S., and Jacobsen, T. K., 2009, "Strength scaling of adhesive joints in polymer-matrix composites", *International Journal of Solids and Structures,* Vol. 46, pp. 741-761.

[A1]

Sørensen, B. F., Gamstedt, E. K., and Jacobsen. T. K., 2000

"Equivalence of J integral and stress intensity factor approach for large scale bridging problems"

International Journal of Fracture, Vol. 104, pp. L31-6

International Journal of Fracture **104**: L31–L36, 2000.

EQUIVALENCE OF J INTEGRAL AND STRESS INTENSITY FACTOR APPROACHES FOR LARGE SCALE BRIDGING PROBLEMS

Bent F. Sørensen, E. Kristofer Gamstedt and Torben K. Jacobsen
Materials Research Department, Risø National Laboratory
DK-4000 Roskilde, Denmark

Abstract. The application of the J integral to problems involving large scale crack bridging is discussed. Using some simple examples for which close form analytical solutions exist, it is shown that there is a complete agreement between analysis based on stress intensity factors and the J integral. A simple method for deriving the bridging law from J integral measurements is outlined.

1. Introduction. In some earlier papers doubt has been raised concerning the use of the J integral for crack problems involving large scale bridging (LSB). In models of specimens possessing LSB the physical bridging (e.g. fibres or grains connecting the two crack faces) is modelled by a bridging law, $\sigma(\delta)$. The local bridging stress, σ, is assumed to depend only on the local crack opening, δ. Evaluating the path independent J integral along a path Γ_{loc} (Fig. 1) locally along the bridged crack faces gives (Rice, 1968; Suo *et al.*, 1992)

$$J_{loc} = J_{tip} + \int_0^{\delta^*} \sigma(\delta) d\delta \tag{1}$$

where J_{tip} is the value of the J integral evaluated just around the crack tip and δ^* is the end-opening of the bridging zone, see Fig. 1. Within linear elasticity stress fields can be added while strain energy, which can be regarded as stress squared, is not additive. Thus, it has been argued, stress intensity factors (of same mode) can be added, but the use of (1) is invalid since it is identical to summing energy terms (Stevens and Guiu, 1994). The purpose of this letter is to show that under LSB there is no conflict between the use of the J integral approach and the stress intensity based approach. This is demonstrated by analysing two problems that have analytical solutions.

2. Basic concepts. Only mode I situations are considered in the following. The stress intensity factor from the applied load is denoted K_a. The stress intensity factor resulting from the bridging stress is K_b. Then, the stress intensity factor at the crack tip, K_{tip}, becomes

$$K_{tip} = K_a + K_b \,. \tag{2}$$

Evaluating the J integral along a path Γ_{tip}, just surrounding the crack tip, gives under plane stress (Rice, 1968)

$$J_{tip} = \frac{K_{tip}^2}{E}, \tag{3}$$

where E denotes the Young's modulus of the bulk material. J_{loc} is defined as the J integral evaluated along Γ_{loc}, see Fig. 1. Finally, J_{ext} is defined as the J integral evaluated along the external boundaries of the specimen, Γ_{ext}, see Fig. 1. In the following it will be shown that the value of K_{tip} calculated from J_{ext} (by setting J_{ext} equal to J_{loc} and calculating J_{tip} by (1) and K_{tip} by (3)) is identical to the result obtained by the use of the stress intensity approach (2).

3. Example I: A DCB specimen loaded with wedge forces. Consider a double cantilever beam (DCB) specimen loaded with wedge forces, see Fig. 2. The distance from the crack tip to the beam-ends where the wedge forces, P_a, are applied is denoted ℓ_a. For simplicity, a very simple bridging law will be used, viz,

$$\sigma(\delta) = \begin{cases} 0 & \textit{for} \quad 0 \le \delta < \delta_0 - \Delta\delta \\ \sigma_0 & \textit{for} \quad \delta_0 - \Delta\delta \le \delta \le \delta_0 + \Delta\delta \\ 0 & \textit{for} \quad \delta > \delta_0 + \Delta\delta \end{cases} \tag{4}$$

where σ_0 is a characteristic stress, δ_0 is a given crack opening and $\Delta\delta$ is a small (positive) change in crack opening, as depicted in Fig. 3. This particular bridging law is chosen, because it allows an easy calculation of K_b. The bridging law can be modelled by two forces, P_b, positioned a distance ℓ_b from the crack tip where the opening δ_b equals δ_0, see Fig. 4. The stress intensity factors are (Broek, 1986)

$$K_a = \frac{P_a \ell_a}{\sqrt{BI}}, \tag{5}$$

where B is the specimen width and I is the moment of inertia, and

$$K_b = -\frac{P_b \ell_b}{\sqrt{BI}}. \tag{6}$$

The minus sign appears because the bridging stresses act to close the crack and thus reduce the crack tip stress intensity. Starting from the crack tip, equations (5) and (6) are combined according to (2) and (3) giving

$$J_{tip} = \frac{P_a^2 \ell_a^2 + P_b^2 \ell_b^2 - 2P_a P_b \ell_a \ell_b}{BEI}. \tag{7}$$

Moving outwards, the J integral evaluated along Γ_{loc} according to (1) gives by (4)

$$J_{loc} = J_{tip} + 2\sigma_0 \Delta\delta \qquad for \qquad \delta^* > \delta_0 + \Delta\delta. \tag{8}$$

To proceed further, σ_0 and $\Delta\delta$ in (8) must be related to P_b. Assume that P_b is uniformly distributed over a length Δx_1 (Fig. 4)

$$\sigma_0 = \frac{P_b}{B\Delta x_1}. \tag{9}$$

Δx_1 relates to $\Delta\delta$ and θ_b, the beam rotation at the position of P_b (i.e., at x_1=-ℓ_b), as

$$\theta_b = tan^{-1}\left(\frac{\Delta\delta}{\Delta x_1}\right) \approx \frac{\Delta\delta}{\Delta x_1} \quad \Rightarrow \quad \Delta\delta \approx \theta_b \Delta x_1, \tag{10}$$

where θ_b is given by the simple beam theory (Gere and Timoshenko, 1984) as

$$\theta_b = \frac{(P_a - P_b)\ell_b^2}{2EI} + \frac{P_a(\ell_a - \ell_b)\ell_b}{EI}. \tag{11}$$

Inserting J_{tip} from (7), σ_0 from (9) and $\Delta\delta$ from (10) and (11) into (8) gives

$$J_{loc} = \frac{P_a^2 \ell_a^2}{BEI} - \frac{P_a P_b \ell_b^2}{BEI}. \tag{12}$$

Both $\Delta\delta$ and Δx_1 vanish from the equations when expressed through P_b. Finally, the J integral along Γ_{ext} is (Olsson and Stigh, 1989; Sørensen and Jacobsen, 2000)

$$J_{ext} = \frac{2P_a\theta_a}{B}. \tag{13}$$

The rotation θ_a is calculated from the simple beam theory as

$$\theta_a = \frac{P_a \ell_a^2}{2EI} - \frac{P_b \ell_b^2}{2EI}. \tag{14}$$

Inserting θ_a from (14) into (13) gives precisely the result in equation (12). Therefore, if the specimen is analysed by calculating J_{ext} according to (13) and (1), one arrives at the same J_{tip} (and thus the same K_{tip}) as one gets by superposition of stress intensity factors (2). Thus, the J integral approach is consistent with the stress intensity approach.

Note that under LSB J_{ext} is *not* equal to K_a^2/E. It is precisely the incorrect presumption ($J = K_a^2/E$) that lead to the erroneous conclusion that under LSB there is a conflict between the K-approach and the J integral approach.

4. Example II: A DCB specimen loaded with pure bending moments. Consider next a DCB specimen loaded with pure bending moments, M, as shown in Fig. 5. Assume the same bridging law as before, i.e. (4). Then we have

$$K_a = \frac{M}{\sqrt{BI}}, \tag{15}$$

while K_b is still given by (6). Inserting (6) and (15) into (2) and (3) gives

$$J_{tip} = \frac{M^2}{BEI} + \frac{P_b^2 \ell_b^2}{BEI} - \frac{2MP_b \ell_b}{BEI}. \tag{16}$$

J_{loc} and σ_0 are still given by (8) and (9). $\Delta\delta$ is related to θ_b by (10), where now

$$\theta_b = \frac{M\ell_b}{EI} - \frac{P_b \ell_b^2}{2EI}. \tag{17}$$

Inserting J_{tip} from (16), $\Delta\delta$ from (10) and (17) into (8) simply gives

$$J_{loc} = \frac{M^2}{BEI}. \tag{18}$$

For this configuration all terms involving P_b cancel out. Evaluating the J integral along the external boundaries gives the same result as (18), see Suo *et al.* (1992) and Sørensen and Jacobsen (2000). Thus, also for this test configuration the J approach (1) is consistent with the K-approach (2).

5. Discussion. To keep the mathematics as simple as possible the simplest form of bridging law, a point force, was chosen in these examples. It is straight forward to extend the analysis to more point forces. Still, a consistent relationship between K_a, K_b and the J integral approach (1) will be found. Since any bridging

stress distribution can be constructed by superposition of point forces, it follows that (1) is valid for any bridging law shape.

Note that for the DCB specimen loaded with pure bending moments J_{ext} can be determined in closed form independent of the bridging law. Thus, this test configuration is particularly useful for characterising LSB (Suo *et al.*, 1992). The bridging law can be derived directly from measured fracture resistance data, if the end-opening of the bridging zone, δ^*, is measured (Suo *et al.* 1992), as

$$\sigma(\delta^*) = \frac{\partial J_R}{\partial \delta^*}, \tag{19}$$

where J_R denotes the fracture resistance, i.e. the value of J_{ext} during crack growth. This approach has been used experimentally by Sørensen and Jacobsen (1998). Specimens of different dimensions gave identical bridging laws, despite having different R-curves.

In conclusion, there is consistency between the J integral approach and the stress intensity approach for large scale bridging problems. Using the J integral approach, bridging laws can be derived in a manner that is much simpler than solving the integral equation involved in the stress intensity approach.

REFERENCES

Broek, D. (1986). *Elementary Engineering Fracture Mechanics*, 4th edition, Mertinus Nijhoff Publishers, Dordrecht and Boston.

Gere, J. M. and Timoshenko, S. P. (1984). *Mechanics of Materials*, second SI edition, PWS Publishers, Boston, 736-737.

Olsson, P. and Stigh, U. (1989). On the determination of the constitutive properties of thin interphase layers - an exact inverse solution. *International Journal of Fracture* **41**, R71-R76.

Rice, J. R. (1968). A path independent integral and the approximate analysis of strain concentrations by notches and cracks. *Journal of Applied Mechanics* **35**, 379-86.

Stevens, R. N. and Guiu, F. (1994). The application of the J integral to problems of crack bridging. *Acta Metallurgica et Materialia* **42**, 1805-10.

Suo, Z., Bao, G. and Fan, B. (1992). Delamination R-curve phenomena due to damage. *Journal of the Mechanics and Physics of Solids* **40**, 1-16.

Sørensen, B. F. and Jacobsen, T. K. (1998). Large scale bridging in composites: R-curves and bridging laws. *Composites part A* **29**, 1443-51.

Sørensen, B. F. and Jacobsen, T. K. (2000). Crack growth in composites: Applicability of R-curves and bridging laws. *Plastic Rubber and Composites* **23**, 119-33.

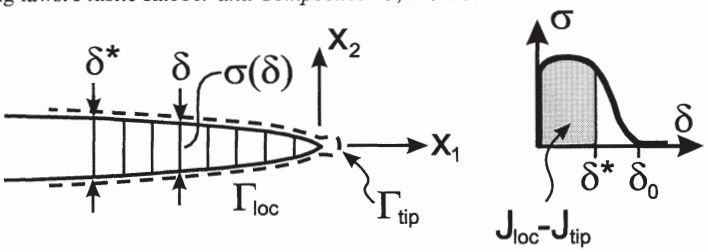

Fig. 1. Principles of crack bridging and bridging laws

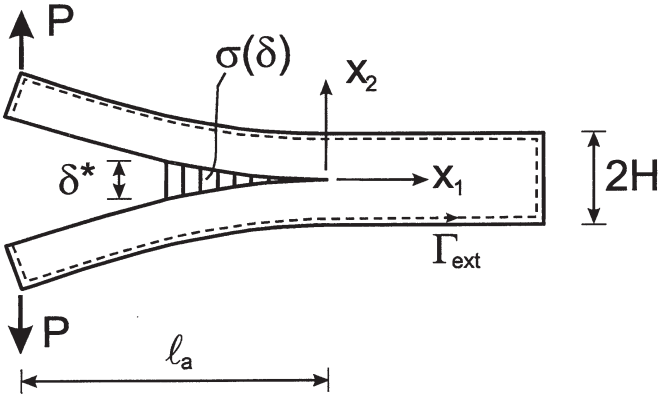

Fig. 2. DCB specimen loaded with wedge forces

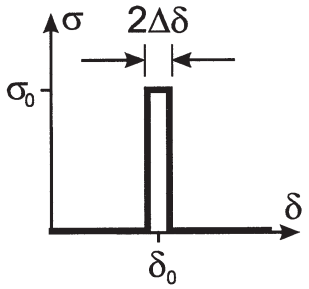

Fig. 3. Bridging law of a point force. Bridging stress as function of crack opening

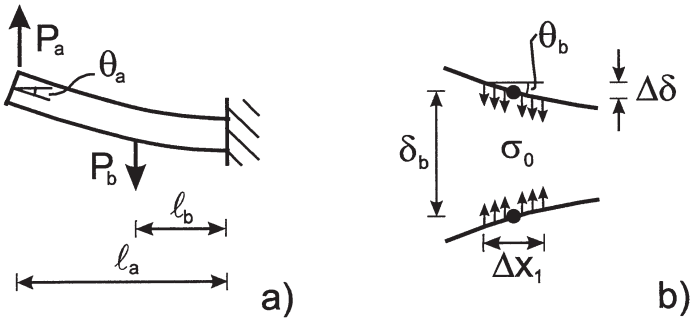

Fig. 4. a) Model of DCB specimen loaded with wedge force, P_a. Bridging is modelled by point force, P_b. b) Geometric relations between $\Delta\delta$, θ_b and Δx_1

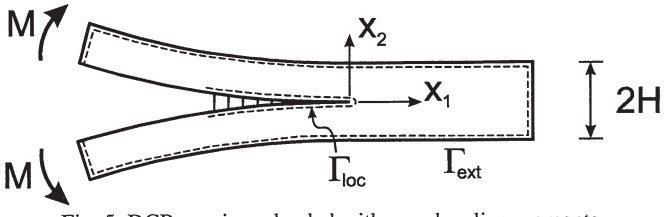

Fig. 5. DCB specimen loaded with pure bending moments

[A2]

Sørensen, B. F., and Kirkegaard, P., 2006

"Determination of mixed-mode cohesive laws"

Engineering Fracture Mechanics, Vol. 73, pp. 2642-61

Available online at www.sciencedirect.com
ScienceDirect
Engineering Fracture Mechanics 73 (2006) 2642–2661
Engineering Fracture Mechanics
www.elsevier.com/locate/engfracmech

Determination of mixed mode cohesive laws

Bent F. Sørensen [a,*], Peter Kirkegaard [b]

[a] Materials Research Department, Risø National Laboratory, Frederiksborgvej 399, P.O. Box 49, DK-4000 Roskilde, Denmark
[b] IT-Service Department, Risø National Laboratory, DK-4000 Roskilde, Denmark

Received 1 November 2005; received in revised form 4 April 2006; accepted 13 April 2006
Available online 22 June 2006

Abstract

A novel approach is proposed for the determination of mixed mode cohesive laws for large scale crack bridging problems. The approach is based on a plane, two-dimensional analysis utilizing the *J* integral applied a double cantilever beam specimens loaded with uneven bending moments. The normal and shear stresses of the cohesive laws are obtained from consecutive values of the fracture resistance, the normal and tangential displacements of the end of the cohesive zone. The data analysis involves fitting and determination of partial differentials. This is done by a numerical method using Chebyshev polynomials. The accuracy of the numerical procedure is investigated by the use of synthetic data. It is found that both the shape and peak stress of the cohesive law can be determined with high accuracy, providing that the data possess low noise and a sufficiently high number of datasets are used. The investigation leads to some practical guidelines for experimental use of the proposed approach.

Keywords: Mixed mode crack bridging; *J* integral; Cohesive laws; Bridging laws

1. Introduction

Cohesive laws, introduced by Dugdale [1] and Barenblatt [2] to describe the mechanical stress-separation behaviour of a failure process zone, are widely used in models of problems involving crack initiation and growth. While cohesive laws represent the entire failure process zone, bridging laws are used for describing crack bridging phenomena behind a crack tip, at which a singular stress field exists. Due to their similarities, we will not make a sharp distinction between bridging laws and cohesive laws in the present paper. A beauty of the bridging/cohesive law approach is that it can be applied to a number of very different problems on various scales. For instance, model studies have given valuable understanding of microscale failure mechanisms, such as the formation of a crack tip plastic zone [3] and the development of fibre-bridged matrix cracks in ceramic matrix composites [4]. Other investigations have used cohesive laws for strength prediction of macroscale specimens, such as the strength of panels with holes or notches and strength of adhesive joints [5–10]. It has been

* Corresponding author. Tel.: +45 4677 5806; fax: +45 4677 5758.
E-mail address: bent.soerensen@risoe.dk (B.F. Sørensen).

0013-7944/$ - see front matter
doi:10.1016/j.engfracmech.2006.04.006

Nomenclature

a_{ij}	Chebyshev coefficients
f	approximate function (product of Chebyshev polynomials)
i	integer subscript
j	integer subscript (coordinate axis; polynomial degree)
k	integer subscript (polynomial degree)
n	shape parameter of power law function
n_i	normal vector
p	integer
r^2	goodness of fit
u_i	displacement field (vector)
x_i	Cartesian coordinate system
$\bar{x}$	transformed normal end opening displacement
$\bar{y}$	transformed tangential end opening displacement
B	specimen width
E	Young's modulus
H	specimen height
L	bridging zone length
J	J integral value
J_0	crack tip fracture energy
J_{ss}	steady-state fracture resistance
J_{tip}	J integral value evaluated around crack tip
M	number of data points per phase angle
M_1	moment applied to one arm of DCB specimens
M_2	moment applied to the other arm of DCB specimens
N	number of data points in the group of datasets (all phase angles)
S	curve length
T_i	Chebyshev polynomial of the first kind of degree i
W	strain energy density
δ	crack opening displacement
δ_0	end opening where cohesive stresses vanish
δ^*	end opening displacement
δ_n	normal displacement
δ_t	tangential displacement
δ_n^*	normal displacement of end opening
δ_t^*	tangential displacement of end opening
φ	phase angle of opening
ε_{ij}	strain tensor
ν	Poisson's ratio
ω	noise parameter
σ_{ij}	stress tensor
ξ	parameter of power law function
σ_n	cohesive normal stress
σ_t	cohesive shear stress
$\hat{\sigma}_n$	peak normal stress
$\Delta\varphi$	difference between phase angles
Δ^2	sum of squared deviations
Γ	integration path for J integral
Γ_{ext}	integration path along external boundaries of specimen

Γ_{loc}	integration path just outside failure process zone
Γ_1	integration path along the lower crack face
Γ_2	integration path along the upper crack face
Γ_{tip}	integration path around the crack tip
Φ	energy potential

shown that under large scale bridging the load carrying capability of a plate with an elliptical hole depends on peak stress, the fracture energy (the area under the stress-separation curve) and the shape of the cohesive law [5]. It is, however, widely assumed, that the peak stress and the fracture energy are the two most important cohesive law parameters for the prediction of strength of components [3,6–8,10].

Micromechanical models have shown that different crack bridging mechanisms give widely different cohesive law shape. For instance, for the problem of crack bridging by weakly bonded, frictional restraint long fibres oriented perpendicular to the crack plane, the cohesive stress increases proportional to the square root of the crack opening [4], whereas crack bridging by intact fibres oriented parallel to the crack plane results in a cohesive stress that decreases with increasing crack opening [11], see Fig. 1. The predicted cohesive laws shapes of both mechanisms have been confirmed experimentally [12,13]. These examples illustrate that it is useful to determine the shape of cohesive laws since they contain valuable information of the nature of the failure mechanism. Knowledge about the failure mechanisms is of importance for the development of better materials: enhancement of strength and fracture resistance can be obtained by microstructural optimisation [14]. Microstructural optimisation is only possible when the correct failure mechanism has been identified. This motivates the desire for the development of methods for the determination of cohesive law shapes.

The present paper concerns the determination of cohesive laws for planar (two dimensional) crack bridging problems. Generally, cohesive laws depend on the local normal and tangential crack opening displacements, δ_n and δ_t. For a symmetric specimen, symmetrically loaded, with a crack advancing along the midplane, the crack opening displacement is normal to the crack plane; the tangential crack opening displacement remains zero ($\delta_t = 0$). Then, the cohesive normal stress, σ_n, depends only on the normal opening, δ_n,

$$\sigma_n = \sigma_n(\delta_n). \tag{1}$$

No shear stress is anticipated in the cohesive zone under pure normal opening, since the stress field in a symmetric specimen loaded symmetrically must be symmetric. Consequently, the shear stress must vanish at every point along the symmetry plane. Conversely, when the crack opening is purely tangential, ($\delta_n = 0$), the cohesive shear stress, σ_t, depends only on the tangential crack opening displacement, δ_t,

$$\sigma_t = \sigma_t(\delta_t), \tag{2}$$

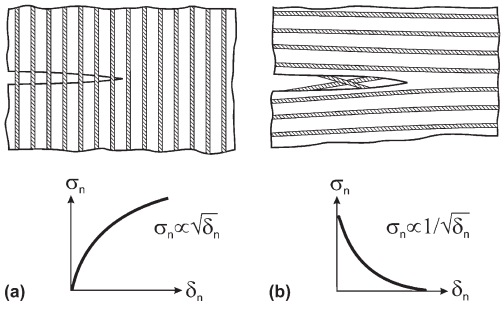

Fig. 1. Two different microscale failure mechanisms give different cohesive laws. (a) Crack bridging by frictionally restrainted fibres and (b) crack bridging by cross-over fibre bridging.

while the normal stress is assumed to be zero. Under openings involving both normal and tangential crack opening displacements (hereafter called mixed mode), the cohesive stresses depend on both the normal and tangential crack opening displacement

$$\sigma_n = \sigma_n(\delta_n, \delta_t) \quad \wedge \quad \sigma_t = \sigma_t(\delta_n, \delta_t). \tag{3}$$

Eq. (3) thus defines the mixed mode cohesive laws. Note, that with the definitions (1)–(3), we adopt the common assumption that the local cohesive stresses depend on the local crack openings but not the opening-path history [7,8,10].

A number of approaches have been developed for the measurement of mode I cohesive laws. Only a limited number of studies concern the measurement of mixed mode cohesive laws under large scale bridging. One proposed procedure assumes that the cohesive laws of the normal and shear stress are decoupled; then the cohesive laws can be obtained from results from a mode I and a mode II test [8,10]. The cohesive laws are identified by modelling; using a pre-selected cohesive law shape, a parameter study is performed and the parameters that give results that best reproduce the test results (e.g. load–displacements relationship) are chosen. Another approach is to identify cohesive law parameters from displacements fields recorded around the failure process zone under various mixed mode loadings [7]. The cohesive law parameters are found by modelling the specimen, as the cohesive law parameters that give a deformation field identical to the measured displacement field. Thus, both approaches require modelling of the particular test specimen used in the experiments, and in both cases the cohesive law shape is assumed from the beginning.

The purpose of the present paper is to develop a new general approach for the determination of mixed mode cohesive laws under large scale bridging. The method proposed here is based on an application of the J integral. In comparison with the existing methods mentioned above, the method proposed here is more general and yet simpler to use, since it does not require modelling of a specific test specimen. However, it requires the use of a fracture mechanics test specimen for which the J integral can be obtained under large scale bridging. The proposed method, which can be considered a generalisation of a J integral method developed for pure mode I [15–17,13], identifies the cohesive law shape rather than assuming it.

Fracture data from experiments contain some scatter, originating from either electrical noise or fracture resistance variations that result from a non-homogenous microstructure of the specimen, e.g. the spatial variation of bridging ligaments along the crack path. We wish to obtain a good description of the fracture properties, meaning cohesive laws that are in as close agreement with the measured data as possible. However, we do not wish the cohesive laws to represent noise or possible non-homogenous microstructure.

In the present paper, we seek to answer, through an analysis of the use of synthetic data, a number of questions regarding the feasibility of the proposed approach for the determination of mixed mode cohesive laws. We investigate how many datasets are required to give accurate results as well as how sensitive the approach is to noise in the data. In that respect the present paper has some similarities with an earlier study of Cox and Marshall [18] on development of a method for the determination of mode I cohesive laws from measurements of the crack opening profile.

The paper is organised as follows: first, the underlying mechanics theory is presented. Next, the numerical model are presented. The method of testing with synthetic data is described next. Effect of a number of parameters on the accuracy of the approach is shown. Finally, some practical recommendations are formulated for experimental use.

2. Basic mechanics

2.1. Problem statement

The situation to be analysed is shown in Fig. 2. The problem is a plane, two-dimensional crack-bridging problem lying in the x_1–x_2-plane. The crack is parallel to the x_1-axis. The origin of the coordinate system is situated at the crack tip and the positive x_1 axis is taken in the direction of crack propagation. The material is taken to be elastic outside the failure process zone. The failure process zone is divided into two parts: the crack tip, where a singular stress field exists, and a bridging zone in the crack wake. The bridging zone extends

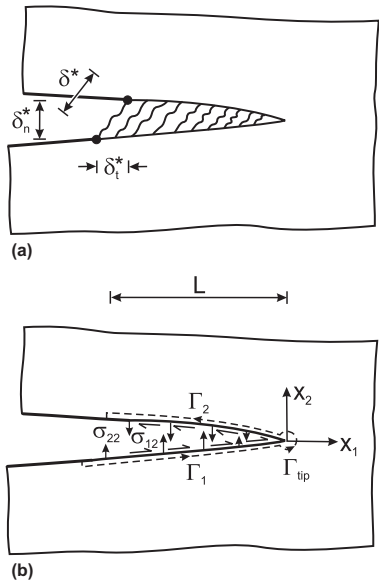

Fig. 2. A crack, experiencing large scale bridging, subjected to mixed mode crack opening displacement. (a) Definition of normal and tangential end opening displacements and (b) integration path for the J integral.

from $x_1 = -L$ to $x_1 = 0$. The present approach is not limited to a small-scale bridging zone. However, small displacements, small rotations and small strains are assumed.

The crack opening displacements in the normal and tangential directions are defined as the difference between the displacements of the upper and lower crack face,

$$\delta_n = u_2^+ - u_2^- \quad \wedge \quad \delta_t = u_1^+ - u_1^-, \tag{4}$$

where superscripts + and − indicate the displacement vector, u_i, of the upper crack face ($x_1 < 0$, $x_2 = 0^+$) and the lower crack face ($x_1 < 0$, $x_2 = 0^-$), respectively.

It is furthermore assumed that the crack opens in a monotonic fashion; neither unloading nor crack closure is permitted. Then, it is reasonable to assume that within the bridging zone the local cohesive stresses is a function only of the local normal and tangential crack opening displacements, as described by (3). The cohesive (or bridging) laws are assumed to be the same for each point along the cohesive zone. Thus, they are considered as material properties, i.e., and independent of specimen geometry. Since the cohesive stresses represent the failure process zone, it is reasonable to assume that a certain crack opening exists, at which the cohesive stresses vanish [17]. The primary purpose of the present paper is to develop an approach that enables the determination of the cohesive laws in the form of (3) for a given material.

2.2. Principle of cohesive law determination

The path independent J integral is defined as [19]

$$J = \int_\Gamma W \, \mathrm{d}x_2 - \sigma_{ij} n_j \frac{\partial u_i}{\partial x_1} \, \mathrm{d}S, \tag{5}$$

where Γ is a contour going around the crack from the lower crack face (u_i^-) to the upper u_i^+ in the counter clockwise direction around the crack tip, n_j is the outwards normal to the contour, W is the strain energy density,

$$W = \int_0^{\varepsilon} \sigma_{ij}\, \mathrm{d}\varepsilon_{ij}, \tag{6}$$

σ_{ij} is the stress tensor, u_i is the displacement vector and S denotes curve length along Γ. Here, indices i and j takes the values 1, 2 and 3, and the Einstein summation rule is employed. No body forces are allowed.

We choose the integration path just outside the failure process zone, Γ_{loc}. As shown in Fig. 2, Γ_{loc} starts just outside the bridging zone ($x_1 = -L$, $x_2 = 0^-$), runs along a path along the lower crack face, Γ_1, around a small circle enclosing the crack tip, Γ_{tip}, and along a path, Γ_2, along the upper crack face to the end of the bridging zone, ($x_1 = -L$, $x_2 = 0^+$). Thus, $\Gamma_{\mathrm{loc}} = \Gamma_1 + \Gamma_{\mathrm{tip}} + \Gamma_2$. Also, $\mathrm{d}x_2 = 0$ along both Γ_1 and Γ_2. Furthermore, $\sigma_{i3} n_3 \partial u_i / \partial x_1 = 0$ for plane problems. Along Γ_1 we find $n_j = (0, -1, 0)$ and $\mathrm{d}S = \mathrm{d}x_1$, while $n_j = (0, 1, 0)$ and $\mathrm{d}S = -\mathrm{d}x_1$ for Γ_2. Then (5) becomes

$$J_{\mathrm{loc}} = \int_{-L}^{0} \sigma_{i2} \frac{\partial u_i^-}{\partial x_1}\, \mathrm{d}x_1 + J_{\mathrm{tip}} + \int_{0}^{-L} \sigma_{i2} \frac{\partial u_i^+}{\partial x_1}\, \mathrm{d}x_1 = \int_{0}^{-L} \sigma_{i2} \left(\frac{\partial u_i^+}{\partial x_1} - \frac{\partial u_i^-}{\partial x_1} \right) \mathrm{d}x_1 + J_{\mathrm{tip}}, \tag{7}$$

where J_{tip} represents the value of the J integral evaluated around the crack tip.

Along Γ_1 and Γ_2 the stresses are identical to those transmitted across the bridging zone, i.e., $\sigma_{22} = \sigma_{\mathrm{n}}$ and $\sigma_{12} = \sigma_{\mathrm{t}}$. Inserting (3) and (4) into (7) gives

$$J_{\mathrm{loc}} = \int_0^{\delta_{\mathrm{t}}^*} \sigma_{\mathrm{t}}(\delta_{\mathrm{n}}, \delta_{\mathrm{t}})\, \mathrm{d}\delta_{\mathrm{t}} + \int_0^{\delta_{\mathrm{n}}^*} \sigma_{\mathrm{n}}(\delta_{\mathrm{n}}, \delta_{\mathrm{t}})\, \mathrm{d}\delta_{\mathrm{n}} + J_{\mathrm{tip}}, \tag{8}$$

where δ_{n}^* and δ_{t}^* are the end-opening and end-sliding of the bridging zone. Furthermore, we adopt the assumption that the stresses are derived from a energy potential,

$$\Phi(\delta_{\mathrm{n}}, \delta_{\mathrm{t}}) \quad \wedge \quad \Phi(0, 0) = 0 \tag{9}$$

so that

$$\sigma_{\mathrm{n}}(\delta_{\mathrm{n}}, \delta_{\mathrm{t}}) = \frac{\partial \Phi(\delta_{\mathrm{n}}, \delta_{\mathrm{t}})}{\partial \delta_{\mathrm{n}}}, \quad \sigma_{\mathrm{t}}(\delta_{\mathrm{n}}, \delta_{\mathrm{t}}) = \frac{\partial \Phi(\delta_{\mathrm{n}}, \delta_{\mathrm{t}})}{\partial \delta_{\mathrm{t}}}. \tag{10}$$

Inserting (10) into (8) and performing the integration we obtain

$$J_{\mathrm{loc}} = \Phi(\delta_{\mathrm{n}}^*, \delta_{\mathrm{t}}^*) + J_{\mathrm{tip}}. \tag{11}$$

Using bridging laws, crack propagation occurs when J_{tip} is identical to the fracture energy of the crack tip, J_0, which is assumed to be a material constant. The value of J_{loc} during crack propagation is denoted J_{R}, the fracture resistance of the material,

$$J_{\mathrm{R}} = \Phi(\delta_{\mathrm{n}}^*, \delta_{\mathrm{t}}^*) + J_0. \tag{12}$$

Using cohesive laws, the crack tip fracture energy, J_0, is build into the cohesive law [8–10]. Here, we retain $J_0 \neq 0$ for a more general treatment, so that both cohesive laws and bridging laws can be analysed in the same manner.

The energy uptake by the crack tip is assumed to be constant, J_0, under cracking. The fracture resistance, J_{R}, increases with increasing crack length, and is assumed to reach a steady-state value, J_{ss}, when the bridging zone is fully developed. The steady-state fracture resistance is attained when the crack opening at the end of the bridging zone is so large that the bridging stresses are zero at that point ($x_1 = -L$). During steady-state crack growth in steady-state specimens, as discussed below, the failure process zone simply translates along the specimen in a self-similar fashion.

Combining (10) and (12) we obtain

$$\sigma_{\mathrm{n}}(\delta_{\mathrm{n}}^*, \delta_{\mathrm{t}}^*) = \frac{\partial J_{\mathrm{R}}(\delta_{\mathrm{n}}^*, \delta_{\mathrm{t}}^*)}{\partial \delta_{\mathrm{n}}^*}, \quad \sigma_{\mathrm{t}}(\delta_{\mathrm{n}}^*, \delta_{\mathrm{t}}^*) = \frac{\partial J_{\mathrm{R}}(\delta_{\mathrm{n}}^*, \delta_{\mathrm{t}}^*)}{\partial \delta_{\mathrm{t}}^*}, \tag{13}$$

since J_0 is assumed to be constant during cracking. It follows from (13) that mixed mode cohesive or bridging laws can be derived by simultaneous measurements of J_{R}, δ_{n}^* and δ_{t}^*. That is the key idea of the paper.

In fracture mechanical testing, a part of the data analysis is to calculate J_{R} from the applied loads. This can be achieved by evaluating the J integral along a path, Γ_{ext}, along the external boundaries of the fracture

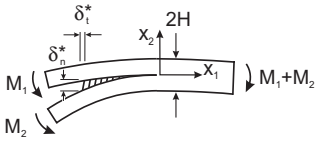

Fig. 3. The double cantilever beam specimen loaded with uneven bending moments (DCB-UBM).

specimen in counter clockwise direction. The result, J_{ext}, must be identical to J_{loc}, since the J integral is path independent [19]. It is advantageous to select a mixed mode test specimen for which J_{ext} can easily be obtained. For large scale bridging problems J_{ext} cannot be determined from linear elastic fracture mechanics solution of stress intensity factors [20]. However, a family of steady-state double cantilever beam (DCB) specimens exists for which J_{ext} can be determined analytically under large scale bridging [17]. DCB specimens belonging to this family are loaded by axial forces and/or bending moments, but not shear (transverse) forces. In principle, any combination of these family members can be used. Here, we propose to use the DCB-specimen loaded with uneven bending moments (DCB-UBM), see Fig. 3. When the distances from the beam ends to the failure process zone are longer than a few times the beam height, the stress states at the beam-ends are unaffected by the stress field around the failure process zone; the beams are then subjected to pure bending. Under these conditions the J integral value can be obtained analytically. For a homogeneous DCB-UBM specimen made of an isotropic material, J_{ext} is found as (plane strain)

$$J_{ext} = (1-\nu^2)\frac{21\left(M_1^2+M_2^2\right)-6M_1M_2}{4B^2H^3E}, \tag{14}$$

where M_1 and M_2 denote the applied bending moments (positive signs are shown in the figure), E and ν denote the Young's modulus and the Poisson's ratio, B is the specimen width and H is the beam height. For plane stress, the factor $1-\nu^2$ should be replaced by unity. J integral solutions for DCB-UBM specimens made of orthotropic materials and multilayers are also available [21].

For $M_1 = -M_2$ (with $M_2 > 0$, according to the definition of positive moments shown in Fig. 3) the specimen opens symmetrically (pure mode I) and $\delta_t = 0$ all along the entire cohesive zone. For $M_1 = M_2$, $\delta_n = 0$ along the cohesive zone (pure mode II). Thus, by varying the ratio of the moments in the range of $-1 < M_1/M_2 < 1$, any combination of δ_t^*/δ_n^* can be obtained.

Experiments should be conducted for various combinations of M_1/M_2, generating a series of J_R–δ_n^*–δ_t^* datasets for various values of δ_n^*/δ_t^*. For a fixed value of δ_n^*/δ_t^*, it is anticipated that the fracture resistance rises to a steady-state level. The steady-state level reflects that the cohesive zone is fully developed so that the cohesive stresses have decreased to zero at the notch root. Different steady-state fracture resistance levels may be attained for different values of δ_n^*/δ_t^*.

It may be convenient to describe the end opening by its magnitude

$$\delta^* = \sqrt{\delta_n^{*2}+\delta_t^{*2}} \tag{15}$$

and phase angle [22], defined as,

$$\varphi = \tan^{-1}\left(\frac{\delta_t^*}{\delta_n^*}\right), \tag{16}$$

see Fig. 4.

2.3. Procedure for data analysis: a numerical J integral based approach

The suggested approach is as follows (Fig. 5). First, fracture mechanics experiments are conducted for various ratios of M_1/M_2. The ratio of M_1/M_2 is fixed throughout an experiment. During the testing, simultaneous values of M_1, M_2, δ_n^* and δ_t^* are recorded until steady-state is attained. For each experiment, J_R is calculated from M_1 and M_2 by (14). Experiments with different ratios of M_1/M_2 will give different datasets with increas-

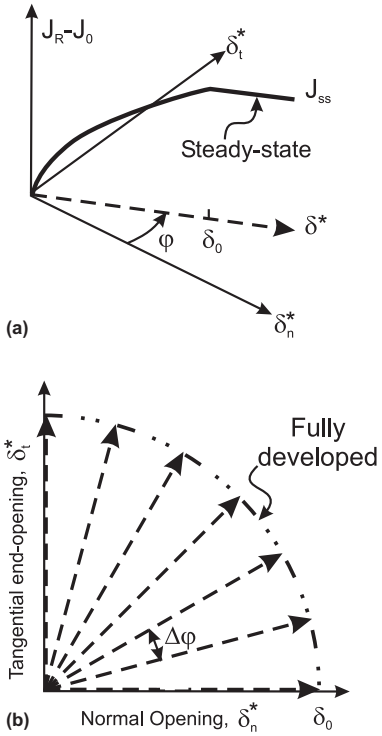

Fig. 4. Anticipated mixed mode fracture resistance curves. (a) Definitions of δ^* and φ for a single experiment. (b) Phase angle of the end-opening of a series of experiments.

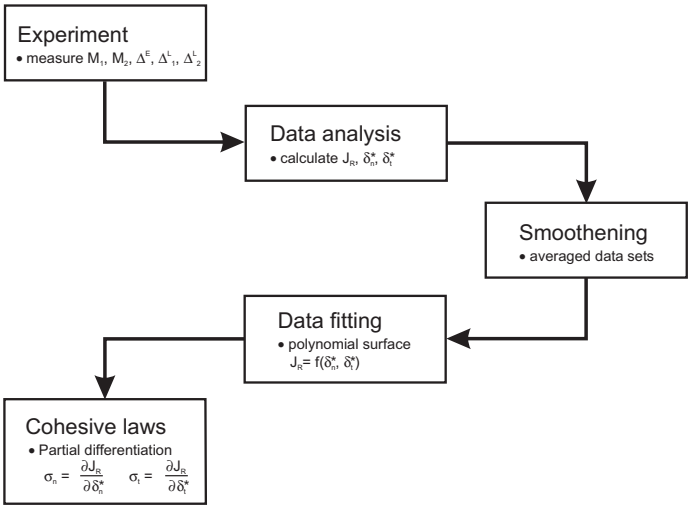

Fig. 5. The suggested approach for determination of mixed mode cohesive laws.

ing values of J_R, δ_n^* and δ_t^*, as shown schematically in Fig. 4. All datasets are now considered together as a group with J_R being a function of δ_n^* and δ_t^*, according to (12). Next, a surface is fitted to the group of datasets. We propose to perform the fitting with a sum of products of Chebyshev polynomials of the form[1]

$$J_R(\bar{x},\bar{y}) = \sum_{i=0}^{k}\sum_{j=0}^{l} a_{ij} T_i(\bar{x}) T_j(\bar{y}), \tag{17}$$

where $T_i(\bar{x})$ and $T_j(\bar{y})$ are the Chebyshev polynomial of the first kind of degree i and j, respectively, and k and l denote the maximum polynomial degree of $T_i(\bar{x})$ and $T_j(\bar{y})$ [23]. Here, $\bar{x}$ and $\bar{y}$ are non-dimensional normal and tangential end opening displacements, and the coefficients a_{ij} are determined as a part of the fitting procedure. Chebyshev polynomials were preferred because (i) they are mutually orthogonal and (ii) minimize the maximum deviation between the supplied data and the fit almost as good as a minimax polynomial, so that the maximum error in the entire fitting interval is less than e.g. for standard polynomials [24]. Furthermore, the use of orthogonal polynomials (here Chebyshev) in two dimensions provides a fast computation of the fit, and subsequently it admits an easy access to the resulting model function as well as its derivatives. Details of the approach are given in Appendix A. Having determined an approximate function for J_R as a function of δ_n^* and δ_t^*, approximate functions for the cohesive stresses can be determined by partial differentiation of the function according to (13).

A computer program was made to perform the data fitting of the J_R data and the partial differentiation, giving σ_n and σ_t, see Appendix A. The program also checks the accuracy of the fit, e.g. by calculating the maximum deviation, for each point, between the input value of J_R and the J_R value of the fit, as well as calculating the root-mean-square and the so-called r^2 value of the whole fit. The procedure of obtaining cohesive laws in this manner is rather quick; the computation time was less than 10 s on a 2.8 GHz personal computer.

2.4. Test of approach with synthetic data

The proposed numerical J integral based approach for determination of mixed mode cohesive laws, as described above, uses experimental data as input. Before initiating an experimental study it is of important to verify that the approach is convenient, i.e., investigate how accurate results the approach can give. Furthermore, it is useful to establish guidelines for the input that the approach requires to deliver accurate results. Therefore, we test the approach by the use of synthetic data. Since the synthetic data should mimic experimental data, the starting point of the approach is the J_R–δ_n^*–δ_t^* data. Cohesive laws obtained via the proposed approach are then compared with the cohesive laws obtained analytically.

Without loss of generality, the crack tip fracture energy, J_0 is set to zero in the following (J_0 is assumed to be constant under crack growth and thus vanishes anyway under the differentiation). For the purpose of the investigation we selected an axisymmetric power law function, given by

$$\frac{J_R(\delta^*)}{J_{ss}} = \begin{cases} \dfrac{(\delta^*/\delta_0+\xi)^n - \xi^n}{(1+\xi)^n - \xi^n} & \text{for } 0 \leqslant \delta^*/\delta_0 \leqslant 1, \\ 1 & \text{for } \delta^*/\delta_0 > 1, \end{cases} \tag{18}$$

as our basic cohesive law. In (18), δ_0 is the end-opening at which J_R reaches J_{ss} and the cohesive stress vanish, ξ and n are dimensionless parameters that control the shape of the J_R curve. Examples of J_R–δ^* curves are given in Fig. 6. The equation for the J_R–δ^* function is simple and yet the shape is physical realistic, since R-curves often possess the highest steepness for small δ^*.

[1] Data could of course be fitted in many other ways. An interesting alternative is the method of regularisation, where the optimal fit is obtained as a compromise between close approximation to data and a smooth model function [24]. Other possibilities are PCA (principal components analysis), or stepwise regression. However, a comparative study of these methods is outside the scope of the present paper.

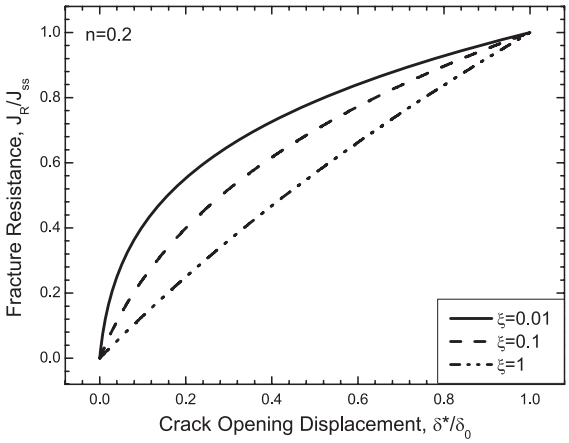

Fig. 6. Examples of model J_R–δ^* curves.

The obtained values of σ_n and σ_t as a function of δ_n^* and δ_t^* are compared with the values obtained by the analytical solution (see Appendix B). For instance, for $\varphi = 0°$ (i.e., pure normal opening, $\delta_n^* = \delta^*,\ \delta_t^* = 0$), the normal stress becomes

$$\sigma_n(\delta^*, \varphi = 0°) = \begin{cases} \dfrac{J_{ss}}{\delta_0} \dfrac{n(\delta_n^*/\delta_0 + \xi)^{n-1}}{(1+\xi)^n - \xi^n} & \text{for } 0 \leqslant \delta^*/\delta_0 \leqslant 1, \\ 0 & \text{for } \delta^*/\delta_0 > 1. \end{cases} \tag{19}$$

We are particularly interested in how accurate it is possible to determine the peak stress, $\hat{\sigma}_n$. Note, that for the power law (18), $\hat{\sigma}_n$ is finite; it occurs at $\delta_n = \delta_t = 0$,

$$\hat{\sigma}_n = \sigma_n(\delta^* = 0, \varphi = 0°) = \frac{J_{ss}}{\delta_0} \frac{n\xi^{n-1}}{(1+\xi)^n - \xi^n}. \tag{20}$$

First, we investigate the effects of parameters using noiseless, synthetic data. Using (15) and (16), datasets of J_R as a function of δ_n^* and δ_t^* were generated from (18) for various phase angles, with a fixed angle, $\Delta\varphi$, between each dataset, see Fig. 4b. The number of data points for one dataset (i.e., for one phase angle) is denoted M, while collectively, the data from all phase angles are called the group of datasets. The total number of data points for the group of datasets (all phase angles) is N. The angle between two consecutive datasets is denoted $\Delta\varphi$. The highest polynomial degree with respect to δ_n^* is k and the highest polynomial degree with respect to δ_t^* is l.

In the last part of this study, the methods ability to handle noise in the data is investigated. Noise was simulated as follows: first, a group of datasets (values of J_R, δ_n^* and δ_t^*) was generated from (18). Next, noise in the form of pseudo-random numbers was added to the J_R, δ_n^* and δ_t^* data. The noise data was Gaussian distributed with zero mean and characterised by a parameter, ω, defined such that the standard deviation of the noise of the J_R–δ_n^*–δ_t^* data was ωJ_{ss}, $\omega\delta_0$ and $\omega\delta_0$, respectively. The actual noise data for the J_R, δ_n^* and δ_t^* were independent, due to the random number generator.

In summary, the following parameters varied in order to test the robustness of the proposed J integral based approach:

- the initial steepness of the J_R curve, parameter ξ;
- the phase angle between datasets, $\Delta\varphi$;
- the number of data points per phase angle, M;

- the highest polynomial degree, k and l, of the Chebyshev polynomials;
- the noise level, ω.

3. Results

3.1. Noiseless data

With the input given as synthetic data points for J_R–δ_n^*–δ_t^*, the output from the data analysis will be σ_n and σ_t as a function of δ_n^* and δ_t^* as (3). Since J_R is axisymmetric (the synthetic J_R-values (18) depend only on δ^*, not on φ), it follows from (B.4) and (B.5) and the universal relation $\sin\varphi = \cos(90° - \varphi)$ that $\sigma_t(\delta^*, \varphi) = \sigma_n(\delta^*, 90° - \varphi)$. This implies that σ_t as a function of δ_n^* and δ_t^* is just a mirror image of σ_n with $\varphi = 45°$ as the mirror plane. Therefore, only results for σ_n will be shown.

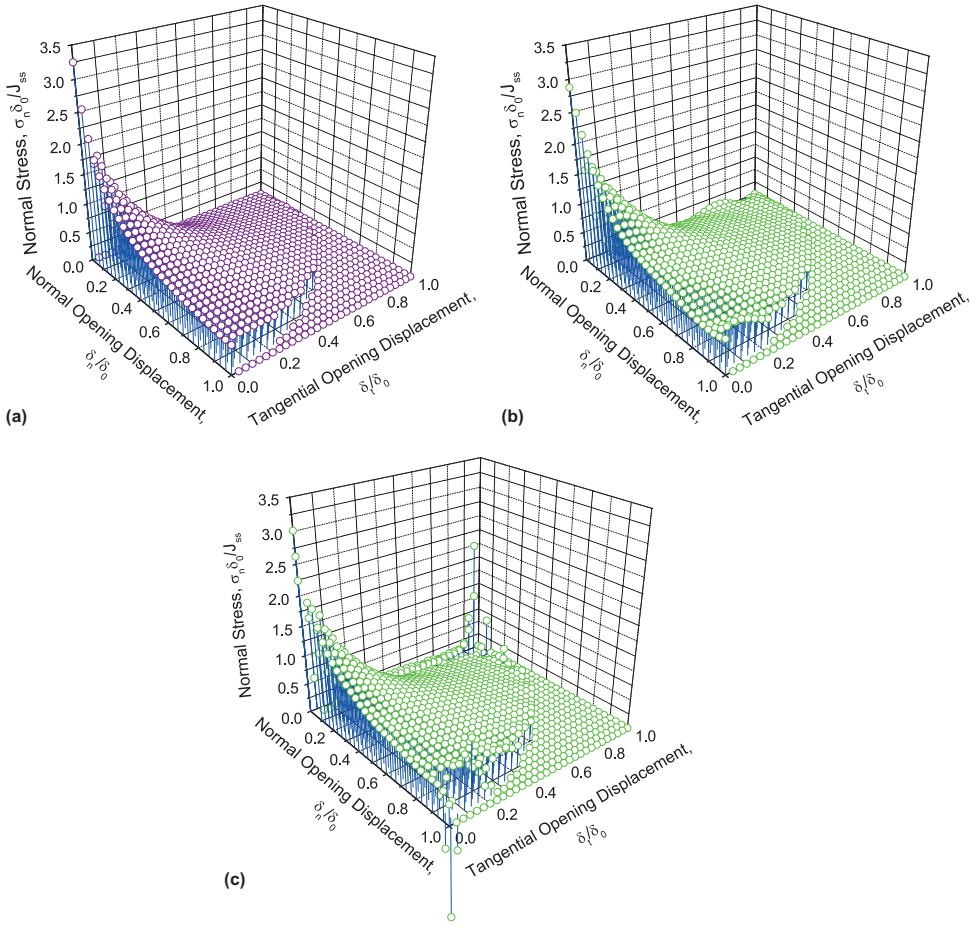

Fig. 7. Examples of cohesive laws; σ_n as a function of δ_n^* and δ_t^*. (a) Analytical solution, (b) σ_n obtained for two values of maximum polynomial degree ($k = l = 6$) and (c) for $k = l = 9$.

As noted above, for the power law (18) the peak stress occurs at $(\delta_n;\delta_t)=(0;0)$. This corresponds to the steepest part of the surface. It is therefore expected that for this idealised cohesive law, $(\delta_n;\delta_t)=(0;0)$ will be the point where the J_R–δ_n^*–δ_t^* fit (and thus σ_n and σ_t) possesses the least accuracy.

Analytical results, σ_n as a function of δ_n^* and δ_t^*, are shown in Fig. 7a, while Fig. 7b and c shows σ_n determined via the numerical J integral based approach applied to the same group of dataset. In these figures, σ_n is set to zero for $\delta^*/\delta_0 \geqslant 1$. This follows from (19). This causes a discontinuous jump in σ_n at $\delta^*/\delta_0=1$. The difference between Fig. 7b and c is in the maximum polynomial degree of the Chebyshev polynomials. For $k=l=6$ (Fig. 7b), the σ_n surface is smooth and comparable to the shape obtained analytically (Fig. 7a), except for a slight waviness near $(\delta_n^*;\delta_t^*)=(\delta_0;0)$ and $(0;\delta_0)$. The waviness is relative insignificant, since it occurs where σ_n is close to zero. For $k=l=9$ (Fig. 7c), however, the σ_n surface shows unacceptable large scatter near $(\delta_n^*;\delta_t^*)=(\delta_0;0)$ and $(0;\delta_0)$. Although the fit containing the larger scatter (Fig. 7c) is a better fit to the *supplied data* in the sense that it has smaller maximum deviation and a smaller r^2 value, it is a poorer solution to the *problem* – the scatter occurs at positions of δ_n^* and δ_t^* where no data is supplied. This illustrates the point that errors can be obtained if high values are chosen for k and l. Low values of k and l are expected also to give a poor fit to the data, since the degree of freedom of the surface is lower. Therefore, selecting the best values of k and l is a main issue in this study.

Fig. 8 shows $\sigma_n(\delta_n;\delta_t=0)$ obtained from the J_R-data for fits using different values of $k=l$. The analytical solution (19) is also shown for comparison. It is seen, that for the parameter chosen, the shape is recovered reasonably well for $k=l\geqslant 3$. However, in order to obtain a peak stress, $\hat{\sigma}_n$, within 10% of the analytical value, $k=l$ must be higher than 3.

The obtained values of $\hat{\sigma}_n$ as a function of k (and l, since the results are obtained with $k=l$) are shown in Fig. 9. The obtained $\hat{\sigma}_n$ values are all below the correct value given by (20), $\hat{\sigma}_n\delta_0/J_{ss}=3.25$ for $\xi=0.1$ and $n=0.2$. For $k=l=5$ the difference is almost 15%. For $k=l=8$ the difference is less than 9%. Higher values of $k=l$ lead to a more accurate estimate of $\hat{\sigma}_n$. However, the convergence is slow. These results suggest that a surface fit with $k=l\geqslant 6$ gives a fairly good estimate of $\hat{\sigma}_n$ and gives the correct shape of the surface.

For fixed $k=l$, a more accurate value of $\hat{\sigma}_n$ can be obtained by increasing the number of data points per dataset, i.e., the number of data points in the radial direction, M, see Fig. 10. However, in comparison with the effect of the parameters k and l (Fig. 9), the effect of M is rather small. But increasing M also increases the computation time. As a pragmatic compromise between the desire for high accuracy and low computation time, $M\approx 500$ seems to be a good choice. A value of M below 100 is not advised.

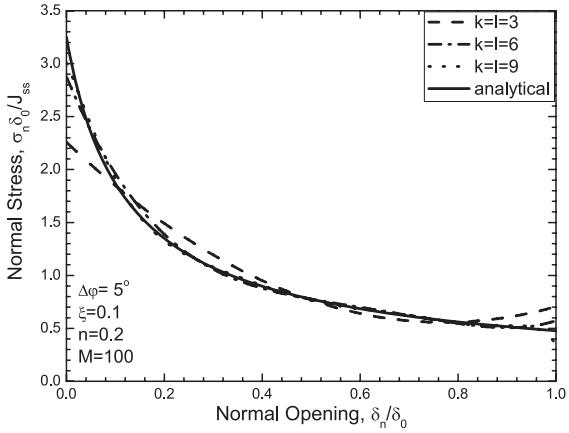

Fig. 8. The normal cohesive stress, σ_n, as a function of pure normal opening, δ_n^* ($\varphi=0°$), determined for various values of the maximum polynomial degree ($k=l$).

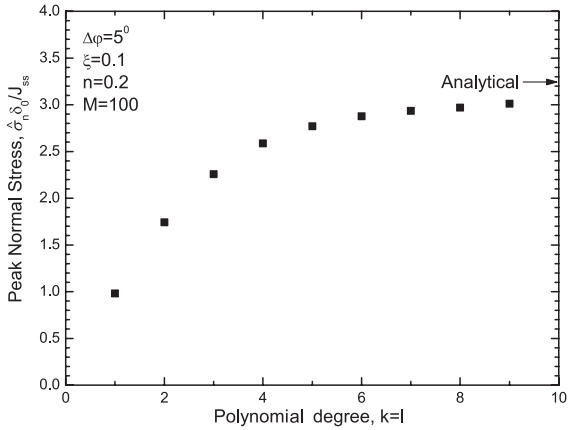

Fig. 9. The peak normal stress, $\hat{\sigma}_n$, as function of the maximum polynomial degree ($k = l$).

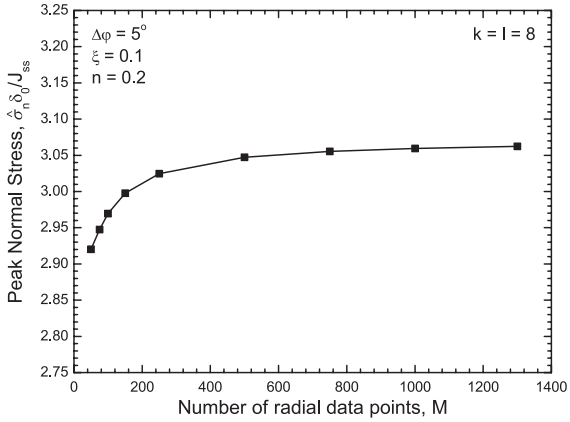

Fig. 10. The peak normal stress, $\hat{\sigma}_n$, as function of the number of data points per phase angle, M.

The maximum polynomial degree that gives a fit without scatter, hereafter denoted $(k = l)_{max}$, depends strongly on the difference between the phase angle between two consecutive datasets, $\Delta\varphi$. As shown by black bars in Fig. 11, $(k = l)_{max} = 8$ is attainable for $\Delta\varphi \leqslant 5°$ and $(k = l)_{max} = 6$ requires $\Delta\varphi \leqslant 7.5°$. The former requires at least 19 datasets while the latter corresponds to 13 different datasets. That requires a lot of measurements, i.e., a lot of experimental work. It is therefore of interest to investigate whether it is possible to obtain approximately the same accuracy (i.e., $k = l \geqslant 6$) with less datasets.

It is useful here to recall that the upper limit in k and l exists because the J integral based approach gives a fitted σ_n–δ_n^*–δ_t^* surface that possesses scatter near $(\delta_n^*; \delta_t^*) = (\delta^*; 0)$ and $(0; \delta^*)$. This suggests that it might be useful to add more data in those areas. One possibility is shown in Fig. 12. Here, data are given for $0 < \delta^*/\delta_0 < 1$ for $\varphi = p\Delta\varphi$, where p is an integer number – the number of datasets –, $p = 0, 1, \ldots, 90°/\Delta\varphi$, supplemented with additional data for $1/2 < \delta^*/\delta_0 < 1$ for $\varphi = \Delta\varphi/2$ and $\varphi = 90° - \Delta\varphi/2$. The results obtained from this group of data are shown as white bars in Fig. 11. Now $(k = l)_{max} = 5$ can be obtained for $\Delta\varphi \leqslant 15°$ corresponding to $p = 6$ (8 datasets). $(k = l)_{max} = 6$ can be obtained for $\Delta\varphi \leqslant 10°$ corresponding to 11 datasets. Thus, the use of the two extra datasets at $\varphi = \Delta\varphi/2$ and $\varphi = 90° - \Delta\varphi/2$ seems to be a feasible approach.

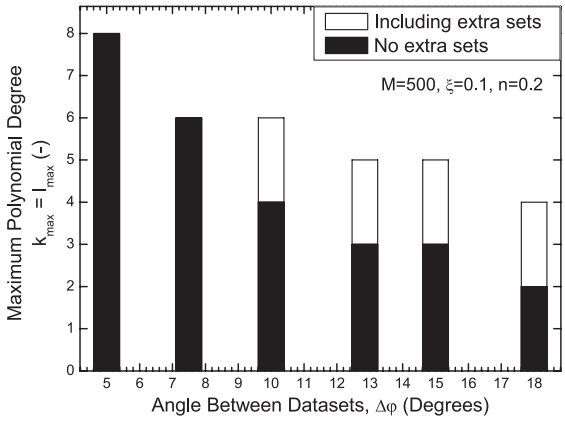

Fig. 11. The maximum polynomial degree that gives a fit without scatter, $(k = l)_{\max}$, shown as a function of the phase angle between the datasets, $\Delta\varphi$. Dark bars represent values obtained for fixed $\Delta\varphi$, while white bars represent values obtained using two extra $\Delta\varphi/2$ datasets.

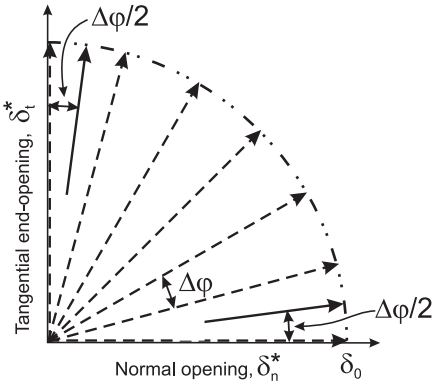

Fig. 12. Approach for reduction the tendency for scatter by adding two additional datasets (solid lines) to original datasets (dashed lines).

The examples shown so far have been constructed with $\xi = 0.1$ and $n = 0.2$, corresponding to J_R–δ^* curves with realistic slope (i.e., moderate $\hat{\sigma}_n$) at $\delta^* = 0$. For steeper curves, it becomes more difficult to determine $\hat{\sigma}_n$ with a good accuracy. The peak stress can readily be determined with an accuracy with 10% of the correct value, if the analysis is conducted with data close to where the peak stress exists, here $(\delta_n^*; \delta_t^*) = (0; 0)$. For instance, using data in the range of $0 < \delta^*/\delta_0 < 0.1$ only, the approach gives satisfactory results for steeper curves (for $\xi = 0.01$ and $n = 0.2$; $\hat{\sigma}_n\delta_0/J_{ss} \approx 13$), even for low polynomial degree, e.g. $k = l = 4$, see Fig. 13. An accurate value of very steep curves (e.g. $\xi = 0.001$ and $n = 0.2$ giving $\hat{\sigma}_n\delta_0/J_{ss} \approx 67$) is obtained for data in the range $0 < \delta^*/\delta_0 < 1/100$ (not shown). These examples may be used as guidelines for the analysis of experimental data.

3.2. Effect of noise in the data

The effect of the noise parameter, ω, on the J_R–δ^* data is illustrated in Fig. 14. The noise variation associated with $\omega = 0.05$ is very large; the noise corresponding to $\omega = 0.01$ is probably most realistic while $\omega = 0.005$ represents data with very low noise.

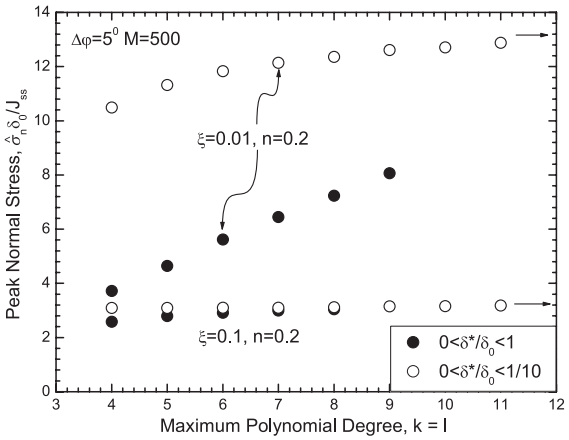

Fig. 13. The peak normal stress, $\hat{\sigma}_n$, as function of the maximum polynomial degree, obtained using the entire group of datasets (filled circles) and data points only in the range of $0 \leqslant \delta^*/\delta_0 \leqslant 0.1$ (open circles). Arrows indicate analytical results.

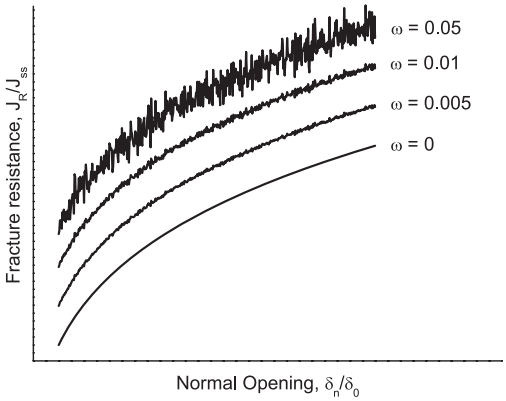

Fig. 14. Synthetic R-curve data (J_R as a function of end-opening, δ^*) with various noise levels.

Fig. 15 shows σ_n as a function of δ_n (for $\varphi = 0°$, i.e., $\delta_t = 0$) obtained by the proposed method from data with different noise levels. For $\omega = 0.005$ the cohesive stress is very similar to that obtained by the use of the noiseless data (Fig. 8). For $\omega = 0.01$ the results is still reasonably good; the shape is established rather well but the peak stress is significantly below the correct value. For $\omega = 0.05$ neither the peak stress nor the cohesive law shape are determined well.

Fig. 16 shows $(k = l)_{max}$ as a function of $\Delta\varphi$ for various ω values. For $\Delta\varphi \geqslant 10°$ results are also given when the approach of using two additional datasets $(1/2 < \delta^*/\delta_0 < 1)$ at $\varphi = \Delta\varphi/2$ and $\varphi = 90° - \Delta\varphi/2$ is used. It is seen in the figure that for $\omega = 0.01$, $(k = l)_{max} = 5$ can be achieved for $\Delta\varphi \leqslant 15°$. For $\omega = 0.05$, $(k = l)_{max} = 3$ for all $\Delta\varphi$'s. This is consistent with expectations: if the data is very noisy, it is not possible with our method to obtain a good fit even though the number of datasets is increased. It is thus essential to keep $\omega \leqslant 0.01$.

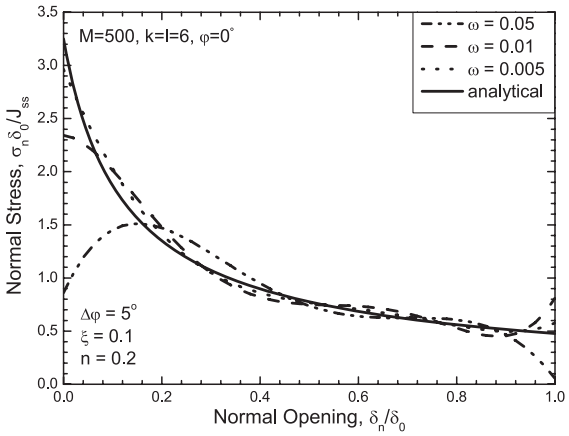

Fig. 15. The normal cohesive stress, σ_n, as a function of pure normal opening, δ_n^* ($\varphi = 0°$), determined from synthetic data with various values of the noise level, ω.

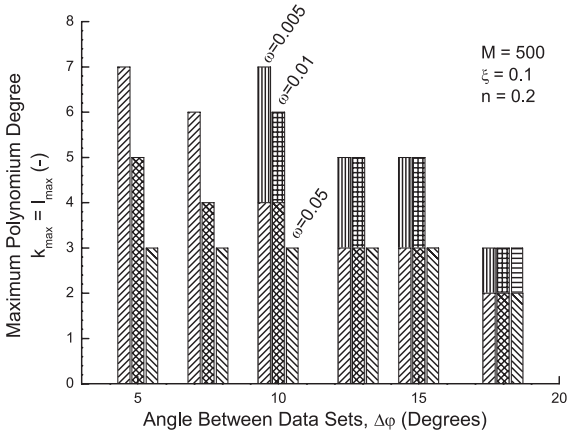

Fig. 16. The maximum polynomial degree that gives a fit without scatter, $(k = l)_{max}$, shown as a function of the phase angle between the datasets, $\Delta\varphi$ for three noise levels (hatched 45°). Results obtained by the use of two additional $\Delta\varphi/2$ datasets are shown by bars hatched 0° and 90°.

The importance of using data with a low ω is further illustrated in Fig. 17, which shows the obtainable value of $\hat{\sigma}_n$ as a function of $\Delta\varphi$ using the appropriate $(k = l)_{max}$ for each group of datasets. For the data with $\omega \neq 0$, $\hat{\sigma}_n$ does not always decrease monotonically with $\Delta\varphi$. This is most likely due to the variation in noise from one group of dataset to another. A typical variation due to the random noise is shown (maximum and minimum values from 20 examples with the same noise level parameter). In practice, data with $\omega = 0.005$ give as good results as noiseless data. For $\omega = 0.01$, there is a loss of accuracy, particular for small $\Delta\varphi$. For $\omega = 0.05$, approximately the same error occurs for $\Delta\varphi$ in the range of 5–18°. In other words, if the noise level is too high, there is no benefit of using smaller $\Delta\varphi$.

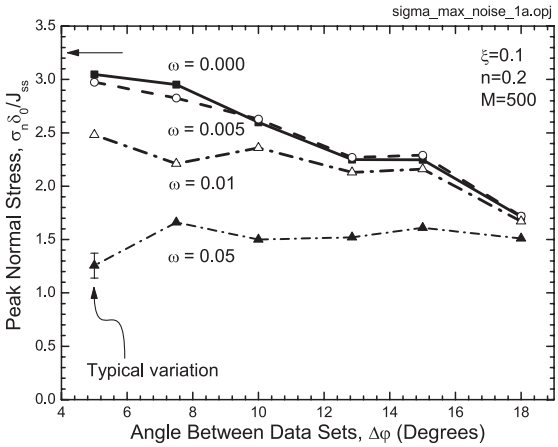

Fig. 17. The peak normal stress, $\hat{\sigma}_n$, shown as a function of the phase angle between the datasets, $\Delta\varphi$, determined from synthetic data with various values of the noise level, ω. Arrows indicate analytical results.

4. Discussion

The preceding results show that it is indeed feasible to determine mixed mode cohesive laws via the J integral approach. The investigations can give practical suggestions for the experimental procedure. For instance, very accurate cohesive laws can be obtained if the data possess sufficiently low noise ($\omega \leqslant 0.01$) and many datasets of different phase angles are used ($\Delta\varphi < 10°$). In order to illustrate the magnitude of ω, we consider a composite that experience large scale bridging during cracking. Take for instance $\delta_0 \approx 1$ mm and $J_{ss} \approx 2$ kJ/m^2. Then $\omega = 0.01$ corresponds to standard deviations of 10 μm and 20 J/m^2, respectively, for the δ^* and J_R data. Since fracture resistance measurements often show the larger variation in J_R (rapid load drops) for $\delta^*/\delta_0 \to 1$, it may be useful to perform data smoothening of the raw data before the analysis is conducted. However, any data smoothing should be done with great care so that important features are not lost. For $\delta^*/\delta_0 \to 1$ the fracture resistance is close to steady-state and the slope of the R-curves is usually relative low. Thus, the associated cohesive stresses are also low.

In comparison with the idealised axisymmetric J_R data used in the present study, real test data may pose additional challenges. For instance, the number of raw data points recorded during one test may differ significantly from the number of data points of another test. It can therefore be convenient to reduce the number of data points individually for each experiment, e.g. by averaging. It is also likely that the slope of the J_R curves for different φ's may differ significantly, so that different data resolution should be used for different experiments. Furthermore, it is anticipated that the opening at which J_R attains a steady-state value, δ_0, can depend on the phase angel of opening, φ, $\delta_0 = \delta_0(\varphi)$. It is thus unlikely that the curve describing the fully developed zone is a circle, as presumed in the present study (see e.g. Fig. 4). An elliptical shape would probably be more realistic. The results presented here could just as well have been made assuming an ellipse rather than a circle. This could easily have been obtained by scaling, e.g., the δ_t^* data points by simple elongations and compressions transformations. However, since the fitting procedure transforms the δ_n^* data points and the δ_t^* data points individually to the range of $[-1;+1]$ (see Appendix A), the numerical values would be exactly the same. Thus, we conclude that the method will work just as well using an ellipse as well as a circle (a constant value for δ_0).

As mentioned, the present approach has some similarities with the approach based on measurement of the crack opening displacement [18]. Both approaches require the measurement of the crack opening displacement during experiments where the crack opens monotonically. In comparison, the present approach has the advantage the crack opening displacement should only be measured at one location. Furthermore, the present

method for extracting the cohesive laws is rather general; it does not require a detailed model with cohesive zones of the test specimen used in the fracture mechanical tests.

Other approaches have been developed for identification of mixed mode cohesive laws. Many of these interpolate the mixed mode cohesive laws from pure mode I and pure mode II measurements. While such methods are practical and useful for engineering purposes, they do not allow the identification of details of the cohesive laws. As mentioned, the shape of the cohesive laws is useful for identifying the underlying microscale toughening mechanisms, which is a prerequisite for microstructural optimisation of materials.

The assumption that σ_n and σ_t are derived from a energy potential implies that the cohesive laws are opening path-independent, i.e., the cohesive stresses depend only on the actual openings and not the opening history. This assumption, which is widely used in modelling [7,8,26], seems reasonably when the crack openings increase monotonically, unless there is clear experimental evidence to do otherwise. However, it is no easy to test the validity of this assumption, and the point deserves further attention.

It is also appropriate to mention that for certain combinations of cohesive laws, specimen geometry, stiffness and loads, the crack opening of long bridged cracks may not increase monotonically during an experiment [25]. In such cases the present approach might not work, since the assumption of a monotonic opening, made to justify the use of a potential function, is violated.

An important question that has not been investigated sufficiently yet is, how strong is the interactions in cohesive laws in real materials. A common presumption is that the normal stress depends only weakly on the tangential crack opening displacement and that the shear stress depends weakly on the normal crack opening displacement so that the cohesive laws can be decoupled [7,8],

$$\sigma_n(\delta_n, \delta_t) \approx \sigma_n(\delta_n) \quad \wedge \quad \sigma_t(\delta_n, \delta_t) \approx \sigma_t(\delta_t). \tag{21}$$

By the use of the present approach, it may be possible to check the validity of such assumptions for specific materials systems and different microscale failure mechanisms.

A fundamental assumption for the approach developed here is that experiments are conducted using specimens that allow an evaluation of the J integral along the external boundaries, J_{ext}, also in the case of large scale bridging. For some specimens, a numerical analysis is required, since J_{ext} cannot be obtained analytically under large scale bridging [20]. However, for the proposed DCB-UBM specimen (Fig. 3), the J integral is obtained analytically. A mixed mode test fixture has been developed and an experimental investigation using the proposed approach is underway.

5. Conclusions

A novel approach for the determination of mixed mode cohesive laws has been proposed. Its capability to determine cohesive laws has been investigated by synthetic data. The approach seems feasible. Mixed mode cohesive laws can be determined accurately if the following requirements are fulfilled:

- the number of different datasets (different loading conditions) should be eight or more,
- the number of data points per dataset should be at least 100,
- the Chebyshev polynomial degree to fit to the J_R-data, $k = l$, should be 3 or higher to provide a reasonably accurate cohesive law shape,
- the peak stress can be determined accurately with a relative low polynomial degree (say, $k = l = 4$) by using only the steepest part of the data, e.g. $0 \leqslant \delta^*/\delta_0 \leqslant 0.1$,
- the standard deviation of the noise in the data should be less than 0.01 times the maximum value of the fracture resistance and the end-opening and end-sliding.

Acknowledgement

This research was partially supported by the Danish Energy Authorities under the Ministry of Economics and Business Affairs through an EFP-2003 fund (J. No. 1363/03-0006).

Appendix A

This appendix gives a short description of the approach used for obtaining an approximate function for $\Phi(\delta_n^*, \delta_t^*)$ by the used of a double Chebyshev series. The data is given as N sets of J_R–δ_n^*–δ_t^* data, which we, for compactness, will denote z, x and y in this appendix. First, the x- and y-values are transformed into the range of $[-1;+1]$ by the following transformations:

$$\bar{x} = \frac{2x - (x_{max} + x_{min})}{x_{max} - x_{min}} \quad \text{and} \quad \bar{y} = \frac{2y - (y_{max} + y_{min})}{y_{max} - y_{min}}, \tag{A.1}$$

where x_{max}, x_{min}, y_{max} and y_{min} are the highest and lowest x- and y-values, respectively, and $\bar{x}$ and $\bar{y}$ are the transformed coordinates.

The approximate function, given by a double Chebyshev series, can be written as

$$f(\bar{x}, \bar{y}) = \sum_{i=0}^{k} \sum_{j=0}^{l} a_{ij} T_i(\bar{x}) T_j(\bar{y}), \tag{A.2}$$

where $T_i(\bar{x})$ and $T_j(\bar{y})$ are the Chebyshev polynomial of the first kind of degree i and j, respectively, and k and l denote the maximum polynomial degree of $T_i(\bar{x})$ and $T_j(\bar{y})$. The coefficients a_{ij} are determined as the ones that minimize the sum of squared derivations;

$$\Delta^2 = \sum_{i=1}^{N} (z_i - f_i)^2, \tag{A.3}$$

where z_i and f_i are the fitted data value (the value of the approximate surface) and the actual data value, respectively, while N denotes the number of data points. The coefficients a_{ij} that give the minimum Δ^2 are found by solving the normal equations of the problem [24,27].

Having determined the coefficients a_{ij}, the partial derivatives $\partial f/\partial \bar{x}$ and $\partial f/\partial \bar{y}$ can be computed. Then $\partial f/\partial x$ and $\partial f/\partial y$ are given by

$$\frac{\partial f}{\partial x} = \frac{2}{x_{max} - x_{min}} \frac{\partial f}{\partial \bar{x}} \quad \text{and} \quad \frac{\partial f}{\partial y} = \frac{2}{y_{max} - y_{min}} \frac{\partial f}{\partial \bar{y}}. \tag{A.4}$$

A computer program was written to perform the computations. The program checks the accuracy of the fit by calculating the goodness of the fit (the so-called r^2), the root-mean-square and the minimal sum of square deviations, Δ^2. The program was tested against known solutions. For instance, for $z = e^x$, $k = l = 6$ and $N = 2412$, the difference between the computed coefficients and the ones tabulated by Clenshaw [28] was about 10^{-6}.

It should be noted that orthogonal polynomials (as the Chebyshev polynomials used here) are stable in the sense that adding the next higher-order polynomial to the set of basis functions (corresponding to increasing k and/or l by unity) only affects the coefficients of the lower-order polynomials (the a_{ij}'s having $i < k$ and $j < l$) slightly. By exploiting this invariance property judiciously, it is possible to make sound decisions about how many polynomial terms should be retained in order to describe the essential features of the model without including too much noise.

Appendix B

For $\delta^* \neq 0$, the partial derivatives related to the Cartesian δ_n^*–δ_t^* coordinate system are obtained from the cylindrical δ^*–φ coordinate system by the use of the chain rule:

$$\frac{\partial J_R}{\partial \delta_n^*} = \frac{\partial J_R}{\partial \delta^*} \frac{\partial \delta^*}{\partial \delta_n^*} + \frac{\partial J_R}{\partial \varphi} \frac{\partial \varphi}{\partial \delta_n^*} = \cos\varphi \frac{\partial J_R}{\partial \delta^*} - \frac{\sin\varphi}{\delta^*} \frac{\partial J_R}{\partial \varphi}, \tag{B.1}$$

$$\frac{\partial J_R}{\partial \delta_t^*} = \frac{\partial J_R}{\partial \delta^*} \frac{\partial \delta^*}{\partial \delta_t^*} + \frac{\partial J_R}{\partial \varphi} \frac{\partial \varphi}{\partial \delta_t^*} = \sin\varphi \frac{\partial J_R}{\partial \delta^*} + \frac{\cos\varphi}{\delta^*} \frac{\partial J_R}{\partial \varphi}. \tag{B.2}$$

For the function (18) we obtain

$$\frac{\partial J_R}{\partial \delta^*} = \frac{J_{ss}}{\delta_0} \frac{n(\delta^*/\delta_0 + \xi)^{n-1}}{(1+\xi)^n - \xi^n} \quad \text{and} \quad \frac{\partial J_R}{\partial \varphi} = 0, \tag{B.3}$$

so that we get ($0° \leqslant \varphi < 90°$):

$$\sigma_n = \frac{\partial J_R}{\partial \delta_n^*} = \cos\varphi \frac{J_{ss}}{\delta_0} \frac{n(\delta^*/\delta_0 + \xi)^{n-1}}{(1+\xi)^n - \xi^n}, \tag{B.4}$$

and ($0° < \varphi \leqslant 90°$)

$$\sigma_t = \frac{\partial J_R}{\partial \delta_t^*} = \sin\varphi \frac{J_{ss}}{\delta_0} \frac{n(\delta^*/\delta_0 + \xi)^{n-1}}{(1+\xi)^n - \xi^n}. \tag{B.5}$$

For $\varphi = 0°$, $\delta_n^* = \delta^*$ and $\delta_t^* = 0$, so that $\sigma_n = \partial J_R/\partial \delta_n^*$ can be obtained directly by differentiation of (18). Likewise, for $\varphi = 90°$, $\delta_n^* = 0$ and $\delta_t^* = \delta^*$, so that $\sigma_t = \partial J_R/\partial \delta_t^*$ is found directly.

References

[1] Dugdale DS. Yielding of steel sheets containing slits. J Mech Phys Solids 1960;8:100–4.
[2] Barenblatt GI. The mathematical theory of equilibrium cracks in brittle fracture. Adv Appl Mech 1962;7:55–129.
[3] Tvergaard V, Hutchinson JW. The relation between crack growth resistance and fracture process parameters in elastic–plastic solids. J Mech Phys Solids 1992;40:1377–97.
[4] Budiansky B, Evans AG, Hutchinson JW. Fiber–matix debonding effects on cracking in aligned fiber ceramic composites. Int J Solids Struct 1995;32:315–28.
[5] Gu P. Notch sensitivity of fiber-reinforced ceramics. Int J Fract 1995;70:253–66.
[6] Suo Z, Ho S, Gong X. Notch ductile-to-brittle transition due to localized inelastic band. J Engng Mater Technol 1993;115:319–26.
[7] Mohammad I, Liechti KM. Cohesive zone modelling of crack nucleation at bimaterial corner. J Mech Phys Solids 2000;48:735–64.
[8] Yang QD, Thouless MD. Mixed-mode fracture analysis of plastically deforming adhesive joints. Int J Fract 2001;110:175–87.
[9] Sørensen BF. Cohesive law and notch sensitivity of adhesive joints. Acta Mater 2002;50:1053–61.
[10] Li S, Thouless MD, Waas AM, Schroeder JA, Zavattieri PD. Use of a cohesive-zone model to analyze the fracture of a fiber-reinforced polymer–matrix composite. Compos Sci Technol 2005;65:537–49.
[11] Spearing SM, Evans AG. The role of fiber bridging in the delamination resistance of fiber-reinforced composites. Acta Metall Mater 1992;40:2191–9.
[12] Marshall DB, Shaw MC, Morris WL. Measurement of interfacial debonding and sliding resistance in fiber reinforced intermetallics. Acta Metall Mater 1992;40:443–54.
[13] Sørensen BF, Jacobsen TK. Large scale bridging in composites: R-curve and bridging laws. Composites A 1998;29:1443–51.
[14] Evans AG, Marshall DB. The mechanical behaviour of ceramic matrix composites. Acta Metall 1989;37:2567–83.
[15] Li VC, Ward RJ. A novel testing technique for post-peak tensile behaviour of cementitious materials. In: Mihashi H, Takahashi H, Wittmann FH, editors. Fracture toughness and fracture energy – testing methods for concrete and rocks. Rotterdam: A.A. Balkema Publishers; 1989. p. 183–95.
[16] Olsson P, Stigh U. On the determination of the constitutive properties of thin interphase layers – an exact solution. Int J Fract 1989;41:R71–6.
[17] Suo Z, Bao G, Fan B. Delamination R-curve phenomena due to damage. J Mech Phys Solids 1992;40:1–16.
[18] Cox BN, Marshall DB. The determination of crack bridging forces. Int J Fract 1991;49:159–76.
[19] Rice JR. A path independent integral and the approximate analysis of strain concentrations by notches and cracks. J. Appl Mech 1968;35:379–86.
[20] Bao G, Suo Z. Remarks on crack-bridging concepts. Appl Mech Rev 1992;45:355–61.
[21] Sørensen BF, Jørgensen K, Jacobsen TK, Østergaard RC. DCB-specimen loaded with uneven bending moments. Int J Fract; 2006 [in press].
[22] Serrano E, Gustafsson PJ. Influence of bondline brittleness and defects on the strength of timber finger-joints. Int J Adhes Adhes 1999;19:9–17.
[23] Weisstein ES. Chebyshev polynomials of the first kind. From mathworld – a wolfram web resource; 1999. Available from: http://mathworld.wolfram.com/ChebyshevPolynomialoftheFirstKind.html.
[24] Press WH, Teukolsky SA, Vetterling WT, Flannery BP. Numerical recipes in Fortran. The art of scientific computering. 2nd ed. Cambridge: Cambridge University Press; 1992. p. 184–94. 664–7, 795–803.
[25] Massabò R, Cox BN. Unusual characteristics of mixed-mode delamination fracture in the presence of large-scale bridging. Mech Compos Mater Struct 2001;8:61–80.
[26] Tvergaard V, Hutchinson JW. The influence of plasticity on mixed mode interface toughness. J Mech Phys Solids 1993;41:1119–35.
[27] Draper NR, Smih H. Applied regression analysis. 3rd ed. New York: Wiley; 1998.
[28] Clenshaw CW. Chebyshev series for mathematical functions. National Physical Laboratory mathematical tables, vol. 5. London: Her Majesty's Stationary Office; 1962.

[A3]

Sørensen, B. F., Jørgensen, K., Jacobsen, T. K.,
and Østergaard, R. C., 2006

"DCB-specimen loaded with uneven bending moments"

International Journal of Fracture, Vol. 141, pp. 163-176

Int J Fract (2006) 141:163–176
DOI 10.1007/s10704-006-0071-x

ORIGINAL ARTICLE

DCB-specimen loaded with uneven bending moments

Bent F. Sørensen · Kenneth Jørgensen · Torben K. Jacobsen · Rasmus C. Østergaard

Received: 20 September 2005 / Accepted: 29 March 2006

Abstract A double cantilever beam specimen loaded with uneven bending moments (DCB-UBM) is proposed for mixed mode fracture mechanics characterisation of adhesive joints, laminates and multilayers. A linear elastic fracture mechanics analysis gives the energy release rate and mode mixity analytically for both isotropic and orthotropic materials. By varying the ratio between the two applied moments, the crack tip stress state can be varied from pure mode I to pure mode II for the same specimen geometry. The specimen allows stable crack growth. A special test fixture is developed to create uneven bending moments. As a preliminary example, the DCB-UBM specimen was used for characterising fracture of adhesive joints between two laminates of thermoset glass fibre reinforced plastic.

Keywords Delamination · Fracture · Mixed mode · J integral

B. F. Sørensen (✉) · K. Jørgensen · R. C. Østergaard
Materials Research Department, Risø National Laboratory, P.O. Box 49, Frederiksborgvej, DK-4000 Roskilde, Denmark
e-mail: bent.soerensen@risoe.dk

T. K. Jacobsen
LM Glasfiber, Rolles Møllevej 1, DK-6640 Luderskov, Denmark

Nomenclature

d	distance between measurement points
h	thickness of core layer in sandwich specimens
ℓ	moment arm
s	spacing between the rollers
B	width of specimen
D	position of the neutral axis of a bimaterial beam
E	Young's modulus
E_1	Young's modulus of core material in sandwich specimens
E_2	Young's modulus of beam material in sandwich specimens
E_{11}	Young's modulus (in the x_1-direction) of the orthotropic specimens
E_{22}	Young's modulus (in the x_2-direction) of the orthotropic specimens
G	shear modulus
G_{12}	shear modulus in the x_1–x_2 plane of the orthotropic specimen
$\mathcal{G}$	energy release rate
H	beam height
I_0	non-dimensional moment of inertia
I_1	non-dimensional moment of inertia
J_0	initial value of fracture resistance
J_{ext}	J integral evaluated along external boundaries
J_{R}	fracture resistance
K_{I}	mode I stress intensity factor

K_{II}	mode II stress intensity factor
M_1	bending moment applied to beam # 1
M_2	bending moment applied to beam # 2
P	applied force
R	radius of roller
δ^*	end-opening of the bridging zone
η	ratio between thickness of core and beam ($\eta = h/H$)
θ	rotation angle of transverse beam
λ	non-dimensional orthotropic parameter
ν	Poisson's ratio
ρ	non-dimensional orthotropic parameter
ψ	phase angle of stress intensity factor
Δ^E	extensometer displacement
Δ	non-dimensional measure of position of neutral axis ($\Delta = D/h$)
Γ_{ext}	integration path along the external boundaries of a specimen
Λ	non-dimensional curve-fitting parameter
Σ	stiffness ratio of sandwich ($\Sigma = E_1/E_2$ under plane stress)

1 Introduction

Many modern components and constructions, from microchips to ships and large wind turbine blades are made of materials arranged in layers. Mixed mode cracking is commonly observed in layered structures, since they often have weak planes such as interfaces between individual layers. Examples of mixed mode failure modes are splitting cracks, delamination of laminates and interface cracks in sandwich structures and adhesive joints. Under mixed mode cracking, the failure process zone is subjected to both normal and shear stresses. Earlier studies have shown that the interfacial fracture energy, expressed in terms of the critical energy release rate, $\mathcal{G}_c$, can depend on the mode mixity. Usually, the critical energy release rate increases when the amount of tangential crack opening displacement ("mode II") near the crack tip becomes larger than the normal crack opening displacement ("mode I") (Cao and Evans 1989; Wang and Suo 1990; Thouless 1990; Liechti and Chai 1992). The increase in macroscopic fracture energy with increasing amount of crack tip sliding has been attributed to various mechanics, such as crack face contact by asperities near the crack tip (Evans and Hutchinson 1989), to differences in the crack tip plasticity (Tvergaard and Hutchinson 1993) and to electrostatic effects between the crack faces (Liang and Liechti 1995).

A number of Linear Elastic Fracture Mechanics (LEFM) mixed mode and mode II test configurations have been developed, such as the asymmetric DCB-specimen, End-Notched-Flexure (ENF), Cracked Lap Shear (CLS) and Mixed Mode Bending (MMB) (Williams 1989; Hashemi et al. 1990; Reeder and Crew 1992; Fernlund and Spelt 1994). Each method has its advantages and drawbacks; see e.g. Shivakumar et al. (1998) for a recent overview of the most used test methods. For instance, the MMB test configurations proposed by Reeder and Crew (1992) and by Fernlund and Spelt (1994) both have the advantage that the entire mode mixity range from pure mode I to pure mode II can be obtained by the same specimen geometry. However, crack growth may be unstable for some mixed mode and mode II specimen configurations, such as the MMB and the ENF tests (Shivakumar et al. 1998; Ozdis and Carlsson 2000). Furthermore, mode II specimens where a transverse force is transmitted between the crack faces are susceptible to friction between the points where the transverse forces are applied (Carlsson and Gillespie 1989; Williams 1989; Hashemi et al., 1990) – the friction coefficient between delaminated surfaces can be as high as 0.4 – 0.6 (Schön 2000). By the use of mode II specimens where a transverse force is transmitted between the crack faces it is therefore difficult to investigate whether toughening mechanisms occur and to quantify their toughening effects.

It is desirable to characterise mixed mode cracking parameters by specimens that (i) enable tests under the full range of mode mixity, so that the same specimen geometry can be used for all mode mixities, reducing possible error sources associated with processing differences, and (ii) allow stable crack growth for all mode mixities. A further complication is that some composites generate fibre bridging during cracking. This leads to a significant rise in the fracture resistance (Albertsen et al. 1995). In many cases, large scale bridging (LSB) develops, which makes a LEFMs analysis invalid (Bao and Suo 1992). Instead, the analysis of the test specimen can be based on the J integral (Suo et al.

1992). Then, (iii) it is preferable to use fracture mechanics test specimens for which the J integral can also be obtained in analytical form under large scale bridging.

The purpose of the present paper is to develop a fairly general fracture mechanics test configuration for characterising mixed mode crack growth. The proposed test configuration fulfils the requirements described above, including the capability of characterizing large scale bridging by the J integral.

The paper is organised as follows: First, the basic mechanics of the proposed specimen is presented. Next, we describe the practical implementation of the test method. Finally, we illustrate the test method by fracture mechanical characterisation of an adhesive joint.

2 Description of test configuration

The proposed test configuration, a double cantilever beam (DCB) specimen loaded with uneven bending moments (DCB-UBM) at the two beams, is shown in Fig. 1a. In the following we analyse the DCB-UBM specimen by the usual assumptions of a small-scale failure process zone, small strains, small displacements and small rotations. The plane stress energy release rate and mode mixity are obtained in closed form for linear-elastic isotropic and orthotropic materials. Plain strain is treated in Appendix A.

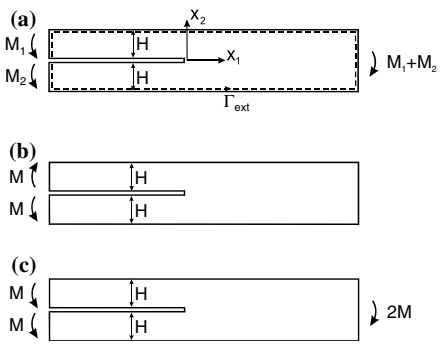

Fig. 1 The double cantilever beam specimen loaded with uneven bending moments (DCB-UBM) (**a**), can be obtained by superposition of a pure mode I specimen (**b**) and a pure mode II specimen (**c**)

2.1 LEFM failure process zone parameters

LEFM is applicable when the failure process zone is much smaller than the smallest specimen dimension (for DCB-specimens, the beam height, H). Then, for crack propagation along a weak plane in a homogeneous material, the singular crack tip stress field is characterised in terms of the energy release rate, $\mathcal{G}$, and the mode mixity, ψ, which is defined as the phase angle of the stress intensity factors (Hutchinson and Suo 1992).

$$\psi = \tan^{-1}\left(\frac{K_{\mathrm{II}}}{K_{\mathrm{I}}}\right) \tag{1}$$

with K_{II} and K_{I} being the mode II and mode I stress intensity factors, respectively. Equation 1 is valid only for homogeneous solids; a slightly different definition is used for the mode mixity for cracks along a bimaterial interface (Hutchinson and Suo 1992).

An appropriate failure criterion for mixed mode crack propagation along a weak plane is of the form (Jensen 1990; Hutchinson and Suo 1992)

$$\mathcal{G} = \mathcal{G}_{\mathrm{c}}(\psi) \tag{2}$$

where $\mathcal{G}_{\mathrm{c}}$ is the critical energy release rate. Equation 2 implies that the critical energy release rate depends on the mode mixity. Usually, $\mathcal{G}_{\mathrm{c}}(\psi)$ increases significantly as ψ approaches 90°.

2.2 J integral and mode mixity

The energy release rate can be calculated by evaluating the path independent J integral (Rice 1968) along a path following the external boundaries of the specimen (Fig. 1a), Γ_{ext}. The only non-zero contributions come from the beam-ends. When the beams are longer than a few times the beam height, the stress states at the beam-ends are unaffected by the stress field around the failure process zone of the crack. The beams are then subjected to pure bending. Under these conditions, the J integral calculation for the isotropic DCB-UBM specimen shown in Fig. 1a gives (plane stress)

$$\mathcal{G} = J = \frac{21(M_1^2 + M_2^2) - 6M_1M_2}{4B^2H^3E} \quad \text{for } |M_1| < M_2, \tag{3}$$

where M_1 and M_2 are the two applied moments, B is the specimen width, H is the specimen height

and E is the Young's modulus. For plane strain the result should be multiplied by $(1\text{-}\nu^2)$, where ν is the Poisson's ratio. Since the J integral analysis of the DCB-UBM specimen is valid for both LEFM and LSB problems, we will subsequently use the symbol J when referring specifically to LSB; otherwise for LEFM problems the symbol $\mathcal{G}$ will be used for the energy release rate. Note from (3) that the energy release rate of the DCB-UBM is independent of crack length. Thus, if the applied moments are measured it is not necessary to measure the crack length during an experiment. Furthermore, for experiments conducted under displacement control ("fixed grips") the moments will decrease during cracking, so that the energy release rate will decrease. Then, crack growth should be stable.

The DCB-UBM specimen (Fig. 1a) can be constructed by a superposition of a pure mode I specimen (Fig. 1b) and a pure mode II specimen (Fig. 1c), both analysed by Hutchinson and Suo (1992). Then, ψ can be obtained as

$$\psi = \tan^{-1}\left(\frac{\sqrt{3}}{2}\frac{M_1 + M_2}{M_2 - M_1}\right) |M_1| < M_2. \tag{4}$$

Plots of $\mathcal{G}$ and ψ as functions of the ratio between the moments are shown in Fig. 2. $\mathcal{G}$ and ψ are both well-behaving in the sense that no rapid variations, with respect to M_1/M_2, occur. The practical implication is that it is not necessary to control M_1/M_2 with a high degree of accuracy. Small changes in M_1/M_2 during an experiment do not change neither $\mathcal{G}$ nor ψ significantly.

The analysis can be extended to specimens of an orthotropic material. It has been shown (Suo 1990; Suo et al. 1991) that for any simple connected plane body of orthotropic material with stresses prescribed at its boundaries, the stress field depends on two non-dimensional elastic parameters, λ and ρ, defined by

$$\lambda = \frac{E_{22}}{E_{11}} \quad \rho = \frac{\sqrt{E_{11}E_{22}}}{2G_{12}} - \sqrt{\nu_{12}\nu_{21}}, \tag{5}$$

where $E_{11}, E_{22}, \nu_{12}, \nu_{21}$ and G_{12} are the in-plane engineering constants (Young's moduli, Poissons' ratios and the shear modulus); the subscripts indicate coordinate axis following standard notation of classic composite literature (Lekhinitskii 1981). Restrictions in the elastic properties lead to the requirements $\lambda > 0$ and $\rho > -1$ (Suo 1990). Typical values are $\lambda = 0.4$ and $\rho = 2$ for unidirectional glass fibre composites and $\lambda = 0.08$ and $\rho = 3$ for a unidirectional carbon fibre composite with the fibre direction parallel to the x_1-axis. For isotropic materials, $\lambda = \rho = 1$.

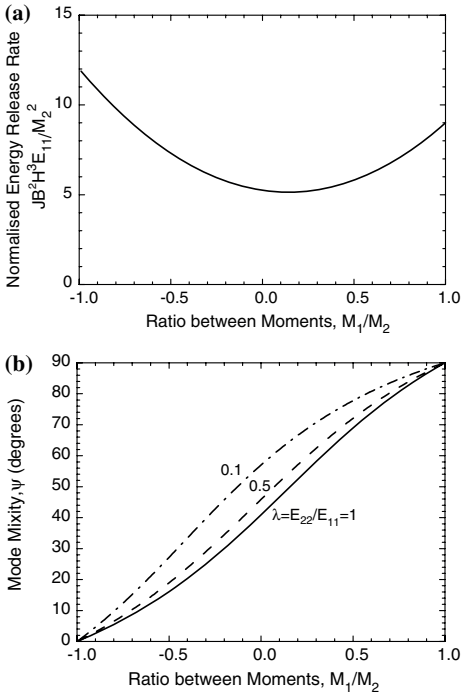

Fig. 2 Plots of (**a**) the normalised energy release rate of the DCB-UBM specimen as a function of the ratio between the applied moments, and (**b**) the resulting mode mixity a function of the ratio between the applied moments

Evaluating the J integral along the external boundaries of the orthotropic DCB-UBM specimen gives (plane stress)

$$\mathcal{G} = J = \frac{21\left(M_1^2 + M_2^2\right) - 6M_1M_2}{4B^2H^3E_{11}} \text{ for } |M_1| < M_2 \tag{6}$$

The mode mixity ψ of the DCB-UBM specimen can be determined analytically. A notable result is that $\psi(\lambda, \rho, M_1/M_2,)$ is independent of ρ for the orthotropic DCB-UBM, $\psi = \psi(\lambda, M_1/M_2)$. This is an exact result, shown first by Suo (1990); a slightly

different proof is given in Appendix B. With the mode mixity of the isotropic specimen given by (4), the mode mixity of the orthotropic specimen can be obtained by the use of the orthotropy rescaling technique (Suo et al. 1991). The result is

$$\psi(\lambda, M_1/M_2) = \tan^{-1}\left\{\lambda^{-1/4}\frac{\sqrt{3}}{2}\frac{1+M_1/M_2}{1-M_1/M_2}\right\}, \quad \text{for } |M_1| < M_2. \tag{7}$$

The mode mixity ψ is shown as a function of M_1/M_2 in Fig. 2b for some values of λ. For fixed M_1/M_2, ψ increases (i.e., the amount of mode II stress intensity increases) with increasing orthotropy (decreasing λ for $\lambda < 1$).

2.3 Practical implementation of test fixture

The principle of creating different bending moments in the two free beams of the DCB-UBM specimen is shown schematically in Fig. 3. Forces of identical magnitude, P, are applied perpendicular to two transverse arms connected to the end of the beams of the DCB specimen. The un-cracked end of the specimen is restricted from rotation but can move freely in the x_1-direction. Different moments are obtained if the length of the two moment arms, ℓ_1 and ℓ_2, of the transverse arms are uneven

$$M_1 = P\ell_1 \quad \text{and} \quad M_2 = P\ell_2. \tag{8}$$

M_1 and M_2 are defined positive when they act in the counter clockwise direction, as shown in Fig 1.

It follows from (7) and (8), that with one of the beam arm fixed, say $\ell_2 \geq 0$, the mode mixity can be changed simply by altering the other moment arm, ℓ_1, (the moment arms ℓ_1 and ℓ_2 are taken positive when the left force of each moment acts in the x_2-direction, as shown in Fig. 3).

Identical forces are obtained by the use of a wire arrangement, see Fig. 4. The idea builds upon earlier fixtures for pure mode I testing (Freiman et al. 1973; Sørensen et al. 1996)[1]. A 1.5 mm thick steel wire runs from the upper part of a tensile test machine, mounted at a 2.5 kN load cell (model 1210AJ-2.5KN-B, Interface Inc., Scottdale, Arizona, USA), via rollers to one of the transverse arms, down to rollers at the lower part of the tensile test machine and up again to another load cell in a similar manner in the other side of the fixture. The rollers at the transverse arms are mounted through holes. This allows easy and well defined adjustments of the moment arms. During an experiment, the force in the wire increases as the lower part of the test machine moves downwards. The gravitational forces of the transverse arms (made in aluminium) are outbalanced by helical springs. Some additional considerations were made to minimize errors in the applied moments as the specimen deforms, see Appendix C.

Typical dimensions of the DCB-UBM specimens are shown in Fig. 5. Specimens can be cut out as rectangular bars from planar plates. Steel parts that fit into the grips are fixed to each beam by four steel screws (M5) and an adhesive.

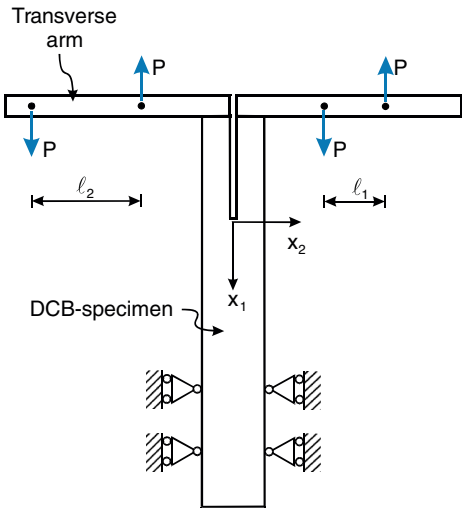

Fig. 3 Schematics of the proposed loading method; the mode mixity is controlled entirely by altering the length of one of the moment arms, e.g. ℓ_1

3 A case study: strength of adhesive joints in polymer matrix composites

We illustrate the usefulness of the DCB-UBM test configuration by studying the strength of adhesive

[1] Since this work was completed, we became aware of a rather similar test apparatus developed by Plausinis and Spelt (1995). Their test apparatus also applies uneven bending moments to a DCB specimen. The two uneven moments are made by two uneven forces that are connected via wires to holes in the neutral axis of the beams.

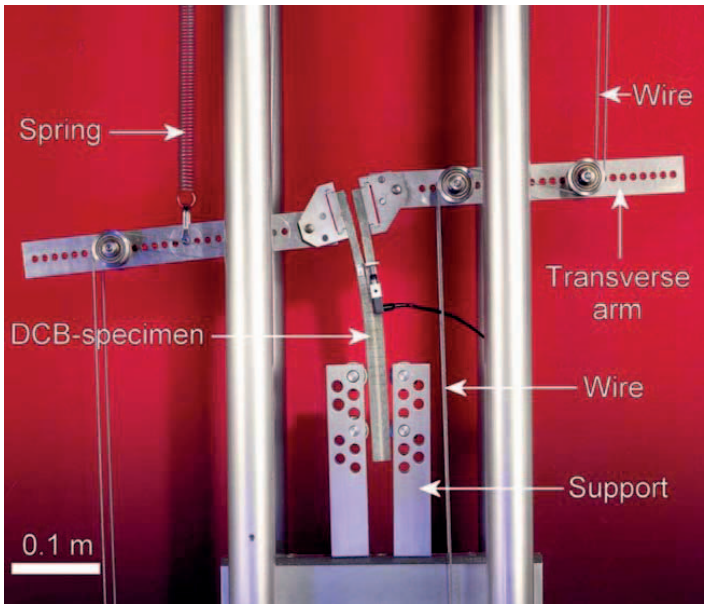

Fig. 4 Photos of the test set-up. Overview over the test fixture

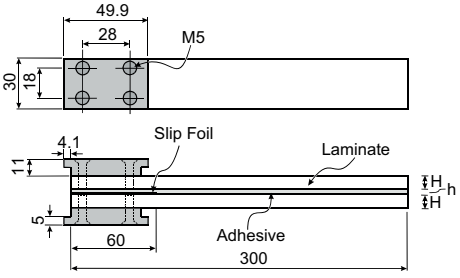

Fig. 5 Sketch of the specimen geometry. Steel parts are attached to the laminates by screws and adhesive. Nominal dimensions: $H = 8$ mm, $h = 3$ mm and $B = 30$ mm

joints. The adherends are made of laminates of plies of a unidirectional thermoset glass fibre reinforced plastic. The lay-up of the adherend laminates was $[\pm 45/0_5]_s$ i.e. almost unidirectional. Since the lay-up is symmetric, the laminates do not posses bending-twisting coupling. The specimen is not elastically homogenous as presumed in the analysis in Section 2; the stiffness of the adhesive layer differs from the stiffness of the laminate. The presence of the adhesive layer is accounted for in the calculation of J; the appropriate J integral solution for the sandwich specimen is given in Appendix D.

3.1 Manufacturing and testing of the DCB-UBM specimens

DCB specimens were processed as follows. First, two plates (300 by 300 mm, thickness approximately 8 mm) were made of a glass fibre/polyester composite. Details of the fibre and matrix types are proprietary. The plates were made by hand-lay up of dry fibre bundles, followed by matrix impregnation by vacuum infusion and post-cured. After consolidation, the two plates were bonded together by a thermoset adhesive. A thin slip foil was placed at the one end of the plates to act as a pre-crack and ease crack initiation. Spacers were used to control the thickness of the adhesive layer (3 mm). The adhesive was post-cured. Specimens, 30 mm in width, were cut from the sandwich plates. Steel parts were fixed to each beam by four steel screws (M5) and an epoxy adhesive (Scotch-Weld DP 460 from 3 M, hardened at 40°C for 2 h). The specimen geometry is shown in Fig. 5.

Prior to the measurements, the specimens were pre-cracked. The pre-cracking was conducted by loading the specimen by a near-symmetrical loading ($M_1/M_2 = -0.45$) until a load drop occurred (The near-symmetric loading was chosen to force the crack towards the adhesive-laminate interface — a symmetric loading might have caused cracking in the middle of the adhesive layer). A crack extension, typically about 5–10 mm in length, had occurred. The crack experienced fibre bridging. However, since the initiation had occurred from a thin inset and not a truly sharp crack tip, the initiation value is not valid. Therefore, in order to enable the determination of the fracture toughness of a sharp un-bridged crack, the crack was machined. The cut was made in the adhesive layer by a band saw until 1–2 mm from the crack tip. The cut was made in the adhesive layer at the laminate interface, effectively removing most of the bridging fibres. The purpose of this re-notching was to create a specimen that had a truly sharp crack tip with very limited fibre bridging.

Following re-notching, steel pins were mounted in holes drilled in the laminates at the end-of the inserts. The pins were separated by a distance, d, see Fig. 6. An extensometer (Instron, type 2620–602), range ±2.5 mm, was mounted at the pins, in a way that it could rotate freely and thereby record the magnitude of the crack opening displacement, Δ^E, see Fig. 6. It should be noted that Δ^E comprises both the end-opening of the bridging zone, δ^*, and the elastic strain in the specimens from $x_2 = -d/2$ to $x_2 = d/2$; however, the latter is assumed to be so small that it can be neglected (Sørensen and Jacobsen 2000), so that $\Delta^E \approx \delta^*$. An LVDT was mounted parallel to the beam to record the tangential displacements at the end of the notch, see Fig. 4.

The specimen was loaded monotonically at a constant displacement rate of 5 mm/min. Data (elapsed time, load, end-opening displacement) were collected at a personal computer using a 16 bit data acquisition board (PCI-DAS6013 from Measurement Computering, MA, USA) and a data acquisition programme (Labtech Notebook Pro, version 12.1, Laboratory Technology Corporation). Loading was continued until a stationary load level (indicating steady-state fracture resistance) was achieved.

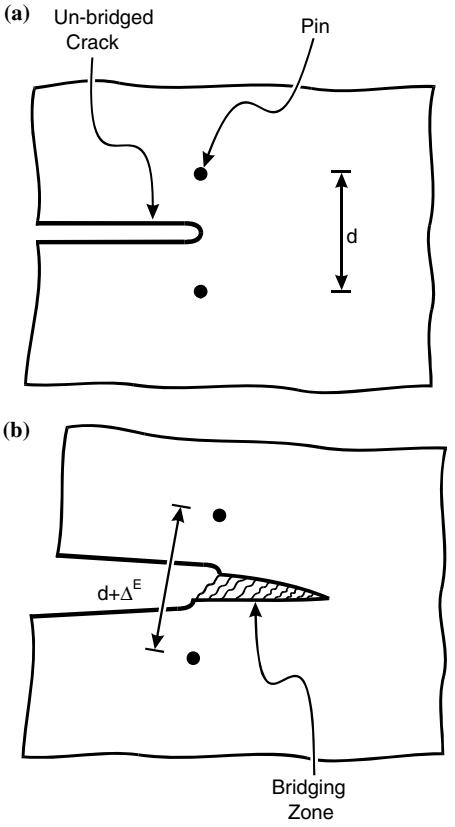

Fig. 6 Schematics illustrating how the total crack opening displacement is measured by an extensometer mounted at two pins, initially separated by a distance, d, before cracking (**a**) and (**b**) during cracking

3.2 Test results — DCB-UBM specimens

Figure 7 shows pictures of some cracking specimens under various mixed mode loadings. The crack propagated along the adhesive/laminate interface towards the beam that was subjected to the highest moment. After some crack extension (typically around 20 mm), a new crack formed at the next interface within the laminate, between the 0 and 45° plies (delamination). Subsequently, both the interface crack and the delamination crack grew simultaneously; usually the delamination crack propagated at the highest rate. The

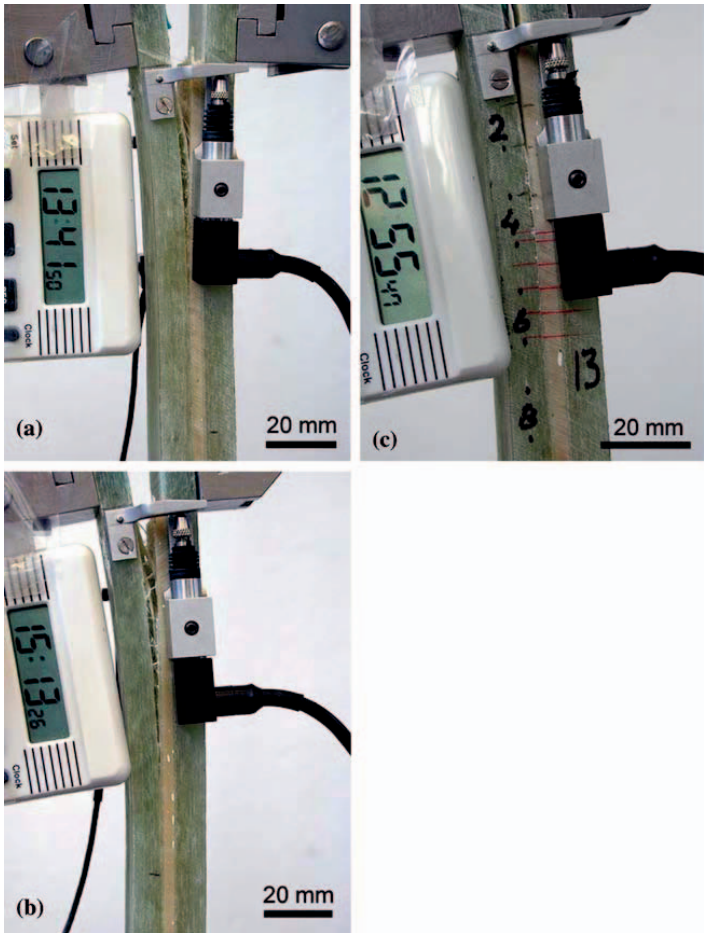

Fig. 7 Photos of specimens subjected to different loading conditions, here expressed in terms of M_1/M_2. (**a**) $M_1/M_2 = -0.45$ ($\psi = 24°$), (**b**) $M_1/M_2 = 0.48$ ($\psi = 73°$), (**c**) $M_1/M_2 = 1.0$ ($\psi = 90°$)

underlying cause for the formation of the delamination crack is not understood. Fibre cross over bridging was observed for both cracking planes, see Fig. 7. The measured fracture resistance of the pure interface crack and the combined interface cracking/delamination differed for some specimens. The failure sequence is shown schematically in Fig. 8.

J_R was calculated from Eq. 21 valid for the sandwich specimen by the use of the elastic data given in Table 1 and $\Sigma = 0.1$ and $\eta = 0.35$. Accounting for the stiffness of the adhesive layer is not very significant for the specimens evaluated here. Neglecting the adhesive layer, i.e. calculating J_R from the Eq 6 (orthotropic specimen) and using the elastic data given in Table 2 (giving $\lambda = 0.3$ and $\rho = 2$), gave a value approximately 10% lower than the sandwich Eq. 21. The nominal mode mixity — also neglecting the adhesive layer — was calculated from (7) with $\lambda = 0.3$.

Figure 9 shows typical results; the fracture resistance, J_R, as a function of end-opening, δ^*. The fracture resistance increases from a relative low value, corresponding to unbridged cracks, to a steady-state level, as the fibre bridging zone evolves. For experiments conducted at a higher nominal mode mixity ψ, the fracture resistance increases faster and attains a higher steady-state level.

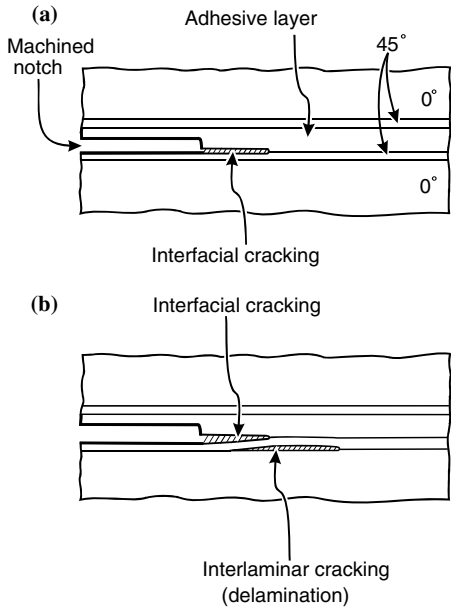

Fig. 8 Schematics of the cracking modes in the DCB-UBM sandwich specimens. Initially, cracking occurs along the adhesive/laminate interface (**a**), however, a delamination crack develops in the laminate (**b**). Subsequently, both cracks propagate, while showing fibre bridging

Since the mode mixity ψ looses its property as a parameter characterising the failure process zone under LSB, attention will be focussed at the initiation of crack growth of unbridged cracks. The initiation fracture resistance, J_0, i.e., corresponding to an unbridged crack, is shown in Fig. 10 as a function of the nominal mode mixity, ψ. Although there is some scatter in the results, it appears that a higher ψ gives a higher J_0. The scatter may be partially attributed to differences in the amount of bridging fibres following the re-notching. The experimental data was fitted (by eye) with the phenomenological criterion proposed by Hutchinson and Suo (1992)

$$J_0(\psi) = J_0^0\{1 - \tan^2[(1 - \Lambda)\psi]\} \quad (9)$$

where J_0^0 is the initial fracture resistance at $\psi = 0°$ and Λ is a dimensionless constant. A fitted curve is shown in Fig. 10; upper and lower bounds are shown as dash-dotted lines. The corresponding parameters are listed in Table 3.

4 Discussion

4.1 Drawbacks and advantages of the DCB-UBM test specimen

The DCB-UBM test configuration proposed in the present study was developed for static fracture tests. However, the concept of applying uneven, pure moments may also be useful for studying fatigue. Indeed, the apparatus by Plausinis and Spelt (1995), which also uses a wire arrangement, has been used successfully for cyclic fracture tests of adhesive joints (Dessereault and Spelt 1997). However, our test fixture uses long wires, and we think that this loading method is probably not well suited for rapid load changes usually used in cyclic loading. Another obvious drawback of our DCB-UBM configuration is that a special fixture is required, but this is also the case for other mixed mode specimens (Reeder and Crews 1992; Fernlund and Spelt 1994; Shivakumar et al. 1998). The mixed mode bending methods proposed by Reeder and Crews (1992) only provides stable crack growth under dominating mode I cracking; under dominating mode II, the crack growth can be unstable (Ozdis and Carlsson 2000). An advantage of the present method (and the one of Plausinis and Spelt (1995)) is that crack growth is stable over the entire mode mixity spectrum. Then, for any mode mixity, the fracture energy can be determined from arrested cracks having truly sharp tips. The measurement is therefore not sensitive to details of the crack starter (notch or film insert). A test is performed rather quickly, since there is no

Table 1 Orthotropic elastic data for the composite laminate (thermoset glass fibre reinforced plastic with the stacking sequence $[+45/-45/0_{10}/-45/+45]$)

E_{11}(GPa)	$\nu_{12}(-)$	E_{22}(GPa)	$\nu_{21}(-)$	G_{12}(GPa)
34	0.27	10	0.08	4

Table 2 Isotropic elastic data for bimaterial specimen. Subscripts indicate material number (material 1: adhesive; material 2: composite)

E_1(GPa)	$\nu_1(-)$	E_2(GPa)	ν_2 (−)
3	0.35	34	0.27

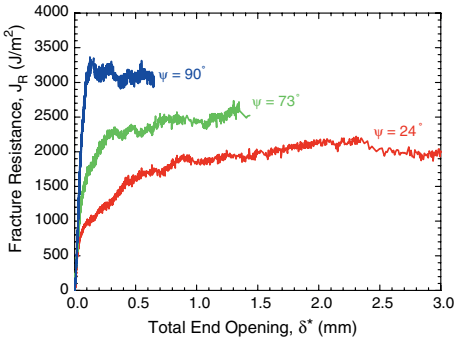

Fig. 9 Measured fracture resistance, J_R, as a function of the nominal mode mixity

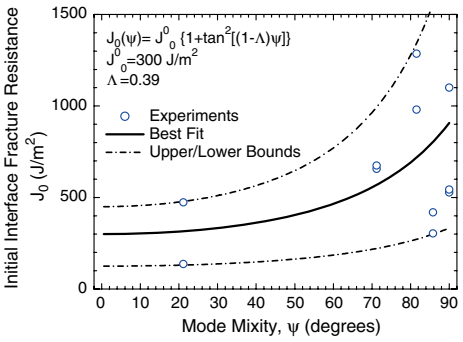

Fig. 10 The initial fracture resistance as a function of the nominal mode mixity. The solid line represents the best fit; dash-dotted are upper and lower bound curves

Table 3 Fitting parameters to $J_0(\psi)$

	J^0_0(J/m^2)	$\Lambda(-)$
Upper bound	450	0.33
Best fit	300	0.39
Lower bound	125	0.42

need to interrupt the test for crack length measurements. The method allows load rate effects to be investigated. The DCB-UBM is also well suited for studying effects of friction between the crack faces since loading–unloading experiments can be conducted under pure mode II or any mode II-dominated stress state. Unlike mode II test configurations where the test specimen is loaded with transverse forces (Carlsson and Gillespie 1989), no contact force must be transmitted between the fracture planes for the DCB-UBM specimen. For the DCB-UBM specimen, crack face contact and frictional interaction can, however, occur if the fracture surfaces are rough. Anyhow, frictional effects are expected to be smaller for the DCB-UBM specimen than e.g. for an ENF specimen. Finally, the J integral solutions hold true also under LSB. No crack length or compliance measurements are needed for the calculation of J. The equations for the fracture resistance (eqs. 3 and 6) are not invalidated by the development of a large-scale bridging zone (Bao and Suo 1992; Suo et al. 1992). This allows the determination of cohesive laws. This will be pursued elsewhere.

4.2 Importance of orthotropic elastic parameters

For many well established composite fracture mechanics test configurations, such as the standard DCB specimen loaded with wedge forces and the end load split specimen, ψ depends on both λ and ρ (Suo et al. 1991; Bao et al. 1992a). Thus, for those specimens, all five elastic constants E_{11} and E_{22}, ν_{12}, ν_{21} and G_{12} must be known before ψ can be determined accurately. For some specimens ψ depends only weakly on ρ, so that the dependency can approximately be ignored (Bao et al. 1992a,b). However, as shown, ψ is exact independent of ρ for the orthotropic DCB-UBM. Thus, under plane stress neither the energy release rate nor the mode mixity of the orthotropic DCB-UBM specimen depend on ρ. This has important implication for practical fracture testing of orthotropic DCB-UBM specimens. Then, only two elastic constants must be known to determine $\mathcal{G}$ and ψ for plane stress: E_{11} and E_{22}. This reduces the amount of experimental work required for determination of elastic properties of orthotropic materials.

Summary and conclusions

A mixed mode test configuration, the DCB specimen loaded with uneven bending moments (DCB-UBM), was proposed for fracture mechanics characterisation of mixed mode cracking. The energy release rate and mode mixity are given

analytically for specimens made of isotropic and orthotropic materials. A special loading fixture based on steel wires was developed.

Crack propagation in adhesive joints between composites made of thermoset glass fibre reinforced plastic was investigated. The initiation fracture energy of an unbridged crack, J_0, was found to increase with increasing mode mixity. In the early stages of cracking, the crack propagated along the adhesive/laminate interface; fibre cross over bridging occurred. In the later stages, a new crack formed at the next interface within the laminate; fibre bridging also occurred here. The fibre bridging resulted in a rising crack growth resistance.

Acknowledgements

This work was supported by an EFP2003 fund (No. 1363/03–0006) from the Danish Ministry of Environmental and Energy. We thank Jens Olsson, Christian H. Madsen and Morten D. Sørensen for experimental help. We also wish to thank an anonymous referee for making us aware of the test apparatus developed by Plausinis and Spelt (1995).

Appendix A: Plane strain

For plane strain, the engineering orthotropic constants E_{11}, E_{22}, ν_{12} and ν_{21} should be replaced with $E'_{11}, E'_{22}, E'_{12}$ and ν'_{21}, respectively in all equations, including the definitions of λ and ρ. The plane strain parameters are (Bao et al. 1992)

$$E'_{11} = \frac{E_{11}}{1-\nu_{13}\nu_{31}} \quad \nu'_{12} = \frac{\nu_{12}+\nu_{13}\nu_{32}}{1-\nu_{13}\nu_{31}}$$
$$E'_{22} = \frac{E_{22}}{1-\nu_{23}\nu_{32}} \quad \nu'_{21} = \frac{\nu_{21}+\nu_{23}\nu_{31}}{1-\nu_{23}\nu_{32}} \tag{10}$$

The shear modulus G_{12} remains unchanged.

Appendix B: Dependency of mode mixity on λ and ρ

For a crack running parallel to the x_1-direction the relationship between the energy release rate, $\mathcal{G}$, and the mode I and II stress intensity factors, K_{I} and K_{II}, can be written as (Suo 1990)

$$\mathcal{G} = \frac{n}{E_{11}}[\lambda^{-3/4}K_{\mathrm{I}}^2 + \lambda^{-1/4}K_{\mathrm{II}}^2] \tag{11}$$

where the constant n depends on ρ only,

$$n = \sqrt{\frac{1+\rho}{2}}. \tag{12}$$

As shown by Suo (1990), the combinations $\lambda^{-3/8}K_{\mathrm{I}}$ and $\lambda^{-1/8}K_{\mathrm{II}}$ are independent of λ. Furthermore, by superposition the stress intensity factors should depend linearly on M_1 and M_2. Thus, we can write

$$\lambda^{-3/8}K_{\mathrm{I}} + i\lambda^{-1/8}K_{\mathrm{II}} = (a+ib)M_1 + (c+id)M_2, \tag{13}$$

where $i = (-1)^{1/2}$ and the four (for the time being unknown) real constants a, b, c and d (units $\mathrm{m}^{-5/2}$) depend on E_{11}, ρ and H but not on λ, M_1 and M_2.

The four unknown parameters are determined by analysing four load cases. First we analyse the two load cases $M_1 \neq 0; M_2 = 0$ and $M_1 = 0; M_2 \neq 0$ separately by inserting (13) into (11) to get $\mathcal{G}$, which is then set equal to $\mathcal{G}$ calculated from (6). This gives

$$|a+ib|^2 = |c+id|^2 = \frac{21}{4n}\frac{1}{B^2H^3} \tag{14}$$

so that (13) can be can written as

$$\lambda^{-3/8}K_{\mathrm{I}} + i\lambda^{-1/8}K_{\mathrm{II}} = \frac{\sqrt{21}}{2\sqrt{n}}\frac{1}{BH^{3/2}}\left[-M_1 e^{i\omega} + M_2 e^{i\omega+\gamma}\right]. \tag{15}$$

Here ω and γ are two non-dimensional phase angles (within the interval $[-90°, 90°]$) that remain to be determined. On dimensional grounds ω and γ should depend on the dimensionless parameters $M_1/M_2, M_1/E_{11}H^3, \lambda$ and ρ. However, due to linearity, ω and γ should not depend on M_1/M_2 and $M_1/E_{11}H^3$. Furthermore, since the left hand side of (15) is independent of λ, so must the right hand side be. Thus, ω and γ should not depend on λ. They can only depend on ρ.

In order to determine γ, we consider a third load case, $\mathrm{M}_1 \neq M_2 \neq 0$, insert (15) into (13), and put the result ($\lambda^{-3/8}K_{\mathrm{I}}$ and $\lambda^{-1/8}K_{\mathrm{II}}$) into (11). Then we obtain

$$\mathcal{G} = \frac{21}{4}\frac{1}{B^2H^3E_{11}}\left[M_1^2 + M_2^2 - 2M_1M_2\cos\gamma\right]. \tag{16}$$

Setting (16) equal to (6) we find

$$\cos\gamma = \frac{1}{7} \tag{17}$$

or $\gamma = 81.78°$. Note that n cancels out so that γ is independent of ρ.

With γ determined, we proceed to find ω. As the fourth loading case we select one particular load combination, $M_2 = -M_1 > 0$. For this load case, the geometry and loading of the specimen is symmetric. Therefore, the shear stress σ_{12} must vanish along the symmetry line ($x_2 = 0$). Consequently, the mode II stress intensity factor, K_{II}, must be zero. Enforcing this condition to (15) gives

$$\sin\omega + \sin(\omega + \gamma) = 0. \tag{18}$$

With γ given by (17) we obtain

$$\tan\omega = -\frac{\sqrt{3}}{2} \tag{19}$$

or $\omega = -40.89°$. It follows from (17) and (19) that *both* γ and ω are independent of ρ and λ. With $\lambda^{-3/8}K_{\mathrm{I}}$ and $\lambda^{-1/8}K_{\mathrm{II}}$ being independent of λ and ρ, the mode mixity ψ can be determined analytically by orthotropic rescaling.

Appendix C: Effects of finite displacement, rotation and friction

The analysis of the test specimen was made under the assumption of small displacements and small rotations. This requires that the difference in beam rotation and deflections ahead and behind the failure process zone (the path where the J integral is evaluated) must be small. However, the deflections and rotations of the complete test specimen can still be finite. As the specimen is loaded, the two beams of the DCB-beams deflect and rotate. The transverse arms also move and rotate, since they are fixed to the ends of the DCB-specimen. Both finite displacements and finite rotation cause the true moments to differ from the nominal moments, Eq. 8. The moments are created by a wire that runs through rollers arranged as shown in Fig. 11. Thus, the true moment arm is

$$\ell = 2R + s\cos\theta, \tag{20}$$

where R is the radius of the rollers, s is the spacing between the centres of the rollers, measured along the transverse beam arm and θ is the angle of the transverse arms with respect to the x_2-axis. In order to reduce the effect of rotation, the transverse arms were angled 10° in the direction opposite of the rotation that they would undergo during loading. Thus, the transverse beam (the moment arm) reaches the neutral position ($\theta = 0°$) after a rotation of 10°. With this design, the error in the applied moment will always be less than 6% as long as the beam-ends rotate less than 20°. Note from (20) that decreasing the spacing between the rollers s, decreases the error. Thus, in most cases, the error will be significantly smaller than 6%.

In order to minimize the effect of the deflection (in the x_2-direction) of the specimen, the vertical distance (the x_1-direction, Fig. 3) between rollers at the upper and lower parts of the test machine should be maximized. In our set-up, this distance exceeds 2 m, so the error in the moment is vanishing.

The friction in the rollers (mounted at ball bearings) and wires were measured by pulling the wire along its direction. The friction was found to increase linearly with the applied load. Based on these experiments, the frictional moment during testing was estimated to be less than 3% of the applied moment, i.e. so small that it could be neglected. This was confirmed by experiments; the difference in the two load signals was insignificant.

Appendix D: DCB-UBM sandwich specimen

Sandwich specimens, e.g. specimens where two skin layers are joined by a thin core layer that is much thinner than other relevant specimen dimensions,

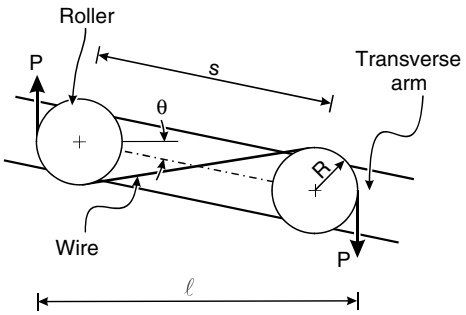

Fig. 11 Geometric relationship between transverse beam rotation angle θ and moment arm ℓ

are often used for characterising interfacial crack growth in bimaterial specimens. This type of specimen is attractive since, if cracking occurs along the interface so that the core layer remains attached to one of the skin layers, the residual stresses do not contribute to the energy release rate (Wang and Suo 1990). The strain energy in the adhesive layer is much smaller than that in the beams. Then, (3) and (6) are applicable. However, if the core thickness, h, is not much smaller than the thickness of the skins, H, the core thickness must be taken into account, as in the following. Assuming that the core and skin to possess isotropic elastic properties, the J integral evaluated along the external boundaries of the sandwich specimen gives (plane stress)

$$\mathcal{G} = J = \frac{1}{B^2 H^3 E_2}\left\{\frac{M_1^2}{2\eta^3 I_0} + 6M_2^2 - \frac{(M_1+M_2)^2}{2\eta^3 I_1}\right\}, \tag{21}$$

where H and E_2 denote the thickness and the Young's modulus, respectively, of the skin layers (material #2). For plane strain, the result should be multiplied by the term $1-\nu_2^2$, where ν_2 is the Poisson's ratio of material #2. The non-dimensional parameters η, I_0 and I_1 depend on the stiffness properties and layer thickness as described below. Equation (21) valid for both small-scale failure process zone and for LSB problems. The non-dimensional parameters η, I_0 and I_1 used in Eq. (21) are defined as follows (Østergaard and Sørensen, in preparation):

$$I_0 = \frac{1}{3}\frac{1}{\eta^3} - \frac{\Delta}{\eta^2} + \frac{\Delta^2}{\eta} + \Sigma\left(\frac{1}{\eta^2} + \frac{1}{n} + \Delta^2 - 2\frac{\Delta}{\eta} - \Delta + \frac{1}{3}\right), \tag{22}$$

$$\eta = \frac{h}{H}, \tag{23}$$

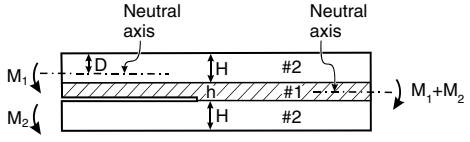

Fig. 12 Definition of geometry and material numbers for the DCB-UBM sandwich specimen

and

$$I_1 = \frac{1}{12}\left(\Sigma + \frac{8}{\eta^3}\frac{12}{\eta^2} + \frac{6}{\eta}\right). \tag{24}$$

The stiffness ratio parameter, Σ, is defined as (plane strain)

$$\sum = \frac{E_1 1-\nu_2^2}{E_2 1-\nu_1^2}, \tag{25}$$

where E_1 and E_2 are the Young's moduli of material #1 (the core layer) and #2 (the skins), respectively, and ν_1 is the Poisson's ratio of material #1. For plane stress (25) becomes $\Sigma = E_1/E_2$. The parameter Δ is a non-dimensional measure of the position of the neutral axis (D denotes the distance from the top of the skin layer to of the neutral axis of the bimaterial beam), see Fig. 12,

$$\Delta = \frac{D}{h} = \frac{1+2\Sigma\eta+\Sigma\eta^2}{2\eta(1+\Sigma\eta)}. \tag{26}$$

The parameters I_0, η, Σ and Δ are identical to the ones derived by Suo and Hutchinson (1990) in their analysis of bimaterial fracture specimens.

References

Adeyemi NB, Shivakumar KN, Avva VS (1998) Delamination fracture toughness of woven-fabric composites under mixed-mode loading. AIAA J 37:517–520

Albertsen H, Ivens J, Peters P, Wevers M, Verpost I (1995) Interlaminar fracture toughness of CFRP influenced by fibre surface treatment: part 1. Experimental results. Compos. Sci Technol 54:133–145

Bao G, Ho, S, Suo Z, Fan B (1992a) The role of material orthotropy in fracture specimens for composites. Int J Solids Struct 29:1105–1116

Bao G, Ho S, Suo Z, Fan B (1992b) Corrigenda. Int J Solids Struct 29:2115

Bao G, Suo Z (1992) Remarks on crack-bridging concepts. Appl Mech Rev 45:355–361

Cao HC, Evans AG (1989) An experimental study of the fracture resistance of bimaterial interfaces. Mech Mater 7:295–304

Carlsson LA, Gillespie JW (1989) Mode-II interlaminar fracture of composites. In Friedrich K (ed) Application of fracture mechanics to composite materials. Elsevier Science Publishers, 133–157

Evans AG, Hutchinson JW (1989) Effect of non-planarity on the mixed mode fracture resistance of bimaterial interfaces, Acta Metallur 37:909–916

Fernlund G, Spelt JK (1994) Mixed-mode fracture characterization of adhesive joints. Compos Sci Technol, 50:441–449

Freiman SW, Mulville DR, Mast PW (1973) Crack propagation studies in brittle materials. J Mater Sci 8:1527–1533

Hashemi S, Kinloch AJ, Williams JG (1990) The analysis of interlaminar fracture in unidirectional fibre-polymer composites. Proc R Soc A 427:173–190

Hutchinson JW, Suo Z (1992) Mixed mode cracking in layered materials, in Hutchinson JW, Wu TY (eds.) Advances in Applied Mechanics, vol 29. Academic Press, Inc., Boston, pp 63–191

Jensen HM (1990) Mixed mode interface fracture criteria. Acta Metallur Mater 38:2637–2644

Lekhnitskii SG (1981) Theory of elasticity of an anisotropic body. Mir Publishing, Moscow

Liang Y-M, Liechti KM (1995) Toughening mechanisms in mixed mode interfacial fracture. Int J Solids Struct 32:957–978

Liechti KM, Chai, Y-S (1992) Asymmetric shielding in interfacial fracture under in-plane shear. J Appl Mech 59:295–304

Ozdis F, Carlsson LA (2000) Characterisation of mixed mode delamination growth in glass/epoxy composite cylinders. J Compos Mater 33:420–441

Plausinis D, Spelt JK (1995) Application of a new constant $\mathcal{G}$ load-jig to creep crack growth in adhesive joints. Int J Adhes Adhes 15:225–232

Reeder JR, Crews JH, Jr (1992) Redesign of the mixed-mode bending delamination testing. J Compos Technol Res 14:12–19

Rice JR (1968) A path independent integral and the approximate analysis of strain concentrations by notches and cracks. J Appl Mech 35:379–386

Schön J (2000) Coefficient of friction of composite delamination surfaces. Wear 237:77–89

Shivakumar KN, Crews JH, Avva VS Jr (1998) Modified mixed-mode bending test apparatus for measuring delamination fracture toughness of laminated composites. J Compos Mater 32:804–828

Suo Z (1990) Delamination specimens for orthotropic materials. J Appl Mech 57:627–634

Suo Z, Hutchinson JW (1990) Interface crack between two elastic layers. Int J Frac 43:1–18

Suo Z, Bao G, Fan B (1992) Delamination R-curve phenomena due to damage. J Mech Phys Solids 40:1–16

Suo Z, Bao G, Fan B, Wang TC (1991) Orthotropy rescaling and implications for fracture in composites. Int J Solids Struct 28:235–248

Sørensen BF, Jacobsen TK (2000) Crack growth in composites: applicability of R-curves and bridging laws. Plas Rubber Compos Process Appl 29:119–133

Sørensen BF, Brethe P, Skov-Hansen P (1996) Controlled crack growth in ceramics: the DCB-specimen loaded with pure moments. J Eur Ceram Soc 16:1021–1025

Thouless, M.D (1990) Fracture of a model interface under mixed mode loading. Acta Metall 38:1135–1140

Tvergaard V, Hutchinson JW (1993) The influence of plasticity on mixed mode interface toughness. J Mech Phys Solids 41:1119–1135

Wang JS, Suo Z (1990) Experimental determination of interfacial toughness curves using brazil-nut-sandwiches. Acta Metall Mater 38:1279–1290

Williams JG (1989) Fracture mechanics of anisotropic materials. In Friederich K (ed) Application of fracture mechanics to composite materials. Elsevier Science Publishers

[A4]

Sørensen, B. F., and Jacobsen, T. K., 2009

"Characterising delamination of fibre composites by mixed-mode cohesive laws"

Composite Science and Technology, Vol. 69, pp. 445-456

Composites Science and Technology 69 (2009) 445–456

Contents lists available at ScienceDirect

Composites Science and Technology

journal homepage: www.elsevier.com/locate/compscitech

Characterizing delamination of fibre composites by mixed mode cohesive laws

Bent F. Sørensen [a,*], Torben K. Jacobsen [b]

[a] Materials Research Division, Risø National Laboratory for Sustainable Energy, The Technical University of Denmark, Building 228, Frederiksborgvej 399, DK-4000 Roskilde, Denmark
[b] LM Glasfiber A/S, R & D Department, Rolles Møllevej 1, DK-6640 Lunderskov, Denmark

ARTICLE INFO

Article history:
Received 6 August 2008
Received in revised form 13 November 2008
Accepted 16 November 2008
Available online 6 December 2008

Keywords:
A. Polymer-matrix composites
B. Delamination
C. Fibre bridging

ABSTRACT

A novel method is used for the determination of mixed mode cohesive laws and bridging laws for the characterisation of crack bridging in composites. The approach is based on an application of the *J* integral. The obtained cohesive laws were found to possess high peak stress values. Mixed mode cohesive stresses were found to depend on both the normal and tangential crack opening displacements. The bridging laws, which are to be used together with a mode mixity dependent crack tip fracture energy, were found to possess relative low bridging stresses; the peak normal bridging stress was approximately 2 MPa during pure Mode I and the maximum shear stress during pure Mode II was about 10 MPa.

1. Introduction

Structures made of laminated composite materials can fail along weak interfaces by failure modes that create a large-scale fracture process zone (FPZ). Examples are crack bridging by fibres during delamination of composite structures such as wind turbine blades, boats and trains and crack bridging of interface cracks in sandwich structures or adhesive joints. From a structural point of view, crack bridging is beneficial, since the formation of a crack bridging zone results in an increasing fracture resistance, in brief called *R-curve* behaviour [1]. For instance, earlier studies of delamination of unidirectional glass fibre/epoxy composites have shown that the fracture resistance can increase significantly due to fibre bridging [2,3]; the steady-state fracture resistance can be several times that associated with initiation of crack growth of an unbridged crack. It is therefore of interest to utilise crack bridging as a means to enhance the fracture resistance and possible increase the damage tolerance of otherwise weak interfaces. Examples of such ideas are tailoring the fibre/matrix interface by fibre treatment [4], and by fibre bundles oriented perpendicular to the crack surface, the so-called z-pins [5].

One complication of mixed mode interface fracture is that the fracture energy of interfaces often depends on the ratio between the shear and normal stresses at the crack tip, usually expressed in terms of the so-called mode mixity [6]. Another complication is that large-scale bridging (LSB) problems should not be analysed by linear elastic fracture mechanics (LEFM) [7]. Instead, when LSB occurs, fibre bridging can be modelled by a stress-separation law [1,7], which is the local bridging stress as a function of the local crack opening.

The purpose of the present study is to determine mixed mode stress-separation laws for a unidirectional fibre composite experiencing delamination. Regarding the mixed mode stress-separation laws as material properties, they must be determined experimentally, so that they can be used as input in models for predicting the structural strength of large structures. Furthermore, the stress-separation laws shape provides information about the bridging mechanism. This has importance in the process of optimizing material properties by microstructural optimisation, where a key question is: Do the toughening mechanisms operating in a given material give stress-separation laws that are similar to those predicted by micromechanical modelling?

Several types of stress-separation laws have been used in the literature. Uncoupled laws, i.e. laws in which the normal stress only depends in the normal opening displacement (but not the tangential crack opening displacement) and the shear stress only depends on the tangential crack opening displacement, are widely used [8–10]. The normal stress and the shear stress both depend on both the normal and tangential crack opening displacement in the stress-separation law proposed by Tvergaard and Hutchinson [11]. Their stress-separation law possesses a trapezoidal shape and gives the same fracture energy for all mode combinations. Other coupled stress-separation laws have been developed [12,13]. In all cases, simple, idealised shapes (e.g. linear softening or a trapezoidal shape) were assumed for the stress-separation relationship.

Here, we use an approach that provides details of mixed mode stress-separation laws. Rather than *assuming* a particular shape and a specific coupling, the present method *determines* the stress-separation law shapes and coupling (if present). We use a *J*

* Corresponding author. Tel.: +45 4677 5806; fax: +45 4677 5758.
E-mail address: bent.soerensen@risoe.dk (B.F. Sørensen).

0266-3538/$ - see front matter © 2008 Elsevier Ltd. All rights reserved.
doi:10.1016/j.compscitech.2008.11.025

integral approach as described by Sørensen and Kirkegaard [14]. However, as explained elsewhere [1,3], under LSB, LEFM solutions for stress intensity factors or energy release rates generally differ from the J integral solution. For most specimens, closed form analytical solutions for J cannot be obtained under LSB, since the J solution depends on the details of the stress-separation law. But a new generation of fracture mechanics test specimens has the prominent feature that J under LSB can be determined by analytical solutions [1]. Examples are the symmetric double cantilever beam (DCB) loaded with pure bending moments for pure Mode I stress-separation laws [1,15–17], and the DCB specimen loaded with uneven bending moments (DCB-UBM) [18] for mixed Mode I and II, see Fig. 1.

The J integral approach used in the present study is new. It is a generalisation of an approach introduced for pure Mode I tests [1,19,20]. The new approach was tested using synthetic data [14]; the investigation showed that the maximum polynomial degrees of Chebyshev polynomials should be three or higher to obtain a reasonably good representation of the shape of the cohesive stresses.

The paper is organised as follows: first we review and define two types of mixed mode stress-separation laws, called bridging laws and cohesive laws, respectively. We sketch the theory behind a J integral based approach for the determination of mixed mode bridging/cohesive laws. Then follows a description of mixed mode J integral fracture mechanical testing by the use of a DCB-UBM specimen. Next, the approach used for analysing the experimental data is explained. Results are presented in the form of fracture resistance curves, cohesive laws and bridging laws. Following a discussion of the results, the major conclusions of the present study are summarised. In order to ease the readability of the paper, some details that are not central to the main results are placed in Appendix A–C.

2. Theoretical background

2.1. Distinctions between cohesive laws and bridging laws

Stress-separation laws, representing the fracture process of materials, were introduced by Dugdale [21] and Barenblatt [22]. It is, however, only within the last decade, that the increase in computational capabilities has made it feasible to use stress-separation laws in advanced numerical models of materials and structures [8,11,23,24].

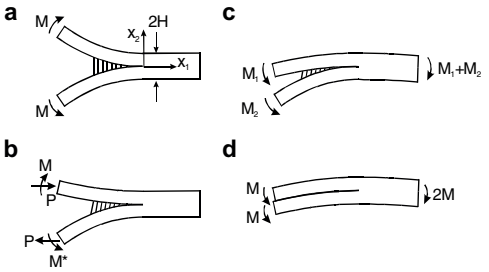

Fig. 1. Examples of specimen configurations for which J integral solutions are independent of details of the bridging/cohesive laws: a DCB specimen loaded with pure bending moments for pure Mode I (a), a DCB specimen loaded with a combination of axial forces and bending moments (b), a DCB specimen loaded with uneven bending moments (DCB-UBM) for mixed Mode I and Mode II (c) and DCB specimen loaded with pure, equal moments for pure Mode II testing (d).

We consider a structure having a crack or a sharp notch in an elastically isotropic material. When loaded with external loads, the stress state at the notch or crack tip causes a local weakening in the material, forming a FPZ. Within the FPZ, the material gradually looses strength, i.e. looses its capability of transmitting stresses across the fracture plane.

We consider two situations, which are rather similar, but possess important differences. In the first case, Fig. 2a, the FPZ of a fibre composite is divided into two parts: the crack tip fracture process zone and the crack wake zone (the bridging zone). The crack tip is characterised in terms of a crack tip fracture energy, J_0. In the crack wake, the stresses transmitted by bridging fibres are described by a stress-separation law called a bridging law [1]. This approach is appropriate when there is a distinct crack tip fracture process in a region having a size that is much smaller than any other relevant structural dimensions. Then, details of the crack tip FPZ can be disregarded and the criterion for crack propagation can be formulated in terms of a critical crack tip stress intensity factor, controlling the stress field around the crack tip [7] or alternatively by J_0, the critical value of the J integral evaluated around the crack tip (Γ_{tip} in Fig. 2c) and the mode mixity, defined as

$$\psi = \tan^{-1}\left(\frac{K_{II}}{K_I}\right), \tag{1}$$

where K_I and K_{II} as the Mode I and Mode II stress intensity factors characterising the stress intensities at the crack tip. Cracking can take place when the J integral evaluated around the crack tip, J_{tip}, equals the energy dissipation at the crack tip (the fracture energy of the crack tip), J_0. We assume that J_0 is a material constant that depends on the mode mixity, viz., $J_0 = J_0(\psi)$ [6].

In the bridging zone, the stress transfer can be modelled by a bridging law, which is a stress-separation law of the form

$$\sigma_n = \sigma_n(\delta_n, \delta_t) \quad \wedge \quad \sigma_t = \sigma_t(\delta_n, \delta_t), \tag{2}$$

where σ_n and σ_t are the normal and shear stress transmitted between the crack faces in the bridging zone, while δ_n and δ_t are the normal and tangential crack opening displacements. Eq. (2) should be understood as follows: the *local* bridging stresses depend on the

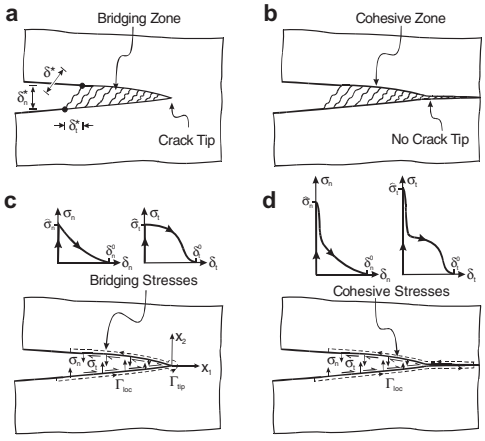

Fig. 2. A long failure process zone can be modelled as a crack tip and bridging zone (a) or as a long cohesive zone with no crack tip (b). The bridging law represents the stress transmitted between the crack faces behind the crack tip (c) while cohesive stresses acting along the entire cohesive zone (d).

local crack opening displacements but *not* on the opening *history*. Since the crack opening displacements vary as a function of the position within the bridging zone, so do the stresses. However, the same stress-opening relationship is assumed at every point along the bridging zone.

In the second case, Fig. 2b, the *entire* FPZ is represented by the stress-separation laws. No crack tip singular stress is present. The stress-separation law is then called a *cohesive law*. Formally, the cohesive laws depend on δ_n and δ_t as also bridging laws do; however, the energy uptake by the crack tip is included in the cohesive laws. Conceptually, the essential difference between cohesive laws and bridging laws is that cohesive laws represent the entire FPZ, including the crack tip. As shown in Fig. 2d, the cohesive zone should remain closed ahead of the crack tip, where the stresses are below the peak normal and tangential stresses, $\hat{\sigma}_n$ and $\hat{\sigma}_t$, so the material remains undamaged. The cohesive laws should only create crack openings and dissipate energy when the cohesive stresses exceed the peak stresses. The peak stress of cohesive laws will normally be higher than those of bridging laws as indicated in Fig. 2d.

The concepts of bridging laws and cohesive laws, as indicated by (2) and Fig 2, are only valid when the crack opening increases monotonically. Furthermore, it is frequently assumed that the cohesive/bridging stresses vanish when the openings exceed critical values, denoted here as δ_n^0 and δ_t^0, respectively, for the normal and tangential crack opening displacements. In general, δ_n^0 and δ_t^0 depend on the ratio between the tangential and normal crack opening displacements, e.g. expressed in terms of the phase angle of opening [25],

$$\varphi = \tan^{-1}\left(\frac{\delta_t}{\delta_n}\right). \tag{3}$$

2.2. J integral analysis of bridging laws and cohesive laws

Crack bridging problems can be analysed by the *J* integral [26]. For the bridging zone, we use an integration path, Γ_{loc}, locally around the bridging zone, including a part that encircles the crack tip, Γ_{tip}. The result is [14]

$$J_{\text{loc}} = \int_0^{\delta_n^*} \sigma_n(\delta_n, \delta_t)\mathrm{d}\delta_n + \int_0^{\delta_t^*} \sigma_t(\delta_n, \delta_t)\mathrm{d}\delta_t + J_{\text{tip}} \tag{4}$$

where δ_n^* and δ_t^* are the normal and tangential crack openings at the end of the bridging zone and J_{tip} is the *J* integral evaluated around the crack tip, Γ_{tip}, as shown in Fig. 2. The integrals can readily be interpreted as the work (per unit cross-section area) of the bridging stresses within the bridging zone.

For the cohesive zone problem, Fig. 2d, a similar integration path is used, except that now the integration path must be extended ahead of the crack tip so that the cohesive stresses at the front of the cohesive zone are below the peak stresses, $\hat{\sigma}_n$ and $\hat{\sigma}_t$ so that the crack remains closed at that position ($\delta_n = \delta_t = 0$). Then, the result of the *J* integral evaluation becomes identical to that of (4) except that J_{tip} vanishes.

The cohesive/bridging stresses (2) are taken to be independent of the opening history. Assume that they are derived from a potential function, Φ, with $\Phi(0, 0)=0$

$$\sigma_n(\delta_n, \delta_t) = \frac{\partial \Phi(\delta_n, \delta_t)}{\partial \delta_n} \qquad \sigma_t(\delta_n, \delta_t) = \frac{\partial \Phi(\delta_n, \delta_t)}{\partial \delta_t}. \tag{5}$$

Then, Eq. (4) becomes

$$J_{\text{loc}} = \Phi(\delta_n^*, \delta_t^*) + J_{\text{tip}}, \tag{6}$$

i.e. the potential function evaluated at the end-openings of the bridging zone. When cracking is modelled by bridging laws, crack propagation occurs when J_{tip} is identical to the crack tip fracture energy, J_0. We denote the value of J_{loc} during cracking by J_R. Then,

$$J_R = \Phi(\delta_n^*, \delta_t^*) + J_0. \tag{7}$$

Assuming that J_0 remains constant during an experiment, we obtain [14]

$$\sigma_n(\delta_n^*, \delta_t^*) = \frac{\partial J_R(\delta_n^*, \delta_t^*)}{\partial \delta_n^*} \qquad \sigma_t(\delta_n^*, \delta_t^*) = \frac{\partial J_R(\delta_n^*, \delta_t^*)}{\partial \delta_t^*}. \tag{8}$$

Thus, by recording J_R, δ_n^* and δ_t^* during experiments, we can determine bridging laws and cohesive laws. Under pure Mode I opening, $\delta_t^* = 0$, so that σ_n is independent of δ_t^*, viz. $\sigma_n = \mathrm{d}J_R/\mathrm{d}\delta_n^*$ and σ_t must be zero due to symmetry. Likewise, $\delta_n^* = 0$ under pure Mode II, σ_t is independent of δ_n^* so that $\sigma_t = \mathrm{d}J_R/\mathrm{d}\delta_t^*$.

2.3. J integral analysis of test specimen

Eq. (4) gives the relationship between bridging/cohesive laws and the *J* integral evaluated around the FPZ. However, to be feasible, fracture tests should be conducted using specimens for which *J* integral solutions are available. In the present study on mixed mode cracking, we use the DCB-UBM configuration. The *J* integral evaluated along the external boundaries of the specimen, Γ_{ext}, gives (plane strain) [18]

$$J_{\text{ext}} = (1-\nu^2)\frac{21(M_1^2+M_2^2) - 6M_1M_2}{4B^2H^3E} \quad |M_1| < M_2, \tag{9}$$

where M_1 and M_2 are the bending moments applied to the two beams (see Fig. 1), *B* and *H* are the specimen width and height, respectively, *E* is the Young's modulus and ν is the Poisson's ratio. For plane stress, $(1-\nu^2)$ should be replaced by unity. Eq. (9) is valid for isotropic materials; accounting for orthotropic elastic properties can easily be made [18]; however in the present case the difference is insignificant and the isotropic case is treated for simplicity. An important point is that the equation for *J* is independent of the crack length, *a*, and details of the bridging/cohesive laws. Eq. (9) is valid for both LSB and LEFM problems. Due to the integration path independence of the *J* integral, J_{loc} must be equal to J_{ext}. So, although the *equation* for J_{ext} (9) is independent of the bridging laws, its *value* does of course depend on the bridging laws, as indicated by (4).

Under LEFM, the crack tip stress field is characterised in terms of *J* and the mode mixity, defined by (1). The result for the isotropic DCB-UBM is [18]

$$\psi = \tan^{-1}\left\{\frac{\sqrt{3}}{2}\left(\frac{1+M_1/M_2}{1-M_1/M_2}\right)\right\} \quad |M_1| < M_2. \tag{10}$$

The Eqs. (9) and (10) are exact solutions that are valid as long as the length of the uncracked beam and the lengths of unbridged parts of the cracked beams are larger than the beam thickness *H*.

In summary, by the use of the DCB-UBM specimen we can calculate the *J* integral from (9) if the applied moments, M_1 and M_2, are recorded during an experiment. Furthermore, if the end-openings δ_n^* and δ_t^* of the bridging/cohesive zone are also recorded during the experiments, the mixed mode bridging/cohesive laws can be determined by the use of (8).

3. Experimental procedures

3.1. Specimen manufacturing

A laminate was manufactured by vacuum assisted resin transfer moulding of polyester into 20 layers of unidirectional E-glass fabrics. After infusion the laminate was post-cured. A 0.035 ± 0.015 mm thick and 60 mm wide perforated release film was placed in the middle of the fabrics along one of the edges in the

middle of the fabrics prior to infusion. The release film (slip foil) acted as crack starter and enabled a good infusion quality. The fibre volume fraction was 55 ± 3% for all specimens; effects of fibre volume fraction on the bridging/cohesive laws were not investigated. A plate, measuring 1200 mm × 600 mm × 18 mm, was manufactured and specimens were subsequently cut from the plate. The specimen length, L, was 300 mm or 600 mm (the latter was used for Mode II dominated experiments). Steel parts were fitted to the composite beams by screws and glue, as indicated in Fig. 3.

Pins were placed in the neutral axis at the end of the slip foil, i.e. at the position to become the end of the bridging zone. An extensometer (range ± 2.5 mm, Instron, 2620-602) was mounted to record the displacements between the pins, Δ^E, see Fig. 4a. Furthermore, a special holder was mounted at the pins. Two linear variable differential transformers (LVDT's) (H. F. Jensen, LDI 8/5) were mounted at the holder, recording tangential displacements, Δ_1^L and Δ_2^L at the neutral axis and at a position, D, 9.3 mm further away, as shown in Fig. 4b. The end-openings δ_n^* and δ_t^* were determined from these measurements (see Appendix A). After preparation, the specimen dimensions (width, B, and height, H) were measured for each specimen.

3.2. Test procedure

The tests were conducted at a special test fixture that applies pure, but uneven bending moments to the specimen via two transverse arms, using a wire and roller arrangement, see Fig. 5.

The force in the wire increases as the lower beam displaces downwards. Details about the test fixture are given elsewhere [18]. The moment ratio was controlled by lengths of the moment arms, ℓ_1 and ℓ_2, since (see Fig. 5)

$$M_1 = P\ell_1 \qquad M_2 = P\ell_2, \tag{11}$$

where P is the force applied via the wires. In Eq. (11) the moments are taken positive anti-clockwise in accordance with Fig. 1c, by defining the moment arms positive as shown in Fig. 5. The load was recorded by two independent 2 kN load cells. In the subsequent data analysis, the average value of the two load cell signals was used in the calculation of the force. The experiments were conducted at a constant displacement rate of the lower beam of the test machine of 5 or 10 mm/min. The tests were terminated when most of the specimen had cracked or a constant, steady-state load had been attained. During the experiments, the elapsed time and data from the load cells, the extensometer and the LVDT's were recorded at a PC at 25 Hz.

Crack initiation was detected visually or by non-linearity at the moment–extensometer relationship. Acoustic emission (Spartan AT, Physical Acoustic Corporation) was used to help to determine the onset of crack initiation. Tests were made for ten different M_1/M_2 ratios. About five specimens were tested for each M_1/M_2 ratio.

3.3. Data analysis

The moments, M_1 and M_2, were determined from the recorded force using (11) and J (plane strain) was calculated from (9) using the measured values of B and H of the actual specimen and E = 37 GPa and ν = 0.3.

The normal- and tangential displacements of the end-opening of the cohesive zone, δ_n^* and δ_t^*, were determined from measurements of Δ^E, Δ_1^L and Δ_2^L, see Appendix A. The data were also cleared for load drops due to rapid (unstable) crack bursts as described in Appendix B.

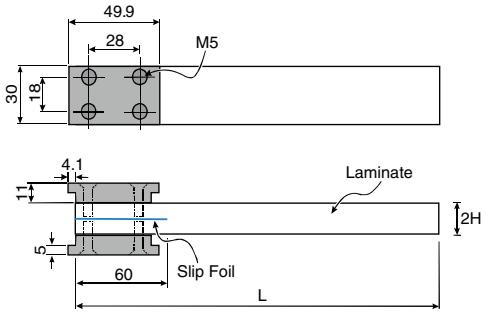

Fig. 3. Geometry and dimensions (in mm) of the used specimen. The beam thickness, H was approximately 9 mm and the specimen length, L, was 300 or 600 mm.

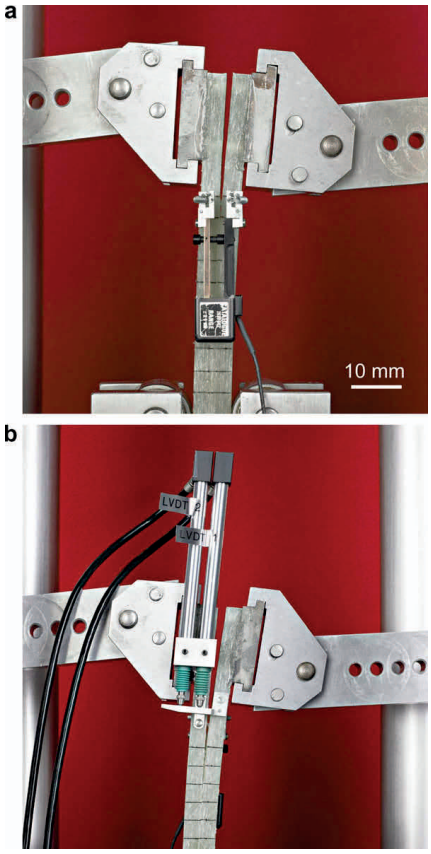

Fig. 4. Instrumentation at the end of the bridging/cohesive zone: (a) an extensometer is mounted at two pins at one side, while (b) two LVDTs are mounted at a special holder at the opposite side.

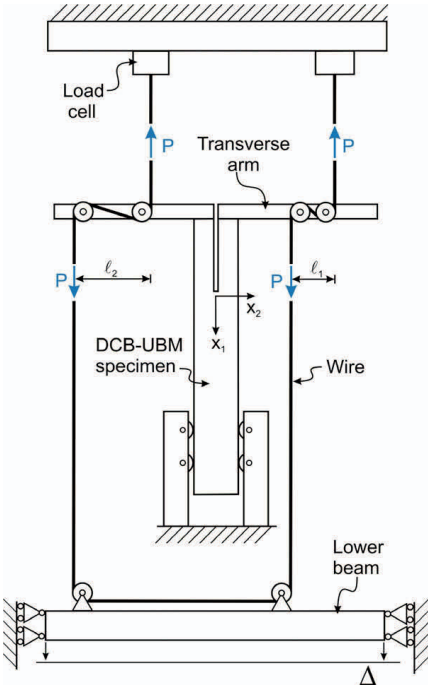

Fig. 5. Illustration of how pure, but uneven bending moments are created by the use of a wire and rollers. The force in the wire increases as the lower beam moves in the x_1-direction.

Having determined J_R as a function of δ_n^* and δ_t^*, we proceeded to determine cohesive/bridging laws. Mixed mode cohesive laws were determined from data for J_R, δ_n^* and δ_t^* following a numerical procedure proposed elsewhere [14]. Only a brief summary of the approach will be given here. A complete set of the J_R, δ_n^* and δ_t^* data from ten experiments spanning the entire spectrum from pure Mode I to Mode II (see Appendix C for the estimation of appropriate moment ratios using an analytical model) were analysed together. The values of the δ_n^*–δ_t^* data were transformed to the range of $[-1; 1]$ using a linear transformation. Denote the transformed values of δ_n^* and δ_t^* by $\bar{x}$ and $\bar{y}$. The J_R, $\bar{x}, \bar{y}$ data were fitted with a sum of products of Chebyshev polynomials as

$$f(\bar{x},\bar{y}) = \sum_{i=0}^{k}\sum_{j=0}^{l} a_{ij} T_i(\bar{x}) T_j(\bar{y}), \tag{12}$$

where $T_i(\bar{x})$ and $T_j(\bar{y})$ are the Chebyshev polynomial of the first kind of degree i and j, respectively. In (12), k and l denote the maximum polynomial degrees of $T_i(\bar{x})$ and $T_j(\bar{y})$. The coefficients a_{ij} were obtained as those that minimize the squared derivations. They were found by solving the normal equations of the problem. Having determined the coefficients a_{ij}, the cohesive stresses were obtained by partial differentiation in accordance with (8). Chebyshev polynomials were preferred for two reasons: (1) They are mutually orthogonal and (2) they minimize the maximum deviation between the supplied data and the fit almost as good as a minimax polynomial.

For the bridging law determination, only J_R data after crack initiation (i.e. data values with $J_R \geqslant J_0$) were used in the determination of bridging laws. Furthermore, for each experiment, the actual J_0-value was subtracted from the J_R values, since the fracture resistance due to the crack bridging is $J_R - J_0$.

4. Fracture resistance results

4.1. Overview of experiments

Initiation of crack growth was detected by acoustic emission and by onset of non-linearity in the load–opening curve, sometimes accompanied by a small load drop. The value of J at the initiation of cracking was denoted J_0. With increasing load, the crack tip moved along the specimen. In Mode I dominated experiments, fibre bridging was visible in the zone between the crack tip and the starter crack (the end of the bridging/cohesive zone). With increasing openings, more ligaments failed at the end of the bridging/cohesive zone. For Mode II dominated experiments, the limited crack openings precluded observations of crack bridging.

Crack growth occurred stably for experiments specified by $M_1/M_2 \leqslant 0.5$, i.e. with no rapid crack extensions. In contrast, for experiments conducted with $M_1/M_2 \geqslant 0.7$, the crack growth occurred as a combination of stable and unstable crack growth (sometimes referred to as "slip-stick" behaviour). Typically, those unstable crack extensions were in the order of 20 mm.

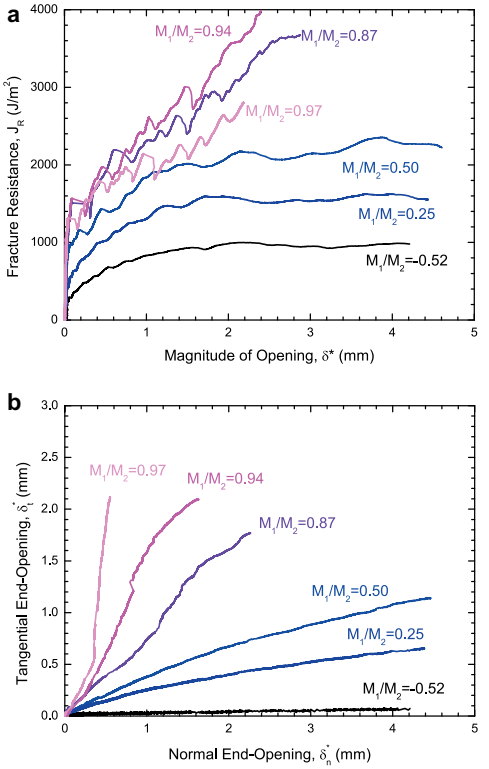

Fig. 6. Representative curves for (a) fracture resistance, J_R, and normal and tangential crack opening displacements (b) as a function of the magnitude of the end-opening, δ^* for various moment ratios.

Parts cut off from Mode II specimens (cut off in the crack wake, about 80 mm from the crack tip) were found to remain attached to each other. These parts had been subjected to a tangential displacement, δ_t, of about 2 mm. This shows that unbroken ligaments were still present. The fracture surfaces were found to be non-smooth due to loose fibres and fibre bundles.

4.2. Mixed mode fracture resistance

Fig. 6a shows typical results for J_R as a function of the magnitude of the opening, δ^*, calculated as

$$\delta^* = \sqrt{\delta_n^{*2} + \delta_t^{*2}}, \tag{13}$$

for various moment ratios. For $M_1/M_2 \leqslant 0.5$, the J_R–δ^* curves are relatively smooth. J_R increases with increasing δ^*, reaching a steady-state level after a crack extension of 2–4 mm. It is not easy to determine the transition to steady-state cracking accurately, since the curves all show some waviness. For $M_1/M_2 \geqslant 0.7$, the J_R–δ^* curves are markedly different. They have a more rough form due to rapid decrease in load and the curves do not flatten out to attain steady-state values. Rather, the J_R–δ^* curves take a nearly constant slope.

The associated end-openings, δ_n^* and δ_t^*, recorded for various M_1/M_2 ratios, are shown in Fig. 6b. It is seen from the figure that the openings increase monotonically (i.e. a decreasing crack opening does not occur). Note also that the experiments cover a large part of the δ_n^*–δ_t^* area. The δ_n^*–δ_t^* opening paths are near-proportional. However, it appears that it is not possible, even for $M_1/M_2 = 0.985$ (not plotted in Fig. 6, since it does not deviate much from data for $M_1/M_2 = 0.97$), to obtain a pure Mode II opening, i.e. where δ_n^* was completely zero. A practical significance of this is that there are no fracture resistance data for $\varphi^* > 77°$.

Values of the end-openings where steady-state is reached, δ_n^0 and δ_t^0, are shown in Fig. 7. There is a large scatter in the data; possibly reflecting the difficulty of determining the transition point accurately. However, for later use we identify an upper bound curve for the openings, such that for openings further away from the origin than the curve, the fracture resistance is assumed to have attained steady-state and the bridging/cohesive stresses are taken to be zero. The phenomenological boundary curve is given by

$$\left(\frac{\delta_n^0 - \delta_n^1}{\delta_{n0}^0 - \delta_n^1}\right)^m + \left(\frac{\delta_t^0}{\delta_{t0}^0}\right)^n = 1, \tag{14}$$

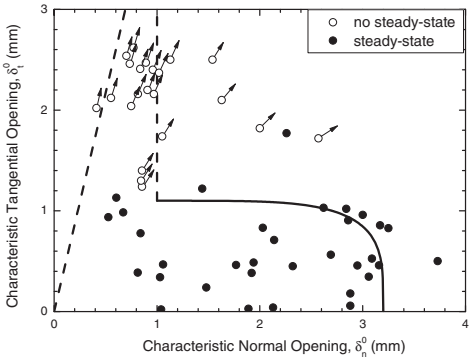

Fig. 7. Values of the steady-state normal and tangential end-openings (black symbols) and values from specimens not attaining steady-state (open symbols). The curve demarks an approximate boundary for the steady-state openings.

Table 1
Fitting parameters for the transition to steady-state.

δ_{n0}^0 (mm)	δ_n^1 (mm)	δ_{t0}^0 (mm)	m (-)	n (-)
3.2	1.0	1.1	3.5	4.0

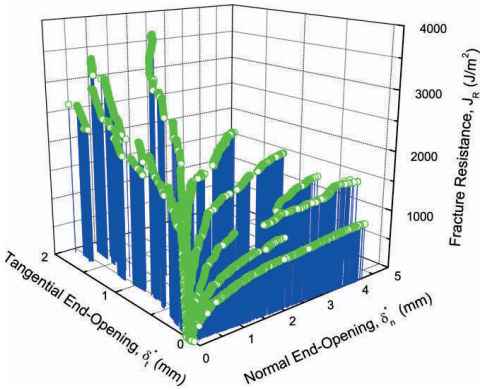

Fig. 8. Fracture resistance curves shown as a function of the normal and tangential end-opening displacements, δ_n^* and δ_t^*.

where δ_{n0}^0, δ_n^1, δ_{t0}^0, m and n are fitting parameters. The fitting function is shown as a solid curve in Fig. 7. The values used in the fit are given in Table 1.

5. Determination of mixed mode cohesive laws

Representative fracture resistance curves, J_R as a function of δ_n^* and δ_t^*, are shown in Fig. 8. The data shown in Fig. 8 were used for the determination of cohesive laws. Results are shown in Fig. 9. For these results, the goodness of fit r^2 was 0.95 or higher.

The cohesive normal stress, σ_n, possesses a peak value of about $\hat{\sigma}_n \approx 8$ MPa near $(\delta_n, \delta_t) = (0,0)$, but decreases rapidly with increasing values of δ_n and δ_t. We observe that, as expected, $\sigma_n \approx 0$ along the line that marks the transition to steady-state, given by (14). Interestingly, in the region near pure Mode II ($\delta_n^* \approx 0$–0.5 mm), σ_n comes out being negative (i.e. compressive) around $\delta_t \approx 0.3$–0.7 mm, with a minimum value about -1.7 MPa. For $\delta_t \approx 1$–2 mm, σ_n increases to a near-constant, positive value around 1–2 MPa.

The cohesive shear stress, σ_t, is shown in Fig. 9b. The peak value, $\hat{\sigma}_t$, is found to be located at $(\delta_n, \delta_t) = (0,0)$. $\hat{\sigma}_t$ is determined to be about 20 MPa. Away from the origin, σ_t decreases to a near-constant value of 1–2 MPa. For $\delta_n \approx 0$, σ_t varies in a wavy fashion around zero, in particularly at $\delta_n \approx 3$ mm. This wavy behaviour is considered invalid, since σ_t is expected to vanish for $\delta_n = 0$ as discussed in Section 2.2. Furthermore, as seen in Fig. 7, the curve selected for the transition to steady-state lies such that the curve encloses nearly all steady-state transition points. However, another curve, entailing a smaller area in the δ_n–δ_t plane could well have been chosen so that this corner ($\delta_n^* \approx 3$ mm) would be excluded from the plot.

6. Determination of bridging laws

When the fracture resistance is described in terms of a bridging law, the energy dissipation at the crack tip, J_0, is excluded from the stress-separation law. However, J_0 itself may depend on the mode mixity.

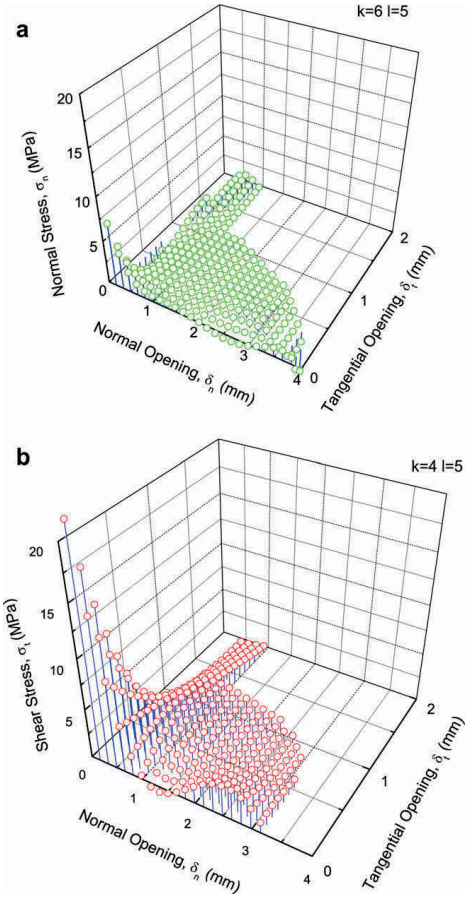

Fig. 9. Cohesive stresses as a function of the normal and tangential displacements, δ_n and δ_t. (a) The normal stress, σ_n, and (b) the shear stress, σ_t.

6.1. Initiation fracture energy

Fig. 10 shows the value of J at the initiation of crack growth, denoted J_0, as a function of the mode mixity. J_0 is seen to increase significantly with increasing ψ. For $\psi \leqslant 40°$, J_0 increases only moderately with increasing ψ. However, for $\psi \geqslant 60°$ J_0 increases rapidly as ψ approaches 90°. For $\psi \approx 90°$, J_0 is approximately ten times higher than the value for $\psi = 0°$. The function [6]

$$J_0(\psi) = J_0^0\{1 + \tan^2[(1-\Lambda)\psi]\} \quad (15)$$

was used to fit the data. In (15), J_0^0 is the value of J_0 at $\psi = 0°$ and Λ is a dimensionless constant. The parameters used in the fit are listed in Table 2.

6.2. Pure Mode I bridging law

The pure Mode I bridging law, obtained for six specimens by numerical differentiation, is shown in Fig. 11. The bridging law is characterised by a peak stress, $\hat{\sigma}_n$, occurring at very small openings, followed by a rapid decrease in the bridging stress σ_n within approximately 0.2 mm beyond which the bridging stress decreases in a slower manner. There is some specimen to specimen variation in the values of the peak stress, $\hat{\sigma}_n$. For one specimen we find $\hat{\sigma}_n \approx 2.9$ MPa; for the additional five specimens $\hat{\sigma}_n$ is in the range of 1.2–1.7 MPa. The opening at which the bridging stress vanishes, δ_n^0, is about 3.5 mm.

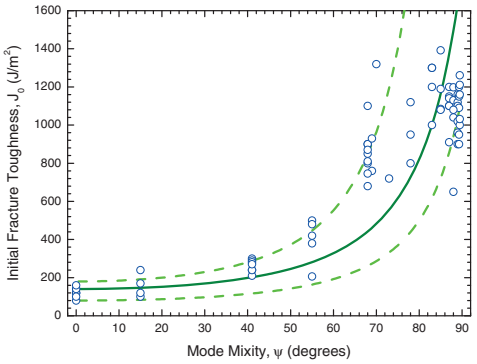

Fig. 10. Crack growth initiation value, J_0, is shown as a function of mode mixity, ψ. Symbols are experimental values; curves are fits.

Table 2
Fitting parameter for J_0.

	Lower bound	Best fit	Upper bound
J_0^0 (J/m^2)	80	140	180
Λ (-)	0.17	0.18	0.08

6.3. Pure Mode II bridging law

As mentioned above (Section 4.1), the Mode II curves contained decreasing J parts, as a result of rapid crack growth. These parts were excluded from the analyses, since these values of J do not cause cracking. Consequently, the obtained Mode II bridging law is not a continuous curve. The result from a representative specimen is shown in Fig. 12. The shear stress, σ_t, is seen to decrease from a peak value, $\hat{\sigma}_t$, of about 10 MPa to about 1–2 MPa after an tangential crack face displacement of about 0.5 mm. σ_t remains in the range of 1–2 MPa for $\delta_t^* > 0.5$ mm. We fit a straight line to the J_R–δ^* ($J_R > J_0$) data. The linear fit is shows as a dashed line in Fig. 12a. Note that the slope of the curve is somewhat lower than the slope of the individual parts of the experimental data. Differentiating the line according to (8), assuming $\delta^* \approx \delta_t^*$, gives $\sigma_t \approx 0.5$ MPa.

6.4. Mixed mode bridging laws

Data from nine representative tests with different M_1/M_2 ratios are shown in Fig. 13; $J_R - J_0$ is shown as a function of δ_n^* and δ_t^*. The subtraction of the ψ-dependent J_0 values does not change the general trends already commented on in Section 5.

Bridging laws, obtained by the approach of fitting Chebyshev polynomials to the data in Fig. 13 and performing the partial differentiation according to (8), are shown in Fig. 14. With the data

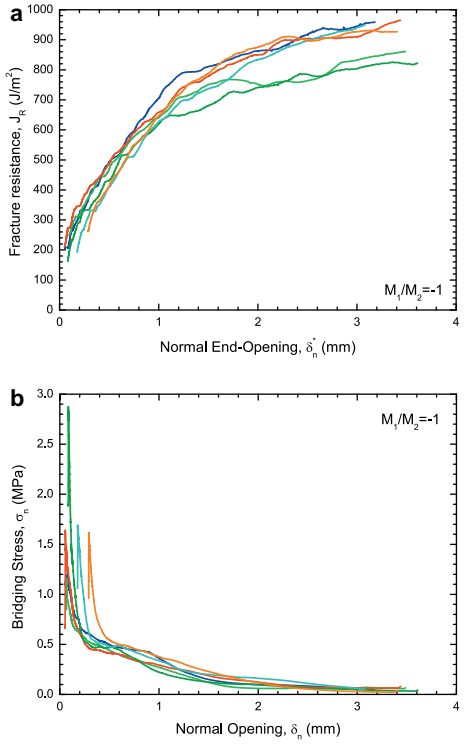

Fig. 11. Pure Mode I data: fracture resistance, J_R as a function of the normal end-opening, δ_n^* (a) and the obtained bridging normal stress, σ_n, as functions of the normal opening, δ_n (b).

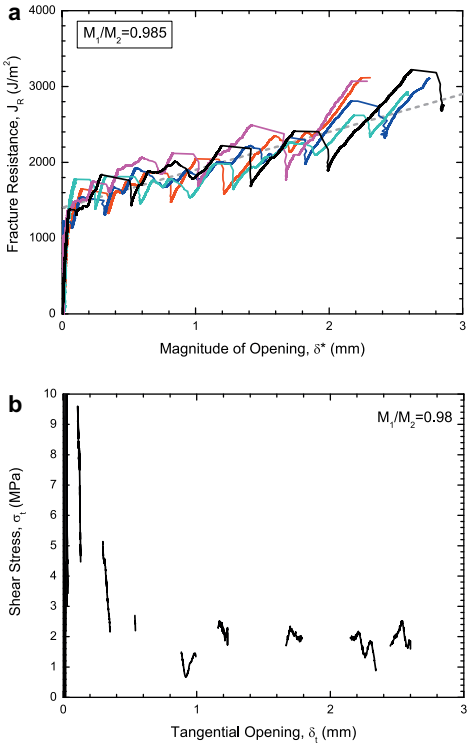

Fig. 12. Data for (near) pure Mode II: the fracture resistance, J_R, is shown as a function of the end-opening, δ^* (a); the obtained bridging shear stress, σ_t, is shown as a function of the tangential opening, δ_t (b).

available in the present study, it is not possible to use as high values for k and l with bridging laws as for cohesive laws.

In the plot, results for δ_n^* and δ_t^* outside the steady-state criterion (14) and $\varphi > 77°$ are excluded. From Fig. 14a we observe that the normal stress, σ_n, has a maximum value, $\hat{\sigma}_n \approx 1$ MPa near $(\delta_n, \delta_t) = (0,0)$. With increasing δ_n and δ_t, σ_n decreases towards zero, except for Mode II dominated openings ($\delta_n \approx 0$), which leads to increasing σ_n for $\delta_t > 1$ mm. For $\delta_n > 0.2$ mm, σ_n has decreased close to zero.

The shear stress, σ_t, is shown as a function of δ_n and δ_t in Fig. 14b. The peak stress, $\hat{\sigma}_t$ at $(\delta_n, \delta_t) = (0,0)$ is found to be about 1.8 MPa. This value is, however, subjected to some uncertainty, since the maximum polynomial degrees, k and l are low (unfortunately, higher values of k and l resulted in unrealistic scatter of the results near $(\delta_n, \delta_t) = (0,0)$). The overall shape of the bridging law is, however, expected to be fairly accurate, except near $(\delta_n, \delta_t) = (0,0)$. Apart from the rising stress near $(\delta_n, \delta_t) = (0,0)$, the bridging shear stress is relatively constant around 0.6 MPa.

7. Discussion

7.1. Comparison of initiation fracture energy

The values for the initiation fracture energy, J_0, can be compared with published results for glass fibre composites. Initiation fracture

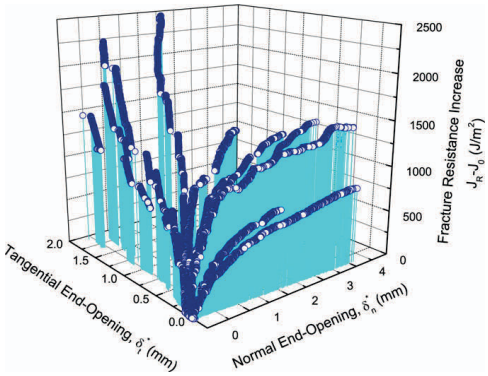

Fig. 13. Representative curves for the fracture resistance increase, i.e. where J_0 are subtracted from J_R to give toughening due to bridging shown as a function of the normal and tangential end-opening displacements, δ_n^* and δ_t^*.

energy data under pure Mode I was reported to be 100–400 J/m^2 for unidirectional glass fibre/epoxy composites [2,3,27] and 300–

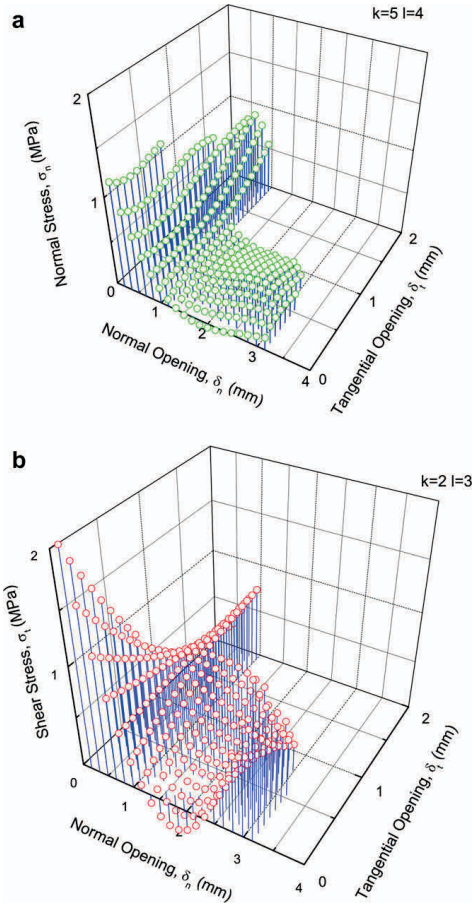

Fig. 14. Bridging stresses as a function of the normal and tangential displacements, δ_n and δ_t. (a) The normal stress, σ_n, and (b) the shear stress, σ_t.

500 J/m^2 for a glass fibre/vinylester composite [28,29]. Our value, J_0^0, is slightly lower, 180 J/m^2. For pure Mode II, initial facture energy values for glass/epoxy are reported to be 1500–2900 J/m^2 and 600–2000 J/m^2 for glass fibre/vinylester. Our values are comparable, around 900–1300 J/m^2.

7.2. Comparison with predictions made by micromechanical models

One of the motivations for determining mixed mode stress-separation is that their shapes can reveal information about underlying toughening mechanism [14]. The Mode I micromechanical model of Spearing and Evans [30] was recently extended to pure Mode II and mixed mode [31]. Under mixed mode crack bridging, bridging fibres and ligaments may be loaded in axial tension or compression. However, only ligaments subject to axial tension were considered in the analytical mixed mode model; ligaments subjected to axial compression were assumed to buckle under a low load. The model predicts that under pure Mode II, σ_t attains a constant value. From our Mode II experiments, Fig. 12, we do obtain a nearly constant value of σ_t, but only for $\delta_t > 0.5$ mm. The fact that unbroken bridging ligaments were still present for $\delta_t^* = 2$ mm (Section 4.1) suggests that the near-constant cohesive stress σ_t found for $\delta_t > 0.5$ mm can be attributed to Mode II crack bridging by unbroken fibres. However, for $0 < \delta_t < 0.5$ mm, σ_t is significantly higher. The difference between the model prediction and the experimental results for σ_t suggests that another toughening mechanism operates for $0 < \delta_t < 0.5$ mm.

The behaviour of ligaments loaded in axial compression has been studied by finite element (FE) simulation [32]. Ligaments loaded in axial compression were found to buckle such that they tend to bend in a direction normal to the crack plane. This generates a compressive stress normal to the crack plane. Thus, the negative normal stress found in the cohesive laws (Fig. 9a) can thus originate from ligaments loaded in axial compression. Furthermore, for the near Mode II experiments we observe from Fig. 6b that the end-opening in the normal direction, δ_n^*, increased to about 0.4 mm as the tangential end-opening, δ_t^*, increased from 0 to 0.5 mm. This is behaviour consistent with the opening that is expected for buckling ligaments.

An alternative mechanism is roughness of the fracture surface. Roughness has two effects: first, it creates a contact zone under dominating tangential crack face displacements. As the crack face surfaces displace relatively to each other, the roughness asperities ride on top of each other, effectively wedging the crack tip open, i.e. causing an opening (dilatation) in the normal direction. Secondly, the crack surface interaction in the contact zone will generate a compressive normal stress and a frictional shear stress opposing the crack face displacements. This mechanism, which is well-known in concrete and other quasi-brittle materials [34], can, at least in principle, explain the negative σ_n value and the high σ_t values obtained for $\delta_n \approx 0$ and $0 < \delta_t < 0.5$ mm.

7.3. Use of Chebyshev polynomials

Chebyshev polynomials were chosen for the data fitting in order to allow a large freedom of the J_R-surface, so that the results would reveal the shape of the bridging/cohesive laws and their dependence on the normal opening and tangential crack opening displacement. It is the authors' experience that the actual bridging/cohesive laws give predictions that are in better agreement with experimental results than more idealised bridging/cohesive laws, such as linear softening [33].

Cohesive laws based on the Chebyshev polynomials can be implemented into FE models, although some modifications might be required, e.g. if initial rising parts are preferred for small openings for numerical purposes. Table 3 includes the coefficients for the Chebyshev polynomials (with $k = l = 3$) for cohesive laws for the present material.

8. Conclusions

A J integral specimen, the DCB-UBM, was found to be suitable for mixed mode fracture mechanics testing of a polymer-matrix

Table 3
Chebyshev polynomial coefficients, a_{ij}, for the transformed data with $\delta_n^* \in [-22.2 \times 10^{-6}; 4.93 \times 10^{-3}]$ m and $\delta_t^* \in [-118 \times 10^{-6}; 2.64 \times 10^{-3}]$ m with $k = l = 3$. Subscripts i and j correspond to row and column number in the table.

i	j			
	0	1	2	3
0	-2.24×10^3	-5.11×10^3	-2.48×10^3	-3.83×10^2
1	-6.15×10^3	-1.05×10^4	-4.57×10^3	-8.49×10^2
2	-3.97×10^3	-6.06×10^3	-2.45×10^3	-2.87×10^2
3	-1.12×10^3	-2.16×10^3	-1.04×10^3	-2.72×10^2

composite that developed large-scale bridging. The end-openings of the fracture process zone could be varied from pure normal opening (Mode I) to nearly pure tangential crack opening displacements (Mode II). Mixed mode cohesive laws, representing the entire FPZ, were found to depend on both the normal and tangential crack opening displacements. The maximum shear stress was significantly higher than the highest normal stress. The cohesive laws are in reasonable agreement with model predictions based on cross-over bridging. However, the results also suggest the existence of a near-tip contact zone due to a non-planar fracture surface. The fracture process was also characterised in terms of a mode mixity dependent crack tip fracture energy and mixed mode bridging laws. The bridging stresses had significantly lower maximum stresses than the cohesive stresses.

Acknowledgements

We thank Christian H. Madsen, Jens Olsson and Erik Vogeley for experimental help. This research was supported by an EFP2005 grant (No. 33031-0078) from the Danish Ministry of Environmental and Energy.

Appendix A. Determination of δ_n^* and δ_t^* from measurements of Δ^E, Δ_1^L and Δ_2^L

We wish to determine the displacements in the normal- and tangential directions of the end-opening of the cohesive zone $(x_1,x_2) = (-\Delta a, 0)$, designated δ_n^* and δ_t^*, respectively. In practice, however, we measure the displacements of two points, A and B in Fig. A-1, located at the neutral axis of the beams, $(x_1,x_2) = (-\Delta a, H/2)$ and $(x_1,x_2) = (-\Delta a, -H/2)$. For the un-deformed specimen, the x_1-axis is parallel to the crack. In the deformed state, point A is rotated an angle θ_1 and point B is rotated an angle θ_2 in counterclockwise direction with respect to the x_1-axis. We assume that $\theta_1 < \theta_2$ since $|M_1| < M_2$ according to (9).

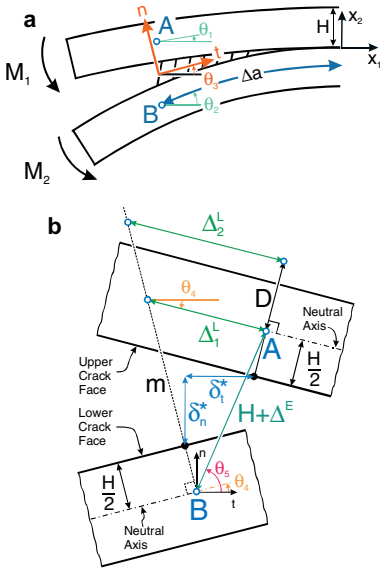

Fig. A-1. Measurement of the end-openings is done at the end of the pre-crack; the opening displacement between the two points A and B, Δ^E, is recorded by an extensometer; two LVDT's, separated a distance D from each other, record the tangential displacements, Δ_1^L and Δ_2^L, respectively.

Two complications are accounted for. The first is that δ_n^* and δ_t^* per definition are the displacements at the end of the FPZ at the crack faces, i.e. at $(x_1,x_2) = (-\Delta a, 0)$, where Δa denotes the crack extension. With the present experimental set-up, the displacements of the crack faces cannot be measured directly. Instead, as mentioned above, we measure displacements at the neutral axis of the beams. The second complication is that the normal and tangential directions (denoted n- and t-directions) must be defined for finite rotations, since the end-opening points of the two beams are subjected to different rotations. In accordance with the approach used in numerical simulation [12], we define normal the t-direction such that it is rotated the *average* angle of the two beams

$$\theta_3 = \frac{\theta_1 + \theta_2}{2}, \tag{A.1}$$

where θ_1 and θ_2 are the rotations of beam number 1 and beam number 2, respectively, as shown in Fig. A-1. Thus, the t-axis is rotated an angle, θ_3, with respect to the x_1-axis. The cohesive laws will thus be referred to the mid-surface between the two crack faces.

Next, we introduce

$$\theta_4 = \frac{\theta_2 - \theta_1}{2}, \tag{A.2}$$

which is always positive. Then, we can write

$$\theta_1 = \theta_3 - \theta_4 \quad \text{and} \quad \theta_2 = \theta_3 + \theta_4. \tag{A.3}$$

We relate the cohesive laws to the n- and t-directions in the deformed state with the t-direction defined such that the t-axis is rotated the mean of θ_1 and θ_2, i.e. θ_3 relative to the x_1-axis. Then, it follows from (A.3) that for the upper beam the angle from the t-axis to the neutral axis is θ_4 in the clockwise direction, while for the lower beam the angle from the t-axis to the neutral axis is θ_4 in the counter-clockwise direction as shown in Fig. A-1.

In the present experiments we use an extensometer to measure Δ^E, the displacement between point A and point B, and two LVDTs to measure the displacements, Δ_1^L and Δ_2^L. Here, Δ_1^L is the distance, parallel to the neutral axis of the upper beam at point A, between point A and a line m (shown dotted in Fig. A-1), from point B oriented perpendicular to the neutral axis of the lower beam. The other distance, Δ_2^L, is the displacement, parallel to Δ_1^L, between the line m and a point a distance D away from A, see Fig. A-1. Finally, define an angle θ_5 between the t-axis and the direction given by point A and point B (see Fig. A-1). Using plane trigonometry we obtain

$$\theta_4 = \frac{1}{2}\mathrm{Arc\,tan}\left(\frac{\Delta_2^L - \Delta_1^L}{D}\right) \tag{A.4}$$

and (measuring angles in radians)

$$\theta_5 = \theta_4 + \frac{\pi}{2} - \mathrm{Arc\,sin}\left\{\frac{\Delta_1^L}{H + \Delta^E}\cos(2\theta_4)\right\}, \tag{A.5}$$

and, neglecting the elastic deformation of the beams,

$$\delta_n^* = (H + \Delta^E)\sin\theta_5 - H\cos\theta_4 \quad \text{and} \quad \delta_t^* = (H + \Delta^E)\cos\theta_5. \tag{A.6}$$

Appendix B. Correction for load drop

When an experiment is conducted under a constant rotation rate ("fixed grips"), the DCB-UBM specimen partially unloads itself as crack growth occurs. Following the rapid load drop, further propagation does not occur until the J value has again reached the previous maximum J_R value, J_{max}. Thus, neither the decrease nor the increase in J represents the J_R values (values of J associated with crack growth).

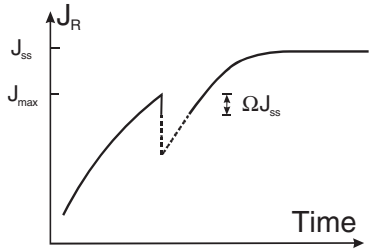

Fig. B-1. Approach for load-drop correction: data values that are ΩJ_{ss} lower than the highest previous maximum J_R-value, here denoted J_{max}, are discarded (dashed curves).

The simple approach for removing load drop data is as follows. Define a tolerance parameter Ω so that the maximum allowable load decrease is ΩJ_{ss}, where J_{ss} is the steady-state (or maximum) value of J_R of the entire experiment. Analysing the data values sequential in the order they were recorded to the data file, we denote the i'th value of the recorded J_R-value by J_i and J_{max} as the maximum J_R-value among the (i-1)'th first J_R-values. If

$$J_i < J_{max} - \Omega J_{ss}, \tag{B.1}$$

J_i is lower than allowed and the data point is disregarded. The approach is visualised in Fig. B-1. The dashed part of the curve represents the discarded data. Typically, in the analysis of the experimental data, values of Ω in the order of 0.005 were used.

Appendix C. Model of deflection of DCB-UBM specimen

In this appendix a model is developed for the analysis of the kinematics of the end-openings of the DCB-UBM specimen. The problem is shown schematically in Fig. A-1. We model the specimen by two beams loaded with different moments, denoted M_1 and M_2, respectively. The model builds upon Kirchoff's assumptions for bending of beams. Effects of bridging/cohesive stresses are neglected; only deformations due to the bending moments are accounted for. Then, since the beams are subjected to pure bending, it is assumed that the beams bend with a constant radius. The analysis accounts for finite rotations and displacements.

With reference to the global x_i-coordinate system, the displacements between the two points at the end of the cohesive zone are given by ($M_2 > |M_1| \neq 0$)

$$\delta_1^* = \left[\frac{EI}{M_2} + \frac{H}{2}\right]\sin\theta_2 - \left[\frac{EI}{M_1} - \frac{H}{2}\right]\sin\theta_1, \tag{C.1}$$

$$\delta_2^* = \left[\frac{EI}{M_2} + \frac{H}{2}\right]\{1-\cos\theta_2\} - \left[\frac{EI}{M_1} - \frac{H}{2}\right]\{1-\cos\theta_1\}, \tag{C.2}$$

where θ_1, the rotation of beam number 1, θ_2, the rotation of beam number 2, and the moment of inertia, I, are given by

$$\theta_1 = \frac{M_1\Delta a}{EI} \qquad \theta_2 = \frac{M_2\Delta a}{EI} \qquad I = \frac{BH^3}{12}, \tag{C.3}$$

and Δa is the crack length, i.e. the length along the neutral axis from the crack tip to the points where the end-openings are determined. In (C.1) and (C.2) δ_1^* and δ_2^* are the end-opening measured in the global x_i-coordinate system. For $M_2 > M_1 = 0$, (C.1) and (C.2) should be replaced by

$$\delta_1^* = \left[\frac{EI}{M_2} + \frac{H}{2}\right]\sin\theta_2 - \Delta a, \tag{C.4}$$

$$\delta_2^* = \left[\frac{EI}{M_2} + \frac{H}{2}\right]\{1-\cos\theta_2\}. \tag{C.5}$$

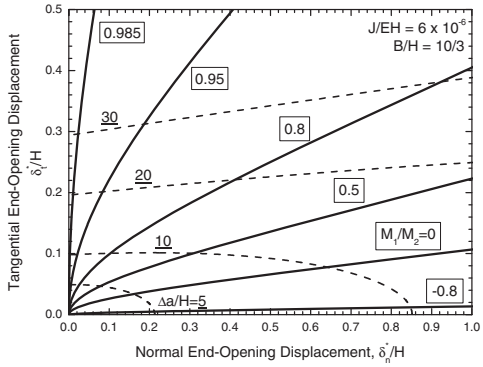

Fig. C-1. End-opening paths predicted for various ratios between the applied moments, M_1/M_2.

As mentioned, the n–t coordinate system is defined such that t-direction is tangential to the mid-plane defined by θ_1 and θ_2. Thus, the t-axis is rotated by an angle, θ_3, with respect to the x_1-axis, where θ_3 is given by (A.1). The displacement vector is transformed to the local coordinate system according to the standard transformation law,

$$\begin{Bmatrix}\delta_t^* \\ \delta_n^*\end{Bmatrix} = \begin{Bmatrix}\delta_1^*\cos\theta_3 + \delta_2^*\sin\theta_3 \\ -\delta_1^*\sin\theta_3 + \delta_2^*\cos\theta_3\end{Bmatrix}, \tag{C.6}$$

where δ_n^* and δ_t^* are the displacements in the normal and tangential directions, respectively.

Strictly speaking, M_1/M_2 cannot reach unity as indicated in (9) and (10). This is due to the kinematics restriction that the two beams cannot physically penetrate each other. The radius of curvature of the neutral axis of beam number 1, R_1, must exceed that of beam number 2, R_2, by at least H, viz. $R_1 \geqslant R_2 + H$. It follows that M_1 must be smaller than M_2. The maximum ratio between the moments can easily be calculated if the deformation due to bridging is neglected

$$\left(\frac{M_1}{M_2}\right)_{max} = \frac{1}{1 + 12\frac{M_2}{BH^2E}}. \tag{C.7}$$

Typically, the ratio $(M_1/M_2)_{max}$ is about 0.99.

Fig. C-1 shows the predicted end-openings, δ_n^* and δ_t^*, as functions of normalised crack extension, $\Delta a/H$, for various fixed ratios between the applied moments, M_1/M_2 (solid lines). The curves were generated under the premise of a constant J value. Thus, the δ_n^*–δ_t^* curves mimic loading paths expected by experiments conducted with proportional loading. The normalised distance between the crack tip and the end-point, $\Delta a/H$, is shown with dashed lines. The following non-dimensional parameters were used: $J/EH = 6 \times 10^{-6}$ and $B/H = 10/3$. The curves are anticipated to be representative for typical composite specimens.

Note from Fig. C-1 that, for a fixed value of M_1/M_2, the δ_n^*–δ_t^* relationship is non-linear for small $\Delta a/H$. With increasing $\Delta a/H$, the relationship becomes almost linear, in particular for $M_1/M_2 \leqslant 0$. Note, that with increasing $\Delta a/H$, the curves turn more towards normal opening. For instance, for $\delta_n^*/H \approx 1$ and $M_1/M_2 = 0$, the tangential opening is only about a tenth of the normal opening, so that the phase angle of the opening is less than six degrees. For comparison, the phase angle of the stress intensity factor of the same specimen analysed by linear elastic fracture mechanics (assuming a small-scale fracture process zone) is

about 41 degrees [6]. In order to achieve tangential end-openings significantly larger than normal openings, M_1/M_2 must be rather close to unity.

Note also from Fig. C-1, that for a fixed $\Delta a/H$, the magnitude of the end-opening decreases significantly with increasing M_1/M_2. In other words, it takes a much larger $\Delta a/H$ to reach the same magnitude in the end-opening during pure tangential opening than during pure normal opening. For instance, $\delta_n^*/H \approx 0.2$ is obtained for $\Delta a/H \approx 5$ for pure normal opening, while for pure tangential opening $\Delta a/H \approx 20$ is required to get $\delta_t^*/H \approx 0.2$. (see Fig. C-1).

References

[1] Suo Z, Bao G, Fan B. Delamination *R*-curve phenomena due to damage. J Mech Phys Solids 1992;40:1–16.

[2] Huang XN, Hull D. Effect of fibre bridging on G_{IC} of a unidirectional glass/epoxy composite. Compos Sci Technol 1989;35:283–99.

[3] Benzeggagh ML, Kenane M. Measurement of mixed-mode delamination fracture toughness of unidirectional glass/epoxy composites with mixed-mode bending apparatus. Compos Sci Technol 1996;56:439–49.

[4] Albertsen H, Ivens J, Peters P, Wevers M, Verpost I. Interlaminar fracture toughness of CFRP influenced by fibre surface treatment: part 1. Experimental results. Compos Sci Technol 1995;54:133–45.

[5] Rugg KL, Cox BN, Massabó R. Mixed mode delamination of polymer composite laminates reinforced through the thickness by z-pins. Compos part A 2002;33A:177–90.

[6] Hutchinson JW, Suo Z. Mixed mode cracking in layered materials. In: Hutchinson JW, Wu TY, editors. Advanced in applied mechanics, vol. 29. Boston: Academic Press, Inc.; 1992. p. 63–191.

[7] Bao G, Suo Z. Remarks on crack-bridging concepts. Appl Mech Rev 1992;45:355–61.

[8] Yang QD, Thouless MD. Mixed-mode fracture analysis of plastically-deforming adhesive joints. Int J Fract 2001;110:175–87.

[9] Li S, Thouless MD, Waas AM, Schroeder JA, Zavattieri PD. Mixed-mode cohesive-zone models for fracture of an adhesive bonded polymer-matrix composite. Eng Fract Mech 2006;73:64–78.

[10] Mohammad I, Liechti KM. Cohesive zone modelling of crack nucleation at bimaterial corner. J Mech Phys Solids 2000;48:735–64.

[11] Tvergaard V, Hutchinson JW. The influence of plasticity on mixed mode interface toughness. J Mech Phys Solids 1993;41:1119–35.

[12] Camanho PP, Davilia CG, de Moura MF. Numerical simulation of mixed-mode progressive delamination in composite materials. J Compos Mater 2003;37:1415–38.

[13] Högberg JL. Mixed mode cohesive law. Int J Fract 2006;141:549–59.

[14] Sørensen BF, Kirkegaard P. Determination of mixed mode cohesive laws. Eng Fract Mech 2006;73:2642–61.

[15] Sørensen BF, Jacobsen TK. Large scale bridging in composites: *R*-curve and bridging laws. Compos part A 1998;29A:1443–51.

[16] Lindhagen JE, Berglund LA. Application of bridging-law concepts to short fibre composites. Part 1: DCB test procedures for bridging law and fracture energy. Comp Sci Technol 2000;60:871–83.

[17] Sørensen BF. Cohesive law and notch sensitivity of adhesive joints. Acta Mater 2002;50:1053–61.

[18] Sørensen BF, Jørgensen K, Jacobsen TK, Østergaard RC. DCB-specimen loaded with uneven bending moments. Int J Fract 2006;141:159–72.

[19] Li VC, Ward RJ. A novel testing technique for post-peak tensile behaviour of cementitious materials. In: Mihashi H, Takahashi H, Wittmann FH, editors. Fracture toughness and fracture energy – testing methods for concrete and rocks. Rotterdam: A.A. Balkema Publishers; 1989. p. 183–95.

[20] Olsson P, Stigh U. On the determination of the constitutive properties of thin interphase layers – an exact solution. Int J Fract 1989;41:R71–6.

[21] Dugdale DS. Yielding of steel sheets containing slits. J Mech Phys Solids 1960;8:100–4.

[22] Barenblatt GI. The mathematical theory of equilibrium cracks in brittle fracture. Adv Appl Mech 1962;7:55–129.

[23] Needleman A. A continuum model for void nucleation by inclusion debonding. J Appl Mech 1987;54:525–31.

[24] Yang Q, Cox BN. Cohesive models for damage evolution in laminated composites. Int J Fract 2005;133:107–37.

[25] Serrano E, Gustafsson PJ. Influence of bondline brittleness and defects on the strength of timber finger-joints. Int J Adhes Adhes 1999;19:9–17.

[26] Rice JR. A path independent integral and the approximate analysis of strain concentrations by notches and cracks. J Appl Mech 1968;35:379–86.

[27] Ducept F, Davies P, Gamby D. An experimental study to validate test used to determine mixed mode failure criteria of glass/epoxy composites. Compos part A 1997;28A:19–29.

[28] Dharmawan F, Simpson G, Hertszberg I, John S. Mixed mode fracture toughness of GFRP composites. Compos Struct 2006;75:328–38.

[29] Stevanovic D, Jar PYB, Kalyanasundaram S, Lowe A. On crack-initiation conditions for mode I and mode II delamination testing of composite materials. Compos Sci Technol 2000;60:1879–87.

[30] Spearing SM, Evans AG. The role of fiber bridging in the delamination resistance of fiber-reinforced composites. Acta Metall Mater 1992;40:2191–9.

[31] Sørensen BF, Gamstedt EK, Østergaard RC, Goutianos S. Micromechanical model of cross-over fibre bridging – prediction of mixed mode bridging laws. Mech Mater 2008;40:220–4.

[32] Østergaard RC, 2007. Interface fracture in composite materials and structures. (PhD thesis) DCAMM special report no. S102. DTU, Denmark. ISSN 0903-1685.

[33] Jacobsen TK, Sørensen BF. Mode I intra-laminar crack growth in composites – modelling of *R*-curves from measured bridging laws. Compos part A 2001;32:1–11.

[34] Carol I, Prat PC, López CM. Normal/shear cracking model: Application to discrete crack analysis. J. Eng. Mech. 1997;123:765–73.

[A5]

Sørensen, B. F., Gamstedt, E. K., Østergaard, R. C.,
and Goutianos, S., 2008

"Micromechanical model of cross-over fibre bridging - prediction of mixed-mode bridging laws"

Mechanics of Materials, Vol. 40, pp. 220-34

Available online at www.sciencedirect.com
ScienceDirect
Mechanics of Materials 40 (2008) 220–234
MECHANICS OF MATERIALS
www.elsevier.com/locate/mechmat

Micromechanical model of cross-over fibre bridging – Prediction of mixed mode bridging laws

Bent F. Sørensen [a,*], E. Kristofer Gamstedt [b], Rasmus C. Østergaard [a], Stergios Goutianos [a]

[a] *Materials Research Department, Risø National Laboratory, Technical University of Denmark, DK-4000 Roskilde, Denmark*
[b] *Solid Mechanics, Royal Institute of Technology, SE-100 44 Stockholm, Sweden*

Received 23 December 2006; received in revised form 21 June 2007

Abstract

The fracture resistance of fibre composites can be greatly enhanced by crack bridging. *In situ* observations of mixed mode crack growth in a unidirectional carbon-fibre/epoxy composite reveal crack bridging by single fibres and by beam-like ligaments consisting of several fibres. Based on the observed bridging mechanism, a micromechanical model is developed for the prediction of macroscopic mixed mode bridging laws (stress-opening laws). The model predicts a high normal stress for very small openings, decreasing rapidly with increasing normal and tangential crack opening displacements. In contrast, the shear stress increases rapidly, approaching a constant value with increasing normal and tangential openings. The solutions for the bridging laws and the resulting toughening due to the bridging stresses are obtained in closed analytical form.

Keywords: Fracture resistance; ESEM testing; Polymer–matrix composites; Potential function

1. Introduction

Some fibre composites experience crack bridging during cracking. Crack bridging is defined here as ligaments that connect the crack faces in the wake behind the tip of an advancing crack. The crack bridging zone can be regarded as a part of the fracture process zone. Crack bridging can increase the fracture resistance of the composite considerably (Foote et al., 1986; Hashemi et al., 1990; Spearing and Evans, 1992; Albertsen et al., 1995; Sørensen and Jacobsen, 1998). A complication in the analysis of crack bridging in composites is that the bridging zone size can be comparable to or larger than the smallest relevant specimen dimensions. This is called large-scale-bridging (LSB). Under LSB, data analysis using linear elastic fracture mechanics is inadequate; classic *R*-curves (i.e., the fracture resistance as a function of crack extension) are specimen geometry and size dependent and cannot be considered being material properties (Bao and Suo, 1992; Suo et al., 1992; Spearing and Evans, 1992; Sørensen

* Corresponding author. Tel.: +45 4677 5806; fax: +45 4677 5758.
E-mail address: bent.soerensen@risoe.dk (B.F. Sørensen).

0167-6636/$ - see front matter © 2007 Elsevier Ltd. All rights reserved.
doi:10.1016/j.mechmat.2007.07.007

and Jacobsen, 1998). Instead, bridging laws (or cohesive laws) can be used as basic material properties for the crack bridging zone (Bao and Suo, 1992; Suo et al., 1992; Sørensen and Jacobsen, 1998; Jacobsen and Sørensen, 2001).

Bridging laws describe the response (under monotonic opening) of crack bridging within the fracture process zone in terms of stress–displacement laws, viz.,

$$\sigma_n = \sigma_n(\delta_n, \delta_t) \ \wedge \ \sigma_t = \sigma_t(\delta_n, \delta_t), \tag{1}$$

where σ_n is the normal stress and σ_t is the shear stress, δ_n and δ_t denote the normal and tangential crack opening displacements, respectively. In the analysis of bridged cracks, crack bridging ligaments are replaced by the bridging stresses as sketched in Fig. 1. Note from Eq. (1), that the normal and tangential stresses are assumed to be functions of both δ_n and δ_t but otherwise independent of position within the bridging zone. It is often assumed that the bridging stresses vanish when the normal and tangential crack opening displacements have exceeded critical values, denoted δ_n^0 and δ_t^0, respectively. The bridging laws are taken as material properties. Their importance on the fracture resistance can be seen by evaluating the path-independent J integral (Rice, 1968) locally around the fracture process zone. The result is (Sørensen and Kirkegaard, 2006)

$$J_{loc} = \int_0^{\delta_t^*} \sigma_t(\delta_n, \delta_t)\, d\delta_t + \int_0^{\delta_n^*} \sigma_n(\delta_n, \delta_t)\, d\delta_n + J_{tip}, \tag{2}$$

where J_{tip} is the J integral value evaluated around the crack tip (Γ_{tip} in Fig. 1b), while δ_n^* and δ_t^* are the end-opening and end-sliding of the bridging zone. Eq. (2) shows that the bridging laws are central to the energy dissipation within the bridging zone. Eq. (2) can be given a physical interpretation as the work (per unit cross-section area) of the bridging stresses. Bridging laws can be determined from experiments or from micromechanical models.

Fibre bridging in unidirectional fibre composites is traditionally divided into two basic cracking modes: crack bridging by fibres oriented perpendicular to the crack plane (Marshall et al., 1985; McCartney, 1987; Hutchinson and Jensen, 1990; Zok and Hom, 1990; Thouless and Evans, 1988; Deve and Maloney, 1991; Kardomateas and Carlson, 1996) and crack bridging by fibres oriented parallel to the cracking plane, denoted fibre cross-over

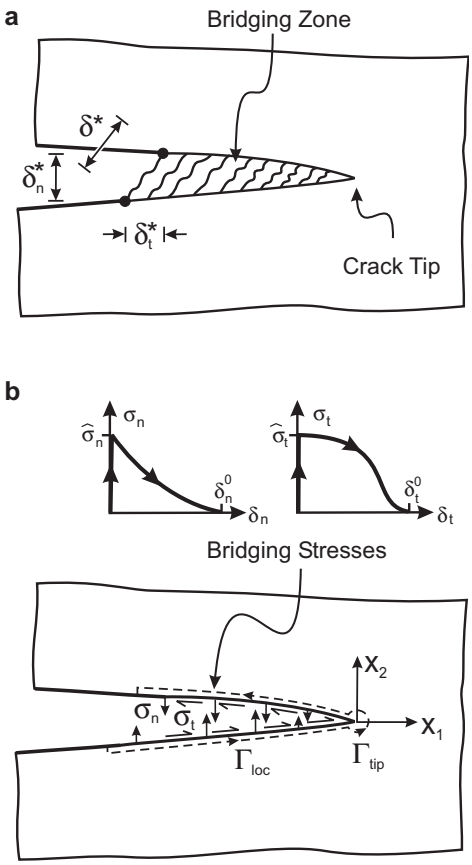

Fig. 1. Schematics of a crack experiencing mixed mode crack bridging. The bridging elements connect the two crack faces (a) and are modelled as surface tractions within the bridging zone (b).

bridging (Bao and Suo, 1992; Spearing and Evans, 1992; Kaute et al., 1993; Shercliff et al., 1994; Sørensen and Jacobsen, 1998). The present paper focuses at the latter.

A number of micromechanical models have been developed for Mode I cracking with fibre cross-over bridging (Spearing and Evans, 1992; Kaute et al., 1993; Ivens et al., 1995). Spearing and Evans (1992) modelled cross-over bridging by a beam peeling off along an interface. Neglecting shear deformation, their model predicts a relationship between the normal stress and normal opening as $\sigma_n \propto \delta_n^{-1/2}$. Since this result comes from a model based on classic beam theory, it is not expected to

be accurate for very short ligaments and the singular stress predicted for $\delta_n \to 0$ should not be taken literally. A bridging law having such a shape was found experimentally for a unidirectional carbon fibre-epoxy composite (Sørensen and Jacobsen, 1998) using a J integral approach developed for cementitious materials by Li and Ward (1989). The agreement between the measured and predicted bridging law shapes suggests that a micromechanical model based on simple beam theory may be adequate to represent cross-over bridging. The model by Kaute et al. (1993) is based on fibre pull out from the matrix. This mechanism was observed *in situ* during testing of ceramic matrix composites (Kaute et al., 1993; Shercliff et al., 1994). The model predicts that a constant bridging stress is attained if the bridging fibres remain intact. However, the bridging stress decreases to zero because of fibre failure, which is predicted by the Weibull model (Weibull, 1939).

The present study concerns mixed mode crack bridging by the cross-over bridging mechanism. First, a mixed mode test fixture is developed for use in an environmental scanning electron microscope (ESEM). Testing in the ESEM allows us to make *in situ* observations to characterise the bridging mechanism. These observations form the basis for the development of a simple model for the prediction of mixed mode bridging laws for fibre-cross-over bridging.

2. Experimental

In order to obtain *in situ* observations of the cross-over bridging mechanism under mixed mode crack opening, some fracture mechanics tests were conducted in the vacuum chamber of an ESEM, using a special mixed mode test fixture. The authors are not aware of a similar mixed mode test fixture for fracture mechanics testing in ESEM. Therefore, we start off with a brief description of the mixed mode test method that we have developed.

The advantage of performing fracture experiments in an ESEM (or a low vacuum scanning electron microscope) is that it is possible to observe newly cracked surfaces, which have not been opened and closed (by earlier loading and unloading of the specimen) before the microscopic observations. In a conventional SEM, the surface to be investigated must be electron conductive. Specimens made of non-conducting materials must be coated with a thin layer of a conductive material (e.g., carbon or gold). However, fracture surfaces formed after the application of the coating would charge up. Furthermore, for ductile materials, such as thermoplastics, the coating can crack at a lower strain than the underlying material (Bradley, 1989). Such problems are eliminated by performing the experiments in an ESEM, where it is not required that the surface is conductive.

2.1. Test specimen geometry and loading

The chosen test specimen is depicted in Fig. 2. It is a geometrically symmetric double cantilever beam (DCB) specimen loaded with a bending moment, M, and an axial force, P, applied at the neutral axis of the cracked beam ends ($x_1 = -a$, $x_2 = H/2$, where a is the crack length and H is the beam height, and x_1 and x_2 are coordinate axis, see Fig. 2). This configuration has been analysed as a general bimaterial specimen by Suo and Hutchinson (1990) and as an orthotropic specimen by Suo (1990). The analysis shows that P and M can represent any load case involving axial forces and moments at the edges.

Evaluating the J integral along the external boundaries of a specimen having isotropic elastic properties gives for plane strain (Suo and Hutchinson, 1990)

$$J_{\text{ext}} = \frac{1-\nu^2}{E}\left[7\frac{P^2}{B^2H} + 12\frac{M^2}{B^2H^3} + 12\frac{PM}{B^2H^2}\right], \qquad (3)$$

where E and ν are the Young's modulus and the Poisson's ratio, respectively, and B is the beam thickness. An important feature of the specimen configuration is that the J integral *equation* is independent of the crack length, a, and valid for LSB problems, since it does not depend on details of the bridging law, as elaborated by Suo et al. (1992) (obviously, J_{loc} equals J_{ext} due to the path independence of the J integral, so that the *value* of

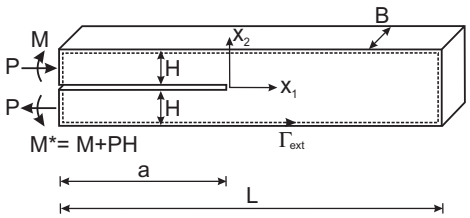

Fig. 2. A DCB specimen loaded with axial force, P, and a bending moment, M, at the beam-ends. The moment M^* is given by moment equilibrium.

J_{ext} depends on the bridging law, as indicated by (2)). In the study of LSB problems, this is advantageous, since this allows the bridging law to be determined directly from experiments (Bao and Suo, 1992; Suo et al., 1992; Sørensen and Jacobsen, 1998, 2003). This is, however, beyond the scope of the present study.

In practice, the combination of an axial force and a bending moment is created by applying a force that is placed a distance D from the crack plane, see Fig. 3. The moment is then given as

$$M = P\left(D - \frac{H}{2}\right). \tag{4}$$

Inserting (4) into (3) gives

$$J_{ext} = \frac{4(1-\nu^2)P^2}{B^2HE}\left(1 + 3\frac{D^2}{H^2}\right). \tag{5}$$

In case of a small scale fracture process zone it is relevant to characterise the stress state by J and the mode mixity, defined as the phase angle of the stress intensity factors,

$$\psi = \tan^{-1}\left(\frac{K_{II}}{K_I}\right), \tag{6}$$

where K_I and K_{II} denote the Mode I and the Mode II stress intensity factors, respectively. For the present test configuration the mode mixity can be obtained from the analysis of Suo and Hutchinson (1990). The result is

$$\psi = \tan^{-1}\left(\frac{H}{\sqrt{3}D}\right). \tag{7}$$

Fig. 4 shows J and ψ as a function of the length D. Note that ψ is rather sensitive to D for $D/H < 1/2$ (ψ varies 45° for $0 < D/H < 1/2$). This, coupled with the fact that the DCB specimen deflects under loading makes it difficult to control the value of ψ accurately during an experiment. In the present study, however, this is of minor concern, since the purpose of our experiments is to observe the micromechanics of mixed mode crack bridging, not to measure actual fracture resistance data. Another issue is that the loading fixture may not be able to deliver a sufficiently high load for high values of ψ (low D), since J decreases rapidly with decreasing D.

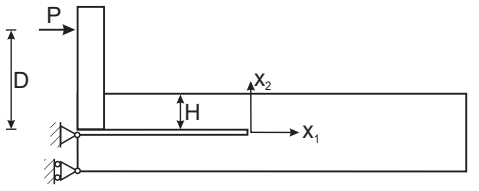

Fig. 3. Practical approach for creating a combination of a bending moment and an axial force by a single force, P, acting a distance D from the cracking plane.

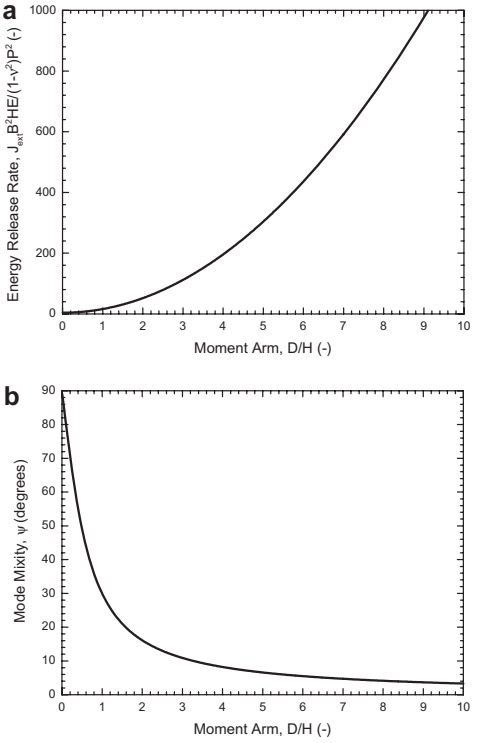

Fig. 4. J integral value (a) and mode mixity (b) as a function of the moment arm, D.

2.2. Specimen manufacturing

DCB specimens were cut from a 1 mm thick plate made of unidirectional carbon-fibre/epoxy composites. The plate was made by stacking plies of prepregs (Sigrafil CE 1007), followed by curing of the laminate in a vacuum bag at 120 °C for 2 h in an autoclave under a pressure of 0.5 MPa. The nominal fibre volume fraction was 60%. Following consolidation, the plate was cut to specimens with nominal dimensions 50 mm × 20 mm × 1 mm. The fibre direction was parallel to the x_1-direction. A

notch was cut to act as a crack starter. The crack plane ($x_2 = 0$) was in the direction of the fibres, orthogonal to the plane of the plies. The cracking was thus intralaminar. The specimen surface to be examined in the ESEM was polished to ease observations.

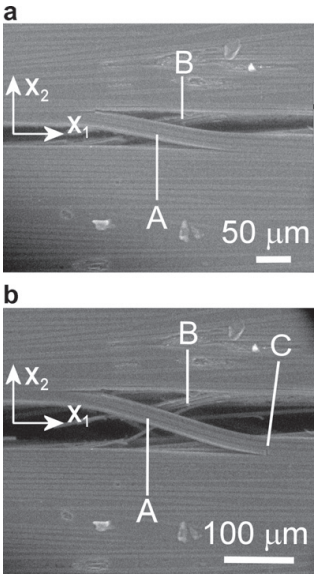

Fig. 5. Micrographs of two ligaments, (A) and (B), that bridge the main crack (a). With increasing opening (b), the ligament length increases and a fibre fails at the point of ligament detachment (C).

2.3. Testing procedure

The experiments were conducted in an ESEM (ElectroScan, model E3) using water as the ionising gas. Typically, the water vapour pressure was 3–5 Torr (~500 Pa) and the temperature was about 20–30 °C. Details of the practical design of the test fixture are given in Appendix A. The loading fixture, including the DCB specimen, was mounted at the *x–y–z* table of the microscope. After the application of the low pressure, the notch and crack tip was brought into the viewing area of the microscope. Then, the load was increased gradually until crack growth was detected visually at the ESEM monitor. Images (secondary electrons) were acquired of microstructural events, such as the formation of bridging ligaments. Experiments were made using different values of D, imposing different normal and tangential crack opening displacements.

2.4. Experimental results

Crack bridging, both in the form of single fibre and ligament bridging, was observed during the mixed mode cracking experiments. Some representative examples are shown in Figs. 5 and 6. In these examples, the loading was mixed mode ($D/H \approx 0.5$). In both cases, the loading was such that one of the beams ($x_2 > 0$) was displaced in the positive

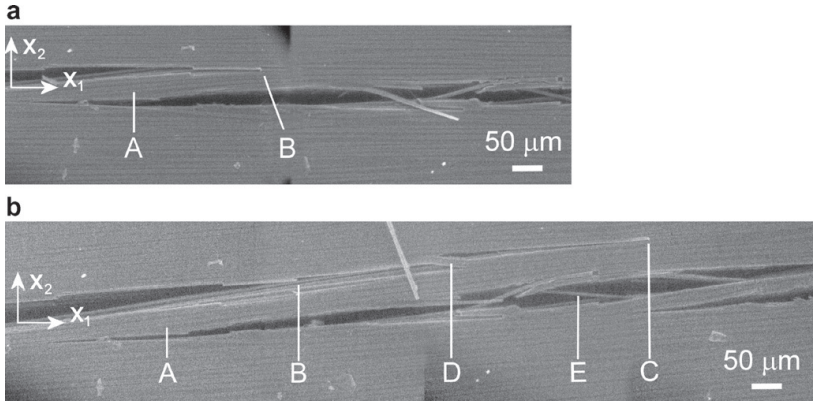

Fig. 6. Micrographs of a large ligament, (A), connecting the crack faces (a). The tip of the interface crack is indicated (B). With increasing opening (b), the crack extends (C), a small ligament loaded in compression forms (D). Single fibre bridging is also seen (E).

x_1-direction and in the positive x_2-direction (mixed mode opening) relative to the other beam of the specimen ($x_2 < 0$), in accordance with Fig. 3.

Fig. 5 shows two beam-like ligaments that have formed at the same x_1-position. Both ligaments consist of a few fibres embedded in the matrix. The two ligaments, however, appear to behave differently. The one in front (labelled A) takes an S-shape as it transmits a compressive force (in the x_1-direction). With increasing opening, the ligament length increases and a fibre fails (C) at the tip of the crack, possibly due to tensile stresses induced by bending. The ligament lying behind (labelled B) also displays fibre failure and appears to split up in single fibre bridges. Splitting of ligaments was, however, only rarely seen. It is noted that the ligaments can remain intact over crack openings that are several times the thickness of the ligaments.

The development of a large beam-like ligament (A) is shown in Fig. 6. With increasing opening, the ligament increases in length as the tip of the interface crack moves from (B) to (C). A small compressive ligament (D) has formed as the crack shifted plane. The small compressive ligament is bend into an S-shape. Single fibre bridging (E) as well as fibre failure is also seen.

The observations made here are in many respects similar to the observations made under pure Mode I experiments (Spearing and Evans, 1992; Sørensen and Jacobsen, 2000). One difference is that under mixed mode crack bridging, ligaments or fibres can be subjected to tensile or compressive force in the fibre direction, dependent on the ligament orientation, as shown in Fig. 5. Mechanically, they deform differently. The ligament subjected to a tensile force is likely to straighten as a string, whereas a ligament subjected to compression is likely to buckle.

3. Micromechanical model

3.1. Model specification

As mentioned above, the mechanism of mixed mode cross-over bridging in the investigated composite is similar to the cross-over bridging mechanism observed under pure Mode I. Therefore, we extend the existing Mode I model of Spearing and Evans (1992) to mixed mode by also including a tangential crack opening displacement. One complication is that ligaments in compression and tensile behave differently. Here, we disregard the ligaments loaded in compression, since they buckle easily and thereby their load-carrying capability vanishes. In contrast, ligaments loaded in tension act as strings and can thus carry a significant higher tensile load. This has been verified in another study of mixed mode ligament bridging where modelling was made by the finite element method (Østergaard et al., in preparation). Therefore, our model only includes ligaments that transmit tensile stresses.

Furthermore, we disregard plasticity and viscoelasticity. This allows us to make an analytical model. Although plastic deformation may occur at crack tips, neglecting plasticity is justified by the fact that fibres are usually very closely spaced (typically, a few microns); it is then anticipated that the effect of plasticity diminishes (Tvergaard and Hutchinson, 1994). We assume that the ligament peels off along a fibre/matrix interface that possesses a constant, mode mixity independent fracture energy, $\mathscr{G}_c$. This assumption will be justified later in the paper (Section 4.4). The mixed mode cross-over bridging mechanism is modelled using classic beam theory (small displacement, small rotations, small strains and shear deformation is disregarded) and smeared-together isotropic elastic properties (extension to orthotropic elastic properties is straightforward). The only failure event that is modelled is the detachment of a ligament along a cracking plane (involving fibre/matrix interface and matrix cracking); fibre failure is not included in the bridging law model. Splitting of ligaments is not modelled, since it was rarely observed and thus considered insignificant.

The model is shown in Fig. 7a shows a main crack with a few bridging ligaments. Fig. 7b shows details of a half bridging ligament. The model is planar. Each ligament is taken to have a rectangular cross-section. The height and width of the ligament are denoted h and b, respectively. Depending on the value of h, the model can represent cross-over bridging by single fibres or by beam-like ligaments consisting of several fibres. In the following, we will therefore make no distinction between the two cases; we will call both ligaments bridging. It is assumed that the number of bridging ligaments are uniformly distributed along the crack area and the number of ligaments per unit cracked areas is denoted η. As a first approximation, η is taken to be constant, i.e., independent of the actual opening path.

The parameters that specify the problem are: δ_n, δ_t, h, b, E, $\mathscr{G}_c$ and η. Thus, we can express the nor-

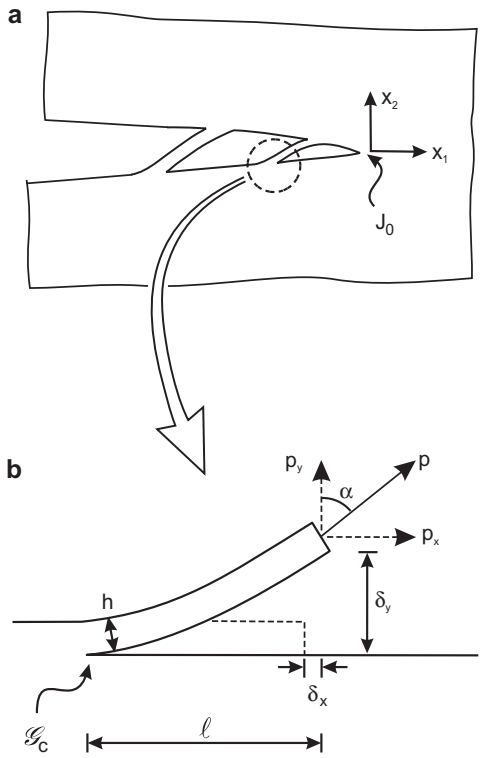

Fig. 7. Definitions of the micromechanical model. A ligament from a bridged crack (a) is modelled by a simple beam model (b).

malised bridging stresses as function of the non-dimensional parameters for a plane problem:

$$\frac{\sigma_n}{\eta bhE} = f\left(\frac{\delta_n}{h}, \frac{\delta_t}{h}, \frac{\mathscr{G}_c}{Eh}\right) \quad \text{and}$$
$$\frac{\sigma_t}{\eta bhE} = g\left(\frac{\delta_n}{h}, \frac{\delta_t}{h}, \frac{\mathscr{G}_c}{Eh}\right), \tag{8}$$

where f and g denote functions that are presently unknown, but are to be determined in the remainder of the paper.

3.2. Prediction of bridging laws

In order to simplify the derivation, we find it convenient to use the half openings of the crack, δ_x and δ_y, defined as

$$\delta_x = \frac{\delta_t}{2} \wedge \ \delta_y = \frac{\delta_n}{2}. \tag{9}$$

Furthermore, we define the ligament length as 2ℓ, see Fig. 7 (the ligament length is not an independent parameter, but must be determined as a part of the solution). In the midpoint of the bridging ligament, the moment vanishes since the plane problem contains 180° rotational symmetry around the midpoint. Then, the only forces at the midpoint are a normal force, p_x and a transverse force, p_y. The relationship between displacements of the beam end (Fig. 7) and the forces can, by the use of classic beam theory (e.g., Beer and Russell Johnston, 1992), be written as

$$\delta_x = \frac{p_x \ell}{bhE} \ \wedge \ \delta_y = 4\frac{p_y \ell^3}{bh^3 E}. \tag{10}$$

We treat p_x, p_y and ℓ as unknowns, with δ_x and δ_y prescribed. Eq. (10) provide two equations for three unknowns. The third equation for the determination of the third unknown, ℓ, is determined by the requirement that the energy release rate of the bridging mechanism equals the fracture energy of the interface, $\mathscr{G}_c$. Following the Mode I micromechanical model of Spearing and Evans (1992), we use the compliance method for this purpose. To do so, we consider the resulting force, p, and the displacement along the resulting force, δ_p. We can thus write the forces as

$$p_x = p\sin\alpha \ \wedge \ p_y = p\cos\alpha, \tag{11}$$

where α is the angle of attack of the force (see Fig. 7b). By the use of (10) and (11) we find the displacement in the direction of the force as

$$\delta_p = 4\frac{p\ell^3}{bh^3E}\cos^2\alpha + \frac{p\ell}{bhE}\sin^2\alpha. \tag{12}$$

According to the compliance method, the energy release rate is given by (Broek, 1986)

$$\mathscr{G} = \frac{p^2}{2b}\frac{\partial C}{\partial \ell}, \tag{13}$$

where C is the compliance defined as the displacement per unit force

$$C = \frac{\delta_p}{p} \tag{14}$$

and ℓ is the crack length for our mechanism. Inserting (12) into (14) and performing the differentiation gives

$$\frac{\partial C}{\partial \ell} = 12\frac{\ell^2}{bh^3E}\cos^2\alpha + \frac{\sin^2\alpha}{bhE}. \tag{15}$$

Inserting (15) into (13), while using (11), we obtain

$$\mathscr{G} = 6\frac{p_y^2\ell^2}{b^2h^3E} + \frac{p_x^2}{2b^2hE}. \tag{16}$$

Now, we express p_x and p_y by δ_x and δ_y by the use of (10), assuming $\ell > 0$. The result is

$$\mathscr{G} = \frac{3}{8}\frac{Eh^3\delta_y^2}{\ell^4} + \frac{Eh\delta_x^2}{2\ell^2}. \tag{17}$$

As the ligament peels off, the energy release rate must be identical to the fracture energy of the interface, $\mathscr{G}_c$. Setting $\mathscr{G}$ (from (17)) equal to $\mathscr{G}_c$ leads to the following equation for the determination of ℓ:

$$8\frac{\mathscr{G}_c}{Eh}\left(\frac{\ell}{h}\right)^4 - 3\left(\frac{\delta_y}{h}\right)^2 - 4\left(\frac{\delta_x}{h}\right)^2\left(\frac{\ell}{h}\right)^2 = 0. \tag{18}$$

Eq. (18) can be considered being a second order equation in $(\ell/h)^2$. The only physically admissible solution ($(\ell/h)^2 > 0$) is

$$\left(\frac{\ell}{h}\right)^2 = \left[\frac{4\mathscr{G}_c}{Eh}\right]^{-1}\left\{\left(\frac{\delta_x}{h}\right)^2 + \sqrt{\left(\frac{\delta_x}{h}\right)^4 + 6\frac{\mathscr{G}_c}{Eh}\left(\frac{\delta_y}{h}\right)^2}\right\}. \tag{19}$$

Eq. (19) is the third equation that – together with the two equations given by (10) – are required for the determination of the three unknowns, σ_n, σ_t and ℓ. Given δ_x and δ_y, we can determine ℓ/h from (19), so that we can calculate the bridging forces from (10).

Using the number of bridging ligaments per unit cracked area, η, Eqs. (9), (10) and (19) we obtain the bridging stresses as

$$\frac{\sigma_n}{\eta bhE} = \frac{\frac{\delta_n}{h}\left[\frac{\mathscr{G}_c}{Eh}\right]^{3/2}}{\left[\left(\frac{\delta_t}{2h}\right)^2 + \sqrt{\left(\frac{\delta_t}{2h}\right)^4 + 6\frac{\mathscr{G}_c}{Eh}\left(\frac{\delta_n}{2h}\right)^2}\right]^{3/2}} \tag{20a}$$

and

$$\frac{\sigma_t}{\eta bhE} = \frac{\frac{\delta_t}{h}\left[\frac{\mathscr{G}_c}{Eh}\right]^{1/2}}{\left[\left(\frac{\delta_t}{2h}\right)^2 + \sqrt{\left(\frac{\delta_t}{2h}\right)^4 + 6\frac{\mathscr{G}_c}{Eh}\left(\frac{\delta_n}{2h}\right)^2}\right]^{1/2}}. \tag{20b}$$

Note that both bridging stresses, σ_n and σ_t, depend on both δ_n and δ_t. Thus, according to our model, the mechanism of cross-over bridging does not result in decoupled bridging laws; it is a coupled mechanism.

For pure Mode I opening ($\delta_t = 0$), Eq. (20a) reduces to

$$\sigma_n = \frac{1}{4}\left[\frac{8}{3}\frac{\mathscr{G}_c}{Eh}\right]^{3/4}\sqrt{\frac{2h}{\delta_n}}\eta bhE \ \wedge \ \sigma_t = 0, \tag{21}$$

i.e., σ_n is inversely proportional to the square root of the normal opening. This result is consistent with the earlier analysis of the pure Mode I fibre cross-over bridging problem when shear deformation is neglected (Spearing and Evans, 1992; Sørensen and Jacobsen, 1998).

Another special case is pure Mode II ($\delta_n = 0$). Then (20b) becomes

$$\sigma_t = \left[\frac{2\mathscr{G}_c}{Eh}\right]^{1/2}\eta bhE \ \wedge \ \sigma_n = 0. \tag{22}$$

Note, that (22) predicts that the shear stress under pure Mode II is constant, independent of the magnitude of the tangential displacement.

3.3. The existence of a potential function

In modelling, bridging laws and cohesive laws are frequently taken to be derived from a potential function (Tvergaard and Hutchinson, 1994). Then, as will be elaborated later, the fracture resistance due to bridging stresses does not depend on the opening path history. It is therefore of interest to investigate whether the bridging stresses of the mixed mode cross-over bridging mechanism can be derived from a potential function, viz.,

$$\sigma_n = \frac{\partial\Phi}{\partial\delta_n} \ \wedge \ \sigma_t = \frac{\partial\Phi}{\partial\delta_t}, \tag{23}$$

where $\Phi(\delta_n, \delta_t)$ is the potential function and $\Phi(0,0) = 0$. A potential function exists if (Creighton Buck, 1978), for a simply connected domain in the δ_n–δ_t plane

$$\frac{\partial\sigma_n}{\partial\delta_t} = \frac{\partial\sigma_t}{\partial\delta_n}. \tag{24}$$

From (8), we have $\partial\sigma_n/\partial\delta_t = \partial\sigma_n/2\partial\delta_x$ and $\partial\sigma_t/\partial\delta_n = \partial\sigma_t/2\partial\delta_y$. Then from (20a), we obtain

$$\frac{\partial\sigma_n}{\partial\delta_t} = -3\frac{\eta b\mathscr{G}_c^{3/2}}{E^{1/2}h^{3/2}} \times \frac{\left(\frac{\delta_t}{2h}\right)^3\left(\frac{\delta_n}{2h}\right)\left\{\left(\frac{\delta_t}{2h}\right)^{-2} + \left[\left(\frac{\delta_t}{2h}\right)^4 + 6\frac{\mathscr{G}_c}{Eh}\left(\frac{\delta_n}{2h}\right)^2\right]^{-1/2}\right\}}{\left\{\left(\frac{\delta_t}{2h}\right)^2 + \sqrt{\left(\frac{\delta_t}{2h}\right)^4 + 6\frac{\mathscr{G}_c}{Eh}\left(\frac{\delta_n}{2h}\right)^2}\right\}^{5/2}} \tag{25}$$

while (20b) gives

$$\frac{\partial\sigma_t}{\partial\delta_n}=-3\frac{\eta b\mathscr{G}_c^{3/2}}{E^{1/2}h^{3/2}}\frac{\left(\frac{\delta_t}{2h}\right)\left(\frac{\delta_n}{2h}\right)\left[\left(\frac{\delta_t}{2h}\right)^4+6\frac{\mathscr{G}_c}{Eh}\left(\frac{\delta_n}{2h}\right)^2\right]^{-1/2}}{\left\{\left(\frac{\delta_t}{2h}\right)^2+\sqrt{\left(\frac{\delta_t}{2h}\right)^4+6\frac{\mathscr{G}_c}{Eh}\left(\frac{\delta_n}{2h}\right)^2}\right\}^{3/2}}. \tag{26}$$

It can be shown that (25) is identical to (26). Then, (24) is fulfilled. We have thus proven that for a simply connected domain a potential function exists for the bridging stresses in Eq. (20). Now, we proceed to find the potential function.

We utilise the fact that the potential function is independent of the integration path. We can therefore select the integration path that we find most convenient. We choose to determine the potential function by integrating along the solid lines shown in Fig. 8,

$$\Phi(\delta_n,\delta_t)=\int_0^{\delta_t}\sigma_t\left(\delta_n=0,\tilde{\delta}_t\right)d\tilde{\delta}_t+\int_0^{\delta_n}\sigma_n\left(\tilde{\delta}_n,\delta_t\right)d\tilde{\delta}_n \tag{27}$$

where $\tilde{\delta}_n$ and $\tilde{\delta}_t$ are integration variables.

Inserting σ_n and σ_t from (20) into (27) and performing the integrations leads to the following equation for the potential function

$$\frac{\Phi(\delta_n,\delta_t)}{\eta bh^2E}=\frac{4}{3}\sqrt{\frac{\mathscr{G}_c}{Eh}}\left\{\left[\left(\frac{\delta_t}{2h}\right)^2+\sqrt{\left(\frac{\delta_t}{2h}\right)^4+6\frac{\mathscr{G}_c}{Eh}\left(\frac{\delta_n}{2h}\right)^2}\right]^{1/2}+\frac{\left(\frac{\delta_t}{2h}\right)^2}{\left[\left(\frac{\delta_t}{2h}\right)^2+\sqrt{\left(\frac{\delta_t}{2h}\right)^4+6\frac{\mathscr{G}_c}{Eh}\left(\frac{\delta_n}{2h}\right)^2}\right]^{1/2}}\right\}. \tag{28}$$

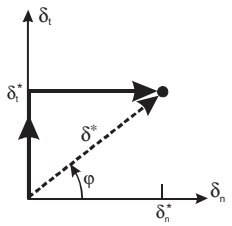

Fig. 8. Integration path for obtaining the potential function (solid line). Magnitude and phase angle of opening are also indicated (dashed line).

It can be verified that partial differentiation of the potential function (28) according to (23) indeed gives σ_n and σ_t (Eq. (20)).

3.4. Model results

Fig. 9 shows the predicted bridging stresses, σ_n and σ_t (both normalised) as a function of the normalised openings, $\delta_n/2h$ and $\delta_t/2h$ with $\mathscr{G}_c/Eh=10^{-4}$ (other values of $\mathscr{G}_c/Eh$ give quantitatively different, but qualitatively similar results). It is seen in Fig. 9 that σ_n decreases rapidly (from a singular value at $\delta_n=\delta_t=0$), towards zero with increasing δ_n and δ_t. In contrast, σ_t increases rapidly, approaching the bridging stress under pure Mode II, given by (22).

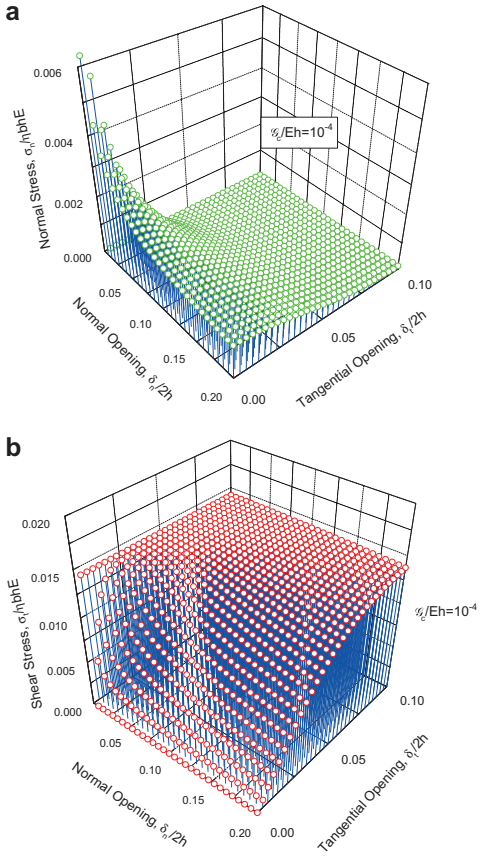

Fig. 9. The predicted bridging stresses (normalised) as a function of the normalised crack opening displacements; (a) the normal stress σ_n, and (b) the shear stress σ_t.

Except for values of $\delta_t/2h$ smaller than approximately 0.1, σ_n is significantly smaller than σ_t.

Using δ_n^0 and δ_t^0 as (arbitrary) upper bounds for δ_n andδ_t, respectively, the domain defined by $\{(0 \leqslant \delta_n \leqslant \delta_n^0 \wedge 0 \leqslant \delta_t \leqslant \delta_t^0) \setminus (0;0)\}$ is simply connected so the potential function Φ is valid within the domain. Fig. 10 shows a plot of Φ as a function of δ_n and δ_t for a part of this domain. For pure Mode I opening ($\delta_t = 0$), Φ is proportional to $\sqrt{\delta_n}$. For pure Mode II opening ($\delta_n = 0$), Φ increases linearly with δ_t. This follows from integration of (21) and (22). The mixed mode solution is a smooth transition between the two pure modes. Except for very small openings, the potential function attains a higher value under dominating Mode II ($\delta_n < \delta_t$) than under dominating Mode I ($\delta_n > \delta_t$).

The potential function depends on the two fracture parameters, η and $\mathscr{G}_c$. From (28) it is clear that Φ depends linearly on η. However, the *shape* of the Φ-surface does not depend on η; it depends only on $\mathscr{G}_c$.

When the bridging stresses are derived from the potential function according to (23), it follows from (2) that the fracture resistance (i.e., the value of the J integral when cracking takes place) can be obtained as

$$J_R = \Phi(\delta_n^*, \delta_t^*) + J_0, \tag{29}$$

where J_0 is the fracture energy of the main crack tip. Eq. (29) reads that the fracture resistance comprises the energy dissipation of the bridging zone and the fracture energy of the main crack tip. The energy dissipation of the bridging zone is simply the potential function evaluated at the end-opening, δ_n^*, and the end-sliding, δ_t^*, of the bridging zone, see Fig. 1a.

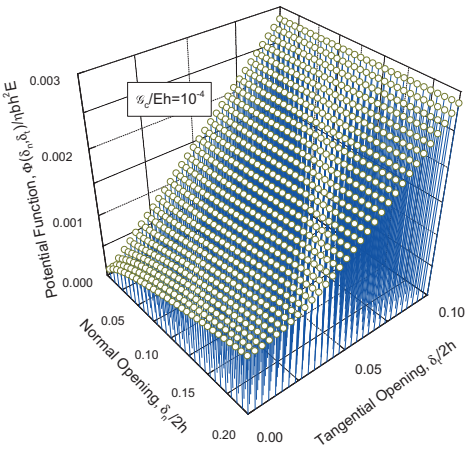

Fig. 10. The predicted potential function (normalised) as a function of the normalised crack opening displacements.

Combining (28) and (29) we can simulate the fracture resistance for the cross-over bridging mechanism. First, define the magnitude of the end-opening, δ^* as (shown as a dashed line in Fig. 8)

$$\delta^* = \sqrt{\delta_n^{*2} + \delta_t^{*2}} \tag{30}$$

and the phase angle of the end-openings as

$$\varphi = \tan^{-1}\left(\frac{\delta_t^*}{\delta_n^*}\right). \tag{31}$$

Then, $\varphi = 0°$ corresponds to pure normal opening (Mode I) and $\varphi = 90°$ corresponds to pure tangential opening (Mode II).

Predicted fracture resistance, calculated from the potential function according to (29), is shown in Fig. 11. Here, $J_0 = 0$ and φ is taken to be constant for each curve. As mentioned, for $\varphi = 0°$, the fracture resistance increases as $\sqrt{\delta^*}$ in agreement with earlier findings (Sørensen and Jacobsen, 1998). For higher values of φ, Φ increases almost linearly with δ^*. For a fixed value of δ^*, a higher value of φ gives a higher normalised Φ. The pure Mode II normalised Φ is several times that of pure Mode I. Thus, under the assumption of constant η and constant h, the cross-over bridging mechanism is a much more effective toughening mechanism under Mode II than under Mode I.

4. Discussion

4.1. Consequences of the existence of a potential function for the bridging stresses

The fact that the bridging stresses are derived from a potential function has two important consequences. Eq. (29) shows that the energy dissipation of the bridging zone is determined directly from the end-opening and end-sliding. More precisely, the energy dissipation within the bridging zone depends only on the *actual* end-opening and end-sliding and *not* on the opening path *history*. In contrast, if the bridging stresses were not derived from a potential function, the energy dissipation within the bridging zone can only be calculated by recording the stress-opening history for each point within the bridging zone and perform the integration, corresponding to Eq. (2), numerically (van den Bosch et al., 2006).

Furthermore, the fact that the energy dissipation within the bridging zone depends only on δ_n^* and δ_t^*

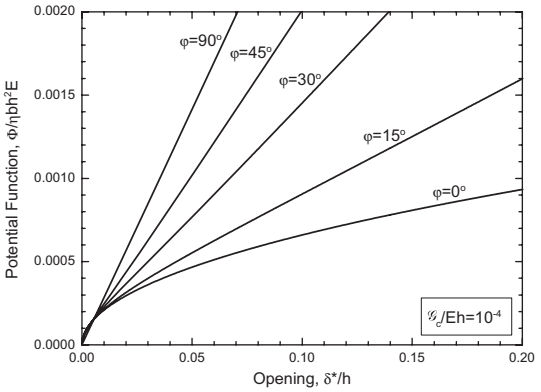

Fig. 11. Predicted mixed mode fracture resistance data. The potential function (normalised) is shown as a function of normalised magnitude of opening for various phase angles.

has implications for models made by the finite element method. In the finite element method the displacements are determined as the primary variables. Therefore, displacements are computed with a better accuracy than, e.g. stresses and strains that are obtained from displacement gradients. It is therefore anticipated that the energy dissipation within the bridging zone can be computed rather accurately by the use of fairly coarse meshes.

4.2. Criterion for fibre failure

Failure of bridging ligaments and bridging fibres is often observed experimentally. Obviously, breakage of the bridging ligaments precludes the full utilisation of the cross-over bridging mechanism. It is therefore relevant to investigate the conditions under which ligaments fail.

Fibres often fail just at the point where they peel off (Kaute et al., 1993; Shercliff et al., 1994), see also Fig. 5b. Assume that all the fibres possess the same tensile strength, σ_{fu} (a more advanced model could incorporate fibre strength variation and scale effects, e.g. by the use of the Weibull function (Weibull, 1939)). A criterion for the occurrence of fibre failure at the point where the ligament peels off can be made by the use of beam theory. The criterion can be stated as follows: failure is assumed to happen when the maximum tensile stress exceeds the fibre strength,

$$6\frac{p_y\ell}{bh^2}+\frac{p_x}{bh}\geqslant\sigma_{fu}. \tag{32}$$

Inserting p_x and p_y from (10) into (32) leads to the following criterion for failure of the ligament

$$\frac{3}{2}\left(\frac{\delta_n}{2h}\right)\left(\frac{h}{\ell}\right)^2+\left(\frac{\delta_t}{2h}\right)\left(\frac{h}{\ell}\right)\geqslant\frac{\sigma_{fu}}{E}, \tag{33}$$

where ℓ/h is given by (19) while δ_n and δ_t are known. It follows from (19), with all other parameters fixed, a higher value of $\mathscr{G}_c$ leads to a lower value of ℓ, which increases the left hand side of (33). For a sufficiently high $\mathscr{G}_c$, the left hand side will be larger than the right hand side of (33). Then, fibre failures are predicted, and fibre bridging is reduced or hindered.

Further insight can be gained by considering the pure Mode I and pure Mode II crack opening histories, since (33) simplify significantly under these conditions. Under pure Mode I ($\delta_t=0$), (19) reduces to

$$\left(\frac{\ell}{h}\right)^2=\sqrt{\frac{3}{8}\frac{Eh}{\mathscr{G}_c}}\left(\frac{\delta_n}{2h}\right). \tag{34}$$

Inserting (34) into (33) leads to the following criterion for fibre failure

$$\frac{\mathscr{G}_cE}{\sigma_{fu}^2h}\geqslant\frac{1}{6}. \tag{35}$$

The left hand side can be regarded as being a non-dimensional fracture parameter. The role of the interface fracture energy, $\mathscr{G}_c$, can be understood as follows. Starting from a sufficiently small value of $\mathscr{G}_c$, the cracking parameter will be lower than the right hand side of (35), so that the fibre failure criterion is not fulfilled. An increase in $\mathscr{G}_c$ increases the cracking parameter. For a sufficiently high $\mathscr{G}_c$, the cracking parameter exceed the right hand side of

(35). Then, fibre fracture is predicted. Note also the effect of the ligament thickness, h. With all other parameter fixed, a smaller value of h results in a higher value of the cracking parameter. Thus, thinner ligaments (e.g. single fibre ligaments) are anticipated to fail at a lower interface fracture energy value than thicker ligaments. For pure Mode II ($\delta_n = 0$), (19) simply becomes

$$\frac{\ell}{h} = \sqrt{\frac{Eh}{2\mathscr{G}_c}}\left(\frac{\delta_t}{2h}\right). \tag{36}$$

Inserting (36) into (33) gives an equation identical to (35), except that the right hand side, the critical value of the non-dimensional parameter, is three times higher for Mode II than for Mode I. Consequently, with all other parameters fixed, the criterion for fibre breakage will be fulfilled at a lower value of $\mathscr{G}_c$ for Mode I crack opening than for pure Mode II.

4.3. Considerations for maximizing fracture resistance of composites

Consider the interplay between the toughening from cross-over bridging and the energy dissipation at the tip of the main crack. As mentioned, if the interface bonding is very strong, the stress in the fibres about to bridge can exceed the fibre strength. Then, fibres fail instead of forming crack bridging. When no fibre bridging develops, the only contribution to toughness comes from the crack tip. On the other hand, if the interface bonding is very weak, a lot of fibre bridging may develop. But the bridging stresses will be very low, since the fibres peel off very easily. Then, the resulting toughening will be low. If fibre bridging is completely absent, the only energy dissipation within the fracture process zone will be the fracture energy of the crack tip, J_0.

The tip of the main crack is likely to propagate along a fibre/matrix interface just as the crack tips of the bridging ligaments. When mode mixity effects are neglected, J_0 must be equal to $\mathscr{G}_c$, the fracture energy of the interface. This reasoning suggests that an optimum interface fracture energy exists, which allows fibre bridging with the highest possible stresses without causing significant fibre failure, leading to maximum toughening.

4.4. Comments regarding the model assumptions

The present model is planar, so that the only way to distinguish between single fibre bridging and ligament bridging is through the parameter $\mathscr{G}_c/Eh$; a ligament consisting of several fibres has a larger h than a single fibre. In reality, however, there is also a geometrical difference. Ligaments are expected to possess approximately rectangular cross-sections, while fibres have a circular cross-section. This is not accounted for in the model.

The present model predicts the fracture resistance under the assumption of a constant ligament density, η. However, the number of bridging ligaments (per unit area) loaded in tension may differ from the number of bridging ligaments loaded in compression. Moreover, the ratio between the numbers of the two types of ligaments may vary as a function of the ratio between the tangential and normal crack opening displacements.

In the present model, the fracture resistance is predicted using a constant ligament height, h. In reality h may be a distribution, ranging from single fibres to thicker multi-fibre ligaments. A more refined model could account for the variation in the height of ligaments. This is under investigation in another study (Østergaard and Sørensen, in preparation).

In practice, the deflection of a bridging ligament can be larger than the ligament thickness h, so that the problem becomes a large displacement problem. Our model does not account for large displacements and large rotations. However, since the model predicts that σ_t approaches the Mode II value for $\delta_t/2h \approx 0.1$, i.e., within the range of small displacements, it is anticipated that this prediction may also be approximately correct under large displacements. On the other hand, the beam model neglects shear deformation, which may be of importance for very small values of ℓ/h. Nevertheless, being based on classic beam theory, our model is expected to be accurate at intermediate crack opening displacements where the majority of the energy dissipation occurs.

Another issue related to large displacements is that large deflections of a bridging ligament result in a shortening (Bisshopp and Drucker, 1945). Thus, under prescribed displacements, a large deflection will induce a tensile stress in the ligament. This stress is not predicted by the present model. A more detailed analysis is required to estimate how large this effect can be.

As mentioned, the model is built upon the assumption that the ligaments peel off at a constant (mode independent) fracture energy, $\mathscr{G}_c$. An approximate analysis (Appendix B) shows that the change

in the mode mixity for ligament bridging is less than 15°, which typically only results in a change of a few percentages in the macroscopic fracture energy of interfaces for moderate mode mixities, $|\psi| < 60°$, (Cao and Evans, 1989; Wang and Suo, 1990; Liechti and Chai, 1992).

Another assumption is the use of fracture energy as the criterion for the propagation of the cracks. Fracture energy is a linear elastic fracture mechanics concept. In reality, the fracture process zone at the interface may not be sufficiently small to justify the application of linear elasticity. A more advanced analysis could model the interface fracture process zone by a cohesive zone.

Finally, a cautious note. Under the assumption made in the present paper, the bridging laws were opening path-independent and could thus be derived from a potential function. However, this finding may not hold true for more realistic, advanced models accounting for ligament splitting and failure, plasticity, etc.

5. Conclusions

A micromechanical model of mixed mode fibre cross-over bridging predicts coupled mixed mode bridging laws; both normal and shear stresses depend on the normal and tangential crack opening displacements. The normal stress decreases rapidly towards zero with increasing normal and tangential crack opening displacements. In contrast, the shear stress increases with increasing normal and tangential crack opening displacements, approaching a constant value, corresponding to the shear stress under a pure Mode II crack opening displacement. The toughening due to the cross-over bridging mechanisms is predicted to be much higher under Mode II and mixed mode than under pure Mode I.

Acknowledgements

The practical design of the mixed mode test fixture was made by Mr. Preben Engbæk, following useful input from Dr. Andy Horsewell. This research was supported by the STVF Frame Work Programme "Interface Design of Composite Materials", Grant No. 26-03-0160. We wish to thank an unknown referee for useful and insightful comments.

Appendix A

The test fixture consists of parts that are made of non-magnetic materials (e.g. austenitic stainless steel) in order to reduce the disturbance of the magnetic lenses in the ESEM. The fixture consists of parts that are mounted at the x–y–z table of the microscope. The specimen and fixture can thus be moved so that a fairly large area (≈ 50 mm by 50 mm) can be viewed. The opening rate of the fixture is controlled by the operator through the microscope's software.

A sketch of the fixture is shown in Fig. A.1. Transverse arms are bonded to the ends of the beams of the DCB-specimen (1) [numbers in parenthesis refer to Fig. A.1]. One of the transverse arms (2) is held fixed (3); it carries the specimen. The other arm (4) is loaded by a force acting in the x_1-direction, through a loading arm (5). The loading arm (5) and the transverse arm (4) are in contact via a V-notch (6). The loading arm is connected to a sledge (7), which is mounted by a screw (8) at a transverse bar (9). The transverse bar (9) is held at its ends by two 0.2 mm thin steel blades springs (10) that are mounted at a fixation plate (11) that can move (by a motor) in the x_1-direction. The loading arm (5) is equipped with four strain gauges (12), which are connected as a Wheatstone Bridge and used as load cell. The steel blades (10) enable the

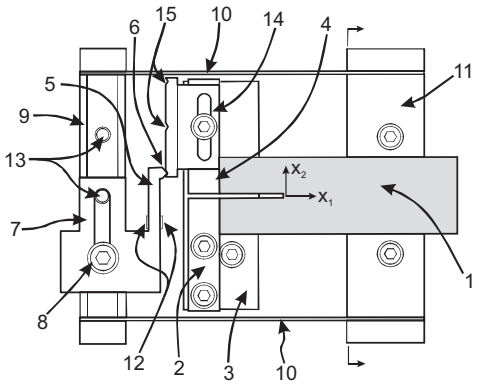

Fig. A.1. Schematics drawing of the loading fixture for the ESEM. (1) test specimen, (2) transverse arm, (3) stationary basis of fixture, (4) free transverse arm, (5) loading arm, (6) tip of loading arm, (7) adjustable sledge, (8) fixation screw, (9) transverse bar, (10) blade springs, (11) moveable basis of fixture, (12) strain gauges, (13) additional fixation thread holes, (14) adjustable part of the transverse arm, (15) additional V-notches.

load cell and the transverse bar (9) to flex such that it follows the deflection of the specimen in the x_2-direction without inducing a significant force in the x_2-direction (the compliance of the fixture towards sideways displacement (i.e. in the x_2-direction) was estimated to 2.5 mm/N). The moment arm D is changed by adjusting the sledge (7) in the x_2-direction – using fixation point (8) or one of the two additional fixation points (13) and moving the adjustable part of the transverse arm (14), using the V-notch (6) or one of the two other V-notches (15). The maximum allowable force is 250 N.

Appendix B

In this Appendix, we estimate the mode mixity of a ligament being peeled off. We utilize a solution given by Suo and Hutchinson (1990). Their problem consists of asymmetric bimaterial specimens loaded with an axial force and a bending moment (the same loading as in Fig. 2). Our problem consists of an axial force, p_x, and a transverse force, p_y. The latter creates a bending moment at the crack tip. We consider two cases. In the first case, the ligament length, 2ℓ, is very small. In the second case, ℓ is large. When ℓ is small, then, according to our model, $p_x \ll p_y$, so that the moment is the dominating crack tip loading. When ℓ is large, our model predicts $p_x \gg p_y$, i.e., the axial force dominates.

Now, we apply the solution given by Suo and Hutchinson (1990). When the moment dominates the crack tip loading (short ℓ) we obtain (assuming $h \ll H$ and assuming the same elastic properties of the ligament as that of the thick part)

$$\psi = \tan^{-1}\left(\frac{1}{\tan\omega}\right), \tag{B.1}$$

where ω is a phase angle tabulated by Suo and Hutchinson (1990). For large ℓ, we simply have

$$\psi = \omega. \tag{B.2}$$

From Table 1 in Suo and Hutchinson (1990) we obtain $\omega = 52.1°$. Then, by (B.1) and (B.2) we find $\psi = 37.9°$ for short ℓ, and $\psi = 52.1°$ for large ℓ.

References

Albertsen, H., Ivens, J., Peters, P., Wevers, M., Verpost, I., 1995. Interlaminar fracture toughness of CFRP influenced by fibre surface treatment: part 1. Experimental results. Compos. Sci. Technol. 54, 133–145.

Bao, G., Suo, Z., 1992. Remarks on crack-bridging concepts. Appl. Mech. Rev. 45, 355–361.

Beer, F.P., Russell Johnston Jr., E., 1992. Mechanics of Materials, second ed. McGraw-Hill, London and New York, pp. 478–489.

Bradley, W.L., 1989. Relationship of matrix toughness to interlaminar fracture toughness. In: Friedrich, K. (Ed.), Application of Fracture Mechanics to Composite Materials. Elsevier Science Publishers, pp. 159–187.

Broek, D., 1986. Elementary Engineering Fracture Mechanics, fourth ed. Mertinus Nijhoff Publishers, Dordrecht and Boston.

Bisshopp, K.E., Drucker, D.C., 1945. Large deflection of cantilever beams. Quart. Appl. Math. 3, 272–275.

Cao, H.C., Evans, A.G., 1989. An experimental study of the fracture resistance of bimaterial interfaces. Mech. Mater. 7, 295–304.

Creighton Buck, R., 1978. Advanced Calculus, third ed. McGraw-Hill, Tokyo, p. 504.

Deve, H.E., Maloney, M.J., 1991. On the toughening of intermetallics with ductile fibers: role of interfaces. Acta Metall. Mater. 39, 2275–2284.

Foote, R.M.L., Mai, Y.-W., Cotterell, B., 1986. Crack growth resistance curves in strain-softening materials. J. Mech. Phys. Solids 34, 593–607.

Hashemi, S., Kinloch, A.J., Williams, J.G., 1990. The analysis of interlaminar fracture in unidirectional fibre–polymer composites. Proc. R. Soc. Lond. A 427, 173–190.

Hutchinson, J.W., Jensen, H.M., 1990. Models of fiber debonding and pullout in brittle composites with friction. Mech. Mater. 9, 139–163.

Ivens, J., Albertsen, H., Weavers, M., Verpost, I., Peters, P., 1995. Interlaminar fracture toughness of CFRP influenced by fibre surface treatment: Part 2. Modelling of the interface effect. Compos. Sci. Technol. 54, 147–159.

Jacobsen, T.K., Sørensen, B.F., 2001. Mode I Intra-laminar crack growth in composites – modelling of R-curves from measured bridging laws. Composites Part A 32, 1–11.

Kaute, D.A.W., Shercliff, H.R., Ashby, M.F., 1993. Delamination, fibre bridging and toughness of ceramic matrix composites. Acta Metal. Mater. 41, 1959–1970.

Kardomateas, G.A., Carlson, R.L., 1996. A micromechanical model for the fiber bridging of macrocracks in composite plates. J. Appl. Mech. 63, 225–233.

Li, V.C., Ward, R.J., 1989. A novel testing technique for post-peak tensile behaviour of cementitious materials. In: Mihashi, H., Takahashi, H., Wittmann, F.H. (Eds.), Fracture Toughness and Fracture Energy – Testing Methods for Concrete and Rocks. A.A. Balkema Publishers, Rotterdam, pp. 183–195.

Liechti, K.M., Chai, Y.-S., 1992. Asymmetric shielding in interfacial fracture under in-plane shear. J. Appl. Mech. 59, 295–304.

Marshall, D.B., Cox, B.N., Evans, A.G., 1985. The mechanics of matrix cracking in brittle-matrix fiber composite. Acta Metall. 33, 2013–2021.

McCartney, L.N., 1987. Mechanics of matrix cracking in brittle-matrix fiber-reinforced composites. Proc. R. Soc. Lond. A 409, 329–350.

Østergaard, R.C., Sørensen, B.F. Prediction of composite scale cohesive laws for delamination with fiber bridging, manuscript in preparation.

Østergaard, R.C., Tvergaard, V., Sørensen, B.F. Prediction of mixed mode cohesive law for fiber bridging, manuscript in preparation.

Rice, J.R., 1968. A path independent integral and the approximate analysis of strain concentrations by notches and cracks. J. Appl. Mech. 35, 379–386.

Shercliff, H.R., Vekinis, G., Beaumont, P.W.R., 1994. Direct observation of the fracture of CAS-glass/SiC composites, part I delamination. J. Mater. Sci. 29, 3643–3652.

Sørensen, B.F., Jacobsen, T.K., 1998. Large scale bridging in composites: *R*-curve and bridging laws. Composites Part A 29, 1443–1451.

Sørensen, B.F., Jacobsen, T.K., 2000. Crack growth in composites: applicability of *R*-curves and bridging laws. Plastic Rubber Compos., Process. Appl. 29, 119–133.

Sørensen, B.F., Jacobsen, T.K., 2003. Determination of cohesive laws by the *J* integral approach. Eng. Fract. Mech. 70, 1841–1858.

Sørensen, B.F., Kirkegaard, P., 2006. Determination of mixed mode cohesive laws. Eng. Fract. Mech. 73, 2642–2661.

Spearing, S.M., Evans, A.G., 1992. The role of fiber bridging in the delamination resistance of fiber-reinforced composites. Acta Metall. Mater. 40, 2191–2199.

Suo, Z., Bao, G., Fan, B., 1992. Delamination *R*-curve phenomena due to damage. J. Mech. Phys. Solids. 40, 1–16.

Suo, Z., 1990. Delamination specimens for orthotropic materials. J. Appl. Mech. 57, 627–634.

Suo, Z., Hutchinson, J.W., 1990. Interface crack between two elastic layers. Int. J. Fract. 43, 1–18.

Thouless, M.D., Evans, A.G., 1988. Effects of pull-out on the mechanical properties of ceramic–matrix composites. Acta Metall. 36, 517–522.

Tvergaard, V., Hutchinson, J.W., 1994. Toughness of an interface along a thin ductile layer joining elastic solids. Philos. Mag. A 70, 641–656.

van den Bosch, M.J., Schreurs, P.J.G., Geers, M.G.D., 2006. An improved description of the exponential Xu and Needleman cohesive zone law for mixed-mode decohesion. Eng. Fract. Mech. 73, 1220–1234.

Wang, J.S., Suo, Z., 1990. Experimental determination of interfacial toughness curves using brazil-nut-sandwiches. Acta Metall. Mater. 38, 1279–1290.

Weibull, W., 1939. A statistical theory of the strength of materials. Ingeniörsvetenskapsakademiens Handlingar 151, Generalstabens Litografiska Anstalts Förlag, Stockholm.

Zok, F., Hom, C.L., 1990. Large scale bridging in brittle matrix composites. Acta Metall. Mater. 38, 1890–1895.

[A6]

Sørensen, B. F., Horsewell, A., Jørgensen, O., Kumar, A. N., and Engbæk, P., 1998

"Fracture resistance measurement method for in-situ observation of crack mechanisms"

Journal of the American Ceramic Society, Vol. 81, pp. 661-9

journal

J. Am. Ceram. Soc., **81** [3] 661–69 (1998)

Fracture Resistance Measurement Method for *in situ* Observation of Crack Mechanisms

Bent F. Sørensen, Andy Horsewell, Ole Jørgensen, and Amar N. Kumar†

Materials Research Department, Risø National Laboratory, DK-4000 Roskilde, Denmark

Preben Engbæk

Engbæk Consulting, Gevninge, DK-4000 Roskilde, Denmark

A special test fixture has been developed for fracture mechanical testing of brittle materials inside an environmental scanning electron microscope. The fixture loads a double cantilever beam specimen with pure bending moments and provides stable crack growth. Crack growth is detected by *in situ* observation and acoustic emission. As an example, crack growth in a cubic-phase yttria-stabilized zirconia is detected easily by *in situ* observation of the crack-tip region. Many fracture toughness measurements are obtained for each specimen, giving high confidence in the measured fracture toughness value. *In situ* observation is useful for the study of toughening mechanisms and subcritical crack-growth behavior and to sort out erroneous measurements (e.g., due to crack branching).

I. Introduction

MANY newly developed materials that are designed for high-temperature applications or electronic devices possess a low crack-growth resistance. This can impede the use of these materials, because components may fail as a result of thermal or mechanical loads. It is necessary to measure the crack-growth resistance of these materials to be able to use fracture mechanics design methods. *Stable* crack growth is necessary to get reliable and unambiguous fracture toughness data. If the fracture toughness values are determined from test configurations that do not allow stable crack growth, then the measurement may be related more to *crack initiation* than *crack growth*. In such cases, the calculated value of the fracture toughness may depend on the geometry of the machined notch.[1] Such problems are bypassed in the testing of metallic materials, where a sharp crack can be created by cyclic loading prior to fracture mechanical testing. This is not feasible for ceramics. Instead, it is advantageous to use test specimens that allow stable crack growth (see Sakai and Bradt[2] for a recent overview of fracture mechanics test methods).

An important issue in the development of new materials is to understand the relationship between microstructural mechanisms and the resulting crack-growth resistance. A detailed understanding of microstructural toughening mechanisms is a prerequisite for the development of micromechanical models. Such models then can be used for microstructural optimization. However, a detailed understanding of how the microstructural toughening mechanisms work requires *simultaneous* crack-growth resistance measurements and microstructural observations.

There are few studies in the literature on *in situ* observations of crack-tip regions in brittle materials.[3–6] The group in Cambridge[4] has developed test facilities in a scanning electron microscope (SEM) for *in situ* observation of fracture mechanisms in ceramics and ceramic composites. A double-cantilever-beam (DCB) specimen loaded with twisting moments (sometimes called the double torsion specimen) has been used for studies of stable crack growth in long-grained alumina.[5] However, for that test configuration, the crack front is curved and the propagation at the top surface differs from that at the bottom,[7] so that the measured *R*-curve behavior represents a nonuniform toughening along the crack front. Rödel *et al.*[4] have used a circular-shaped Mode I specimen with a chevron-notched crack for studying crack-wake bridging in alumina ceramics. Crack growth without the chevron notch is unstable in nature for that test configuration. Liechti and Chai[8] have developed a technique for measuring interfacial fracture energy of a bilayer specimen held between rigid translating grips. That technique requires that the displacements of the rigid grips be controlled accurately. However, when transparent materials (glass and epoxy) are used, the crack-opening displacement can be measured accurately by optical interferometry. The energy release rate, $\mathcal{G}$, decreases with crack length for the double-cleavage-drilled compression specimen.[9] Thus, this specimen allows stable crack growth, but the crack length must be recorded to calculate $\mathcal{G}$. This may be inconvenient, especially for some fracture mechanisms, where no clear crack front exists, such as void formation in ductile interlayers.[10]

In this paper, we describe a fracture mechanics technique that allows *in situ* observations during the measurement of crack-growth resistance. The proposed method is to load a DCB specimen with pure bending moments. This technique has proved to be capable of generating stable crack growth in essentially brittle materials, such that crack growth rates can be measured under various environments.[11] The method also has been used for measuring *R*-curve behavior of transformation-toughened ceramics.[12] The current design is a compact development of an earlier fixture designed for a standard test machine.[12] Sohn *et al.*[13] have developed another design for loading a DCB specimen by pure moments inside an SEM. The bending moments in that arrangement are applied by four-point bending of beams bonded perpendicular to the ends of the beams of the DCB. However, in that setup, the external beams slide over fixed supports (unlike the original, but more space demanding, wire arrangement proposed by Freiman *et al.*[11]) as the DCB opens. Therefore, that technique is sensitive to loading-point friction. A transverse force, of the magnitude of the friction coefficient times the contact force, may be present between the beams and the supports.

M. Thouless—contributing editor

Manuscript No. 191269. Received January 21, 1997; approved June 26, 1997.

Supported in part by the Engineering Science Centre (at Risø) for Structural Characterization and Modeling of Materials and in part by the Energy Research Program of the Danish Ministry of Energy.

†On leave from Indian Institute of Technology, New Delhi 110016, India.

The controlled crack growth in the new method presented here is performed inside the vacuum chamber of an environmental scanning electron microscope (ESEM). This allows *in situ* observation of crack-propagation mechanisms. The ESEM offers several advantages in comparison with conventional SEMs. The specimens in conventional SEMs must be coated by gold or carbon to be conductive. The coating layer may peel off as cracking occurs and new crack faces charge up. This is unfortunate, because it makes it difficult to perform accurate observations of, e.g., details of the crack-tip process zone, and it limits the resolution of measurements of the crack-opening displacement. Such problems do not occur in the ESEM, which does not require specimens to be coated, because water vapor in the poor vacuum ionizes and prevents charging. Moreover, the ESEM is not sensitive to contamination. Therefore, it is not required that the operator wear gloves during handling of the test specimen or the fixture.

The material studied in this paper is a fully-stabilized cubic-phase yttria-stabilized zirconia (YSZ). This material is under consideration for use in solid-oxide fuel cells because of its electrochemical properties.[14] Unlike partially-stabilized (tetragonal-phase) zirconia ceramics, the cubic-phase zirconia exhibits no transformation toughening, and the fracture energy is therefore independent of crack length. The fracture energy of cubic-phase zirconia has been evaluated as ~10–20 J/m^2 by other techniques.[15] Therefore, this material may be an excellent material to test with this new method.

II. Fracture Mechanics Considerations

If the decrease in the potential energy (per unit width of the specimen) during an incremental crack growth of the system is denoted by $\mathcal{G}$ (the energy release rate), the Griffith criterion for crack growth can be formulated as follows: crack growth takes place when the decrease in the potential energy during an incremental crack growth equals or exceeds the energy consumed in the fracture process; i.e., $\mathcal{G} \geq \mathcal{R}$, where $\mathcal{R}$ is the crack-growth resistance. Crack growth is stable if $d\mathcal{G}/da < d\mathcal{R}/da$ (where a is the crack length) and is unstable if $d\mathcal{G}/da > d\mathcal{R}/da$.

The DCB specimen consists of two beams, each with thickness H and width B. Each beam end is loaded with a bending moment M (Fig. 1). Crack growth takes place in the midplane between the beams, such that the crack growth is in pure Mode I. The plane strain energy release rate can be determined by taking the J-integral[16] along the boundaries of the specimen, giving

$$\mathcal{G} = 12(1-\nu^2)\frac{M^2}{EB^2H^3} \tag{1}$$

where E and ν are Young's modulus and Poisson's ratio, respectively. The specimen is a steady-state specimen, implying that, under a fixed moment, $\mathcal{G}$ is independent of the crack length a. Therefore, when $\mathcal{G}$ is calculated, it is not necessary to know a if M is recorded. $\mathcal{G}$ also can be expressed by the end-rotation θ as

$$\mathcal{G} = \frac{1-\nu^2}{12}\frac{EH^3}{a^2}\theta^2 \tag{2}$$

Fig. 1. Schematic showing a DCB specimen loaded with pure bending moments.

It follows from Eq. (2) that, if the test is performed in rotation control, then

$$\frac{d\mathcal{G}}{da} = \left.\frac{\partial \mathcal{G}}{\partial a}\right|_{\theta\ \text{constant}} = -\frac{1-\nu^2}{6}\frac{EH^3}{a^3}\theta^2 < 0 \tag{3}$$

such that crack growth is stable, even in materials with constant fracture toughness: $d\mathcal{R}/da = 0$. This is the prime advantage of the DCB loaded with pure moments.

III. Design of Test Method

(1) Principle of Loading

In our design, the bending moments are created by a thin steel band that runs through specially designed grips in such a manner that the steel band loads the grips by two tensile forces of identical magnitude. This creates pure bending moments. The moments are transferred onto the beams of the DCB specimens by brads (separated by the distance l) that load the beams by compressive forces. If the friction from the ball bearings of the rollers is neglected, then the force in the steel band has the same magnitude everywhere, and it follows that each beam is loaded with a pure moment:

$$M = P(2R + d) \tag{4}$$

where P is the applied tensile force, R the radius of the rollers, and d the horizontal distance between the centers of the rollers (Fig. 2). Note that M does not depend on the distance between the brads (l), unlike the local contact forces at the brads. Load-point friction can be minimized by a proper choice of l (see Appendix A). Care has been taken to minimize other error sources, as discussed in Appendix A.

(2) Instrumentation

Figure 3 shows the entire fixture, made entirely of nonmagnetic materials. The base part is mounted during use on an x–y–z stage at a door of the vacuum chamber of the ESEM (Model E3, ElectroScan Corp., Wilmington, MA). The base consists of a gear device that is designed such that the base opens symmetrically. This is utilized in the fixture; when the DCB specimen opens, the crack plane does not move out of the picture field. The base is driven by a motor. The speed of the base fixture is controlled through the software of the microscope. The speed can be set between 1 and 100 μm/s, corresponding to a rotation rate $d\theta/dt$ (where t is the time) of ~5×10^{-4} to 5×10^{-2} deg/s. The grips lie on platforms that are bolted to the base fixture. The steel band is fixed at both ends of the platforms. The applied load, P, is measured by two strain gauges (Type CEA-06-125UN-125, Measurements Group, Raleigh, NC) bonded onto a beam at one of the ends, and a self-temperature-compensation half-bridge Wheatstone bridge strain recorder (Type P-3500, Measurements Group) is used.

The load reading was calibrated using calibration weights (TM-M, Instron Corp., Danvers, MA). An accuracy of ±0.05 N (corresponding to ±2 μm at the strain indicator) was obtained for the load reading. This was equivalent to an accuracy of ±0.004 N·m in the moment.

Teflon tapes can be bonded onto the brads of the grips and the specimen (or adaptor) to minimize loading-point friction. The opening displacement, δ, of the fixture is measured by a linear-variable differential transducer (LVDT) (Type UCA 5C, H. F. Jensen, DK) (see Fig. 2). M is plotted versus δ; crack growth results in a nonlinear curve. The effect of the forces from the LVDT is analyzed in Appendix A. Finally, crack growth can be detected by acoustic emission (AE); an AE transducer (Model U80-220, Physical Acoustic Corp. (PAC), Princeton, NJ) is fixed to the uncracked end of the DCB specimen, and AE signals are collected (Model Spartan AT, PAC) through a preamplifier (Model 1220A, PAC). The number of AE events is shown as a function of time at a monitor. A sketch of the experimental setup is shown in Fig. 4.

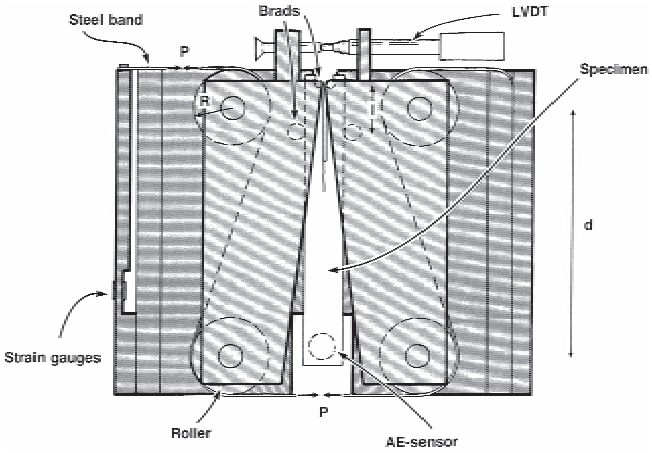

Fig. 2. Schematic showing how DCB specimens are loaded with pure bending moments by utilizing a steel band and rollers.

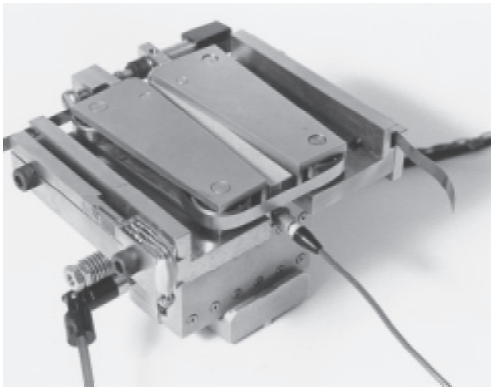

Fig. 3. Photograph of the fracture mechanics fixture.

(3) Specimen Design

Two specimen designs have been used (Fig. 5). One design (Fig. 5(a)) has notches machined for the brads of the grips. Because machining is difficult or expensive for some materials, another design has been developed (Fig. 5(b)). A 45° cut is made to the beam ends, and two special steel adapters are bonded to the beam ends. Although the adapters are designed for a specific beam thickness (currently adapters exist for specimen thickness of 3 or 7 mm), they also can be used for thicker specimens. The crack should be only slightly longer than the adaptors. A stress analysis by the finite-element method[12] has shown that the distance from the crack tip to the points of attack of the compressive forces can be less than the beam thickness, H, without changing $\mathcal{G}$ from the value given by Eq. (1).

A side groove must be introduced to guide the direction of the crack for specimens of isotropic and homogeneous materials, which do not possess a weak crack plane. Grooves can be made in both sides of the specimen to ensure symmetrical deformation. If the moment of the onset of crack growth is recorded, the plane strain energy release rate for a specimen with side grooves can be calculated from[11]

$$\mathcal{G} = 12(1-\nu^2)\frac{M^2}{EBbH^3} \tag{5}$$

where b is the remaining ligament of side-grooved specimens (i.e., the beam width, B, minus the side-groove depth). Equation (5) accounts for the fact that the changes in strain energy occur over the full width B, whereas fracture energy is consumed only over the width b. Other effects of side grooving can be neglected if the groove is thin.[17]

(4) Experimental Procedure

The loading is performed by a constant displacement speed of the base fixture. This results in an approximately constant rotation rate of the beam ends of the DCB specimen. Initially, the relationship between M and δ during loading and unloading is measured to assess the magnitude of friction, as proposed by Charalambides *et al.*[18] (see also Appendix B). If the hysteresis is significant, the friction should be reduced, e.g., by solid lubrication. When the frictional effects are small, the measurement of crack-growth resistance can proceed. The specimen is loaded slowly until crack growth occurs. As soon as crack growth has been detected (by the nonlinear moment-opening curve, by AE events, or by *in situ* observation of the crack-tip region at the ESEM monitor), the movement of the base fixture is stopped, leading to crack-growth arrest. The new crack length is measured, either using the internal coordinates of the x–y–z stage or measuring micrographs. Because the crack arrests under rotation control, the specimen can be examined in detail before unloading or reloading is continued. For viscoelastic materials or materials prone to stress corrosion cracking, it may be necessary to unload the specimen somewhat to avoid time-dependent cracking.

IV. Example of Test

(1) Material and Specimen Preparation

The material tested in this paper was a cubic-phase YSZ (8 mol% yttria) processed by isostatic pressing. The specimens were sintered at 1600°C for 2 h. This resulted in a dense microstructure with a grain size of ~10 μm. Young's modulus, E, was measured to be 200 GPa, and the Poisson's ration, ν, was ~0.3.[19] Specimens with a 45° cut at the beam ends (Fig. 5(b)) were machined using diamond tools. The specimens were ~65 mm in length, H = 10 mm in thickness, and B = 5 mm in

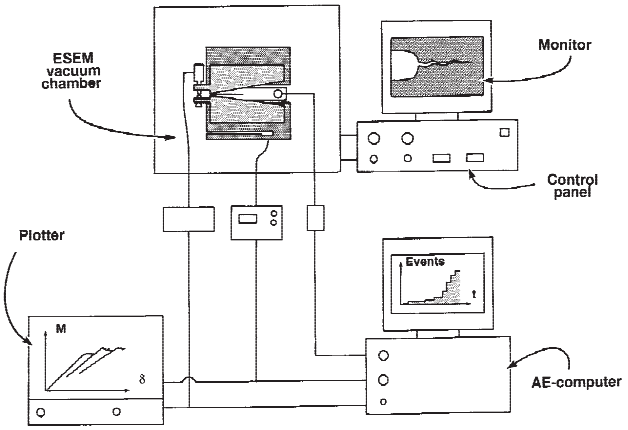

Fig. 4. Principle of the experimental setup for fracture mechanics testing inside the ESEM.

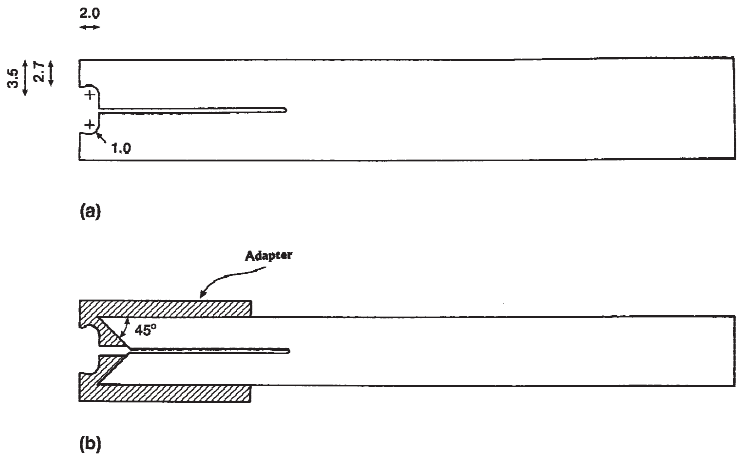

Fig. 5. Geometry of DCB specimens: (a) specimen where the loading-point notch is made directly in the test specimen and (b) specimen where adaptors are used to minimize specimen machining.

width. A single side groove (thickness of 1 mm, and $b/B \approx 0.5$) was machined. The other face was polished (down to 4 μm diamond paste) to make crack-tip observations easier.

(2) Initiation of a Sharp Crack

The particular tests described here were conducted at a water vapor pressure of 2.5 torr (330 Pa) and the rotation rate ($d\theta/dt$) was 3.8×10^{-3} deg/s. The M–δ curve was particularly useful for the detection of crack initiation from the machined notch, because crack-growth resulted in a nonlinear relationship. Visual observation of the notch was not particularly useful for the detection of crack initiation, because the entire notch region could not be observed at the same time (a clear view of a crack requires a magnification of about 1500×), and it was not known a priori at which location a crack would initiate. As with other fracture mechanics test methods for ceramics, initiation of a sharp crack from the machined notch could cause problems; a higher load sometimes was required for *initiation* than for subsequent *propagation*. A stiff adhesive tape was wrapped around the specimen ~5 mm away from the notch to avoid complete fracture of the test specimen. This imposed a constraint in a zone ahead of the notch. When the crack initiated, it grew unstably into the constraint zone, where it was arrested. Then the specimen was unloaded, the tape was removed, and the specimen was ready for fracture toughness measurement.

(3) Detection of Growth of a Sharp Crack

Typical M–δ curves, recorded during crack growth, are shown in Fig. 6. Crack growth resulted in nonlinearity during loading, although it was sometimes undetectably small. The nonlinearity during unloading was attributed to friction or to stable crack growth during unloading. Once a crack had initiated, it could be seen easily at the ESEM monitor. Sometimes crack growth was detected by AE, sometimes not. Visual observation of the crack-tip region (magnification of ~1500× and a scan speed of 1 Hz, using partial field mode) was the best

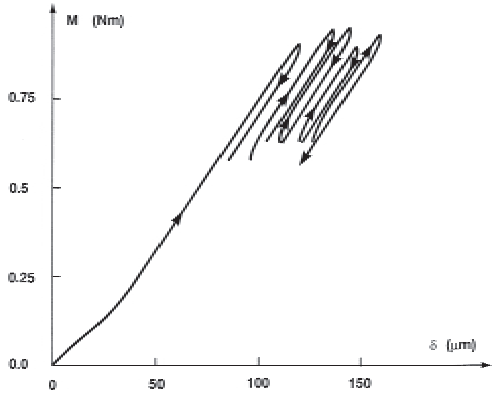

Fig. 6. Typical measured moment–opening displacement curves. Small crack growth causes only a slight nonlinearity during loading. Nonlinearity during unloading is attributed to friction. (Offsets between unloading and reloading are artificial.)

means of determining crack growth. Crack propagation could be controlled in such a manner that the crack growth was small, typically 30–50 μm per increment. Therefore, many (in the order of a hundred) measurements could be made on each specimen.

(4) In situ Observations

In most cases, the crack propagated as a single Mode I crack. However, on a few occasions, the crack branched into two. When the load was increased, one of the cracks continued to grow, while the other did not, and eventually closed again (Fig. 7); it was difficult to see the crack thereafter. When there were two competing cracks, a higher value of the overall $\mathcal{G}$ was necessary to initiate further crack growth. Thus, *in situ* observation was a useful tool to evaluate which fracture mechanics measurements were valid and which were invalid.

Figure 8 shows micrographs of a crack-tip region. Note that, although the crack is a straight Mode I crack in a macroscopic sense, the crack path may have some amount of Mode II at the scale of the grains. The crack deviates ~1 μm from a straight line over a distance of 100 μm. This deviation is smaller than the grain size. This is consistent with the observation that the crack path is dominantly through the grains. At a few locations (less than every tenth grain), the crack grows along the grain boundary, as shown in Fig. 9. In this situation, a thin grain has peeled off and flipped over during the crack growth.

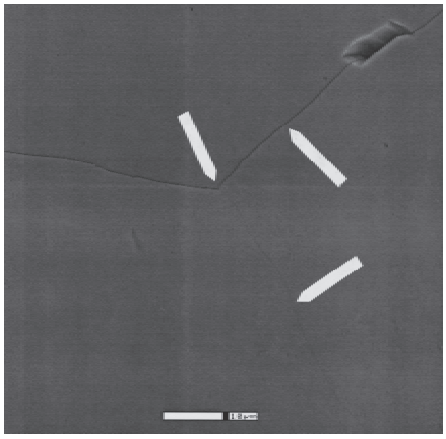

Fig. 7. Example of crack branching. Crack (originally grown from the left) has branched into two cracks. Angles between the cracks are ~120°. Upper crack has continued to grow and turns into a Mode I crack. Lower crack eventually closes and is barely visible.

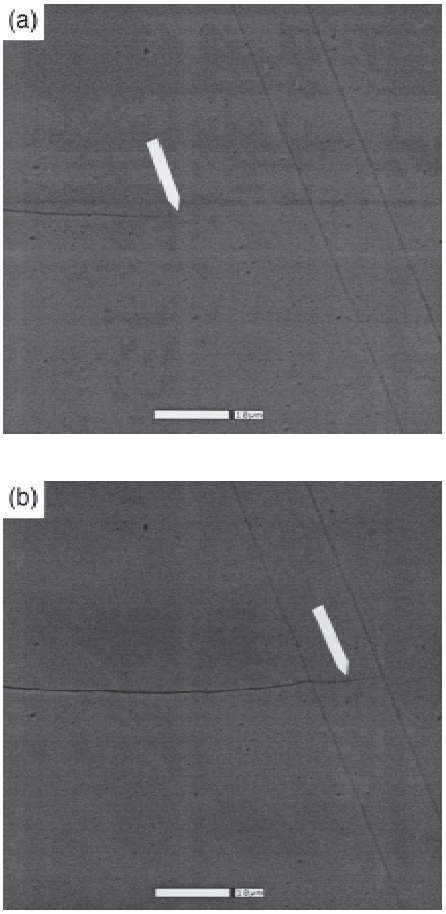

Fig. 8. (a) Example of crack-tip region. Crack path is fairly straight, going through the grains (grain structure is not visible). (b) Crack has been grown and arrested after ~30 μm of growth.

(5) Crack-Opening Profile

The near-tip crack-opening displacement is measured from micrographs taken of the surface of the specimen at a magnification of 10 000×. The accuracy of the measurements from the micrographs corresponds to only a few nanometers. However, because it is difficult to focus accurately at such a high magnification, it is estimated that the error on the measurements is ~30 nm. The measured crack-opening profile is plotted in Fig. 10, with the theoretical crack-opening profile predicted by linear elastic fracture mechanics. The relationship between $\mathcal{G}$ and the near-tip crack-opening displacement, Δu_2, at

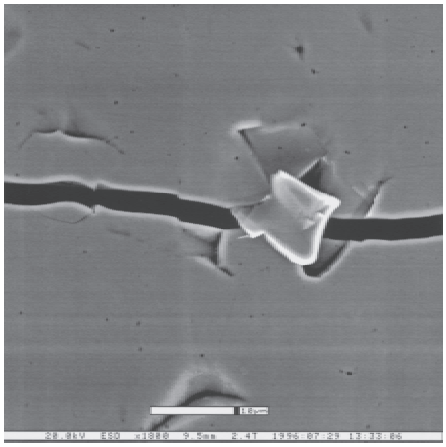

Fig. 9. Micrograph showing a thin grain that has peeled off during crack propagation.

a distance, r, from the crack tip is (for a pure Mode I crack under plane strain conditions[20])

$$\Delta u_2(r) = 4\left(\frac{2(1-\nu^2)\,\mathcal{G}\,r}{\pi E}\right)^{1/2} \tag{6}$$

At the specimen surface, where the crack opening is measured, the stress state is plane stress. However, the overall deformation, including the crack-opening displacement, is likely to be dominated by the plane strain conditions. Figure 10 shows that, for $r < 200$ μm, the difference between the experimental data and the theoretical predictions is smaller than the error bars. The experimental data lie slightly below the theoretical prediction for larger values of r. It is most likely that this difference is due to the fact that Eq. (6) is valid only in the vicinity of the crack tip. Indeed, a finite-element analysis of DCB specimens[21] indicates that the region near the crack tip, where the stress field differs <10% from the asymptotic crack tip solution (the K-field), is ~3% of the beam thickness, H. This corresponds to 300 μm for the present specimens.

(6) Measured Crack-Growth Resistance in YSZ

In situ observations of the crack-tip region allowed detailed investigation of crack growth of very sharp cracks. Some interesting features were identified. Once crack growth had initiated, the crack grew with a constant velocity if $\mathcal{G}$ was constant. If $\mathcal{G}$ was increased while the crack was growing, the crack growth velocity increased. If $\mathcal{G}$ was decreased, the speed of crack growth decreased. Thus, we could define three distinct values of $\mathcal{G}$ as being relevant for the crack growth, i.e., the crack-growth resistance corresponding to the onset of crack growth ($\mathcal{G}_i$), fast fracture ($\mathcal{G}_f$), and crack arrest ($\mathcal{G}_a$). Similar phenomena have been observed in ceramics subjected to stress corrosion cracking in aggressive environments.[11,22] More details will be given in a future publication.[23]

The value of $\mathcal{G}$ at the onset of crack growth ($\mathcal{G}_i$) was measured to be ~4 J/m^2. Results were very consistent within each specimen, but some variation was found from specimen to specimen. $\mathcal{G}_a$ was found to be 3 J/m^2, whereas $\mathcal{G}_f$ was found to be ~6–10 J/m^2. The measured values of $\mathcal{G}_f$ were slightly lower than fracture toughness values reported for cubic-phase zirconia using other test techniques.[15]

We believe that other methods, where fracture toughness is determined by the peak load of a test configuration with no stable crack growth, may overestimate the fracture toughness values, because the load for crack initiation may be higher than for crack propagation.

V. Discussion

(1) Importance of in situ Observations

It is recognized that determining the onset of crack growth by visual inspection is a subjective criterion that may differ from person to person. Furthermore, the detection of crack growth depends on magnification and scan speed of the microscope picture. However, we believe that visual observation of the crack-tip area allows us to determine the onset of crack growth earlier than by other means. Thus, the present method is expected to give a smaller scatter in the measured values of $\mathcal{G}_i$.

In materials where micromechanical toughening phenomena occur in connection with crack growth, *in situ* observation of the crack-path selection is a very direct way of relating any changes in the measured overall crack-growth resistance to a specific microstructural feature. Such a direct relationship between microstructural cause and overall effect on the crack-growth resistance is a requisite for the development of mechanism-based toughening models.

(2) Advantages and Disadvantages of the New Technique

In summary, the advantages of the present technique are as follows:

(i) Stable crack growth is attained when the experiment is conducted under rotation control. Therefore, it is not necessary to perform the test in a servo-hydraulic test machine controlled by the signal from a clip gauge measuring the crack opening. The method thus can be used for characterizing R-curve behavior.

(ii) The crack growth resistance can be measured from a truly sharp crack.

(iii) The energy release rate for this steady-state specimen can be calculated from the moment alone, independent of the crack length, such that the crack-growth resistance can be measured with high confidence and accuracy.

(iv) The nature and mechanisms of crack growth can be observed and directly related to the measured crack-growth resistance. In particular, features such as the onset and arrest of crack growth can be studied in detail under a high magnification.

The disadvantages of the present technique are as follows:

(i) The specimen size is larger than many other test specimens for fracture mechanics testing of ceramics, such that specimens may be difficult to process.

(ii) A special test fixture is required.

(iii) In comparison with conventional fracture mechanics testing, the technique is more time consuming because of the setup of fixture and startup of the ESEM. This may be balanced by the fact that many fracture mechanics measurements can be obtained from each specimen, such that the actual amount of time and material used per measurement are quite small.

(3) Implications of $\mathcal{G}_i$, $\mathcal{G}_f$, and $\mathcal{G}_a$ in YSZ

The fact that, for YSZ, the values of $\mathcal{G}_i$, $\mathcal{G}_f$, and $\mathcal{G}_a$ are different implies that it is not possible to assign a single fracture toughness value to YSZ. This may have implications for the interpretation of the fracture energy values obtained by other methods. For instance, for the single-edge notched-beam (SENB) test, the calculation of the fracture energy may be overestimated,[1] because the fracture toughness is determined by the onset of crack growth from a machined notch, which may be a crack *initiation* problem, rather than a crack *propagation* problem. If the crack growth really does start from a truly sharp crack (and this is difficult to validate in the SENB test), it is likely that the recorded value of fracture energy is $\mathcal{G}_i$. We base this assumption on the fact that the crack growth, once

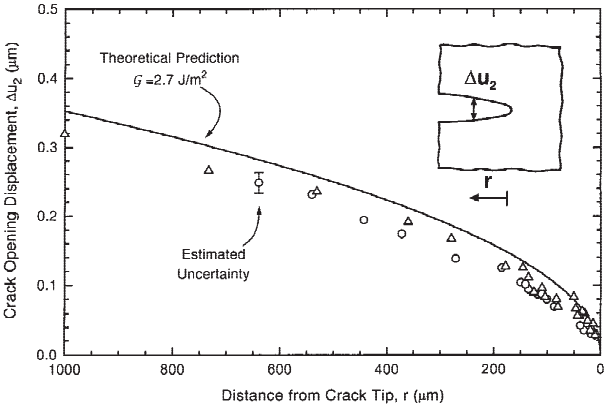

Fig. 10. Near-tip crack-opening displacement as measured from micrograph and theoretical crack-opening profile from linear elastic fracture mechanics. Different symbols refer to measurements obtained at different crack-tip positions. $\mathcal{G}$ is similar for the two data sets.

it has started, is unstable for that test configuration. In the chevron-notched beam test, valid fracture toughness values are determined by the maximum applied load, which corresponds to a transition from slow to fast crack growth. Thus, this method is likely to give a value of the fast-fracture crack-growth resistance, $\mathcal{G}_f$.

The finding that the values of $\mathcal{G}_i$, $\mathcal{G}_f$, and $\mathcal{G}_a$ are different also may be very important for design purposes. Clearly, $\mathcal{G} < \mathcal{G}_f$ is not a fail-safe design criterion. A conservative design criterion is to design components so $\mathcal{G} < \mathcal{G}_a$ (rather than $\mathcal{G} < \mathcal{G}_f$). This ensures that no subcritical crack growth occurs under normal loading conditions, even though an accidental overloading ($\mathcal{G}_i < \mathcal{G} < \mathcal{G}_f$) might initiate crack growth. It also underlines the importance for the development of test methods that are capable of measuring whether $\mathcal{G}_i$, $\mathcal{G}_f$, and $\mathcal{G}_a$ differ from each other, such as in the method presented here.

VI. Summary

A fracture mechanics test facility (a double-cantilever specimen loaded with pure bending moments) has been developed for *in situ* studies inside an environmental scanning electron microscope. The energy release rate for this loading configuration is independent of crack length, such that the crack-growth resistance is calculated from the applied moment alone. Moreover, for this steady-state specimen, the crack-growth resistance is determined from the growth of a truly sharp crack tip, because the crack growth is stable. Many measurements can be obtained for the same specimen. *In situ* observations enable changes in the crack-growth resistance to be related directly to microstructural mechanisms.

APPENDIX A

Sources of possible error are considered in this appendix. Using the simple models summarized here, we designed the fixture such that the contribution of each error source was negligibly small.

(1) Loading-Point Friction

Assume that Coulombic friction exists between the specimen (or adapter) and the grips. Then the frictional force at the loading point is

$$\mathcal{F} = \mu \frac{M}{l} \tag{A–1}$$

where M is the applied moment, given by Eq. (3), μ the friction coefficient between grips and specimen (or adapter), and l the horizontal distance between the loading points (see Fig. A1). The frictional force creates a bending moment $\tilde{M}$ in the beam, which can be written as

$$\frac{\tilde{M}}{M} = 1 - \mu \frac{h}{l} \tag{A–2}$$

where h is the vertical distance between the loading points. It is thus important to minimize h/l. For the current design, h = 2.5 mm and l = 12 mm. Assuming μ = 0.3 (estimated to be an upper bound for realistic values) gives $\tilde{M}$ as 6% less than M.

(2) Friction between Grips and Base

As a ''worse case'' situation, the frictional forces $\mathcal{F}^*$ between the grips and base plane are assumed to act as far away from each other as possible, as indicated in Fig. A2. In this case

$$\mathcal{F}^* = \mu \frac{mg}{2} \tag{A–3}$$

where μ is now the friction coefficient between grips and base, m the mass of one grip plus half the weight of the test specimen and half the weight of the LVDT, and g the gravity acceleration (9.82 m/s^2). In this case, the moment M^* in the specimen arm is

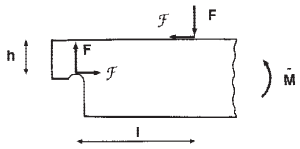

Fig. A1. Friction from loading points.

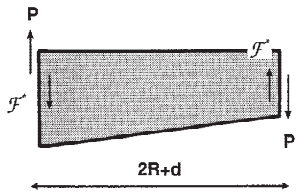

Fig. A2. Friction between grips and base plate.

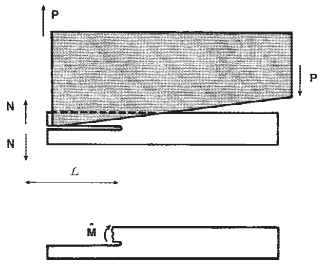

Fig. A3. Effects of force from the LVDT.

$$\frac{M^*}{M} = 1 - \mu \frac{mg}{2P} \tag{A–4}$$

where P is the force in the steel band. For instance, $\mu = 0.3$, $P = 6$ N, and $m = 0.2$ kg (the mass of one grip is 0.13 kg) gives M^* as 5% less than M.

(3) Effect of Force from LVDT

The force from the LVDT transducer (N) may increase the bending moment $\hat{M}$ at the position of the crack tip (see Fig. A3) as

$$\frac{\hat{M}}{M} = 1 + \frac{N}{P}\frac{L}{2R + d} \tag{A–5}$$

where L is the distance from the LVDT transducer to the crack tip. The value of N for the current LVDT transducer is 0.8–1.3 N (the largest value exists when the LVDT is fully compressed). For instance, assuming $P = 10$ N, $2R + d = 80$ mm, and $L = 50$ mm gives $\hat{M}$ as ~8% more than M. The error increases as the crack length increases. Also, the error is larger for lower values of P.

(4) Effects of Twisting of the Beam Arms

If the forces F do not act exactly at the front-to-rear midplane of the beams, they induce a torsion moment $M_t = Fs$, where s is the distance between the forces (see Fig. A4). The associated energy release rate due to torsion is[2,5] (plane strain)

$$\mathcal{G}_t = 6\,(1 + \nu)\,\frac{F^2 s^2}{B^2 H^3 E}\,\frac{1}{\xi} \tag{A–6}$$

where ξ is a dimensionless function of the thickness-to-width ratio of the beams. Thus,

$$\frac{\mathcal{G}_t}{\mathcal{G}} = \frac{1}{2\,(1 - \nu)}\,\frac{s^2}{l^2}\,\frac{1}{\xi} \tag{A–7}$$

Inserting $s = B$ (worse case) gives $\mathcal{G}_t/\mathcal{G} = 0.18$ (with $\xi = 0.69$ for $H/B = 2.0$). Therefore, to minimize the effect of twisting, the top faces of the adaptors have been rounded to ensure that the forces act at the midplane ($s \approx 0$).

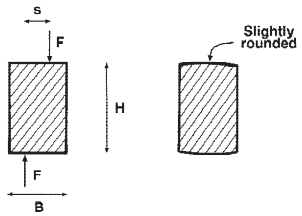

Fig. A4. Forces off the midplane may induce twisting of the beams.

APPENDIX B

This appendix describes some simple experiments that were undertaken for the assessment of frictional effects.

(1) Friction from the Rollers

The steel band was led from the load cell beam, through a single grip and fixed at the other end of the base fixture. The steel band was not tightened. The load reading was set to zero. The grip then was pulled in the direction away from the load cell beam. Frictional forces at the rollers induced a force in the steel band. This force, P, was measured by the load cell. The frictional moment (M_r) due to friction at the rollers was calculated per grip as

$$M_r = PR \tag{B–1}$$

This gave $M_r < 10^{-4}$ N·m.

(2) Friction between Grips and Base

The moment M^* induced by friction between the grips and base was estimated from an experiment where no specimen was inserted into the fixture. As the base opened, the fixed steel-band caused the grips to rotate. By measuring the force at the load cell, we calculated M^* from the recorded load, using Eq. (4). This gave $M^* \approx 0.02$ N·m.

Another estimate of the friction between grips and base is obtained from the hysteresis in the M–δ curves. Hysteresis recorded during loading and unloading in cases that no damage, plasticity or crack growth occurs can be attributed to friction. We can assume that the friction creates a moment counteraction to the rotation of the grips. The frictional forces change direction during the initial stages of loading and unloading. This is likely to be the reason for the nonlinear parts of the M–δ curves after load reversal. Once the friction has changed direction completely, the frictional moments become constant, such that the M–δ response becomes linear. Thus, the true moment at the beam during loading is the applied moment, M_L, minus the frictional moment, M^*, (where the subscript L indicates loading). The true moment at the beam during unloading, where the direction of the frictional forces is reversed, is $M_U + M^*$ (where the subscript U indicates unloading). When the openings (δ) during loading and unloading are identical, the true moments acting at the specimen during loading and unloading must be identical (see Fig. B1). Thus, M^* can be measured from the recorded difference $\Delta M = M_L - M_U$, as

$$M^* = \frac{\Delta M}{2} \tag{B–2}$$

Based on several experiments, we have found $\Delta M \approx 0.07$ N·m, giving $M^* \approx 0.04$ N·m.

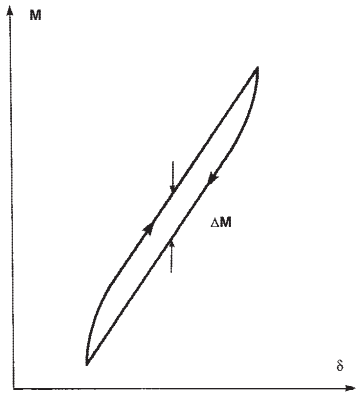

Fig. B1. Constant frictional moments result in linear moment–opening curves.

Acknowledgments: We would like to thank Kjeld Larsen for specimen preparation, Sven Aagesen for cutting the specimens, Palle V. Jensen for polishing the specimens, and Jan Larsen for help with the instrumentation. Useful discussions with Dr. Peter V. Hendriksen and Dr. Carsten Bagger are acknowledged.

References

[1]T. Nishida, Y. Hanaki, and G. Pezzotti, ''Effect of Notch-Root Radius on the Fracture Toughness of a Fine-Grained Alumina,'' *J. Am. Ceram. Soc.,* **77**, 606–608 (1990).

[2]M. Sakai and R. C. Bradt, ''Fracture Toughness of Brittle Materials,'' *Int. Mater. Rev.,* **38**, 53–78 (1993).

[3]O. Ø. Mouritsen and B. N. Karihaloo, ''A Technique for *in situ* SEM Study of the Fatigue Behaviour of Metals and Ceramics,'' *Mater. Forum,* **15**, 360–65 (1991).

[4]J. Rödel, J. M. Kelly, and B. R. Lawn, ''In situ Measurements of Bridging Crack Interfaces in the Scanning Electron Microscope,'' *J. Am. Ceram. Soc.,* **73**, 3313–18 (1990).

[5]G. Vekinis, M. F. Ashby, and P. W. R. Beaumont, ''*R*-Curve Behaviour of Al_2O_3 Ceramics,'' *Acta Metall. Mater.,* **38**, 1151–62 (1990).

[6]G. Vekinis, H. R. Shercliff, and P. W. R. Beaumont, ''Dynamic Testing of Ceramics and Ceramic Composites in the SEM,'' *Met. Mater.* (*Inst. Met.*), **7**, 279–84 (1991).

[7]P. S. Leevers, ''Crack Front Shape Effects in the Double Torsion Test,'' *J. Mater. Sci.,* **17**, 2469–80 (1982).

[8]K. M. Liechti and Y.-S. Chai, ''Biaxial Loading Experiments for Determining Interfacial Fracture Toughness,'' *J. Appl. Mech.,* **58**, 680–87 (1991).

[9]C. Janssen, ''Specimen for Fracture Mechanics Studies on Glass''; pp. 10.23–10.30 in *Proceedings of the 10th International Congress on Glass.* Ceramic Society of Japan, Tokyo, Japan, 1974.

[10]M. R. Turner, B. J. Dalgleish, M. Y. He, and A. G. Evans, ''A Fracture Resistance Measurements Method for Bimaterial Interfaces Having Large Debond Energy,'' *Acta Metall. Mater.,* **43**, 3459–65 (1995).

[11]S. W. Freiman, D. R. Mulville, and P. W. Mast, ''Crack Propagation Studies in Brittle Materials,'' *J. Mater. Sci.,* **8**, 1527–33 (1973).

[12]B. F. Sørensen, P. Brethe, and P. Skov-Hansen, ''Controlled Crack Growth in Ceramics: The DCB-Specimen Loaded with Pure Moments,'' *J. Eur. Ceram. Soc.,* **16**, 1021–25 (1996).

[13]K.-S. Sohn, S. Lee, and S. Baik, ''Analytical Modeling for Bridging Stress Function Involving Grain Size Distribution in a Polycrystalline Alumina,'' *J. Am. Ceram. Soc.,* **78**, 1401–405 (1995).

[14]C. Bagger, N. Christiansen, P. V. Hendriksen, E. J. Jensen, S. S. Larsen, and M. Mogensen, ''Techno-Economic Problems of SOFC Commercialization''; pp. 167–74 in *High-Temperature Electrochemistry: Ceramics and Metals,* Proceedings of the 17th Risø International Symposium on Materials Science. Edited by F. W. Poulsen, N. Bonanos, S. Linderoth, M. Mogensen, and B. Zarchau-Christensen. Risø National Laboratory, Roskilde, Denmark, 1996.

[15]J. D. French, H. M. Chan, M. P. Harmer, and G. A. Miller, ''High-Temperature Fracture Toughness of Duplex Microstructures,'' *J. Am. Ceram. Soc.,* **79**, 58–64 (1996).

[16]J. R. Rice, ''A Path-Independent Integral and the Approximate Analysis of Strain Concentrations by Notches and Cracks,'' *J. Appl. Mech.,* **35**, 379–86 (1968).

[17]C. C. Wu, K. R. McKinney, and D. Lewis, ''Grooving and Off-Center Crack Effects on Applied-Moment Double-Cantilever-Beam Tests,'' *J. Am. Ceram. Soc.,* **68**, C-166–C-168 (1984).

[18]P. G. Charalambides, H. C. Cao, J. Lund, and A. G. Evans, ''Development of a Test Method for Measuring the Mixed Mode Fracture Resistance of Bimaterial Interfaces,'' *Mech. Mater.,* **8**, 269–83 (1990).

[19]H. L. Toftegaard; unpublished research.

[20]G. R. Irwin, ''Analysis of Stress and Strains Near the End of a Crack Traversing a Plate,'' *J. Appl. Mech.,* **24**, 361–64 (1957).

[21]S. S. Wang, J. F. Mandell, and F. J. McGarry, ''An Analysis of the Crack Tip Stress Field in DCB Adhesive Fracture Specimens,'' *Int. J. Fract.,* **14**, 39–58 (1978).

[22]T. A. Michalske, B. C. Bunker, and S. W. Freiman, ''Stress Corrosion of Ionic and Mixed Ionic/Covalent Solids,'' *J. Am. Ceram. Soc.,* **69**, 721–24 (1983).

[23]A. N. Kumar and B. F. Sørensen, ''Fracture Resistance and Stable Crack Growth Behavior in 8 mol% YSZ Ceramics''; unpublished work. □

[A7]

Sørensen, B. F., 2002

"Cohesive law and notch sensitivity of adhesive joints"

Acta Materialia, Vol. 50, pp. 1053-61

Pergamon

Acta Materialia 50 (2002) 1053–1061

Acta MATERIALIA

www.actamat-journals.com

Cohesive law and notch sensitivity of adhesive joints

Bent F. Sørensen *

Materials Research Department, Risø National Laboratory, DK-4000 Roskilde, Denmark

Received 18 July 2001; received in revised form 18 October 2001; accepted 18 October 2001

Abstract

A large non-linear zone develops during fracture of a polyurethane adhesive bonded to steel adherends. The fracture process zone was characterised by a traction-separation law, a so-called cohesive law. The cohesive law was determined experimentally by the use of a J integral based approach on double cantilever beam sandwich specimens loaded with pure bending moments. The cohesive law shape was found to be highly non-linear. The cohesive stress increased with increasing separation, reached a peak and then decreased with increasing opening. The effects of loading rate and thickness of the adhesive layer on the cohesive law were investigated. An excellent agreement was found between measured strengths of bonded panels having a central notch and strength predictions based on cohesive law parameters.

Keywords: Bonding; Fracture & fracture toughness; Crack velocity

1. Introduction

For a number of different materials fracture involves Large Scale Bridging (LSB) [1–4]. A fracture process zone experiencing crack bridging can be modelled by a Dugdale/Barenblatt type cohesive zone, where the cohesive traction, σ, is assumed to vary along the failure process zone, but to depend only on the local opening, δ; $\sigma = \sigma(\delta)$. A critical opening, δ_c, exists, beyond which the cohesive stress vanishes [5].

An important consequence of LSB is that R-curves (fracture resistance as a function of crack extension) depend on specimen geometry [5–8] and are thus ineffective for materials characterisation [9]. Instead, the cohesive law, $\sigma(\delta)$, should be taken as the basic fracture property [9,10].

An advantage of using a cohesive law as the basic fracture property is that the shape of cohesive laws can be predicted by micromechanical models [7,11]. In theory the microstructure may be tailor-made to produce the cohesive law that optimises the strength of a specific component. However, industrial design of components with cohesive laws cannot be based solely on cohesive laws predicted by micromechanical models; cohesive laws must be determined experimentally.

For most measurement methods $\sigma(\delta)$ is determined by comparing a measured property (e.g. an R-curve [12] or a crack opening profile [13]) with predictions based on idealised cohesive laws. Two methods are particular attractive, since they yield the cohesive law fairly directly without requiring interpretation through detailed fracture mechanics

* Tel.: +45-4677-5806; fax: +45-4677-5758.
E-mail address: bent.soerensen@risoe.dk (B.F. Sørensen).

1359-6454/02/$22.00
PII: S1359-6454(01)00404-9

models. The first one is direct tension experiments [14]. The other method, which will be used in the present paper, is to derive the cohesive law from simultaneous measurements of the J integral and the end-opening of the cohesive zone [15].

We define the failure process zone to include both the volume containing the non-linear elastic deformation and the decohesion zone, in which adhesive separation occurs (see Fig. 1) (this cohesive law approach can be used irrespective of whether the failure occurs interfacially or cohesively). Therefore, in the present study, the separation δ in the cohesive law will represent the displacement across the adhesive layer (in principle the elastic deformation of the adhesive could be subtracted from δ, so that the cohesive law represents only the decohesion zone). Any non-linearity, being a frontal process zone or a crack wake bridging zone will thus be included in the cohesive law.

The problem that we study in the following is mode I crack growth in steel/adhesive sandwich specimens. The adhesive is a polyurethane elastomer, which has a failure strain of several hundred percents. Its stress–strain behaviour is highly non-linear and depends on loading rate. During fracture of the joint a large non-linear zone develops. When the thickness of the adhesive layer, h, is small in comparison with the thickness of the adherends, H, the sandwich specimens can be used as a probe for studying LSB.

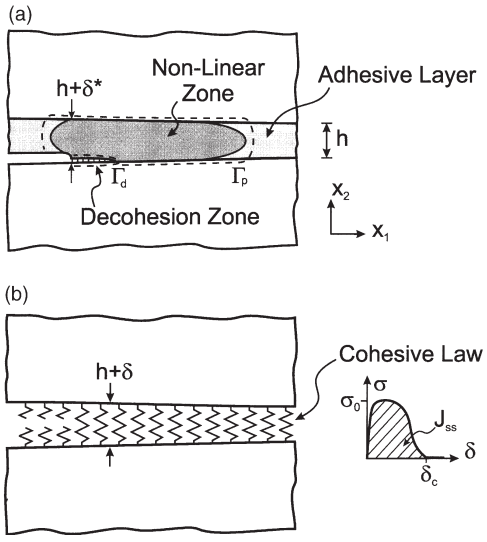

Fig. 1. (a) The failure process zone, defined by the external boundaries Γ_p, contains a non-linear elastic zone and a decohesion zone, Γ_d. (b) The entire adhesive layer is modelled by the cohesive law.

The interfacial fracture resistance of polyurethane/metal joints have been studied by blister, peel and tensile tests [16,17]. The (steady-state) fracture resistance, calculated on the basis on linear elastic fracture mechanics models, was found to increase with increasing loading rate, from about 100 J/m^2 at low loading rates to more than 1000 J/m^2 for high loading rates [17].

The concept of cohesive laws has only recently been applied to adhesive joints [18,19]. Studies include loading rate dependent cohesive laws [20, 21]. However, in all cases idealised cohesive laws were used. One of the aims of the present paper was to provide details about the *shape* of the cohesive law of adhesive joints (i.e. determining the cohesive law without presuming any idealised shape), so that future model studies can be based on realistic cohesive law shapes. The effect of loading rate and adhesive layer thickness on the cohesive law shape was investigated experimentally. The strength of panels joined by an adhesive bonding containing a central notch was predicted from the cohesive law and was subsequently determined experimentally.

2. Basic mechanics

2.1. Derivation of cohesive law

We wish to determine the cohesive law of steel/polyurethane adhesive joints. The J integral can be applied, if the bulk materials possess reversible (i.e. elastic) stress–strain behaviour [22]. Clearly, this is the case for steel adherends, which are loaded below their yield stress ($\sigma_y \approx 990$ MPa). The adhesive is an elastomer, which has a non-linear but elastic stress–strain behaviour. Thus, the application of the J integral is valid for the present

problem. Evaluating the J integral along a path Γ_p just outside the failure process zone gives [22]

$$J = \int_0^{\delta^*} \sigma(\delta)\mathrm{d}\delta \tag{1}$$

where δ^* is the end-opening of the cohesive zone. J reaches a steady-state value, J_{ss}, when δ^* attains δ_c. As Eq. (1) indicates, the entire failure process zone is described by the cohesive law (for some cohesive zone problems an additional term J_{tip} is added to the right side of the equation in order to described the energy dissipation at the front of the failure process zone, e.g. in the case of a sharp crack tip. This is, however, not necessary for the present failure mechanism, as will be discussed later). Due to its path independence, the J integral attains the same value as Eq. (1) when evaluated along the external boundaries of the specimen. This will be used below. Differentiation with respect to δ^* gives [5,15]

$$\sigma(\delta^*) = \frac{\partial J}{\partial \delta^*} \tag{2}$$

Thus, by recording J and the end-opening δ^* simultaneously the cohesive law can be obtained. In practice the data can be differentiated numerically. Alternatively, the data can be fitted by any function, and it is fairly easy to see how well the slope of the fitting curve matches the experimental data. We will use both approaches in the present study.

2.2. Measurement of J

Now we return to the point of calculating the J integral from the external loads. Test wise, we prefer to use a test configuration for which (a) the J integral can be determined directly from specimen geometry and load level, independent of the details of the cohesive law (because the cohesive law is initially unknown), (b) the J integral is independent of the crack length (this is particularly useful for the present problem, for which it is difficult to define a definite crack front), and (c) the crack growth is stable, so that the entire $\sigma(\delta)$ can be determined. One of the few test configurations that fulfil these demands is the double cantilever beam (DCB) specimen loaded with pure bending moments [5,9].

Evaluating the J integral along the external boundaries of the DCB specimen loaded by pure bending moments [Fig. 2(a)] gives (plane strain) [5]

$$J = 12(1-\nu^2)\frac{M^2}{B^2H^3E} \tag{3}$$

where M is the applied moment, E and ν are the Young's modulus and Poisson's ratio of the adherends, B and H are the width and height of the adherends, respectively (the contribution from the adhesive layer can be neglected, since the layer stiffness and thickness h are small in comparison with those of the adherends).

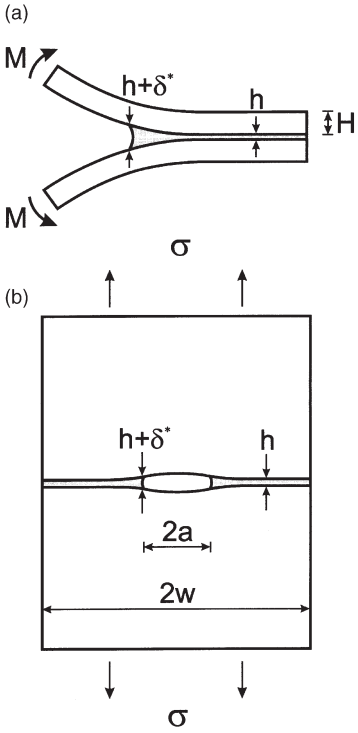

Fig. 2. Schematics of the specimens used in the present study: (a) DCB sandwich specimen loaded with pure bending moments and (b) bonded panels with a central notch.

3. Experimental procedure

3.1. Specimen preparation

Steel/polyurethane adhesive (Sikaflex 228, Sika Corporation) DCB specimens ($H = 5$ mm, $B = 10$ mm) were processed as follows. Steel adherends (Impax Supreme, Uddeholm) were machined by milling. Faces to be bonded together were subsequently plane polished. Prior to the bonding the adherends were cleaned and degreased by acetone. Teflon-coated inserts (10 mm long) of a well-defined thickness were placed at the ends of the zone to be bonded. The inserts (1.0 or 0.25 mm in thickness) ensured a uniform bond thickness. The adhesive fluid was applied between the inserts. The adherends were joined and placed in a fixture (pre-treated with a slip grease), held together by tape and pressed together by a constant pressure (~0.01 MPa). Following the manufacturers recommendation the specimens were left at least 10 days for hardening at room temperature (for the polyurethane adhesive, hardening is assisted by moisture [23]). Pins, for mounting of extensometers, were inserted into small holes drilled through the neutral axis of each beam. The pins were located at the end of the adhesive layer and served to measure the end-opening of the cohesive zone. The specimen geometry and the load introduction (pure bending moments) are shown in Fig. 3.

Steel panels (200 mm in width, 200 mm in height and 10 mm in thickness) were glued together by a butt-joint, as shown schematically in Fig. 2(b). A central notch was formed by placing an insert (1 mm thick) prior to the application of the adhesive. Inserts of different lengths were used for creating different notch sizes. The joining procedure was similar to that of the DCB specimens.

3.2. Test procedure

The pure bending moments were applied to the DCB sandwich specimens by a loading arrangement that uses wires and special grips [24]. The experiments were conducted at room temperature at a screw-driven materials testing machine (Instron TT) under constant cross head speed of 1 or 100 mm/min; each type of experiment took about 10 min and 10 s, respectively. As explained, the end-opening of the cohesive zone was recorded by the two extensometers mounted at the neutral axis of the beams. Thus, the measured value, Δu_2^*, comprises the deformation of the entire adhesive layer, δ^*, and the elastic deformation (in the x_2-direction) of half the thickness of the beams. For the present experiments the elastic deformation of the beams is so small (less than 1.5 μm) that it can be neglected [25]. Thus, the measured value, Δu_2^*, is to a very good approximation equal to the stretch of the adhesive layer, δ^*. In subsequent modelling the entire adhesive would simply be modelled by non-linear springs representing the cohesive law (see e.g. Yang et al. [19]), as indicated in Fig. 1(b). Data for elapsed time, the applied moment and

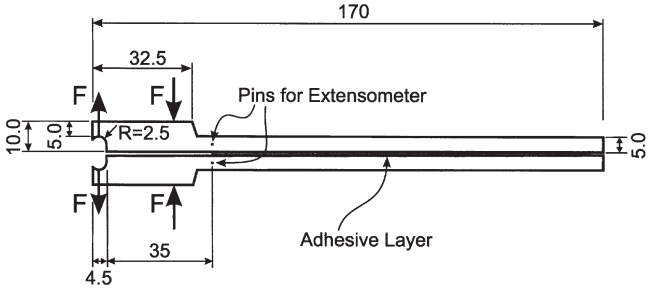

Fig. 3. Schematics showing dimensions (in mm) of the DCB-specimens as well as the applied forces, F, that create the pure bending moments.

end-opening were recorded at a frequency of 2 and 50 Hz, respectively for the two loading rates.

The bonded panels were loaded in uniaxial tension under a constant cross head velocity (0.5 mm/min). Typically, an experiment took about 3 min. The end-opening of the adhesive layer (at the central notch) was measured by the use of a clip-gauge. Data for elapsed time, applied load and end-opening were recorded (5 Hz) during the experiments.

4. Results

4.1. Failure process zone

Photographs of the failure process zone are shown in Fig. 4. Separation occurs by decohesion, i.e. along the interface rather than by cohesive failure inside the adhesive layer. The separation front appears to extend further along the specimen edges than at the centre of the specimen. It is difficult to define a clear position of the process zone front. In some cases the decohesion shifted interface after a debond length of approximately 10–30 mm (different for different specimens), creating a bridge consisting of the adhesive layer between the fracture surfaces.

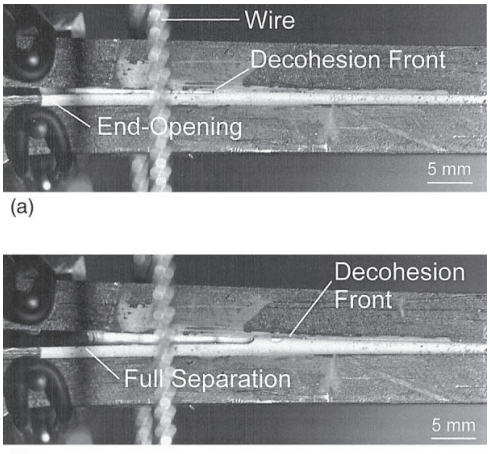

Fig. 4. Photographs of the failure process zone (h = 1 mm, loading rate: 1 mm/min). (a) δ^* = 0.75 mm, (b) δ^* = 1.5 mm. Wires are part of the loading arrangement.

4.2. J–δ^* curves

Fig. 5 shows measured J–δ^* curves for the two different loading rates and for two different adhesive layer thicknesses. J increases with increasing δ^*, reaching a steady-state value, J_{ss} (note that the separation corresponding to steady-state is in the order of mm's, i.e. not an order of magnitude smaller than H, confirming that the failure is indeed a LSB problem).

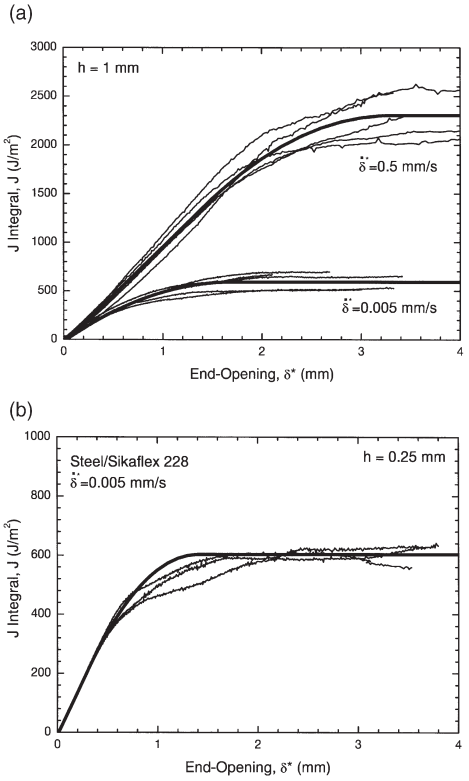

Fig. 5. Measured J–δ^* curves for various adhesive layer thicknesses and loading rates (thin lines). (a) h = 1.0 mm; $\dot{\delta}^* \approx 0.005$ mm/s and $\dot{\delta}^* \approx 0.5$ mm/s, (b) h = 0.25 mm; $\dot{\delta}^* \approx 0.005$ mm/s. Thick lines are J–δ^* relationships obtained by integration of a multi-linear function fitted to the $\sigma - \delta^*$ data of Fig. 6.

J_{ss} is attained approximately when decohesion begins at the end of the adhesive layer. There is some specimen to specimen variation in the J–δ^* curves, in particular for large openings, probably due to variation in the failure process zone evolution as just described. Obviously, from Fig. 5, an higher loading rate results in a higher steady-state fracture resistance. The end-opening rate, $\dot{\delta}^*$, was approximately 0.005 and 0.5 mm/s for the two loading rates. The values of J_{ss} agree well with the results of Briscoe and Panesar [16]. The J–δ^* curves for the specimens having a thin adhesive layer ($h = 0.25$ mm) do not differ significantly from the specimen having $h = 1$ mm.

4.3. Cohesive laws

We now proceed to calculate the cohesive laws. First we do that by numerical differentiation (see Appendix A) of the J–δ^* data according to Eq. (2). Results are shown in Fig. 6. Due to noise in the data, $\sigma(\delta)$ is not well defined for $\delta < 0.02$ mm. As for the parent J–δ^* data, there is some specimen to specimen variation, in particular for large openings (for a given δ the variation in σ is less than ±20% of the maximum value). The effect of loading rate on the cohesive law is strong [Fig. 6(a,b)]; the maximum cohesive stress is about 0.6 MPa for the slowest loading rate ($\dot{\delta}^* \approx 0.005$ mm/s) and nearly twice as high for the high loading rate ($\dot{\delta}^* \approx 0.5$ mm/s). Also, δ_c increases from about 1.7 mm to nearly twice as much for the high loading rate. The shape of the cohesive law differs significantly for the two loading rates. For the slow loading rate the cohesive stress rises to a maximum at a fairly small crack opening (~0.1 mm), and decreases nearly linearly with increasing δ. For the high loading rate the stress also rises rapidly, but to a much higher maximum stress, which remains almost constant until $\delta \approx 1.5$ mm and decreases thereafter. A loading rate dependent cohesive law has recently been measured by Liechti and Wu [21].

The cohesive law for $h = 0.25$ mm is shown in Fig. 6(b). The curves are fairly similar to those obtained for $h = 1.0$ mm, although the shape of the decreasing part is more non-linear for $h = 0.25$ mm than for $h = 1.0$ mm.

We also want to approximate the cohesive law with a simple analytical function. A multi-linear

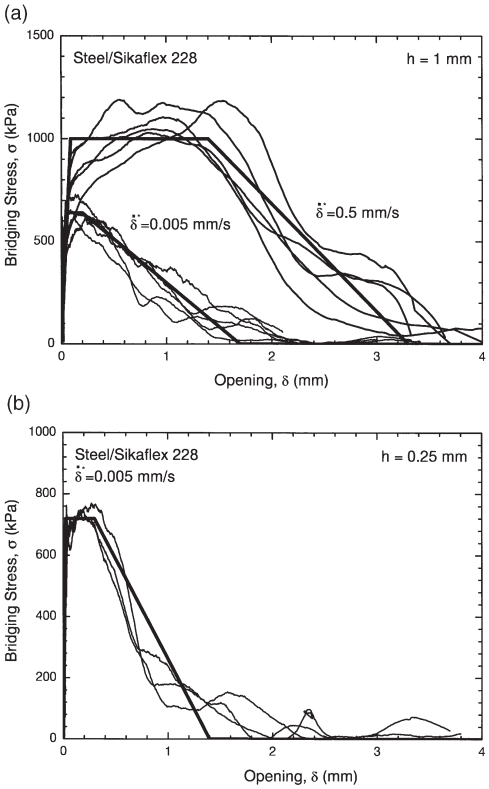

Fig. 6. Derived cohesive law curves (thin lines) for (a) $h = 1.0$ mm; $\dot{\delta}^* \approx 0.005$ mm/s and $\dot{\delta}^* \approx 0.5$ mm/s, (b) $h = 0.25$ mm; $\dot{\delta}^* \approx 0.005$ mm/s. Thick lines represent multi-linear curve fit [Eq. (4)].

cohesive law proposed by Tvergaard and Hutchinson [26]

$$\sigma(\delta) = \begin{cases} \sigma_0 \dfrac{\delta}{\delta_1} & \text{for } 0 \le \delta < \delta_1 \\ \sigma_0 & \text{for } \delta_1 \le \delta < \delta_2 \\ \sigma_0 \left(\dfrac{\delta_c - \delta}{\delta_c - \delta_\sigma} \right) & \text{for } \delta_2 \le \delta \le \delta_c \\ 0 & \text{for } \delta > \delta_c \end{cases} \tag{4}$$

fits the σ–δ^* data reasonable well with the parameters given in Table 1. The parameter σ_0 is the

Table 1
Parameters for multi-linear cohesive law [Eq. (4)] as a function of layer thickness, h and end-opening rate, $\dot{\delta}^*$

	σ_0 (MPa)	δ_1 (mm)	δ_2 (mm)	δ_c (mm)
h = 1 mm, $\dot{\delta}^* \approx 0.005$ mm/s	0.64±0.08	0.05±0.01	0.2±0.1	1.7±0.2
h = 1 mm, $\dot{\delta}^* \approx 0.5$ mm/s	1.0±0.2	0.09±0.01	1.4±0.3	3.3±0.2
h = 0.25 mm, $\dot{\delta}^* \approx 0.005$ mm/s	0.72±0.04	0.03±0.01	0.3±0.2	1.4±0.2

maximum cohesive stress, while δ_1, δ_2 are characteristic openings and δ_c is the opening for which the cohesive stress vanishes ($0 < \delta_1 < \delta_2 < \delta_c$). The model curves are shown as thick curves in Fig. 6 and—integrated according to Eq. (1)—in Fig. 5. As already discussed the maximum cohesive stress σ_0 increases with increasing loading rate, δ_1 is rather insensitive to the loading rate and thickness variation, while δ_2 and δ_c increase with increasing loading rate.

4.4. Notch sensitivity of bonded panels

Fig. 7 shows the tensile strength of the bonded panels (normalised by the maximum cohesive stress, σ_0 = 0.64 MPa) as a function of notch size, $2a$ (normalised by the specimen width, $2w$). The end-opening rate, $\dot{\delta}^*$, was about 0.01 mm/s, i.e., fairly similar to that of the slowest DCB tests. Points represents experimental results, while curves are theoretical predictions [27]. The experimental data fall on the straight line indicating completely notch insensitive behaviour, as discussed below.

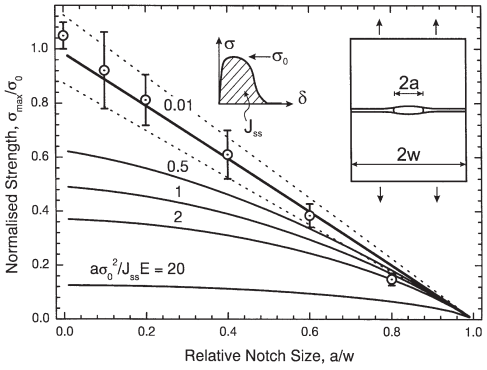

Fig. 7. Strength of bonded panels; experimental results for specimens having $2w$ = 200 mm (points represents average of at least three specimens, while error bars indicate standard deviation) are plotted together with theoretical predictions (solid lines) for various values of the notch sensitivity parameter, α. Dotted lines correspond to predictions based on upper and lower values of σ_0.

5. Discussion

5.1. Shape of the cohesive law

The cohesive law of the adhesive joint was highly non-linear. The initial part, where σ rises, is likely to be purely elastic straining of the layer without decohesion. The decohesion is assumed to occur at σ_0 and at the decreasing part, i.e. for $\delta_1 < \delta < \delta_c$. The shape of the cohesive law was found to be quite different for the two loading rates. For the low loading rate a simple linear softening cohesive law ($\delta_1/\delta_c = \delta_2/\delta_c = 0$) would be a fair approximation, but not for the high loading rate, where δ_2 is significantly larger than δ_1. The role of the shape of the cohesive law on the strength of components has only been investigated for a few geometries, but the shape of the cohesive law appears to be relatively unimportant for the strength of panels having a central notch [27,28].

5.2. Non-linear stress–strain behaviour

In joints where the sandwich layer possesses *non-reversible* stress–strain characteristics (e.g. due to plasticity or phase transformation) the steady-state fracture resistance scales with the thickness of the non-linear zone [26,29]. In contrast, for the present experiments the adhesive possesses *reversible* stress–strain behaviour. Although a larger non-linear zone may develop in specimens

having larger h, the value of the J integral (evaluated along Γ_p or outside) does not depend on the size of the zone deforming non-linear elastically; the only contribution to the J integral comes from the decohesion process itself (the J integral evaluated along Γ_d, sometimes called the intrinsic fracture toughness). This argument may explain why the measured cohesive laws were similar for different thicknesses.

5.3. Accuracy of approach

It is appropriate to comment on the accuracy of the present approach for determining the cohesive law. The approach relies on differentiation of J with respect to δ^*. In practice there is always noise in the measured data, so the data must be smoothed one way or the other. Care must be taken to ensure that the smoothening does not induce significant errors in the computed $\sigma-\delta^*$ data. The accuracy can be evaluated by comparing the predicted J–δ^* curve (integrated from the $\sigma-\delta^*$ data in accordance with Eq. (1)) with the raw J–δ^* data, as in Fig. 5. Thus, this approach enables a fairly direct way of evaluating the accuracy of the derived $\sigma(\delta)$. The approach for determining the cohesive law from data of the crack opening profile is known to be quite sensitive to noise in the data; quite different cohesive laws can give very similar crack opening profiles [13]; i.e. the method does not ensure an accurate solution. For that approach it is thus quite difficult to evaluate the accuracy of the cohesive law obtained. The approach used in the present study appears more promising; since it involves only differentiation it is less sensitive to data inaccuracy. However, for fracture process zones that possess small δ_c, the opening should be measured with a technique that has a high accuracy such as laser interferometry [30].

5.4. Cohesive law and notch sensitivity

The relationship between cohesive laws and the notch sensitivity of bonded panels can be evaluated by a non-dimensional notch sensitivity parameter [27]

$$\alpha = \frac{a\sigma_0^2}{J_{ss}E'} \tag{5}$$

where a is half the length of the notch, $E' = E/(1-\nu)$ for plane strain and $E' = E$ for plane stress, where E is the Young's modulus and ν is the Poisson's ratio of the plates. For the steel plates bonded together by the polyurethane adhesive investigated here we find $0 < \alpha < 0.01$ for components of common size ($a < 1$ m). Suo et al. [27] have proposed a model that predict the tensile strength of notched panels, based on knowledge of the cohesive law parameters expressed through α. For $\alpha \approx 0$ the bonded panels are predicted to be completely notch insensitive, so that the tensile strength, σ_{max}, is [27]

$$\frac{\sigma_{max}}{\sigma_0} = 1 - \frac{a}{w} \tag{6}$$

which is the straight solid line in Fig. 7. Note, that there is no curve fitting or calibration involved in the prediction of the strength of the bonded panels. The predictions are based solely on σ_0 and α. Both σ_0 and α were determined from the cohesive law parameters obtained *independently* by the DCB tests (at the lowest loading rate). The fact that the strength of the bonded panels, determined experimentally (points in Fig. 7), were found to be in good agreement with the model prediction provides confidence in the approach (2) and in the applicability of the model of Suo et al. [27].

Finally, an independent check on σ_0 was obtained as follows. For bonded panels having $a/w = 0$ and $\alpha \approx 0$ the tensile strength σ_{max} is expected to be identical to σ_0, since this experiment is equivalent to a direct tensile experiment (another method for measurement of the cohesive law [14]); this is also clear from Eq. (6). The measured value of $\sigma_{max}(a/w = 0)$ differed less from σ_0 (determined by the J integral approach) than the experimental uncertainty of σ_0, see Table 1. This close agreement between σ_0 and $\sigma_{max}(a/w = 0)$ is encouraging, since the two ways of determining σ_0 and $\sigma_{max}(a/w = 0)$ are completely different.

6. Concluding remarks

The study provides information on the shape of cohesive law of a polyurethane/steel joint. The cohesive law was obtained directly by differen-

tiation, revealing a highly non-linear relationship between cohesive stress and separation. With δ defined as the separation across the entire adhesive layer, cohesive laws were approximated by a multi-linear function: For low δ the cohesive stress σ increased nearly linearly with δ, then σ reached a maximum value σ_0 and decreased nearly linearly with increasing δ. The cohesive law parameters were combined into a notch sensitivity index, α. Steel panels (laboratory size) bonded by the polyurethane adhesive were predicted to be completely notch insensitive; this was confirmed by experiments. Furthermore, the strength of the bonded panels having a central notch were in excellent agreement with model predictions based entirely on σ_0 and α.

Acknowledgements

Thanks to Claus Mikkelsen for specimen preparation, Jens Olsson for experimental help and to Helmuth Toftegaard for help with the numerical differentiation. Useful discussions with John W. Hutchinson, Torben K. Jacobsen and E. Kristofer Gamstedt are acknowledged. This work was funded by the Risø Engineering Science Centre for Structural Characterisation and Modelling of Materials.

Appendix A

The procedure used for numerical differentiation is briefly described here. Consider a data file consisting of N sets of values for J and δ^*. Focus at data set number i. A second order polynomium was fitted (least squares) to the data sets ranging from $i-n$ to $i+n$, where n is a fixed integer, $2 < n < N/2$. The slope of the polynomium $\sigma(\delta^*) = (\partial J/\partial \delta^*)$ was assigned to the ith value of δ^*. The procedure is performed for $\forall\, i \in [n, N-n]$. The integer n was chosen such that the differentiated curve was neither too scattered (reflecting too few data sets for each polynomium fit; n too low) nor too smooth (reflecting too little freedom in the shape of the differentiated curve). Values of $n =$ 20–30 was found to give satisfying results.

References

[1] Zok F, Hom CL. Acta Metall Mater 1990;38:1895.
[2] Wang Y-L, Nair SV. J Am Ceram Soc 1998;81:1157.
[3] Bao G, Zok F. Acta Metall Mater 1993;41:3515.
[4] Lindhagen JE, Gamstedt EK, Berglund LA. Comp Sci Technol 2000;60:2883–96.
[5] Suo Z, Bao G, Fan B. J Mech Phys Solids 1992;40:1.
[6] Cox BN. Acta Metall Mater 1991;39:1189.
[7] Spearing SM, Evans AG. Acta Metall Mater 1992;40:2191.
[8] Sørensen BF, Jacobsen TK. Composites A 1998;29:1443.
[9] Bao G, Suo Z. Appl Mech Rev 1992;45:355.
[10] Hillerborg A. Int J Fract 1991;51:95.
[11] Hutchinson JW, Jensen HM. Mech Mater 1990;9:139.
[12] Flinn BD, Lo CS, Zok FW, Evans AG. J Am Ceram Soc 1993;76:369.
[13] Cox BN, Marshall DB. Int J Fract 1991;49:159.
[14] Cotterell B, Mai YW. Fracture mechanics of cementitious materials. London: Blackie, 1996.
[15] Li VC, Ward RJ. In: Mihashi H, Takahashi H, Wittmann FH, editors. Fracture toughness and fracture energy—testing methods for concrete and rocks. Rotterdam: A.A. Balkema; 1989.
[16] Briscoe BJ, Panesar SS. Proc R Soc Lond A 1991;433:23.
[17] O'Kane WJ, Young RJ. J Adhesion 1993;41:203.
[18] Shetty SP, Spearing SM. Scripta Mater 1997;37:787.
[19] Yang QD, Thouless MD, Ward SM. J Mech Phys Solids 1999;47:1337.
[20] Landis CM, Pardoen T, Hutchinson JW. Mech Mater 2000;32:663.
[21] Liechti KM, Wu J-D. Mech Phys Solids 2001;49:1039.
[22] Rice JR. J Appl Mech 1968;35:379.
[23] Burchardt B, Diggelmann K, Koch S, Lanzendörfer B. Elastic bonding, the basic principles of adhesive technology and a guide to its cost-effective use in industry. Landsberg (Lech): Verlage Moderne Industrie, 1998.
[24] Sørensen BF, Brethe P, Skov-Hansen P. J Eur Ceram Soc 1996;16:1021.
[25] Sørensen BF, Jacobsen TK. Plastic Rubber and Composites. Process Applic 2000;29:119.
[26] Tvergaard V, Hutchinson JW. J Mech Phys Solids 1992;40:1377.
[27] Suo Z, Ho S, Gong X. J Engng Mater Technol 1993;115:319.
[28] Gu P. Int J Fract 1995;70:253.
[29] Budiansky B, Hutchinson JW, Lambropoulos JC. Int J Solids Struct 1983;19:337.
[30] Stigh U, Andersson T. In: Williams JG, Pavan A, editors. Fracture of polymers, composites and adhesives. Amsterdam: Elsevier; 2000.

[A8]

Sørensen, B. F. and Jacobsen, T. K., 1998

"Large scale bridging in composites: R-curve and bridging laws"

Composites part A, Vol. 29A, pp. 1443-51

Composites Part A **29A** (1998) 1443–1451
1359-835X/98/$ - see front matter

PII: S1359-835X(98)00025-6

Large-scale bridging in composites: R-curves and bridging laws

Bent F. Sørensen* and Torben K. Jacobsen
Materials Research Department, Risø National Laboratory, DK-4000 Roskilde, Denmark
(Received 10 October 1997; revised 5 January 1998; accepted 16 January 1998)

Large-scale bridging was studied experimentally in a unidirectional carbon fibre/epoxy matrix composite material. For intralaminar cracks a significant increase in the crack growth resistance occurred with increasing crack extension. The increase in the crack growth resistance was attributed to fibre cross-over bridging. The R-curve behaviour, i.e. the relationship between crack growth resistance and crack extension depended on specimen geometry. Therefore, R-curves are not material properties when large-scale bridging occurs. The bridging law (the relationship between the local crack opening δ and the local bridging traction σ) was measured. The bridging law was found to be independent of specimen geometry. A bridging law can therefore be used as a material property in composites with large-scale bridging. The bridging stress was related to the crack opening as $\sigma \propto \delta^{-1/2}$. © 1998 Published by Elsevier Science Ltd. All rights reserved.

(Keywords: laminates; delamination; fracture toughness)

INTRODUCTION

Most unidirectional fibre composites exhibit high tensile strength in the fibre direction. The tensile strength in the transverse directions is usually much lower. Therefore, delamination is a major problem in laminated fibre composites. Also, intralaminar crack growth is of importance, e.g. as tunnel or transverse cracking in 90° plies in cross ply laminates, or splitting cracks around holes and notches.

It is well established that fibre cross-over bridging can enhance the crack growth resistance during crack growth[1–6]. The rising crack growth resistance is usually described by the concept of *R-curves*, i.e. the crack growth resistance $\mathcal{G}_R$ as a function of crack extension Δa (see, e.g. Broek[7] or Heuer[8] for comprehensive descriptions of R-curves). When the bridging is restricted to a zone much smaller in length than any specimen dimension (small-scale bridging) the R-curve can be regarded as a material property. However, for many crack growth problems that involve fibre bridging the bridging length (the length of the crack where bridging occurs) can be comparable with or exceed a specimen dimension. This is called *large-scale bridging*. In situations with large-scale bridging the shape of the R-curve is no longer a material property, as it depends on the specimen geometry[3,9–11]. For instance, Spearing and Evans[3] who studied fibre cross-over bridging of unidirectional composites showed that Double Cantilever Beam (DCB) specimens with a higher bending stiffness required a longer crack extension before the steady-state crack growth resistance was attained. Therefore, instead of characterizing large-scale bridging by R-curves, it has been proposed to use the concepts of a *bridging law*[9,11]. The bridging law is the relationship between the local crack opening displacement δ and the local bridging stress σ.

Many papers are devoted to the calculation of bridging laws from micromechanical models[12–15]. However, since many micromechanisms may operate simultaneously it may be more efficient to use phenomenological bridging laws, in which the effects of the various mechanisms are smeared together. A number of papers cover the calculation of R-curves from idealized bridging laws[9,11,14,16]. Then, by fitting the computed R-curves to measured R-curves an approximative bridging law can be obtained.

Another way of obtaining the bridging law is to measure the near tip crack opening profile and use fracture mechanics analysis to calculate the bridging traction by adjusting the bridging stress until the computed crack opening profile matches the measured one[14,17].

A more direct method for measuring bridging law for the problem of fibre cross-over was proposed by Kaute *et al.*[4]. A delamination specimen of a unidirectional fibre composite was cracked along its length in such a manner that the two specimen parts were still held together by bridging fibres. By loading the specimen in the transverse direction a relationship was obtained between the bridging stress and the crack opening. A similar approach has been used by Brenet *et al.*[18] for the measurement of the bridging law in the fibre direction.

* Corresponding author.

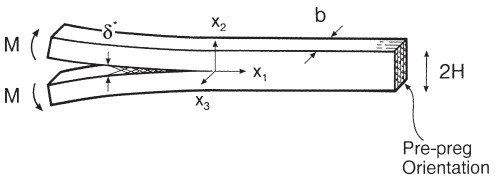

Figure 1 The geometry and loading of the DCB specimen loaded with pure bending moments

Finally, it has been proposed that the bridging law can be obtained by simultaneous measurement of the crack growth resistance and the end-opening of the bridging zone[11]. This approach, which is based on an application of the J integral, is the one that will be used in the following.

The purpose of this paper is to study intralaminar fibre bridging in a unidirectional polymer matrix composite, and to measure both the R-curve and the bridging-law characteristics. The objective is to evaluate if the large-scale bridging law can be obtained in a fairly simple manner, and whether it is a property independent of specimen geometry.

PRINCIPLE OF MEASURING BRIDGING LAWS

In the following an experimental approach is described for the measurements of bridging laws. The approach is based on the application of the path independent J integral[19].

In general, under large-scale bridging, the global J integral (the J integral taken along the external boundaries of the specimen) depends on the bridging law[20]. A prerequisite for the following approach is that a specimen configuration must be used for which the J integral taken along the external edges is independent of the details of the bridging law.

For the symmetric DCB specimen loaded with pure bending moments M (*Figure 1*) the crack growth occurs under pure mode I. The energy release rate for this specimen is determined by the J integral taken along the external boundaries. The result is[11,21] (plane strain)

$$\mathcal{G} = 12(1-\nu_{13}\nu_{31})\frac{M^2}{b^2H^3E_{11}} \tag{1}$$

where E and ν are Young's modulus and Poisson's ratio, respectively (indices indicate the direction of the orthotropic material, *Figure 1*), b is the specimen width and H the beam height. As pointed out by Bao and Suo[20] a prominent feature of this test configuration is that the global J integral is independent of the bridging law. This is in contrast to most other fracture mechanics test specimens, including the DCB specimen loaded with wedge forces. For all these specimens the global J integral (and thus the applied energy release rate) depends on the details of the bridging law, and it is not identical to the energy release rate of a specimen without bridging[11], as it has been presumed in some experimental studies.

Consider now the DCB specimen (*Figure 1*) having a crack with bridging fibres across the crack faces near the crack tip. The closure stress σ (acting in the x_2-direction) is assumed to depend only on the local crack opening δ. The bridging law $\sigma = \sigma(\delta)$ is assumed to be identical at each point along the bridging zone. The relationship between σ and δ is presently unknown, but since fibres will fail when loaded sufficiently, it is assumed that a maximum crack opening δ_0 exists, beyond which the closure traction vanishes. Shrinking the path of the J integral to the crack faces and around the crack tip gives[19]

$$\mathcal{G} = \int_0^{\delta^*} \sigma(\delta)\,\mathrm{d}\delta + \mathcal{G}_0 \tag{2}$$

where $\mathcal{G}_0$ is the energy release rate at the crack tip (equal to the fracture energy dissipation at the crack front), the integral is the energy dissipation in the bridging zone and δ^* is the end-opening of the bridging zone (at the notch root). When δ^* attains δ_0 the R-curve reaches its steady-state value $\mathcal{G}_{ss}$ and the bridging zone maintains a self-similar opening profile and a constant length. During subsequent crack growth the bridging zone translates along the beam with the crack tip, leaving behind the crack faces free of traction, because the ligaments have broken there. Note, that such a self-similar crack growth requires the use of a steady-state specimen, such as the DCB specimen loaded with pure bending moments.

The bridging law can be determined experimentally as follows[11,22]: by measuring δ^* together with the R-curve, the bridging law can be determined by

$$\sigma(\delta^*) = \frac{\partial \mathcal{G}_R}{\partial \delta^*}. \tag{3}$$

Although this approach is not new[22], it has not previously, as far as the authors know, been applied to the measurement of bridging laws in unidirectional fibre composites experiencing large-scale bridging.

EXPERIMENTAL METHODS

The material examined in the present study is a unidirectional carbon fibre/epoxy composite. A rectangular plate was processed in-house from pre-pregs (Sigrafil CE 1007). The laminate was encapsulated in a vacuum bag and cured at 120°C for 2 h under an autoclave pressure of 0.5 MPa. The nominal fibre volume fraction was 60%. The following elastic properties were used based on the information of the supplier: $E_{11} = 130$ GPa, $\nu_{13} = \nu_{31} = 0.3$. The nominal specimen width b was 5 mm. Eight specimens of different heights (ranging from $H = 1.5$ to 10 mm) were cut from the plate, such that the notch (cut by a 0.3 mm diamond wire saw) was parallel with the fibre direction and perpendicular to the plane of the plate. The subsequent crack growth was therefore intralaminar, as indicated in *Figure 1*. Prior to testing a broad face of each specimen was polished to ease observation of crack growth.

Extensometers were mounted at each face of the specimens just at the end of the notch to record δ^* as a

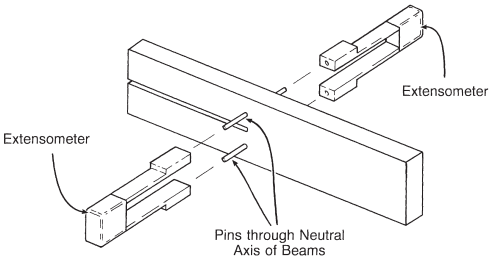

Figure 2 Schematic drawing showing how extensometers, for the measurement of δ^*, were mounted at pins through the neutral axes of the beams

function of M. The extensometers were mounted at pins such the rotation of the beams were not constrained by the extensometers. In order to minimize the influence of the pins on the stress state in the beams the pins were mounted by glue in holes through the neutral axis of the beams (*Figure 2*).

The pure bending moments were applied to the specimens using a special fixture[23] mounted at a screw-driven tensile testing machine. The cross head displacement rate was 2 mm min^{-1}. An acoustic emission (AE) system (Spartan AT, Physical Acoustic Corporation) with one sensor and pre-amplifier was used for the detection of crack growth. Data for M, δ^* and AE signals were collected and stored for later analysis.

Two different testing procedures were used. The first procedure involved successive loading until crack growth was detected, whereafter the specimen was unloaded to about 25% of the peak moment. Surface replicas were taken after each unloading, in order to record the crack extension. The value of $\mathcal{G}_R$ (defined as the value where the relationship between M and δ^* became non-linear) was associated with the crack length Δa before the loading. This was in order to relate $\mathcal{G}_R$ to the bridging length just at the onset of crack growth. This procedure provides data for both $\mathcal{G}_R$–Δa and $\mathcal{G}_R$–δ^* plots. The second procedure consisted of a continuous loading until most of the specimen was cracked. This procedure gave data for the $\mathcal{G}_R$–δ^* relationship, sufficient to determine $\sigma(\delta)$ by the use of eqn (3). This type of experiment was much faster than the first type.

The experiments on the thinnest specimens ($H = 1.5$ mm) were conducted inside the vacuum chamber of an Environmental Scanning Electron Microscope (ESEM), utilizing a smaller but similar fixture as described elsewhere[24]. Only data for R-curve plots were obtained (δ^* was not measured). Acoustic emission was also used in these experiments. The best means of detecting crack growth was visual observation of the crack tip region at a magnification of about 500 × .

EXPERIMENTAL RESULTS

Observations

For the first loading procedure many loading/unloading sequences were performed for each specimen. Usually, the first crack growth resulted in a significant load drop and crack length of 1–5 mm. This 'pop-in' is probably due to the fact that the load to initiate a crack from a machined notch may require a higher $\mathcal{G}$ than for propagation of a truly sharp crack. Therefore, the value of $\mathcal{G}_R$ at initiation was not used in the plots. All subsequent crack growth was completely stable, and crack extensions less than 1 mm could easily be obtained if desired.

The fibre bridging was visible with the naked eye. It was observed that the debond length of the bridging ligaments became longer as the crack opening increased. Also, more bridging ligaments failed as the crack opening increased. Eventually, the fibre bridging vanished completely at the notch, corresponding to the point where the R-curves attained their steady-state values. From this point on, the bridging length remained approximately the same, moving along with the crack tip. *Figure 3* shows an ESEM micrograph of fibre bridging. Both single fibre and beam-like fibre bundle bridging ligaments are present.

During the experiments it was noted that the AE signals appeared at low loads, before non-linearity of the M–δ^* relationship (see *Figure 4*). Detailed investigations with replicas indicated that no crack growth had taken place after the first AE counts.

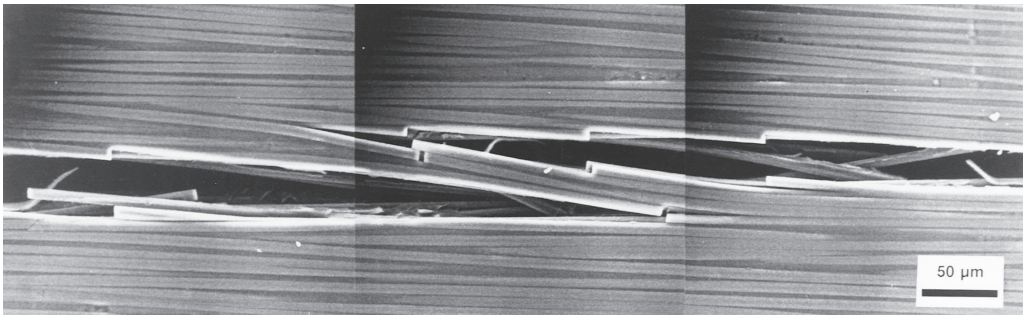

Figure 3 ESEM micrograph showing beam-like bridging of fibre bundles and single fibres. The crack tip is outside the picture to the right-hand side

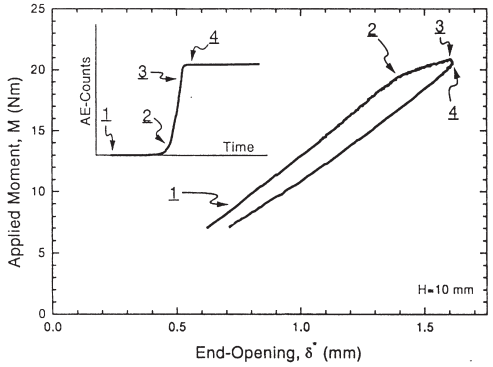

Figure 4 Example of a loading–unloading curve, and the accompanying acoustic emission events

This was confirmed by the *in-situ* observations in the ESEM. We presume that these AE signals can originate from debonding of the bridging ligaments. When the M–δ^* relationship became non-linear many AE counts appeared. Shortly after the unloading was commenced no more AE counts appeared, see *Figure 4*.

By extrapolation of the loading–unloading curves it was found that the curves do not go through the origin, i.e. in the load-free state there was a permanent crack opening. A similar behaviour was found by Spearing and Evans[3]. This behaviour was attributed to fibres and fibre bundles that had peeled off or partially debonded, so that they have been displaced from their original sites and thereby wedge the crack open, preventing complete closure of the crack faces.

Measurements of R-curve behaviour

Figure 5 shows the measured R-curve (the relationship between $\mathcal{G}_R$ and the crack extension from the notch Δa) for three nominally identical specimens ($H = 4.0$ mm). The initial value of $\mathcal{G}_R$, denoted $\mathcal{G}_0$, is about 300 J m^{-2}. With increasing crack extension $\mathcal{G}_R$ increases in an almost linear fashion until a steady-state value $\mathcal{G}_{ss}$ is reached. The crack extension corresponding to the steady-state Δa_{ss} was found to be 50 mm for this specimen geometry. $\mathcal{G}_{ss}$, determined as the average value of the $\mathcal{G}_R$ values for $\Delta a > \Delta a_{ss}$ was 2075 J m^{-2}. The scatter in the data is about $\pm$ 13%. Such a scatter is typical for R-curve measurements[1,3], and probably reflects that the amount of bridging of fibre bundles varies slightly along the crack length. Had the specimen width been larger the effect of discrete bridging ligaments might have been smaller.

R-curves measured on specimens with different beam heights are shown in *Figure 6*. The R-curves are different for different specimen geometries. The data for $H = 1.5$ mm should be taken with some caution, since it was not possible to obtain crack growth in the middle of the specimen; the cracks initiated from the corners of the notch root. The crack growth was therefore vaguely mixed mode. Also, due to the large deflection of the beams, the experiment had to be terminated after a crack extension of about 30 mm. Nevertheless, the measured data for $H = 1.5$ mm follow the same trend as the data from other geometries. $\mathcal{G}_R$ increases rapidly for the thinner specimens. With increasing H, $\mathcal{G}_R$ increases at a slower rate (due to the finite specimen length the experiment with $H = 10$ mm was terminated before steady-state was attained). This behaviour is attributed to the fact that for a given crack extension Δa the thinner specimens will experience a larger crack opening.

Figure 6 includes computed R-curves. The only available analysis for a DCB loaded with pure bending moments is that by Suo *et al.*[11], who used a linear softening law

$$\sigma(\delta) = \sigma_0 + S\delta, \quad 0 < \delta < \delta_0 \tag{4}$$

where σ_0 is the initial bridging stress at zero crack opening

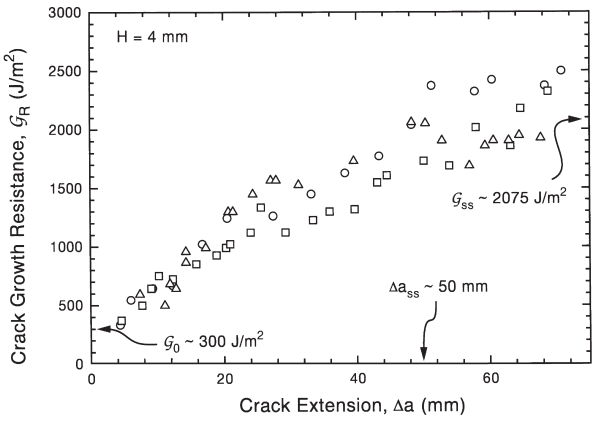

Figure 5 The crack growth resistance as a function of crack extension (R-curve) for three specimens with identical geometry

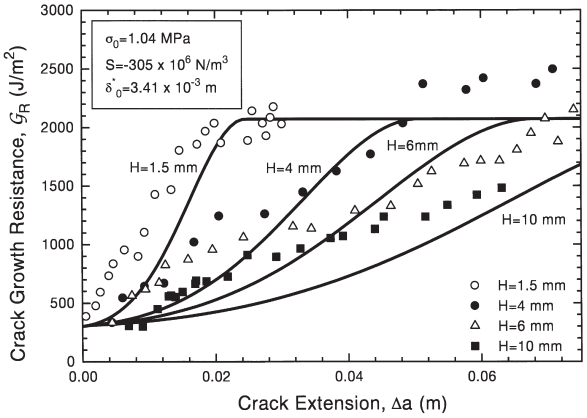

Figure 6 Typical curves showing the crack growth resistance as a function of crack extension (R-curve) for specimens with different geometries. Solid lines are computed R-curves, using a linear softening bridging law

and $S = -\sigma_0/\delta_0 < 0$. The model parameters, σ_0, S and δ_0 were determined from the R-curve data in *Figure 5*. Details of this approach are described in Appendix A.

The predicted R-curves follow the major trends of the experimental results (Δa_{ss} increases with increasing H), but there are differences in the details. The computed curves do not rise sufficiently sharp and lie below the experimental data for small crack extensions.

Measurements of bridging law

The $\mathcal{G}_R$–δ^* data recorded on two nominally identical specimens ($H = 6$ mm) loaded continuously are shown in *Figure 7(a)*. Only data after crack initiation are included in the figure (initial value of δ^* after 'pop-in' was close to 50 μm). The waviness of the curves is attributed to the progression of fibre bundle delamination and fibre fracture. $\mathcal{G}_{ss}$ is reached at $\delta^* = \delta_0 = 4$ mm. The function

$$\mathcal{G}_R = \mathcal{G}_0 + \Delta\mathcal{G}_{ss}\left(\frac{\delta^*}{\delta_0}\right)^{1/2}, \quad 0 < \delta^* < \delta_0 \tag{5}$$

(where $\Delta\mathcal{G}_{ss} = \mathcal{G}_{ss} - \mathcal{G}_0$) fits the data well. *Figure 7(b)* shows the $\mathcal{G}_R$–δ^* data recorded from the loading/unloading experiments for $H = 4$, 6 and 10 mm along with the curve fit (5). The data points for all specimen geometries follow eqn (5) closely. (The scatter is of the same order of magnitude as for the R-curve of nominally identical specimens, see *Figures 5, and 7(a)*). This indicates that the bridging law $\sigma(\delta)$ is readily independent of specimen geometry and thus a material property, since σ and $\mathcal{G}_R$ are interlinked by eqn (2).

The bridging law is now found by eqns (3) and (5)

$$\sigma(\delta^*) = \frac{\Delta\mathcal{G}_{ss}}{2\sqrt{\delta_0\delta^*}} \quad 0 < \delta^* < \delta_0 \tag{6}$$

This bridging law is shown in *Figure 8* along with the linear softening law (4). Note, that the measured non-linear bridging law (6) has much higher stress values for small values of δ than the linear softening law (4). This appears to be the reason why the computed R-curves (*Figure 6*) do not follow the sharp rise of the measured $\mathcal{G}_R$–Δa data.

DISCUSSION

Form of the bridging law

Spearing and Evans[3] assumed a linear softening bridging law for the fibre cross-over bridging in a ceramic matrix composite. However, in the appendix of their paper they derived a mechanism-based model for the bridging law of intact fibre bundles that bridge the crack faces. The bridging ligaments were assumed to deflect like cantilever beams. When the terms associated with shear deformation are neglected, their equation reduces to the same form as eqn (6), i.e. $\sigma(\delta) \propto \lambda/\delta^{1/2}$, where λ is a parameter that depends on the bending stiffness of the ligament and the debonding fracture energy Γ_i, see Appendix B. This suggests that the bridging law shape (6) may be of more general nature for the problem of fibre cross-over bridging. Further experimental work is required to test this hypothesis.

For a given material system the bridging law may depend on, e.g. fibre surface treatment[6] and process conditions. The characterization technique developed here may be useful in such material development.

As far as the authors know, the only measurement of bridging law for fibre cross-over bridging is that measured on a unidirectional ceramic matrix composite by Kaute *et al.*[4]. They pulled a cracked specimen in the transverse direction and measured the resulting σ–δ relationship. The σ–δ curve was found to increase almost linearly to a maximum stress and then decrease almost linearly to zero. However, care must be taken to interpret the initial part of their σ–δ curves, since bridging ligaments must have developed already during the initial splitting of the

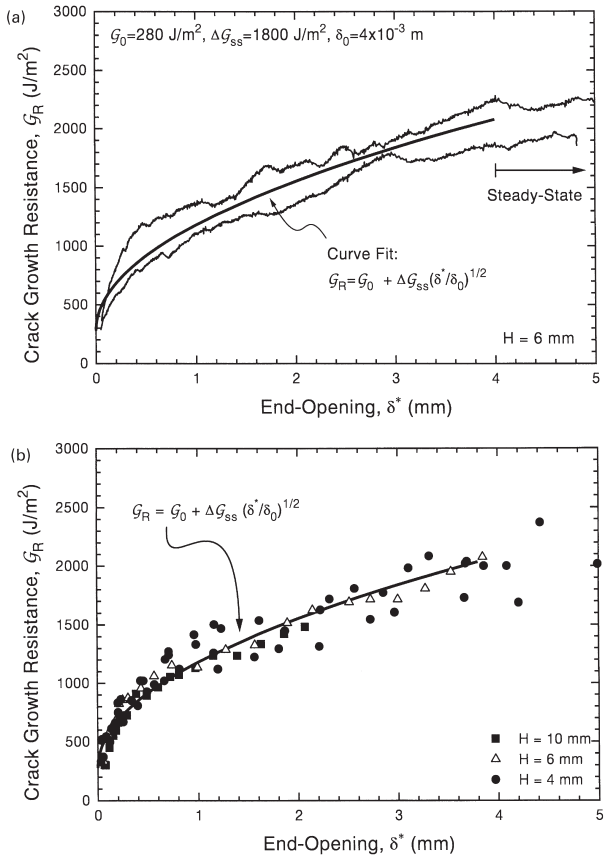

Figure 7 The crack growth resistance as a function of end-opening. (a) Data from two identical specimens loaded without interruption, and (b) for seven specimens (three different values of *H*) subjected to many loading and unloadings

specimen. During the subsequent transverse tensile test no significant debonding of fibre bundles is anticipated until the opening reached the one that was attained during specimen splitting. This is likely to be the reason for the first linearly elastic part of their σ–δ curve. The decreasing part of the σ–δ curve is almost linear, i.e. different from the shape measured in the present work. Kaute *et al*.[4] noted a lot of fibre pull out, apparently due to the weak interfacial bonding between fibres and matrix in the ceramic matrix composite. This mechanism is not present in the polymer matrix composite examined here. The difference in the micro-mechanisms between the ceramic and polymer matrix composite is a plausible reason for the difference in bridging law shape of the two materials.

Additional comments

Note that conventional R-curve measurements require the measurement of the crack length, such that a procedure must consist of repeated loading, unloading and measurement of crack length. This is fairly time consuming (in the order of several hours per specimen). On the other hand, it is fast to measure the bridging law by continuous loading (in the order of a few minutes). This is possible because only M and δ^* should be measured (a DCB specimen loaded with pure bending moments is a steady-state configuration; it is not necessary to know the crack length Δa to compute $\mathcal{G}_R$). Thus, not only is the measurement of bridging laws the correct way to characterize large-scale bridging. It is also fast to perform the experiments.

Having determined the bridging law of a material, the next step is to use this material property in the design of composite structures. Usually this can only be done by numerical modelling. Examples of such can be found elsewhere[20,25]. Also, for a given geometry R-curves can be computed, e.g. for the DCB specimen with applied bending

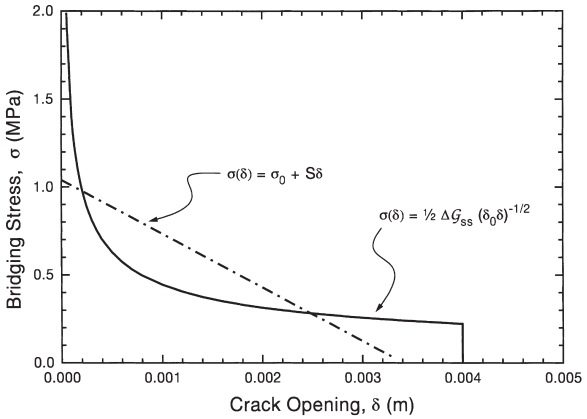

Figure 8 The measured bridging law; the local bridging stress as a function of the local crack opening

moments and the non-linear bridging law. To do this requires extensive finite element analysis of the coupled problem[11]. This is beyond the scope of this paper.

CONCLUSIONS

Effects of fibre cross-over bridging on crack growth resistance of a unidirectional carbon fibre epoxy composite were investigated by loading DCB specimens with pure bending moments. The bridging law was determined experimentally by the measurement of the end-opening of the bridging zone.

R-curves were found to depend on the geometry of the test specimens. The bridging law, on the other hand, was found to be independent of specimen geometry, i.e. a material property.

The measured bridging law was found to be of the following form:

$$\sigma(\delta) = \frac{\Delta \mathcal{G}_{ss}}{2\sqrt{\delta_0 \delta}}$$

The form of the bridging law coincides with that predicted by the model of Spearing and Evans[3]. The proposed way of measuring the bridging law by the use of DCB specimens loaded with pure bending moments is fast and efficient.

ACKNOWLEDGEMENTS

We would like to thank Claus Mikkelsen, Finn Jensen, Jørgen Lindbo and Helmer Nilsson for specimen preparation. The work was partly funded by the Risø Engineering Science Centre for Structural Characterization and Modelling of Materials and the Danish Programme for Wind-Energy, EFP95.

APPENDIX A. R-curves based on linear bridging laws

Suo *et al.*[11] have analysed the coupled problem of large-scale bridging in DCB specimens loaded with pure bending moments. A bridging law of the form of a linear spring

$$\sigma(\delta) = \sigma_0 + S\delta, \quad 0 < \delta < \delta_0 \tag{A1}$$

was used. They presented their results in dimensionless form, and equations were used to curve-fit the parameters determined by finite element analysis. Thus, with the parameters σ_0, S and δ_0 known R-curves ($\mathcal{G}_R$–Δa) can be computed. The procedure is reviewed in the following. The condition for crack growth is

$$\delta^* = \alpha_1 (\Delta a)^2 C \frac{M}{b} - \alpha_2 (\Delta a)^4 C \sigma_0 \tag{A2}$$

$$\sqrt{\mathcal{G}_0} = \alpha_3 \sqrt{C} \frac{M}{b} - \alpha_4 (\Delta a)^2 \sqrt{C} \sigma_0 \tag{A3}$$

where

$$C = 12(1-\nu^2)/EH^3 \tag{A4}$$

and the effective stiffness ratio of the spring to the beams is

$$\Sigma = S(\Delta a)^4 C \tag{A5}$$

and the non-dimensional parameters are related as follows:

$$\alpha_4 = \alpha_1/2, \quad \alpha_3 = (1 - \Sigma\alpha_1^2/2)^{1/2}, \quad \alpha_2 = (1-\alpha_3)/\Sigma. \tag{A6}$$

The coefficient α_1 depends on Σ and $\Delta a/H$ only. It was fitted by[11]

$$\alpha_1 = A \exp[-B\Sigma(\Sigma + \Sigma_0)^{-1/2}] \tag{A7}$$

$$A = 1 + 1.325(H/\Delta a) + 0.35(H/\Delta a)^2 \tag{A8}$$

$$B = 0.353 + 0.374(H/\Delta a) + 0.373(H/\Delta a)^2 - 0.23(H/\Delta a)^3 \tag{A9}$$

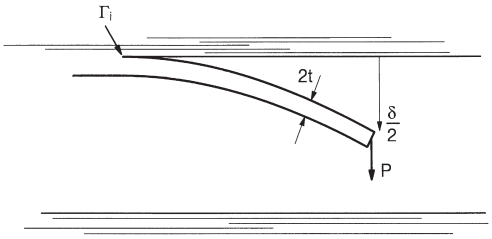

Figure 9 Cantilever beam used for modelling ligament bridging

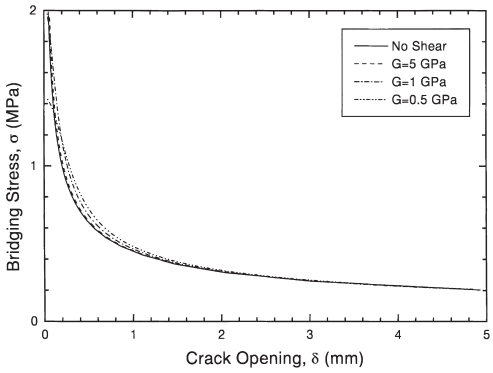

Figure 10 Plot showing the shape of the ligament bridging model and a comparison between eqns (B1) and (B2)

and

$$\Sigma_0 = 6.127\exp[-2.586(H/\Delta a) + 0.564(H/\Delta a)^2]. \quad \text{(A10)}$$

It is of interest to see the difference between a linear softening bridging law and the measured non-linear bridging law (6). Assuming the linear softening law (A1) with $S = -\sigma_0/\delta_0$, the parameters σ_0, S and δ_0 can be determined from traditional R-curves ($\mathcal{G}_R$–Δa), as follows[11].

From *Figure 5* we read off $\mathcal{G}_0$ to be 300 J m^{-2}, Δa_{ss} = 50 mm and $\mathcal{G}_{ss}$ = 2075 J m^{-2}. Specializing eqn (A1) to steady-state gives $\Delta\mathcal{G}_{ss} = \frac{1}{2}\sigma_0\delta_0$. With C, $\mathcal{G}_{ss}/\mathcal{G}_0$ and $\Delta a_{ss}/H$ known we read off from Fig. 8 in the paper by Suo *et al.*[11] that $\Sigma = -2.5$, which by eqn (A5) gives $S = -305$ MPa m^{-1}. Since $S = -\sigma_0/\delta_0$ for the linear softening law, we can eliminate σ_0, so we get

$$\delta_0 = \left(\frac{-2\Delta\mathcal{G}_{ss}}{S}\right)^{1/2} \quad \text{(A11)}$$

which gives δ_0 = 3.41 mm and σ_0 = 1.04 MPa. This bridging law is also shown in *Figure 8*.

With the parameters σ_0, S and δ_0 known R-curves can be computed. For a given crack extension Δa the moment required to give crack growth is computed from eqn (A3) and $\mathcal{G}_R$ is then found by eqn (1). R-curves (for different values of H) computed in this manner are shown in *Figure 6*.

Table 1 Ligament parameters ($I = 2Wt^3/3$)

$2t$ (μm)	W (μm)	E (GPa)	Γ_i (J m^{-2})	G (GPa)
50	500	140	20	0.5–5

APPENDIX B. Ligament bridging

The pronounced R-curve behaviour is attributed to ligaments bridging the intralaminar crack. A simple model for this behaviour has been proposed by Spearing and Evans[3]. They assumed that the bridging ligament could be approximated by a cantilever beam of rectangular section subjected to an end load, P, see *Figure 9*.

The ligaments can deform in shear and bending. During loading the ligaments can peel away by overcoming a fracture resistance, Γ_i. The displacement relationship is given by[3]

$$\delta = \frac{2P}{3EI} \times \left[\left(\frac{2W\Gamma_i}{P^2} - \frac{t^2}{2IG}\right)EI\right]^{3/2} + \frac{Pt^2}{IG}\left[\left(\frac{2W\Gamma_i}{P^2} - \frac{t^2}{2IG}\right)EI\right]^{1/2} \quad \text{(B1)}$$

where E is Young's modulus, G the shear modulus, W the beam width, $2t$ the beam height, and I the second moment of area. If the shear deformation is neglected and a number of ligaments per unit crack surface area N is assumed, the average bridging stress can be related to δ as

$$\sigma = \frac{1.3732N(EI)^{1/4}(W\Gamma_i)^{3/4}}{\delta^{1/2}} \quad \text{(B2)}$$

The bridging stress is thus of the following form:

$$\sigma = \frac{\lambda}{\delta^{1/2}} \quad \text{(B3)}$$

where $\lambda = 1.3732N(EI)^{1/4}(W\Gamma_i)^{3/4}$. Eqn (B3) has a similar form as the measured bridging law. λ can be regarded as a parameter measuring the strength of the ligament bridging and it can be found from the experimental data as

$$\lambda = \frac{\Delta\mathcal{G}_{ss}}{2\delta_0^{1/2}} \quad \text{(B4)}$$

For the present experimentally obtained bridging law we find λ = 14.2 kPa m$^{1/2}$.

In order to investigate the effect of shear deformation a comparison between eqns (B1) and (B2) was performed. The ligament parameters shown in *Table 1* were determined from optical and ESEM observations. The value of Γ_i was assumed. By varying the shear modulus G from 0.5 to 5 GPa the stress-opening curves shown in *Figure 9* were obtained by using eqn (B4) to determine N. The curves in *Figure 10* show that the difference between eqns (B1) and (B2) decreases as the crack opening increases, but increases with lower shear modulus. It is also noted that the curves for G = 5 and 1 GPa follow the same trend as the simple

model (B2). However, eqn (B1) predicts a finite value of σ for $\delta = 0$ as shown for $G = 0.5$ GPa. From the experiments though it seems that the simpler expression (B2) is sufficient for describing most of the bridging law.

REFERENCES

1. Hashemi, S., Kinloch, A. J. and Williams, J. G., The analysis of interlaminar fracture in unidirectional fibre–polymer composites. *Proc. R. Soc. Lond.*, 1990, **A427**, 173.
2. Zok, F., Sbaizero, O., Hom, C. L. and Evans, A. G., Mode I fracture resistance of a laminated fiber-reinforced ceramic. *J. Am. Ceram. Soc.*, 1991, **74**, 187.
3. Spearing, S. M. and Evans, A. G., The role of fiber bridging in the delamination resistance of fiber-reinforced composites. *Acta Metall. Mater.*, 1992, **40**, 2191.
4. Kaute, D. A. W., Shercliff, H. R. and Ashby, M. F., Delamination, fibre bridging and toughness of ceramic matrix composites. *Acta Metall. Mater.*, 1993, **41**, 1959.
5. Shercliff, H. R., Vekinis, G. and Beaumont, P. W. R., Direct observation of the fracture of CAS-glass/SiC composites, part I delamination. *Journal of Materials Science*, 1994, **29**, 3643.
6. Albertsen, H., Ivens, J., Peters, P., Wevers, M. and Verpost, I., Interlaminar fracture toughness of CFRP influenced by fibre surface treatment: part 1 Experimental results. *Composite Science and Technology*, 1995, **54**, 133.
7. Broek, D., *Elementary Engineering Fracture Mechanics*, 4th edn. Martinus Nijhoff, Dordrecht, 1986.
8. Heuer, A. H., Transformation toughening in ZrO_2-containing ceramics. *J. Am. Ceram. Soc.*, 1987, **70**, 689.
9. Cox, B. N., Extrinsic factors in the mechanics of bridged cracks. *Acta Metall. Mater.*, 1991, **39**, 1189.
10. Zok, F. and Hom, C. L., Large scale bridging in brittle matrix composites. *Acta Metall. Mater.*, 1990, **38**, 1895.
11. Suo, Z., Bao, G. and Fan, B., Delamination R-curve phenomena due to damage. *J. Mech. Phys. Solids*, 1992, **40**, 1.
12. Budiansky, B., Amazigo, J. C. and Evans, A. G., Small scale crack bridging and the fracture toughness of particulate reinforced ceramics. *J. Mech. Phys. Solids*, 1988, **36**, 167.
13. Hutchinson, J. W. and Jensen, H. M., Models of fiber debonding and pullout in brittle composites with friction. *Mechanics of Materials*, 1990, **9**, 139.
14. Cox, B. N. and Marshall, D. B., The determination of crack bridging forces. *Int. J. Fracture*, 1991, **49**, 159.
15. Bao, G. and Song, Y., Crack bridging for fiber composites with slip-dependent interfaces. *J. Mech. Phys. Solids*, 1993, **41**, 1425.
16. Foote, R. M. L., Mai, Y.-W. and Cotterell, B., Crack growth resistance curves in strain-softening materials. *J. Mech. Phys. Solids*, 1986, **34**, 593.
17. Fett, T., Evaluation of the bridging relation from crack-opening-displacement of the measurements by use of the weight function. *J. Am. Ceram. Soc.*, 1995, **78**, 945.
18. Brenet, P., Conchin, F., Fantozzi, G., Reynaud, P., Rouby, D. and Tallaron, C., Direct measurement of the crack bridging tractions: a new approach of the fracture behaviour of ceramic-matrix composites. *Comp. Sci. Technol.*, 1996, **56**, 817.
19. Rice, J. R., A path independent integral and the approximate analysis of strain concentrations by notches and cracks. *Journal of Applied Mechanics*, 1968, **35**, 379.
20. Bao, G. and Suo, Z., Remarks on crack-bridging concepts. *Appl. Mech. Rev.*, 1992, **45**, 355.
21. Suo, Z., Delamination specimens for orthotropic materials. *Journal of Applied Mechanics*, 1990, **57**, 627.
22. Li, V. C. and Ward, R. I., A novel testing technique for post-peak tensile behaviour of cementitious materials. In *Fracture Toughness and Fracture Energy—Testing Methods for Concrete and Rocks*, eds. H. Mihashi, H. Takahashi and F. H. Wittmann. A. A. Balkema, Rotterdam, 1989, p. 183.
23. Sørensen, B. F., Brethe, P. and Skov-Hansen, P., Controlled crack growth in ceramics: the DCB-specimen loaded with pure moments. *J. Euro. Ceram. Soc.*, 1996, **16**, 1021.
24. Sørensen, B. F., Horsewell, A., Jørgensen, O. and Kumar, A. N., A fracture resistance measurements method for in-situ observation of crack mechanisms. *J. Am. Ceram. Soc.*, in press.
25. Gu, P., Notch sensitivity of fiber-reinforced ceramics. *Int. J. Fracture*, 1995, **70**, 253.

[A9]

Jacobsen, T. K., and Sørensen, B. F., 2001

"Mode I Intra-laminar crack growth in composites - modelling of R-curves from measured bridging laws"

Composites part A, Vol. 32, pp. 1-11

ELSEVIER

Composites: Part A 32 (2001) 1–11

composites
Part A: applied science and manufacturing

www.elsevier.com/locate/compositesa

Mode I intra-laminar crack growth in composites — modelling of R-curves from measured bridging laws

T.K. Jacobsen[a,*,1], B.F. Sørensen[b]

[a]*Research and Development Department, LM Glasfiber A/S, Rolles Møllevej 1, 6640 Lunderskov, Denmark*
[b]*Materials Research Department, Risø National Laboratory, P.O. Box 49, 4000 Roskilde, Denmark*

Received 10 January 2000; revised 10 July 2000; accepted 20 July 2000

Abstract

In this paper R-curves for mode I crack growth in composites are modelled based on measured bridging laws. It is shown that simulated and measured R-curves are in good agreement. Simulations show that variations in the measured bridging law parameters can explain the scatter in overall R-curves. Finite element procedures for treating a generalised nonlinear law for intra-laminar fibre bridging (longitudinal splitting) in combination with R-curve modelling are demonstrated for mode I loading. The difference between calculating the crack growth resistance by linear elastic fracture mechanics and by the *J* integral for the double cantilever beam specimen loaded by wedge forces is elucidated. It is shown that calculating the crack growth resistance by linear elastic fracture mechanics results in overestimation of the steady-state crack growth resistance. © 2000 Elsevier Science Ltd. All rights reserved.

Keywords: A. Polymer-matrix composites (PMCs); B. Fracture toughness; B. Delamination; C. Finite element analysis (FEA)

1. Introduction

Crack bridging results in rising crack growth resistance with increasing crack extension (R-curve behaviour). Several cracking problems involve large-scale bridging (LSB). Fig. 1 shows an example of intra-laminar crack growth of a unidirectional fibre composite. Under LSB, experiments have shown that R-curves depend on specimen geometry [1–3]. Therefore, it has been proposed [4] that under LSB, the failure process should be described by a bridging law, viz. the relationship between the local crack-opening displacement δ and the local bridging traction σ resulting from the bridging ligaments, $\sigma = \sigma(\delta)$.

Adopting the bridging law as the basic material law, a number of studies [1,3–13] have predicted the fracture behaviour of test specimens or components by the use of idealised bridging laws, e.g. rectilinear or linear bridging laws. Studies that focus on the measurement of real bridging laws are, for example, those of Li and Ward [12], Kaute et al. [13], Brenet et al. [14], Sørensen and Jacobsen [2], Lindhagen [15] and Andersson and Stigh [16]. A discussion of these experimental methods can be found in Sørensen and Jacobsen [17]. A simplified approach, where the crack-opening profile is assumed to increase *linearly* with the distance from the crack tip and the bridging law shape is assumed a priori, can be used to determine the resulting bridging stresses [5]. Recently, we have, by the use of a *J*-integral-based approach, measured the bridging law under mode I conditions during transverse splitting of a unidirectional carbon-fibre/epoxy composite [2]. The bridging law was fitted by the function

$$\sigma(\delta) = \frac{\Delta J_{ss}}{2}\left(\frac{\delta}{\delta_0}\right)^{-1/2}, \qquad \text{for } \delta_t < \delta < \delta_0, \tag{1}$$

where ΔJ_{ss} is the increase in crack growth resistance due to

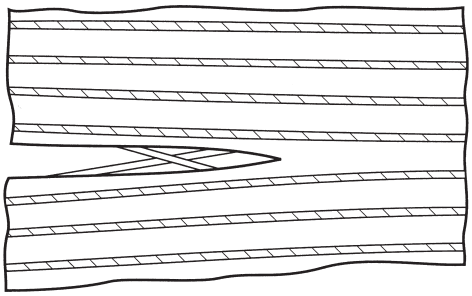

Fig. 1. Schematics of intra-laminar crack growth (longitudinal splitting).

* Corresponding author. Tel.: +45-4677-5818; fax: +45-4677-5758.
[1] Currently at Risø National Laboratory.
E-mail address: torben.jacobsen@risoe.dk (T.K. Jacobsen).

PII: S1359-835X(00)00139-1

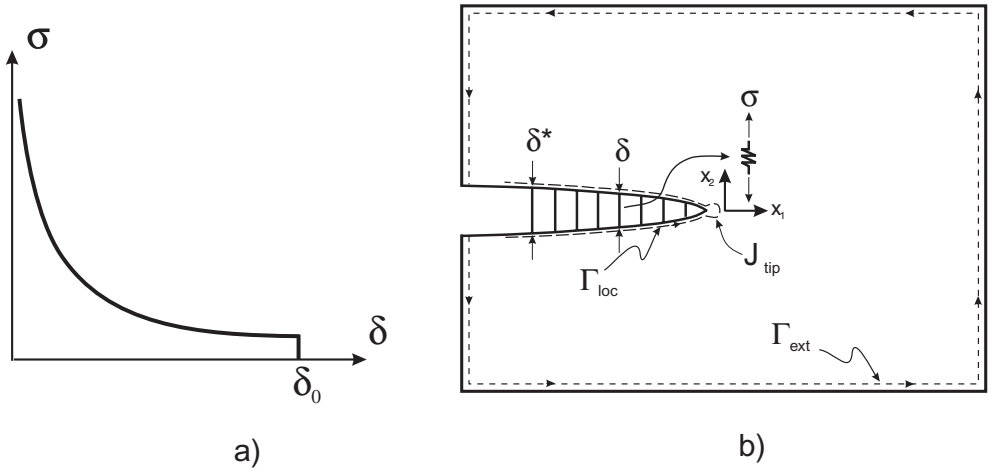

Fig. 2. (a) Nonlinear softening bridging law, and (b) J integral paths and definition of bridging law parameters.

bridging (from zero to steady-state bridging), δ_0 is the crack opening where the bridging stress vanishes and δ_t is the minimum detectable crack opening (experimentally, $\sigma(\delta)$ was only determined for a small, but finite crack opening $\delta_t \approx 30$–50 μm). In these experiments, the crack bridging mechanism was identified as fibre cross-over bridging, see Fig. 1. Spearing and Evans [1] developed a model for this bridging mechanism. Modelling the bridging ligaments by beams in bending, their model gave the bridging law (neglecting shear deformations)

$$\sigma(\delta) = \lambda \delta^{-1/2}, \tag{2}$$

where λ is a parameter that depends on stiffness and geometry of the bridging ligaments as well as the fracture energy of the interface between fibre and matrix. Note that the micromechanics-based bridging law given by Eq. (2) has the same functional form as the measured bridging law (1). An alternative model, which assumes that tension and not bending of the fibres controls the bridging tractions on the crack faces, has been proposed by Kaute et al. [18]. The model by Kaute predicts an initial rising bridging stress followed by an exponential decaying bridging stress. The model by Spearing and Evans predicts a finite value of bridging stress at zero crack opening and a monotonic decaying bridging stress with increase in crack opening. More work is needed to establish and verify the underlying micromechanics.

In an earlier paper [2] we also measured R-curves (J_R–Δa curves, where J_R is the crack growth resistance and Δa is the crack extension) for various beam heights of the double cantilever beam (DCB) specimen. A model, using a linear softening bridging law [4] was used for simulating R-curves. Although the R-curves predicted by this model were in qualitative agreement with the measured J_R–Δa data (including a strong specimen dependence), there were significant differences in the shape of the measured and predicted R-curves. For small crack extensions the model data were always somewhat lower than the measured J_R data. The purpose of the present paper is to demonstrate that, by using the measured bridging law (1), we can calculate J_R–Δa curves that are in much better agreement with the experimentally observed J_R–Δa curves than the ones based on linear softening. Modelling of test specimens including bridging laws represents a first step. The second step is to use bridging laws in analysis of industrial components. If modelling with bridging laws can simulate the physical crack behaviour of test specimens of various sizes well, it can be anticipated that the approach will work well on arbitrary component geometries.

The paper is organised as follows. First, we propose a more general description of the nature of fibre bridging resulting from longitudinal splitting and mode I loading (Fig. 1). Secondly, some details on the finite element model are provided. Thirdly, R-curves are simulated and compared with experimental results.

2. Problem statement

The fact that the measured bridging law (1) and the micromechanical modelling (2) both show the same bridging law shape has led us to believe that the power law shape (2) is of a more general nature for mode I fibre cross-over bridging, see Fig. 2a. Therefore, we propose a general class of bridging laws for pure mode I crack

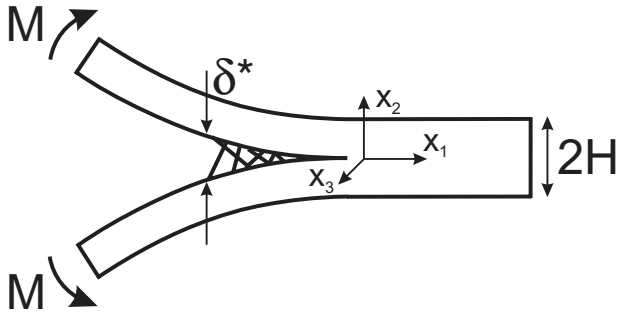

Fig. 3. DCB specimen loaded with pure moment.

bridging given by

$$\sigma(\delta) = \begin{cases} (n+1)\dfrac{\Delta J_{ss}}{\delta_0}\left(\dfrac{\delta}{\delta_0}\right)^n, & \text{for } 0 < \delta \le \delta_0 \\ 0 & \text{for } \delta > \delta_0 \end{cases} \tag{3}$$

where n is a shape parameter, $-1 < n < 0$.

First, we calculate the energy uptake by the fracture processes occuring near the crack tip (process zone) and the bridging fibres. Since the nonlinear fracture zone is large, it is characterised by the energy release rate J, which is calculated by use of the path-independent J integral [19]. The J integral is evaluated in counter-clockwise direction along the contour Γ_{loc} going around the crack from one crack face to the other just outside the bridging zone, see Fig. 2b. The result is

$$J = J_{tip} + \int_0^{\delta^*} \sigma(\delta)\, \mathrm{d}\delta, \tag{4}$$

where J_{tip} is the J integral evaluated at a contour at the crack tip and δ^* is the end-opening of the crack bridging at the notch root. During cracking J will be equal to the overall fracture resistance J_R and J_{tip} will be identical to the fracture energy J_0 of the crack tip. Inserting Eq. (3) into Eq. (4) and performing the integration give

$$J_R = J_0 + \Delta J_{ss}\left(\frac{\delta^*}{\delta_0}\right)^{n+1}, \qquad \text{for } 0 < \delta^* < \delta_0. \tag{5}$$

In this paper we analyse a specific fracture mechanics test specimen namely the DCB specimen shown in Fig. 3, which is widely used for evaluating crack growth resistance of materials. We have in previous papers favoured an approach based on applying a pure bending moment [2,17], instead of the conventional method of applying a wedge force. The reasons for this are that the applied energy release rate J (the J integral evaluated along the external boundaries Γ_{ext} of the specimen, see Fig. 2b) is independent of: (i) the crack length, and (ii) the details of the bridging law [4]. This is *not* the case for wedge force loaded DCB specimens. For a pure bending moment M and plane strain conditions, J is given by [20]

$$J = 12(1 - \nu_{13}\nu_{31})\frac{M^2}{b^2H^3E_{11}}, \tag{6}$$

where M is the applied moment, ν is Poisson's ratio, b is the width of the specimen, H is the height of one beam, E is Young's modulus of the beam and indices indicate coordinate

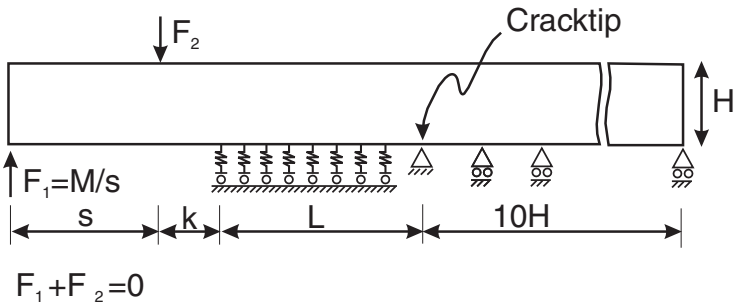

Fig. 4. Problem statement and boundary conditions for pure moment loaded DCB specimen. For symmetry reasons only one loading arm is considered.

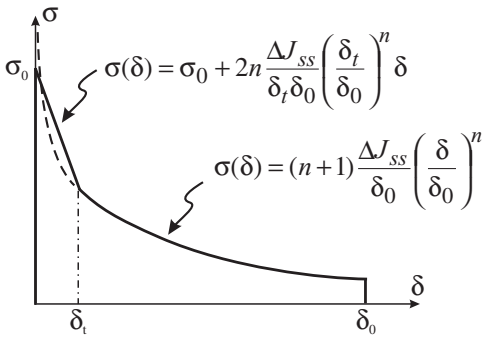

Fig. 5. Schematics of practical implementation of the nonlinear bridging law.

directions shown in Fig. 3. For plane stress the term $(1 - \nu_{13}\nu_{31})$ in Eq. (6) vanish.

3. Modelling procedures

The coupled beam–spring problem shown in Fig. 4 was solved by finite element calculations. Owing to symmetry only one beam of the DCB specimen is considered. We have used plane strain conditions, but plane stress conditions may have been just as appropriate. The bridging length is denoted by L. As long as $\delta^* < \delta_0$ the bridging length is equal to the crack extension Δa ($L = \Delta a$). The un-cracked part of the specimen is roller-supported (a symmetry condition) and it has the length $10H$. The node at the crack tip has no degree of freedom. The external bending moment was applied to the specimen by the use of two load points, where the forces F_1 and F_2 are equal and opposite in magnitude; this results in a pure bending moment M. The distance between the forces was $s = 0.05$ m and the distance k from F_2 to the initial notch root was for simplicity set to zero. No disturbance of the J_{tip} value was found for various k values (>0) with the chosen s. However, this is, in general, not the case as shown by finite element calculations by Sørensen et al. [21] in a study of unbridged DCB specimens. The increment in bending moment was prescribed by controlling the rotation of the beams by the use of a procedure outlined in Appendix A. The mesh was made up by eight-noded iso-parametric plane strain solid elements. For each fixed crack extension the load was applied incrementally until the J integral around the crack tip J_{tip} was equal to the intrinsic fracture energy J_0. Three J integral contours were evaluated very close to the crack tip (element length nearest crack tip ~50 μm). It was ensured that there was no contribution from the bridging fibres to J_{tip} by requiring that the magnitude of the three contour integrals differed by less than 1% and that J_{tip} did not show any spatial dependence. The bridging zone was divided into 58 elements. An in-house-developed Fortran program was used for automatically setting up the mesh, loading type (pure moment or wedge force) and distributing the bridging stresses correctly to each node of the bridged elements, see Appendix A. The finite element runs were carried out by the use of the commercial finite element program ABAQUS (Version 5.8). J_R was computed from Eq. (6) using the applied moment, i.e. $J_R = J$ at the value of M where the crack growth criteria $J_{tip} = J_0$ is fulfilled.

The bridging law (3) has a singularity in $\delta = 0$; $\sigma \to \infty$ as $\delta \to 0$. An infinite stress at zero crack opening is probably not physically acceptable. In fact, the previously mentioned measured $\sigma(\delta)$ data were only valid above a certain crack opening δ_t (typically 30–50 μm) owing to the measurement technique used. More refined techniques have been employed more recently to measure smaller crack openings accurately [3,16,22]. Furthermore, the micromechanical model by Spearing and Evans [1] predicts a finite bridging stress when shear deformation of the bridging ligaments is included in the model [2]. Therefore, in the present work a linear softening behaviour was used below a transition crack-opening displacement δ_t. A maximum stress σ_0 is defined at zero crack-opening displacement. To prevent crack inter-penetration a very stiff behaviour was employed in compression (similar to the stiffness of the composite). The bridging law was implemented as follows, see also Appendix B and Fig. 5

$$\sigma(\delta) = \begin{cases} \sigma_0 + 2n\dfrac{\Delta J_{ss}}{\delta_t \delta_0}\left(\dfrac{\delta_t}{\delta_0}\right)^n \delta, & 0 \le \delta \le \delta_t \\ (n+1)\dfrac{\Delta J_{ss}}{\delta_0}\left(\dfrac{\delta}{\delta_0}\right)^n, & \delta_t \le \delta \le \delta_0 \\ 0, & \delta > \delta_0 \end{cases} \tag{7}$$

where σ_0 is given by

$$\sigma_0 = (1-n)\frac{\Delta J_{ss}}{\delta_t}\left(\frac{\delta_t}{\delta_0}\right)^{n+1} \tag{8}$$

The bridging fibres were approximated by 1D springs having the nonlinear behaviour given in Eq. (7). To get energy consistency the maximum stress σ_0 was determined such that the area under the σ–δ curves from $\delta = 0$ to $\delta = \delta_t$ for Eqs. (3) and (7) were identical, see Appendix B.

4. Case study

4.1. Experiments

In a previous paper [2] we measured R-curves and bridging laws of a unidirectional carbon/epoxy composite by DCB specimens loaded with pure bending moments. The crack extended in the intra-laminar direction (longitudinal splitting). Four different beam heights were employed to investigate the effect of specimen size and R-curve behaviour. For simplicity the material is assumed to be elastically isotropic and homogeneous. Specimen characteristics

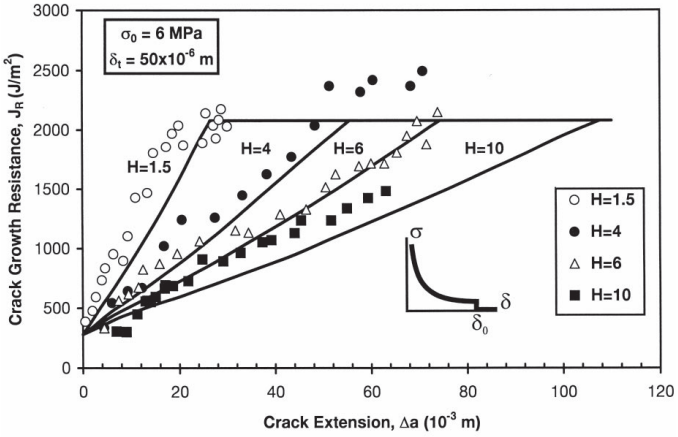

Fig. 6. Experimental and simulated R-curves for a unidirectional carbon/epoxy material.

were: $E_{11} = 130$ GPa, $\nu_{13} = \nu_{31} = 0.3$, $b = 0.005$ m and $H = (0.0015, 0.004, 0.006$ and 0.01 m). The measured R-curves are shown in Fig. 6. For clarity, only one set of data for each beam height is shown. Measured J_R–δ^* data points (crack growth resistance versus end-opening at the initial notch root) obtained from five specimens are shown in Fig. 7.

4.2. Modelling of R-curves

4.2.1. Effect of specimen size

Based on the J_R–δ^* data points in Fig. 7 the bridging law parameters (ΔJ_{ss}, n and δ^*) shown in Table 1 were determined by a best fit to all data points in Fig. 7. Inserting these values into Eq. (8) gives the maximum bridging stress $\sigma_0 = 6$ MPa. Simulations were performed to investigate if there would be an effect of the choice of σ_0. Fig. 8 shows a computed R-curve for $\sigma_0 = 20$ MPa ($\delta_1 = 4.6$ μm and $H = 0.004$ m). Only for very short crack extensions $\Delta a < 0.006$ m a slightly higher J_R was calculated for $\sigma_0 = 20$ MPa than for $\sigma_0 = 20$ MPa. To provide consistency throughout the rest of the paper we use $\delta_t = 50$ μm ($\sigma_0 = 6$ MPa) in all simulations.

The simulated R-curves are shown in Fig. 6. It is seen that there is a reasonably good agreement between experimental and simulated R-curves. However, it is noted that the experimental points seem to rise more steeply in the

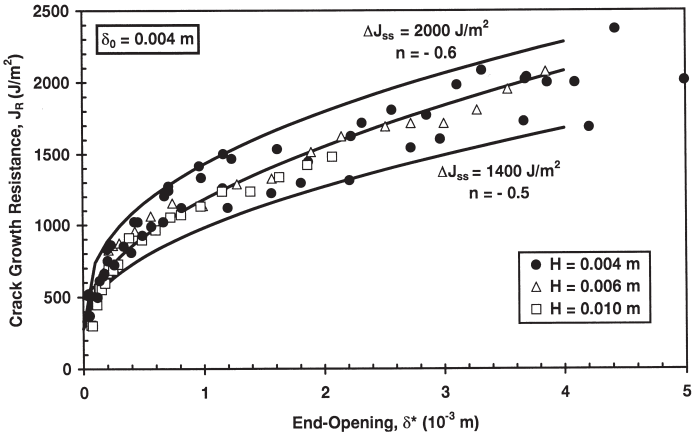

Fig. 7. The crack growth resistance as a function of end-opening for $H = 0.004$ m. Upper and lower curve fits define the experimental scatter band. Middle curve is the best fit to all points. Experimental results from five specimens.

Table 1
Fitted bridging law parameters

	ΔJ_{ss} (J/m^2)	n (–)	δ_0 (m)
Upper bound	2000	−0.6	0.004
Best fit	1800	−0.5	0.004
Lower bound	1400	−0.5	0.004

beginning of the R-curve compared with the simulated R-curve. This may be attributed to the uncertainty of the σ–δ data for small δ as discussed previously.

4.2.2. Linear versus nonlinear bridging law

In the earlier experimental paper [2] a linear softening bridging law $\sigma(\delta) = \sigma_0 + S\delta$ was used for simulating the R-curve behaviour based on results in the paper by Suo et al. [4]. The parameters for the linear bridging law were derived from the experimental R-curves (see insert in Fig. 9). The following parameters were computed [2]: $S = -305 \times 10^6$ N/m^3, $\sigma_0 = 1.04$ MPa, $\delta_0 = 3.41 \times 10^{-3}$ m. A comparison between R-curves calculated by the use of the linear and the nonlinear softening law (3) is shown in Fig. 9. The areas under the bridging law curves are equal in accordance with Eq. (4). It is evident that the R-curves have quite different shapes. The linear-law-based R-curve is S-shaped whereas the nonlinear-law-based R-curve is almost a straight line. At low J_R values small increments in applied moment give large crack extensions for the linear law. Note that the R-curves coincide at $\delta^* = 0.98 \times 10^{-3}$ m corresponding to $J_R = 1172$ J/m^2. This δ^* is the point where Eq. (4) gives the same J_R result for both bridging laws.

4.2.3. Specimen to specimen variations

Experimentally, specimen to specimen variations were observed for both the bridging law and the R-curves. For $H = 4$ mm three experiments were performed. The experimental J_R–δ^* and J_R–Δa data points are shown in Figs. 7 and 10, respectively. An upper bound, lower bound and best fit to the J_R–δ^* data are shown in Fig. 7 and summarised in Table 1. The upper and lower bound bridging laws were subsequently used for simulating upper and lower "scatter bands" for the R-curves. The modelled scatter band is shown in Fig. 10. It is seen that the simulated lower bound R-curve is in good agreement with the experiments, but there are a few data points that lie above the simulated upper bound. Nevertheless, the experimental trend of an increasing scatter in R-curve measurements is clearly reflected in the simulations.

4.2.4. Pure moment versus wedge force loaded DCB specimen

Fig. 11 shows a DCB specimen loaded by wedge forces, P. The J integral around the external boundary now depends on the details of the bridging law and the crack extension [4,17]. For clarity, we use the symbol $\mathcal{G}$ for the energy release rate calculated by linear elastic fracture mechanics (LEFM). The LEFM calculation of $\mathcal{G}$ is valid when fibre bridging occurs under small-scale bridging and the crack tip process zone is small compared with specimen dimensions. The *nominal* crack growth resistance $\mathcal{G}_R$ is given by (plane strain)

$$\mathcal{G}_R = 12(1 - \nu_{13}\nu_{31})\frac{P^2 l^2}{b^2 H^3 E_{11}}, \tag{9}$$

where l is the distance from the wedge force to the crack tip. Under LSB $\mathcal{G}_R$ does not equal the J integral over the external boundary of the DCB specimen. However, LEFM calculations have often been used for test specimens experiencing LSB. As shown experimentally by Mai and Hakeem [23], numerically by Suo et al. [4] and analytically by Sørensen

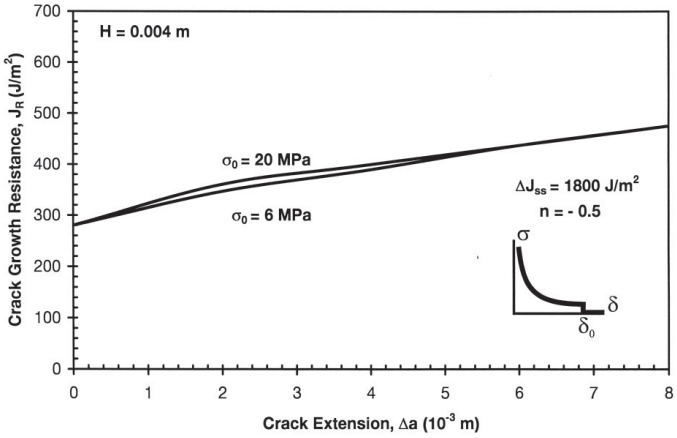

Fig. 8. Effect of maximum stress σ_0 on R-curve behaviour.

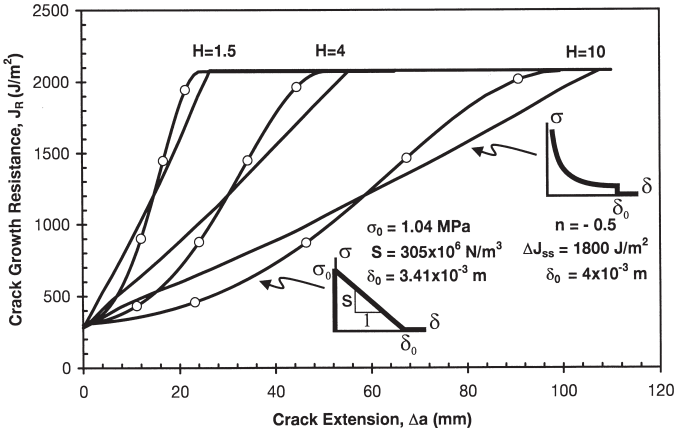

Fig. 9. Comparison of simulated R-curve behaviour for a linear softening law (circular symbols) and the nonlinear softening power law.

and Jacobsen [17] nominal R-curves can exhibit "overshoot", i.e. $\mathscr{G}_R > J_R$. Evaluating the J integral over the external boundaries, it can be shown [17,24] that the J integral can be calculated if θ, the rotation of the beam where the wedge force is applied ($x_1 = -l$), is measured. Then J and thus J_R can be calculated by

$$J = \frac{2P\theta}{b}. \tag{10}$$

The reason for $\mathscr{G}_R > J_R$ is that the fibre bridging causes the rotation of the beam θ to be smaller than modelled by the standard beam theory. A procedure that included measurement of the beam-end rotation θ was used by Andersson and Stigh [16] to derive the complete stress–displacement relation for an adhesive layer.

Fig. 11c shows simulations of R-curve behaviour calculated by nominal crack growth resistance $\mathscr{G}_R$ in Eq. (9) and by the J integral J_R of Eq. (10) for $H = 0.004$ m, $L_1 = 0.05$ m and the bridging law parameters shown in Fig. 11. Curve AB corresponds to $\delta^* < \delta_0$ (incipient fibre bridging, see Fig. 11a) and curve BC corresponds to $\delta^* \geq \delta_0$ (see Fig. 11b). After the maximum $\mathscr{G}_R$ value has been reached, the bridging zone length L and $\mathscr{G}_R$ decreases with increasing Δa. $\mathscr{G}_R$ approaches J_R and L the steady-state bridged crack length L_{ss} of the DCB specimen loaded with pure bending moments. The simulation for part BC thus requires the

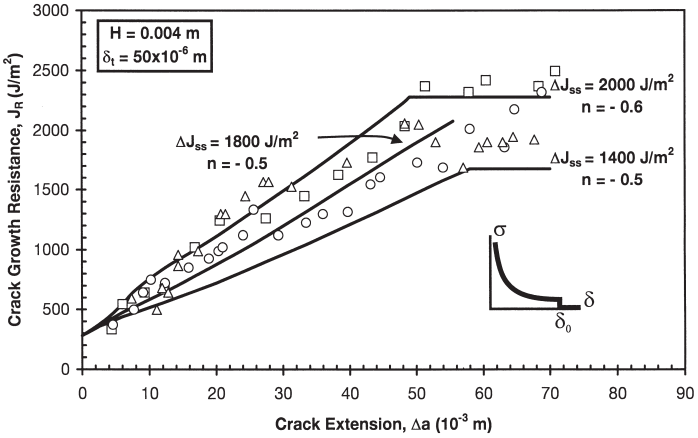

Fig. 10. The crack growth resistance as a function of crack extension for $H = 0.004$ m. Upper and lower curves define the simulated scatter band. Middle curve is the simulated R-curve based on the J_R–δ^* best fit to all points.

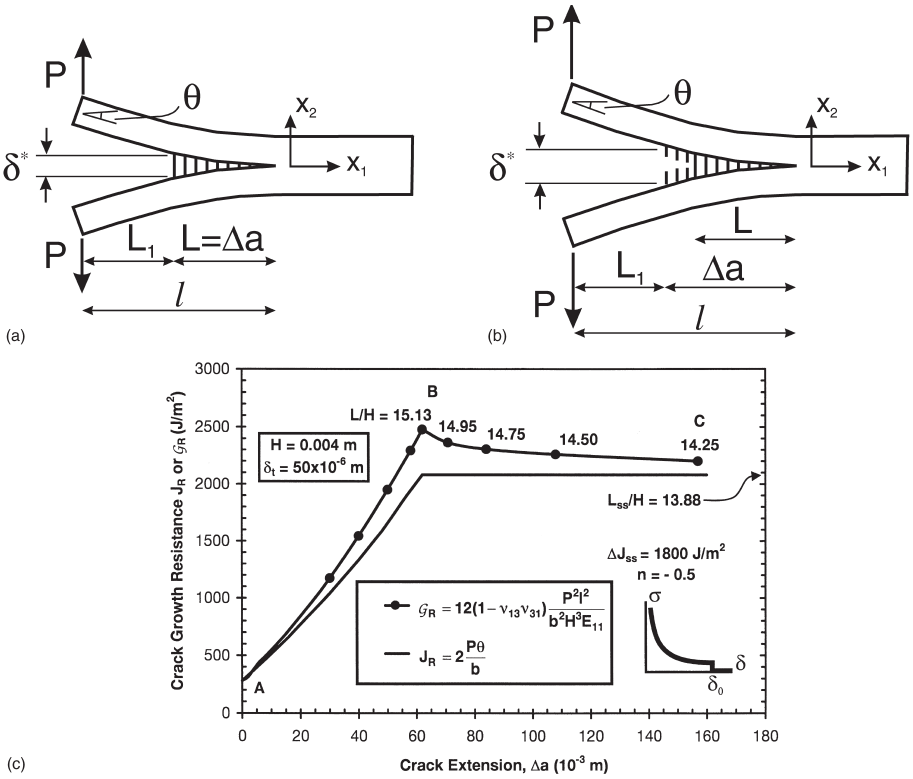

Fig. 11. Wedge force loaded DCB specimen. (a) Incipient fibre bridging (curve AB). (b) Situation after maximum crack growth resistance has been reached (curve BC). (c) Simulated R-curves based on nominal crack growth resistance and J integral.

determination of L, such that δ at $x_1 = -L$ equals δ_0 and $J_{tip} = J_0$. This is an iterative numerical process. For the carbon/epoxy material, a maximum overshoot $\mathcal{G}_R = 1.18J_R$ was calculated at point B corresponding to $L/H = 15.13$.

Fig. 11 can also be used for explaining the influence of pre-cut notch length on the crack length required to attain steady-state. Such an effect has been observed experimentally by Rhee [25]. As the crack extension becomes large this corresponds to a long pre-cut notch L_1. We estimate, for the present material, bridging law and beam height ($H = 0.004$ m), that $\mathcal{G}_R/J_R < 1.01$ for a pre-cut notch length $L_1 > 0.25$ m.

5. Conclusions

The purpose of this paper was to model R-curves based on measured bridging laws. The approach was to measure the bridging law, subsequently insert this law into a finite element code and then simulate experimental R-curves. It was demonstrated that R-curves could be simulated by the measured nonlinear law with an accuracy better than by using, for example, a linear bridging law. The excellent agreement between simulations and experiments provides confidence in the measured bridging law shape and that the physical crack extension can be modelled by implementing bridging laws in finite element codes. The effect of specimen geometry on the R-curve behaviour was clearly shown and it is concluded that under large-scale bridging, an R-curve is not a material property.

Comparison of the nonlinear bridging law (3) with the linear softening law shows that large differences in crack growth behaviour can be expected, although the areas under the linear and nonlinear bridging law curves are the same. Specimen to specimen variations in measured bridging laws were used as input to the R-curve simulations for $H = 4$ mm. It was shown that the simulated R-curve scatter band could explain the experimental scatter in R-curves.

We suggest using the bridging law as material property. The bridging law can be determined by measuring the end-opening of the bridging zone and the *J* integral, for example, on either a wedge force loaded DCB specimen (where in addition the rotation must be measured) or a pure moment loaded DCB specimen. The use of the nominal energy release rate should be avoided as in this case R-curves can exhibit erroneous "overshoot" tendencies, see Fig. 11.

The industrial potential of the method is indeed large as the fibre bridging contributions to the crack growth resistance can be derived as an independent quantity in a fast and reliable way using the pure bending moment loading method. Applications are, for example, gelcoat adhesion to backing laminate, adhesive bonds and inter-laminar fracture resistance.

It is believed that the outlined experimental method for in situ measurements of the bridging law based on the *J* integral approach can be used for simulating meaningful crack extensions in components. However, in real components a mixed-mode situation is usually encountered. The next logical step is therefore to develop experimental methods for simultaneously measuring opening and sliding displacements by the use of test configurations that are independent of the details of the bridging laws and loading method. To our knowledge experimental data on measurements of mixed-mode bridging laws are not available in the literature. However, it is straightforward to extend the finite element code to include springs simulating the sliding (mode II) behaviour [10]. However, only experiments can show whether a distinct separation in modes can be justified from a modelling point of view or more advanced coupled mixed-mode bridging laws are necessary.

Acknowledgements

T.K.J. was supported partly by a grant from the Akademiet for Tekniske Videnskaber (ATV) through grant no. EPD015 Risø. B.F.S. was supported by The Engineering Science Centre at Risø for Structural Characterisation and Modelling of Materials. P. Gudmundson and A. Wikström, Solid Mechanics Department at KTH in Sweden are gratefully acknowledged for suggesting the displacement controlling procedure.

Appendix A. Finite element procedures for crack bridging simulations

A.1. Equivalent node forces

To be able to capture the square-root singularity at the crack tip in the elastic continuum it is usually recommended to use eight-node iso-parametric plane strain solid elements. Around the crack tip the mid-point nodes were moved to the quarter points, see Fig. A1. In order to distribute the crack bridging stresses correctly on the solid elements, the equivalent node forces were calculated using the principle of virtual work and the shape functions, N_i [26].

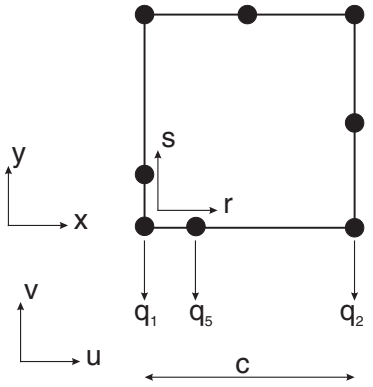

Fig. A1. Eight-noded element with quarter-point nodes used for the first element at the crack tip.

The local coordinate system is given by *r–s*, the global coordinate system by *x–y* and global displacements are denoted *u* and *v*, see Fig. A1. The equivalent nodal force at a node, q_i, is equal to the sum of the nodal forces from each element connected to the node, q_i^e

$$q_i = \sum q_i^e. \tag{A1}$$

The contribution to q_i from each element is given by [26]

$$q_i^e = \int_0^1 N_i(r)\sigma(r)\,\frac{\mathrm{d}x}{\mathrm{d}r}\,\mathrm{d}r, \tag{A2}$$

where $\sigma(r)$ is the distributed stress acting on the element along $(r,0)$, i.e. it is the bridging stress on the crack face.

In our case we consider only one of the beams of the DCB specimen. Denote half of the total crack opening by *v*, i.e. $v = \delta/2$. The bridging law is of the form $\sigma(\delta) = \lambda\delta^n = \lambda^* v^n$, where $\lambda^* = \lambda 2^n$. The global length of the element is *c* and the nodal coordinates are $x_1 = 0$, $x_5 = c/2$, and $x_2 = c$. The contribution from one element to the nodal forces is then

$$q_i^e = \lambda^* c \int_0^1 N_i(r)[N_1(r)v_1 + N_2(r)v_2 + N_5(r)v_5]^n\,\mathrm{d}r \tag{A3}$$

as $\mathrm{d}x/\mathrm{d}r = c = x_2 - x_1$.

Eq. (A3) can only be solved by incorporating it in a constitutive material model — it cannot be implemented using, for example, standard spring elements to simulate the effect of bridging. A significant simplification can be reached by assuming that the displacements are equal along the element, i.e.

$$v_1 = v_2 = v_5 = v. \tag{A4}$$

This assumption further implies that the bridging stress is

the same along the element and q_i^e can now be written as

$$q_i^e = \int_0^1 N_i \sigma \frac{dx}{dr} dr \tag{A5}$$

For each node (1,2,5) with $x_1 = 0$, $x_2 = c$, $x_5 = c/2$

$$q_1^e = q_2^e = \tfrac{1}{6}\sigma c, \tag{A6}$$

$$q_5^e = \tfrac{4}{6}\sigma c. \tag{A7}$$

For the quarter-point nodes at the crack tip the coordinates are: $x_1 = 0$, $x_2 = c$, $x_5 = c/4$

$$q_1^e = 0, \tag{A8}$$

$$q_2^e = \tfrac{2}{6}\sigma c, \tag{A9}$$

$$q_5^e = \tfrac{4}{6}\sigma c. \tag{A10}$$

A.2. Displacement controlling algorithm for pure moment loaded DCB specimen

The purpose is to formulate a method for controlling the displacement (rotation) of the pure moment loaded DCB specimen and calculate the resulting forces and thus the applied bending moment, see Fig. 4. The displacements v_1 and v_2 of two nodes are to be controlled such that the resulting forces in the two nodes, F_1 and F_2, are identical in magnitude but different in direction, so they apply a pure bending moment. To accomplish this, v_1 and v_2 are interconnected by two additional so-called dummy nodes A and B, having displacements v_A and v_B, respectively. In the following we derive the necessary relationship between v_1, v_2, v_A and v_B. The displacement of node A is defined as

$$v_A = v_1 - v_2. \tag{A11}$$

Note that $\theta = \arctan(v_A/s) \approx v_A/s$ is the rotation of the beam, with s being the difference in x-coordinates between nodes 1 and 2, see Fig. A2. The displacement in node B is set to

$$v_B = v_1 + v_2. \tag{A12}$$

Using the principle of virtual work the applied incremental elastic energy dw is given by

$$dw = F_1\, dv_1 + F_2\, dv_2. \tag{A13}$$

Similarly, the incremental elastic energy applied to nodes A and B is

$$dw = F_A\, dv_A + F_B\, dv_B, \tag{A14}$$

where F_A and F_B are the forces in nodes A and B, respectively. Finally, since we want to apply a pure moment the following force balance must be required, i.e.

$$F_1 + F_2 = 0. \tag{A15}$$

The forces in the dummy nodes, F_A and F_B, must (according to the principle of virtual work) perform the same incremental work as F_1 and F_2. Inserting Eqs. (A11) and (A12) into Eq. (A14) gives

$$dw = (F_A + F_B)\, dv_1 + (F_B - F_A)\, dv_2. \tag{A16}$$

Therefore, Eq. (A16) must be equal to Eq. (A13) and the following force relations are obtained

$$2F_A = F_1 - F_2 \qquad \textit{and} \qquad 2F_B = F_1 + F_2. \tag{A17}$$

Prescribing $F_B = 0$ in Eq. (A17) fulfils Eq. (A15), i.e. applies a pure bending moment, and gives $F_A = F_1$, i.e. the resulting force in node 1 is provided by the reaction force in node A. Thus, the constraints between v_1, v_2, v_A and v_B in Eqs. (A11) and (A12) do apply the correct constraints. The multi-point constraints (A11) and (A12) are provided to the finite element code as

$$2v_1 - v_A - v_B = 0 \qquad \textit{and} \qquad 2v_2 + v_A - v_B = 0. \tag{A18}$$

In summary, v_A is the prescribed displacement difference between nodes 1 and 2, corresponding to the rotation of the beam and F_A is the applied force to the beam by which the bending moment $M = F_1 s$ can be calculated. v_A is thus the loading parameter that is increased during the simulations, corresponding to a higher moment. Note that with v_A given, Eq. (A18) provides two constraints, but there are three unknown displacements v_1, v_2 and v_B. However, v_B is a free parameter that is determined as a part of the total finite element solution, because the beam must be able to deflect freely; only the rotation θ is controlled.

A.3. The beam-end rotation of the wedge loaded DCB specimen

The external J integral of the wedge loaded DCB specimen is calculated by Eq. (10). In the finite element computations the rotation θ shown in Figs. 11a and A3 is

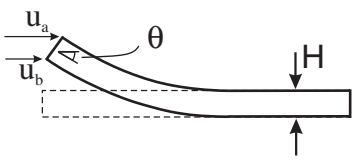

Fig. A2. Displacements used for controlling the rotation and applying a pure moment to the beam arm of a DCB specimen.

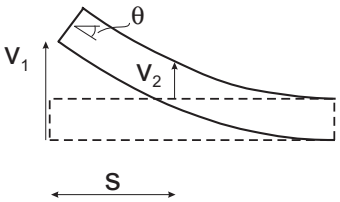

Fig. A3. Definition of rotation of the end of the beam of a DCB specimen loaded by wedge forces.

approximated by

$$\theta = \arctan\left(\frac{u_a - u_b}{H}\right) \approx \frac{u_a - u_b}{H}, \tag{A19}$$

where u_a and u_b are the displacements in the x-direction of the upper and lower edge of the beam end, respectively. In the finite element calculations small rotations are assumed and θ is thus proportional to the difference of the displacements in loading points a and b, see Fig. A2.

Appendix B. Derivation of the maximum bridging stress

Fig. 5 shows how the nonlinear bridging law is implemented in the finite element code. The maximum stress σ_0 is found by requiring that the area W_2 of the linear softening law in the range $0 \le \delta \le \delta_t$ must equal the area W_1 of the general bridging law (3) in this range. Area W_1 is given by

$$W_1 = \int_0^{\delta_t} (n+1)\frac{\Delta J_{ss}}{\delta_0}\left(\frac{\delta}{\delta_0}\right)^n \mathrm{d}\delta = \Delta J_{ss}\left(\frac{\delta_t}{\delta_0}\right)^{n+1}. \tag{B1}$$

Area W_2 is given by

$$W_2 = \frac{1}{2}(n+1)\Delta J_{ss}\left(\frac{\delta_t}{\delta_0}\right)^{n+1} + \frac{1}{2}\sigma_0\delta_t. \tag{B2}$$

By setting $W_1 = W_2$ the maximum stress at a given δ_t is

$$\sigma_0 = (1-n)\frac{\Delta J_{ss}}{\delta_t}\left(\frac{\delta_t}{\delta_0}\right)^{n+1}. \tag{B3}$$

References

[1] Spearing SM, Evans AG. The role of fiber bridging in the delamination resistance of fiber-reinforced composites. Acta Metall Mater 1992;40:2191.

[2] Sørensen BF, Jacobsen TK. Large-scale bridging in composites: R-curves and bridging laws. Compos A 1998;29:1443.

[3] Cotterell B, Mai Y-W. Fracture mechanics of cementitious materials. 1st ed. Glasgow/London: Blackie/Chapman & Hall, 1996.

[4] Suo Z, Bao G, Fan B. Delamination R-curve phenomena due to damage. J Mech Phys Solids 1992;40:1.

[5] Hu X-Z, Mai Y-W. General method for determination of crack-interface bridging stresses. J Mater Sci 1992;27:3502–10.

[6] Foote RML, Mai Y-W, Cotterell B. Crack growth resistance curves in strain-softening materials. J Mech Phys Solids 1986;34:593.

[7] Bao G, Suo Z. Remarks on crack-bridging concepts. Appl Mech Rev 1992;45:355.

[8] Suo Z, Ho S, Gong X. Notch ductile-to-brittle transition due to localized inelastic band. J Engng Mater Technol 1993;115:319.

[9] Östlund S, Nilsson F. Cohesive zone modelling of damage at the tip of cracks in slender beam structures. Fatigue Fracture Engng Mater Struct 1993;16:663.

[10] He M-Y, Wu B, Suo Z. Notch sensitivity and shear bands in brittle matrix composites. Acta Metall Mater 1994;42:3065.

[11] Gu P. Notch sensitivity of fiber-reinforced ceramics. Int J Fracture 1995;70:253.

[12] Li VC, Ward RJ. A novel testing technique for post-peak tensile behaviour of cementious materials. In: Mihashi H, Takahashi H, Wittmann FH, editors. Fracture toughness and fracture energy-testing methods for concrete and rocks, Rotterdam: A.A. Balkema, 1989. p. 183.

[13] Kaute DAW, Shercliff HR, Ashby MF. Delamination, fibre bridging and toughness of ceramic matrix composites. Acta Metall Mater 1993;41:1959.

[14] Brenet P, Conchin F, Fantozzi G, Reynaud P, Rouby D, Tallaron C. Direct measurements of the crack bridging tractions: a new approach of the fracture behavior of ceramic-matrix composites. Comput Sci Technol 1996;56:817.

[15] Lindhagen J. Notch sensitivity and bridging laws in glass mat composites. PhD dissertation, Department of Materials and Manufacturing Engineering, Div Pol Eng, Luleå University of Technology, Report no. 41, 1998. p. 1402.

[16] Andersson T, Stigh U. An experimental method to determine the complete stress-elongation relation for a structural adhesive layer loaded in peel. In: Delegate Manual 2nd ESIS TC4 Conference on Polymers and Composites, 1999. p. 52.

[17] Sørensen BF, Jacobsen TK. Crack growth in composites: applicability of R-curves and bridging laws. Plast Rubber Compos 2000;29:119.

[18] Kaute DAW, Shercliff HR, Ashby MF. Modelling of fibre bridging and toughness of ceramic matrix composites. Scripta Metall Mater 1995;32:1055.

[19] Rice JR. A path independent integral and the approximate analysis of strain concentrations by notches and cracks. J Appl Mech 1968;35:379.

[20] Bao G, Ho S, Suo Z, Fan B. The role of material orthotropy in fracture specimens for composites. Int J Solids Struct 1992;29:1105.

[21] Sørensen BF, Brethe P, Skov-Hansen P. Controlled crack growth in ceramics: the DCB specimen loaded with pure moments. J Eur Ceram Soc 1996;16:1021.

[22] Raddatz O, Schneider GA, Claussen N. Modelling of R-curve behaviour in ceramic/metal composites. Acta Mater 1998;46:6381.

[23] Mai YW, Hakeem MI. Slow crack growth in cellulose fibre cements. J Mater Sci 1984;19:501.

[24] Olsson P, Stigh U. On the determination of the constitutive properties of thin interphase layers — an exact inverse solution. Int J Fract 1989;41:R71.

[25] Rhee KY. Delamination resistance behaviour in unidirectional graphite-epoxy composites. J Mater Sci Lett 1997;16:1888.

[26] Zienkiewicz OC. The finite element method. 3rd version, 1982. ISBN 0-07-084072-5.

[A10]

Sørensen, B. F., Goutianos, S., and Jacobsen, T. K., 2009

"Strength scaling of adhesive joints in polymer-matrix composites"

International Journal of Solids and Structures, Vol. 46, pp. 741-761

International Journal of Solids and Structures 46 (2009) 741–761

Contents lists available at ScienceDirect

International Journal of Solids and Structures

journal homepage: www.elsevier.com/locate/ijsolstr

Strength scaling of adhesive joints in polymer–matrix composites

Bent F. Sørensen [a,*], Stergios Goutianos [a], Torben K. Jacobsen [b]

[a] Materials Research Division, Risø National Laboratory for Sustainable Energy, The Technical, University of Denmark, P.O. Box 49, DK-4000 Roskilde, Denmark
[b] LM Glasfiber A/S, R&D Department, Rolles Møllevej 1, DK-6640 Lunderskov, Denmark

ARTICLE INFO

Article history:
Received 21 July 2008
Received in revised form 18 September 2008
Available online 1 October 2008

Keywords:
Crack bridging
Cohesive laws
Experiments
Modelling

ABSTRACT

The fracture of adhesive joints between two glass-fibre laminates was studied by testing double cantilever beam test specimens loaded by uneven bending moments. A large-scale fracture process zone, consisting of a crack tip and a fibre bridging zone, developed. The mixed mode fracture resistance increased with increasing crack length, eventually reaching a steady-state level (*R*-curve behaviour). The steady-state fracture resistance level increased with increasing amount of tangential crack opening displacement. Cohesive laws, obtained from fracture resistance data, were used for prediction the load carrying capacity of 2-m long "medium size" adhesive joint specimens subjected to four point flexure. Medium size specimens were manufactured and tested. A good agreement was found between the predicted and measured strength values of the medium-size specimens. Thus, the scaling from small specimens to medium-size specimens was successfully achieved.

1. Introduction

Many large components, such as ships, aircrafts and wind turbine blades are made of composite structures that are joined by adhesive bonds. It is therefore of great interest to establish engineering approaches for safe design of adhesively bonded composite structures. Traditionally, two different approaches have been used (Kinlock, 1987; Matthews, 1987): The one approach is to design against crack initiation; the other concerns crack growth. Typically, a criterion for crack initiation is a maximum stress criterion, i.e., it is assumed that crack initiation takes place when a stress component reaches a critical value. Crack growth criteria are typically based on linear elastic fracture mechanics. Then, it is assumed that crack propagation takes place when the energy release rate reaches a critical value, denoted the crack tip fracture energy. However, crack growth in fibre composites can be complicated by the occurrence of crack bridging during crack growth. Crack bridging occurs in the form of many single fibres or fibre bundles that connect the crack faces in the crack wake behind the crack tip. The bridging fibres restrain the crack opening and raise the fracture resistance (*R*-curve behaviour), see e.g. Suo et al. (1992). The fracture resistance enhancement due to fibre bridging can be large in comparison with the crack tip fracture energy (Albertsen et al., 1995; Sørensen and Jacobsen, 1998; Feih et al., 2005).

Since crack bridging is a large-scale fracture process zone, it should not be characterised in terms of linear elastic fracture mechanics (LEFM). Instead, the fracture process zone can be modelled by non-linear fracture mechanics, e.g. by a cohesive zone model (Dugdale, 1960; Barenblatt, 1962; Foote et al., 1986; Hillerborg, 1991; Cox and Marshall, 1991; Suo et al., 1992; Östlund, 1995). Crack bridging is then represented by surface tractions along the crack face. The relationship between the local traction and the local opening is usually taken to be a material property called the cohesive law (or a bridging law if a crack tip stress singularity is retained (Bao and Suo, 1992)). In finite element simulations, the mesh should be sufficiently refined so that cohesive/bridging tractions are obtained with a adequately spatial resolution; at least

* Corresponding author. Tel.: +45 4677 5700; fax: +45 4677 5758
E-mail address: bent.soerensen@risoe.dk (B.F. Sørensen).

0020-7683/$ - see front matter © 2008 Elsevier Ltd. All rights reserved.
doi:10.1016/j.ijsolstr.2008.09.024

10 elements should be in the active cohesive zone (Turon et al., 2007). A useful tool in the analysis of bridged cracks is the integration-path independent J integral (Rice, 1968), which can be applied to large-scale bridging problems (Suo et al., 1992).

Cohesive laws have been used in the characterisation and modelling of adhesive joints (Yang et al., 1999; Mohammad and Liechti, 2000; Kafkalidis and Thouless, 2002; Sørensen, 2002). Li et al. (2005, 2006) used cohesive laws to represent the fracture process zone of adhesively bonded polymer–matrix composites consisting of randomly oriented glass fibres in a polypropylene matrix. First, Mode I and Mode II cohesive laws were obtained from experiments. Next, mixed mode cracking of a sandwich single-shear lap specimen was predicted using Mode I and a Mode II cohesive laws that were unrelated except being coupled through a failure criterion. The model predictions were compared with experimental results and a good agreement was found.

In other studies, the cohesive laws represent the entire adhesive layer (Yang and Thouless, 2001; Sørensen, 2002). Then, the openings δ_n and δ_t comprise both elastic deformation of the adhesive layer and the opening of the fracture process zone. The cohesive law must give an elastic opening with increasing stress even before the peak stress is reached.

In the papers listed above, the determination of mixed mode cohesive laws required significant computational efforts, e.g. by incremental finite element models of test specimens to fit global specimen response e.g. the load-displacement curve (Yang et al., 1999; Kafkalidis and Thouless, 2002) or a near crack tip displacement field (Mohammad and Liechti, 2000; Liechti and Wu, 2001). This is an iterative process. Typically, a number of finite element analyses with different cohesive zone parameters are performed, before the correct cohesive law parameters are identified. Obviously, it is of interest to develop simpler and more direct approaches for the measurements of mixed mode cohesive laws. One such approach is to derive cohesive laws from fracture resistance data, using a J integral approach. This approach has been used primarily for mode I (Li and Ward, 1989; Sørensen and Jacobsen, 1998; Sørensen, 2002). Only a few recent studies aim to determine details of mixed mode cohesive laws (Högberg et al., 2007; Sørensen and Jacobsen, 2008). In the present study, we determine the fracture resistance for various nominal mode mixities. However, we only determine cohesive laws (using the J integral approach) for pure Mode I and Mode II.

The major aim of the present study was to predict the strength of the adhesive joints from properties determined from smaller laboratory specimens. In the present study, the major complication is the development of a large-scale bridging zone that prevents the use of LEFM. Instead, the large-scale fracture process zone is modelled by a cohesive zone.

The paper is organised as follows: first, the basic mechanics of crack bridging, cohesive law, and the analysis of the DCB-UBM (double cantilever beam specimens loaded with uneven bending moments) test specimen is presented. Next, we describe the practical test set-up. Two model approaches, used (an analytical and a numerical) for predicting the strength of the medium size specimens, are described. Results from the DCB-UBM test specimens are then given. Next follows the test results of the medium size specimens. Model predictions are presented and compared with the experimental results. Finally, the methods are discussed and major conclusions are drawn.

2. Basic mechanics

2.1. Concepts of cohesive laws

The stress transferred across the crack faces of the fracture process zone can be described in terms of cohesive laws (sometimes called traction–separation laws). Then, the local normal stress σ_n and the local shear stress σ_t in the fracture process zone are taken to be functions of the local crack opening in the directions normal and tangential to the local crack plane, denoted δ_n and δ_t, respectively, i.e., as

$$\sigma_n = \sigma_n(\delta_n, \delta_t), \quad \sigma_t = \sigma_t(\delta_n, \delta_t). \tag{1}$$

It is commonly assumed that when the openings reach critical values, denoted δ_n^0 and δ_t^0 respectively, the cohesive stresses have decreased to zero. The critical openings may depend on the ratio between δ_t^0 and δ_n^0.

Evaluation of the J integral along a path Γ_{loc} around the fracture process zone gives (Sørensen and Kirkegaard, 2006)

$$J = \int_0^{\delta_n^*} \sigma_n(\delta_n, \delta_t)\mathrm{d}\delta_n + \int_0^{\delta_t^*} \sigma_t(\delta_n, \delta_t)\mathrm{d}\delta_t, \tag{2}$$

where δ_n^* and δ_t^* are the normal- and tangential crack opening displacement at the end of the cohesive zone, see Fig. 1. We denote the value of the J integral during cracking by J_R, the fracture resistance. When δ_n^* and δ_t^* reaches critical values, δ_n^0 and δ_t^0, the fracture resistance attains a (constant) steady-state value, denoted, J_{ss}. Eq. (2) can then readily be interpreted as the work per unit area of the cohesive stresses.

In the present study, the cohesive laws are taken to represent a fracture process zone that initially has no thickness. Then, on physical grounds, the normal and shear stresses ahead of the crack must surpass some peak stresses, (denoted $\hat{\sigma}_n$ and $\hat{\sigma}_t$, respectively) before damage develops and crack opening begins (see Fig. 1).

Under pure normal opening, $\delta_n^* \neq 0$, $\delta_t^* = 0$ (in the following denoted pure Mode I), the last integral in (2) becomes zero. Then, it follows (Li and Ward, 1989; Olsson and Stigh, 1989; Suo et al., 1992):

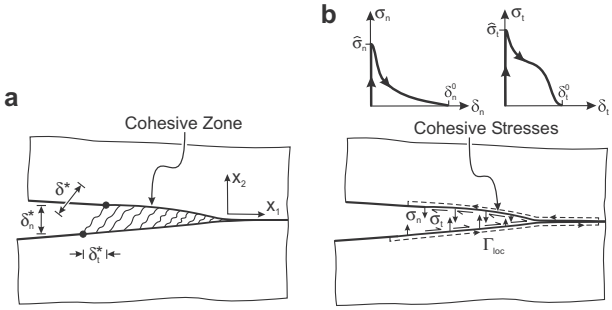

Fig. 1. Mixed mode crack bridging and schematic cohesive laws.

$$\frac{dJ_R}{d\delta_n^*} = \sigma_n(\delta_n^*). \tag{3}$$

The pure Mode I cohesive law can thus be obtained from the fracture resistance of a Mode I experiment by differentiation if the end-opening δ_n^* is recorded during the experiment.

Likewise, under pure tangential opening (in the remainder of the paper referred to as pure Mode II), $\delta_n^* = 0$. Then, the first integral in (2) vanishes so that

$$\frac{dJ_R}{d\delta_t^*} = \sigma_t(\delta_t^*). \tag{4}$$

Thus, the pure Mode II cohesive law can be obtained from fracture resistance data of a Mode II experiment if the end-sliding δ_t^* is measured during the experiment. A generalisation of this approach to the determination of mixed mode cohesive laws is given by Sørensen and Kirkegaard (2006). In the present study, we limit our analysis to the pure modes and use Eqs. (3) and (4).

2.2. Analysis of the DCB-UBM specimen

In the present study, the basic fracture mechanical properties are determined by the use of a DCB-UBM specimen, see Fig. 2. This specimen has the prominent feature that the *J* integral solution can be determined analytically under large-scale bridging (LSB). In the present study, isotropic linear elastic properties are assumed outside the fracture process zone. Small strains, small rotations and small displacements are assumed.

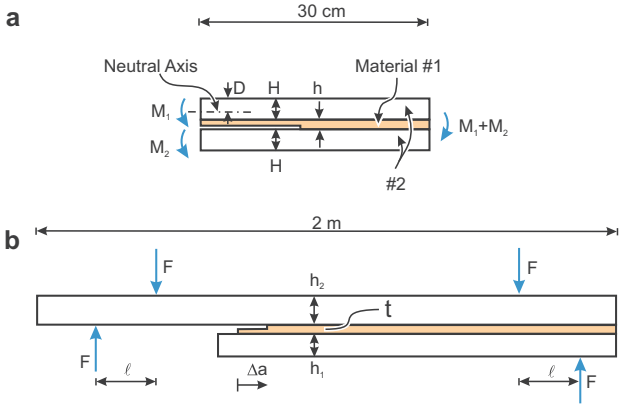

Fig. 2. Fracture mechanics parameters are obtained from double cantilever beam specimens loaded with uneven bending moments (DCB-UBM) (a) and used for the prediction of the load-carrying capability of "medium size" specimens subjected to four-point flexure (b).

The J integral can be evaluated along a path along the external boundaries of the specimen. When the beams outside the fracture process zone are longer than a few times the beam height, the J integral result is independent of crack length. The only non-zero contributions come from the beam-ends, which are subjected to pure bending. Under plane stress, the only stress component that enters the analysis is the normal stress in the direction parallel to the specimen (the x_1-directions). The result for a DCB-UBM specimen sandwich specimen is (Sørensen et al., 2006; Østergaard and Sørensen, 2007)

$$J = \frac{1}{B^2H^3E_2}\left\{\frac{M_1^2}{2\eta^3 I_0} + 6M_2^2 - \frac{(M_1+M_2)^2}{2\eta^3 I_1}\right\}, \tag{5}$$

where M_1 and M_2 denote the applied bending moments (positive signs are shown in Fig. 2), B is the specimen width, H and E_2 denote the thickness and Young's modulus, respectively, of the beams (material #2). For plane strain, the result should be multiplied by the term $1-\nu_2^2$, where ν_2 is the Poisson's ratio of the beams (material #2). The non-dimensional parameters η, I_0 and I_1 are given by (Suo and Hutchinson, 1990; Østergaard and Sørensen, 2007)

$$\eta = \frac{h}{H}, \tag{6}$$

where h is the thickness of the adhesive layer (material # 1),

$$I_0 = \frac{1}{3}\frac{1}{\eta^3} - \frac{\Delta}{\eta^2} + \frac{\Delta^2}{\eta} + \Sigma\left(\frac{1}{\eta^2} + \frac{1}{\eta} + \Delta^2 - 2\frac{\Delta}{\eta} - \Delta + \frac{1}{3}\right), \tag{7}$$

and

$$I_1 = \frac{1}{12}\left(\Sigma + \frac{8}{\eta^3} + \frac{12}{\eta^2} + \frac{6}{\eta}\right). \tag{8}$$

For plane stress, the stiffness ratio parameter, Σ, is defined as

$$\Sigma = \frac{E_1}{E_2} \tag{9}$$

where E_1 and E_2 are Young's moduli of the adhesive layer (material #1) and the beams (material #2), respectively. For plane strain,

$$\Sigma = \frac{E_1}{E_2}\frac{1-\nu_2^2}{1-\nu_1^2}, \tag{10}$$

where ν_1 is Poisson's ratio of the adhesive layer (material #1). In (7), the parameter Δ is a non-dimensional measure of the position of the neutral axis (D denotes the distance from the top of the skin layer to of the neutral axis of the bimaterial beam), see Fig. 2,

$$\Delta = \frac{D}{h} = \frac{1+2\Sigma\eta+\Sigma\eta^2}{2\eta(1+\Sigma\eta)}. \tag{11}$$

As mentioned, the J integral result is independent of crack length; the DCM-UBM is a steady-state specimen. For most other well known fracture mechanics test specimens (including the traditional DCB specimen loaded with transverse forces) the J integral evaluated around the external boundaries cannot be determined in closed analytical form under LSB (Suo et al., 1992).

For crack growth initiation (i.e., the onset of growth of a sharp crack with no fibre bridging), the LEFM concepts of energy release rate, $\mathcal{G}$, and the mode mixity, ψ, are applicable. Then, for the DCB-UBM specimen $\mathcal{G} = J$ as given by (5). In the following, we will use a nominal mode mixity, denoted ψ_{nom}, calculated without accounting for the adhesive layer, i.e., calculated by analysing the homogenous specimen (Sørensen et al., 2006)

$$\psi_{\text{nom}} = \tan^{-1}\left(\lambda^{-1/4}\frac{\sqrt{3}}{2}\frac{M_1+M_2}{M_2-M_1}\right), \quad |M_1| < M_2, \tag{12}$$

where λ is a dimensionless orthotrophy parameter introduced by Suo (1990). In the following, we take $\lambda = 0.3$.

For an interface crack in a bimaterial specimen, the mode mixity is usually defined as the phase angle of $K\hat{h}^{i\varepsilon}$:

$$\psi = \frac{\text{Im}\left[K\hat{h}^{i\varepsilon}\right]}{\text{Re}\left[K\hat{h}^{i\varepsilon}\right]}, \tag{13}$$

where $K = K_1 + iK_2$ is the complex stress intensity factor (Rice, 1988; Hutchinson and Suo, 1992), $\hat{h}$ is a characteristic length, $i = (-1)^{1/2}$ and ε is a bimaterial constant (sometimes called the oscillating index)

$$\varepsilon = \frac{1}{2\pi}\ln\frac{1-D_\beta}{1+D_\beta}, \tag{14}$$

where D_β is one of the two Dundurs' parameters, that depends on the elastic constant of the bimaterial problem (plane strain conditions) (Dundurs, 1969)

$$D_\alpha = \frac{\overline{E}_1 - \overline{E}_2}{\overline{E}_1 + \overline{E}_2}, \quad D_\beta = \frac{\mu_1(1-2\nu_2) - \mu_2(1-2\nu_1)}{2\mu_1(1-\nu_2) + 2\mu_2(1-\nu_1)}, \tag{15}$$

where $\overline{E}_j = E_j(1-\nu_j^2)$ is the plane strain modulus and μ_j is the shear modulus ($\mu_j = E_j/2(1+\nu_j)$) of material number $j = 1,2$.

Suo and Hutchinson (1989) have analysed the problem of a crack lying above an adhesive layer (denoted material #2 in their study) in a sandwich specimen for which the adhesive layer thickness is much smaller than all other specimen dimensions. Selecting the layer thickness as the reference length in the mode mixity definition (13), $\hbar = h$, the mode mixity of the interface crack can be written as

$$\psi = \psi_{\text{nom}} + \omega(D_\alpha, D_\beta), \tag{16}$$

where ω is a phase angle that depends only on the two Dundurs' parameters. For the present material system (Table 1), we obtain $D_\alpha = -0.83$ and $D_\beta = -0.18$. From Table 1 in Suo and Hutchinson (1989), we obtain $\omega(D_\alpha = 0.8; D_\beta = 0.2) = -10.5^\circ$ (note that we have labelled materials differently from Suo and Hutchinson; this merely changes the sign of D_α and D_β).

Knowing ψ, the phase angle of the crack opening displacements within the K-dominated zone,

$$\varphi = \tan^{-1}\left(\frac{\delta_t}{\delta_n}\right), \tag{17}$$

where δ_n and δ_n are the crack openings in the normal and tangential directions, respectively, can be calculated from (Rice, 1988)

$$\varphi = \psi - \varepsilon \ln\left(\frac{h}{r}\right) - \arctan(2\varepsilon), \tag{18}$$

where r is the distance from the crack tip. We will use the relation (18) as a means to check the accuracy of the numerical model.

However, since the main part of the present study concerns large-scale bridging, for which ψ looses it significance as a parameter controlling the fracture process zone, we will henceforward use ψ_{nom} as an approximate measure of the loading of the fracture process zone.

2.3. Analysis of medium size specimens

The medium size specimen (Plausinis and Spelt, 1995) is essentially the half of the so-called UCSB four point flexure specimen analysed earlier by Charalambides et al. (1989). This specimen is also a steady-state fracture specimen; J is independent of the crack length and the analysis is valid for both LEFM and LSB ($\mathcal{G} = J$). The result is (plane stress)

$$J = 6\frac{M^2}{W^2 h_2^3 E}\left\{1 - \frac{1}{(1+(h_1/h_2))^3}\right\}, \tag{19}$$

where M is the applied moment, W is the specimen width and E is Young's modulus of the beams and h_1 and h_2 are the thicknesses of the short and long beam, respectively (see Fig. 2b). With the set-up shown in Fig. 2b, $M = F\ell$, where F is the applied load and ℓ is the moment arm. In the result given by (19), the presence of the adhesive layer is neglected.

Knowing the steady-state fracture resistance, J_{ss}, the load at steady-state cracking, F_{ss}, can be predicted from (19). The result is (plane stress)

$$\frac{F_{ss}\ell}{W\sqrt{J_{ss}h_2^3 E}} = \frac{1}{\sqrt{6}\sqrt{1 - \dfrac{1}{(1+(h_1/h_2))^3}}}. \tag{20}$$

Neglecting the presence of the adhesive layer, the nominal mode mixity, ψ_{nom}, is 40.9° for $h_1/h_2 = 1$, and increasing relatively slowly with decreasing h_1/h_2 ratio to about 49° for $h_1/h_2 = 0.1$ (Charalambides et al., 1989). As for the DCB-UBM specimens, the true mode mixity of a sharp interface crack lying at the upper interface of the adhesive layer is estimated to be about 10.5° lower.

Table 1
Isotropic elastic data for bimaterial specimen.

E_1 (GPa)	ν_1 (dimensionless)	E_2 (GPa)	ν_2 (dimensionless)
3	0.35	34	0.27

Subscripts indicate material number (material #1: adhesive; material #2: composite).

3. Experimental methods

3.1. Manufacturing of specimens

The DCB-UBM adhesive joint specimens were made from a polymer–matrix composite containing long, aligned glass fibres. The plates were made by hand-lay up of dry fibre fabrics, followed by matrix impregnation by vacuum infusion and post-cured. The layup of the laminates was [±45, 0_8, ±45], i.e., almost unidirectional. A thin slip foil was placed at the one end of the plates to act as a pre-crack and ease crack initiation. Then, an adhesive was applied to the surface of the one plate. The other plate was then placed on the adhesive. Spacers were used to control the thickness of the adhesive layer, h, to approximately 3 mm. Following post-curing, specimens, 30 mm in width, were cut from the sandwich plates. Steel parts were fixed to each beam by four steel screws (M5) and an epoxy adhesive. The specimen dimensions were identical to those used in an earlier study (Sørensen et al., 2006). The elastic data for the adhesive (materials #1) and the laminate (material #2) are listed in Table 1.

The medium size specimens were made in a similar manner as the DCB-UBM specimens, i.e., by vacuum infusion and post-curing. The lay-up was predominately unidirectional fibres oriented parallel to the beam direction. After curing, two laminates, having uneven lengths, were joined by an adhesive layer. A pre-cut was made to act as a crack starter.

Six medium size specimens were made. There were two specimens for three different thicknesses of the shorter beam, $h_1 = 10$ mm, $h_1 = 32.5$ mm and $h_1 = 60$ mm. For all specimens, the length of the longest part was 2000 mm, the width, W, was 60 mm nominally, and the thickness, h_2, was nominally 60 mm. The length of the shorter laminate was 1380 mm and the width was 60 mm. The thickness, t, of the adhesive layer was approximately 5 mm. The elastic properties of the adhesive and laminate were taken to be identical to those of the DCB specimen (Table 1).

3.2. Test procedures

The DCB-UBM experiments were conducted by the use of a special test set-up utilising a wire and rollers (Sørensen et al., 2006). The experiments were conducted in two parts, (i) crack initiation and (ii) monotonic loading following re-notching.

In the first part, the specimen was loaded near-symmetrical loading ($M_1/M_2 = -0.45$) until crack growth initiated from the slip foil. Typically, a significant load drop and a relative large crack extension occurred in connection with crack initiation. The associated crack opening displacement was about 20–40 μm. The rapid crack growth and the associated load drop prevented detailed measurements of the initial part of the cohesive laws. Therefore, the crack tip position was marked up at the side of the specimen, the specimen was unloaded, and a cut was made in the adhesive layer by a band saw until 1–2 mm from the crack tip (re-notching). The purpose of this re-notching was to create a specimen that had a truly sharp crack tip with very limited fibre bridging.

Following re-notching, steel pins (diameter 1.4 mm) were placed in holes drilled in the laminates at the x_1 position of the crack tip. The pins were positioned at the mid-plane of the laminates to minimise their effect on the stress state in the specimen. An extensometer (Instron, type 2620-602) was mounted at the pins, in a way that it could rotate freely and thereby record a crack opening displacement, δ_m, see Fig. 3. At the other face, an LVDT (H. F. Jensen, type LDI 8/1 MR) was mounted parallel to the adhesive layer in a special holder to measure the tangential displacements (denoted δ_t^*) at the end of the cohesive zone.

Then, in the second part, the specimen was loaded monotonically at a constant displacement rate (5 mm/min). Loading was continued until a stationary load level (indicating steady-state fracture resistance) was achieved. During the experiments, data for the applied moments, the extensometer and the LVDT were recorded at a PC using a data acquisition programme.

The medium size specimens were tested in four point flexure in a purpose-made fixture. The fixture consists of two parts. The lower part (an I-beam) was supported at the ends by rods against the ground and the midpoint was supported at lower part of the test machine. The upper part was mounted with a spherical bearing that allowed the part to rotate. This ensured

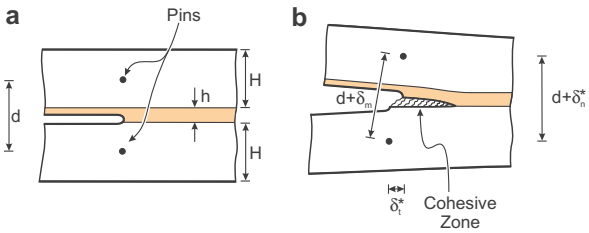

Fig. 3. Schematics illustration showing the geometric relationship between the normal displacement, δ_n^*, and tangential displacement, δ_t^*, and the measured displacement, δ_m: (a) before and (b) after the development of a cohesive zone.

that the loading was statically determinate, although the specimen deformed non-symmetrically. The fixture was mounted at an Instron 1511 test machine. The end-opening of the crack, δ_m, was measured by an LVDT (H. F. Jensen, type TCA B/L 5S) that could rotate freely. Therefore, δ_m could not be separated into displacements in the tangential and normal directions.

Like the DCB-UBM tests, the testing of the medium size specimens consisted of two parts: (a) crack initiation and (b) crack growth. The medium size specimens were tested under a constant cross head speed of 2 or 5 mm/min. Data for load, the end-opening and the crack length were recorded during the experiment.

3.3. Data analysis

For the DCB-UBM specimens, J_R was calculated from Eq. (5), by the use of the elastic data listed in Table 1. For Mode I, δ_n^*, the displacement normal to the crack plane, was taken to be equal to δ_m. For mixed mode experiments, δ_n^* was calculated by the law of Pythagoras, see Fig. 3,

$$\delta_n^* = \sqrt{(d+\delta_m)^2 - \delta_t^{*2}} - d, \tag{21}$$

where d is the initial distance between the points at which the displacements are recorded. It should be noted that (21) is only valid for small rotations. The displacement δ_m comprises both the stretch of the cohesive zone and the elastic deformation of the specimen from $x_2 = -d/2$ to $x_2 = d/2$; however, the elastic deformation is assumed to be so small that it can be neglected (Sørensen and Jacobsen, 2000). In the present experiments, the pins were mounted at the neutral axis of the beams, so that $d = H + h$. Having determined the end-openings, δ_n^* and δ_t^*, Mode I and Mode II cohesive laws were calculated from experimental results by (3) and (4) by the numerical differentiation scheme (using piecewise fitting) described by Sørensen (2002).

The magnitude of the end-opening was calculated as

$$\delta^* = \sqrt{\delta_n^{*2} + \delta_t^{*2}}, \tag{22}$$

and the phase angle of the end-openings, φ^*, was calculated from the normal and tangential crack opening displacements as

$$\varphi^* = \tan^{-1}\left(\frac{\delta_t^*}{\delta_n^*}\right). \tag{23}$$

The value of φ^* at the onset of steady-state cracking is denoted φ_0^*.

4. Modelling of crack propagation in medium size specimens

The interfacial crack growth in the medium size specimens was modelled by the finite element (FE) method using the commercial code Abaqus, version 6.7 (2007). In order to reduce the computational time, only a part of the specimen, 1.5 m in length, was modelled as shown in Fig. 4(a). Denote the displacement vector by u_i (where the subscript refers to the coordinate axis (1 or 2) for the plane problem). The boundary conditions were specified as follows. The edge at $x_1 = 1.5$ m was constrained in the x_1-direction ($u_1 = 0$). Additionally, the node at $(x_1, x_2) = (1.5\text{ m}, 0\text{ m})$ was constrained in the x_2-direction ($u_2 = 0$).

The external bending moment, $M = F\ell$, was applied to the left side of the specimen (Fig. 2b) by prescribing the displacements of two nodes in increments using a procedure that creates a pure bending moment (Jacobsen and Sørensen, 2001). The computations were terminated when the crack approached the specimen end.

The composite beams were modelled as a linear elastic orthotropic solid under plane stress conditions. Young's modulus in the x_1-direction and major Poisson's ratio are given as material #2 in Table 1. The minor Young's modulus (in the x_2-direction) was 10 GPa and the in-plane shear modulus was 4 GPa. The adhesive layer was also modelled as a linear elastic solid with the elastic properties of material #1 in Table 1. Four-node elements (quadrilaterals) and triangular 3-node reduced integrations elements were used. The combination of rectangular and triangular elements was selected in order to control the mesh transition and keep the number of elements low. The smallest element was 0.1 by 0.1 mm^2.

Crack growth can cause convergence difficulties when implicit FE methods are used. Although a number of numerical stability methods exist to overcome these difficulties, an explicit FE method is more robust (Belytschko et al., 2000). However, often noise is present in the solution. In the present study, an explicit solver was used to solve the problem under quasi-static conditions. In the solution procedure, viscous damping was also necessary for convergence. In all simulations, it was ensured that the sum of the kinetic energy and the energy dissipated by viscosity was less than 1% of the total energy.

The crack growth at the interface between the upper composite beam and the adhesive was modelled using 4-node cohesive elements of a finite but very small thickness ($h_t = 0.01$ mm) corresponding to 0.2% of the adhesive thickness. A finite (instead of zero) thickness was preferred in order to avoid interpenetration of the two surfaces adjacent to the cohesive elements. The length of the cohesive elements in the cohesive zone (in the x_1-direction) was 0.1 mm. This small size ensured that enough elements (typically more than 100) were active in the fracture process zone, giving accurate stresses (Turon et al., 2007). The cohesive law parameters were approximated from the DCB-UBM experiments as described later in Section 5.2. In the FE model, the cohesive laws were taken to have a bilinear shape. Schematics of the pure Mode I and Mode II cohe-

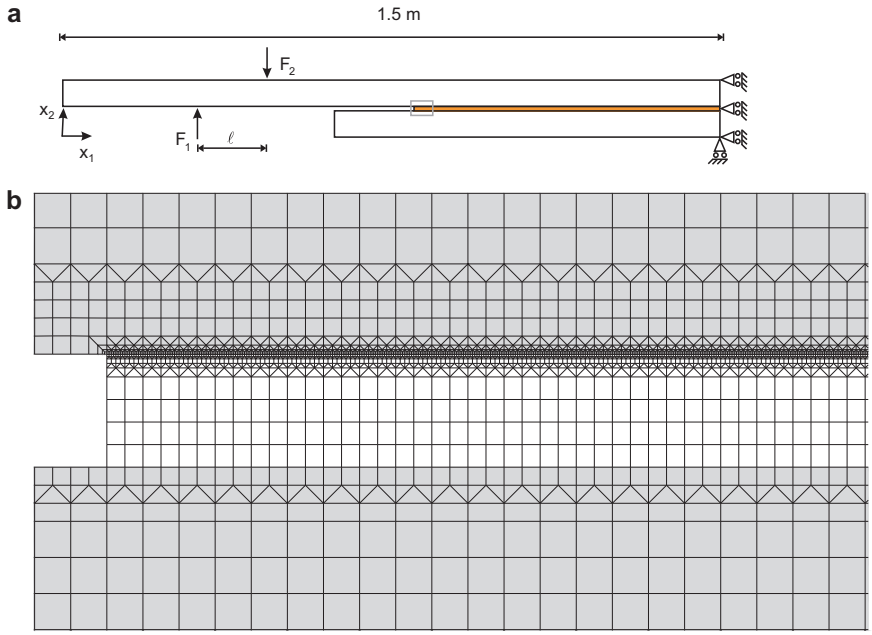

Fig. 4. Geometry, loads and boundary conditions of the finite element model. (a) Typical FE mesh near the cohesive zone. The mesh shown corresponds to the rectangular area (b).

sive laws, including parameters, are shown in Fig. 5. Note from Fig. 5 that the cohesive laws have initial rising parts with stiffnesses k_n and k_t for Mode I and Mode II respectively. In the present study, this is purely a numerical feature intended to make the numerical model run smoothly; as discussed in Section 2.1, no opening should occur before the cohesive normal and shear stresses exceed $\hat{\sigma}_n$ and $\hat{\sigma}_t$, respectively. Therefore, k_n and k_t were assigned high values ($k_n = k_t \cong 14\, E_1/h_t$). Then, the cohesive laws were practically linear softening.

A quadratic traction–interaction failure criterion was chosen for damage initiation in the cohesive elements:

$$\left(\frac{\hat{\sigma}_n(\varphi)}{\hat{\sigma}_n}\right)^2 + \left(\frac{\hat{\sigma}_t(\varphi)}{\hat{\sigma}_t}\right)^2 = 1. \tag{24}$$

Here $\hat{\sigma}_n$ is the peak stress of the cohesive law for pure Mode I and $\hat{\sigma}_t$ is the peak stress under pure Mode II. Each cohesive stress component is calculated from its conjugate opening and the relative stiffness of the cohesive zone (Camanho et al., 2003). The points along the cohesive zone where the criterion is fulfilled constitute the active cohesive zone, and represents the crack extension.

More details of the cohesive elements are given in Appendix A.

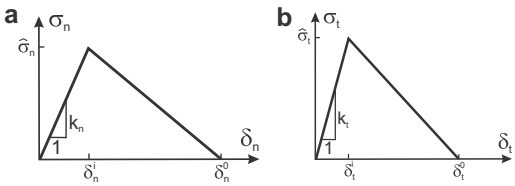

Fig. 5. Schematics illustration of idealised cohesive laws used in the FE model of the present study; the cohesive stresses are shown as a function of opening: (a) pure normal opening and (b) pure tangential opening.

5. Experimental results

5.1. Fracture resistance results from DCB-UBM tests

Initially, the crack propagation occurred along the adhesive/laminate interface towards the beam that was subjected to the highest moment. After some, say, 20 mm crack extension, a new crack formed at the next interface within the laminate. Subsequently, both the delamination crack and the interface crack grew. The cracking history is shown schematically in Fig. 6. Bridging in the form of fibre cross-over bridging was observed for both cracking planes. Fig. 7 shows the damage evolution in a typical mixed mode test specimen.

Typical results for the fracture resistance, J_R, are shown in Fig. 8. Here, the loading is expressed in terms of the nominal mode mixity, ψ_{nom}, as calculated by (12). It is obvious from Fig. 8 that the fracture resistance depends strongly on ψ_{nom} and on the magnitude of the crack opening.

The initiation and steady-state values of the J_R-data are shown in Fig. 9. The experimental points are shown as points. J_{ss} lies around 2 kJ/m^2 for $0° < \psi_{nom} < 70°$. For $\psi_{nom} > 70°$, J_{ss} increases with increasing ψ to about 4.0 kJ/m^2.

The values for the crack growth initiation value, J_0, data were fitted with the phenomenological criterion proposed by Hutchinson and Suo (1992)

$$J_0(\psi_{nom}) = J_0^0\{1 + \tan^2[(1-\Lambda)\psi_{nom}]\}, \tag{25}$$

where J_0^0 is the initial fracture resistance at $\psi_{nom} = 0°$ and Λ is a dimensionless constant. A similar fit was also made to the steady-state fracture resistance, J_{ss}. The fitted curves are included in Fig. 9; upper and lower bounds are shown as dash-dotted lines. The corresponding parameters are listed in Table 2.

Fig. 10 shows the critical opening, defined as the magnitude of the crack opening displacement at the point where the fracture resistance attains a steady-state value (and the cohesive zone is fully developed), as a function of the phase angle of the end-opening, φ_0^*. A few observations can be made from Fig. 10. Under dominating normal opening ($\varphi_0^* \approx 0°$), the critical opening is of the order of a few mm's, in agreement with earlier results of similar materials under pure Mode I (Sørensen and Jacobsen, 1998; Feih et al., 2005). With increasing φ_0^*, steady-state is attained over a much smaller end opening.

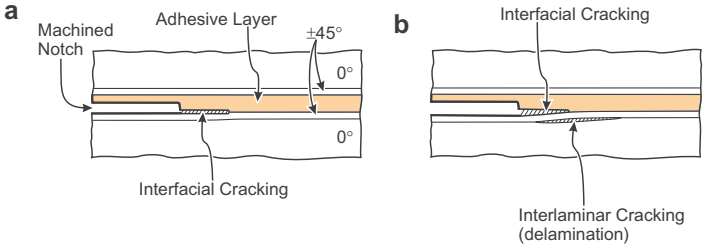

Fig. 6. Schematics illustration of the cracking history in the DCB-UBM specimens. The crack propagation starts along the adhesive layer/laminate interface (a) but later a delamination crack forms in the laminate (b).

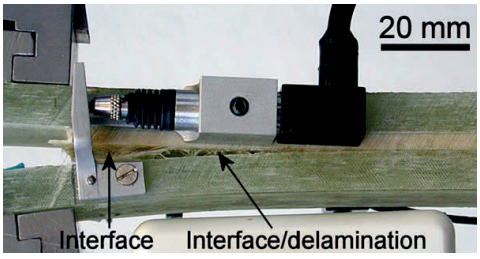

Fig. 7. Photo of a specimen subjected to mixed mode cracking ($M_1/M_2 = -0.45$).

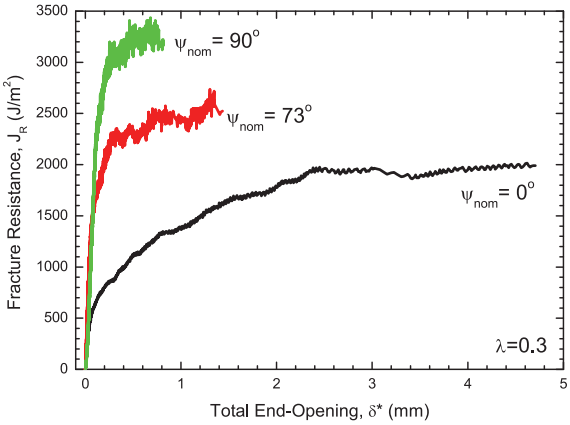

Fig. 8. Measured fracture resistance, J_R, as a function of the end-opening for various values of the phase angle of the end-opening at the onset of steady state.

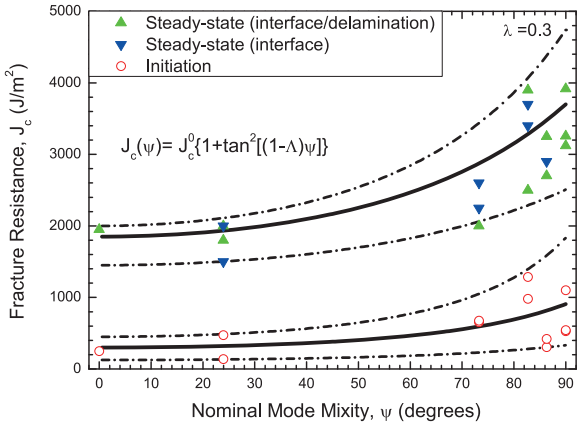

Fig. 9. The measured initiation and steady-state fracture resistance, denoted J_0 and J_{ss}, respectively, are shown as functions of the nominal mode mixity. Values for interfacial as well as delamination crack are shown.

Table 2
Fitting parameters to J_0 and J_{ss}.

	Initiation		Steady-state	
	J_0^0 (J/m^2)	Λ (dimensionless)	J_{ss}^0 (J/m^2)	Λ (dimensionless)
Upper bound	450	0.33	2000	0.45
Best fit	300	0.39	1850	0.5
Lower bound	125	0.42	1450	0.55

5.2. Determination of cohesive laws

Fig. 11 shows cohesive law obtained from Mode I and Mode II experiments by differentiation of the fracture resistance data according to (3) and (4). For Mode I (Fig. 11a), the peak cohesive normal stress, $\hat{\sigma}_n$, is about 12 MPa. With increasing

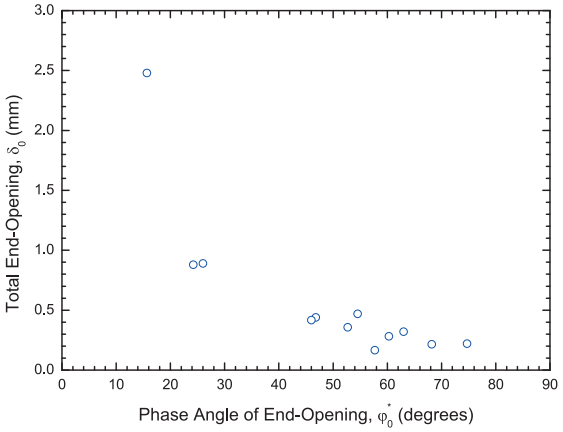

Fig. 10. The mixed-mode opening at the onset of steady-state cracking as a function of the phase angle of opening.

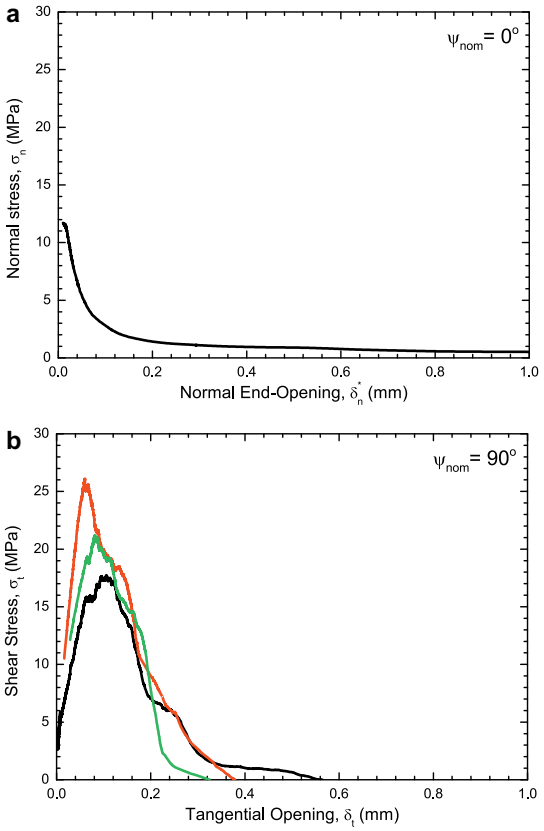

Fig. 11. Cohesive laws obtained by the *J* integral approach: (a) pure mode I ($\psi_{nom} = 0°$) and (b) pure Mode II ($\psi_{nom} = 90°$).

δ_n, σ_n decreases rapidly to about 3 MPa at an opening of about 0.1 mm. Beyond this opening σ_n decreases more slowly; $\sigma_n \approx 0.5$ MPa for $\delta_n = 1$ mm.

The pure Mode II cohesive law (Fig. 11b) is markedly different. The cohesive shear stress, σ_t, rises nearly linearly to a peak value, $\hat{\sigma}_t$, of about 17–26 MPa at a tangential crack opening displacement of about 0.06–0.09 mm. With increasing δ_t, σ_t decreases nearly linearly to zero at a tangential opening of 0.32–0.5 mm. Note that the peak stress of the shear stress during pure Mode II is higher than that the peak stress of pure Mode I and that the shape of the two cohesive laws are quite different.

5.3. Determination of idealised cohesive laws

Approximate, idealised cohesive laws were constructed for the FE simulations. The peak stress and critical crack opening for both Mode I and Mode II are selected so that the area under the stress–separation curves equals the steady state fracture energy, J_{ss} (believed to be the parameter that is determined most accurately in the experiments) in Mode I and Mode II, respectively. For each Mode, three sets of parameters, corresponding to the best fit, lower and upper bounds were determined. In deriving the Mode I cohesive laws for the lower bound, both the peak stresses and critical crack openings were decreased so that the energy dissipation of the fracture process zone was equal to the lower bound curve of the steady-state fracture resistance (Fig. 9). Likewise, upper bound cohesive law were made by increasing both the peak stresses and critical crack openings to obtain a fracture energy corresponding to the upper bound curve of the steady-state fracture resistance.

Table 3
Fitting parameters for cohesive laws.

	Mode I		Mode II	
	Peak stress, $\hat{\sigma}_n$ (MPa)	Critical opening, δ_n^0 (mm)	Peak stress, $\hat{\sigma}_t$ (MPa)	Critical opening, δ_t^0 (mm)
Upper bound	2.76	1.45	22.72	0.42
Best fit	2.64	1.40	20.15	0.37
Lower bound	2.30	1.24	16.67	0.30

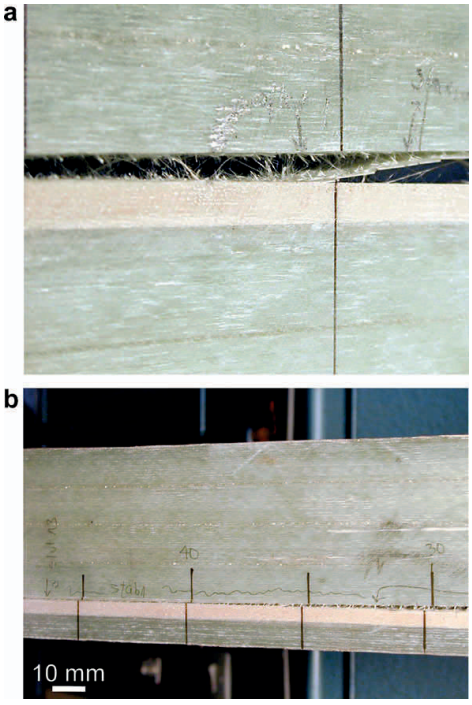

Fig. 12. (a) Early stage of cracking of a medium size specimen having $h_1/h_2 = 1$. Cracking occurs along the adhesive/laminate interface as well as inside the laminate. (b) Cracking of a medium size specimen having $h_1/h_2 = 0.17$.

The identified cohesive law parameters are shown in Table 3. Effects of other cohesive laws parameters are exploited in Appendix B.

5.4. Results for medium size specimens

In all experiments, a crack initiated from the pre-cut notch, but immediately grew out to the interface between the adhesive and the laminate of the long beam. This was expected; a crack loaded such that a mixture of Mode II and Mode I exists at the crack tip seeks to propagate in the direction to become a Mode I crack (Thouless and Evans, 1990). The first part of the crack growth took place along the adhesive/laminate interface. Thereafter, separation occurred in the external lamina (oriented 45° with respect to the longitudinal direction of the beam) of the laminate, see Fig. 12. Then, extensive fibre bridging occurred. Usually, the crack propagation occurred stably, but rapid, unstable crack jumps were also observed.

For the specimens having small h_1/h_2, it was observed that, for long crack lengths, a significant part of the crack, in particularly near the crack tip, experienced a very small normal opening, $\delta_n \approx 0$, indicating Mode II dominated cracking, see Fig. 12b.

Examples of measured data, the moment, $F\ell$, as a function of crack opening, δ_m, are shown in Fig. 13. The moment is shown as a function of the end-opening for a monotonic test and a test with several unloading and reloading cycles. The two curves follow each other reasonably well. The moment attains a steady-state value of about 3.5 kNm after a crack opening of about 2 mm. Note, that the unloading-reloading curves show non-linearity and increasing hysteresis with increasing

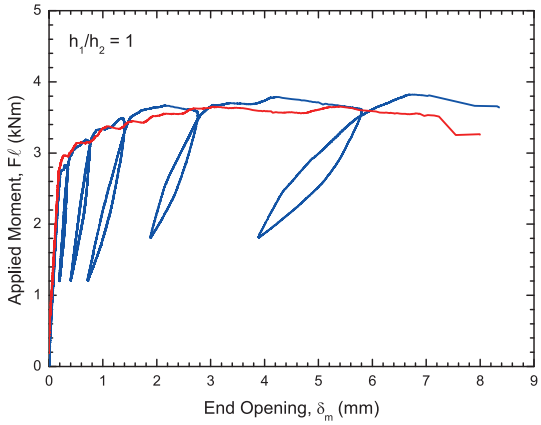

Fig. 13. Example of relationship between applied force and crack opening under monotonic loading and partial unloading and reloading ($h_1/h_2 = 1$).

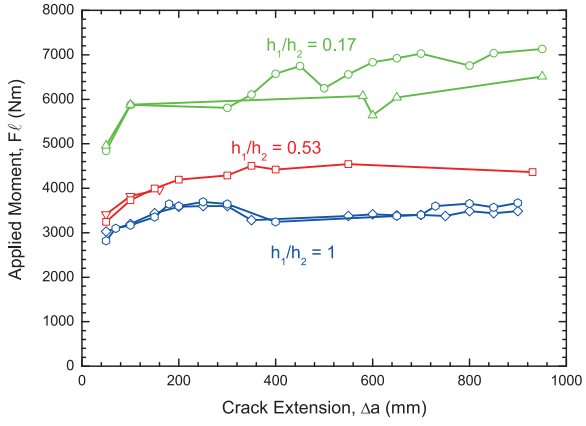

Fig. 14. Measured force-at-crack-growth as a function of crack extension. Points represent experimental values; curves are model predictions.

end-opening (corresponding to a longer crack). Since the fibre composite had most of the fibre in the length direction, the hysteresis is unlikely to be due to viscoelasticity in the polymer. Instead, the hysteresis may be attributed to frictional contact between the crack faces or broken fibres that prevents the crack from closing.

The measured force (at the point of cracking) is shown as a function of crack length in Fig. 14 (only data after crack initiation are present in the figure). The figure shows that the required force increases to a steady-state value, that depends on the thickness ratio, h_1/h_2. Specimens having a smaller h_1/h_2 value require a higher force to generate crack growth.

6. Modelling results

6.1. Validation of the finite element model

Fig. 15 shows model predictions from the FE model; the moment, $F\ell$, is shown as a function of crack opening, δ_m, for $h_1/h_2 = 1$ under monotonic loading. The cohesive laws used for Mode I and Mode II, correspond to the parameters given in Table 3. The results of Fig. 15 agree well with the experimental data depicted in Fig. 13 for the same h_1/h_2. The moment attains a steady-state value of 3.4 kNm. This value is somewhat lower that the value obtained experimentally. The steady-state value is attained at a crack opening of about 2 mm. This corresponds well with the experimental results.

6.2. Strength predictions from FE simulations

The numerical predictions for the moment, $F\ell$, as a function of the crack extension are presented in Fig. 16a for $h_1/h_2 = 1$. Results based on different cohesive laws (upper, lower and average) are shown. The curves show similar trend: the fracture load increases to a near-constant (steady-state) value after some crack extension. In the same figure, experimental data (Fig. 14) are also included to facilitate the comparison between experiments and FE predictions. Fig. 16b and c shows results for $h_1/h_2 = 0.53$ and 0.17, respectively. The numerical predictions show, like the experimental results, that an increasing moment is required to cause fracture of the specimens as the ratio h_1/h_2 decreases. Most of the experimental data are within the bounds of the predictions.

Next, in Fig. 17 the phase angle of the end of the fracture process zone, φ^*, is shown as a function of crack extension for the three h_1/h_2 ratios. The phase angles for the initiation of cracking are almost the same for the three different geometries, $\varphi^* \approx 30$–33°. As the crack extends, φ^* increases to a steady-state value, denoted φ_0^*. The increase in φ^* is higher as the h_1/h_2 ratio decreases. φ_0^* takes a value of about 70–72° for $h_1/h_2 = 0.17$. In other words, for small h_1/h_2, the amount of Mode II increased. This finding is in agreement with the experimental observations of Fig. 12b.

6.3. Strength predictions from analytical model

The steady-state force to propagate the crack along the interface in the medium size specimens can be predicted from the fracture resistance data of the DCB-UBM specimens using Eq. (20). To do so, we must first determine the appropriate value of

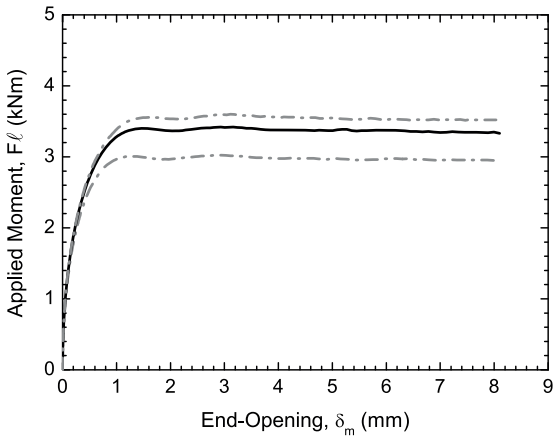

Fig. 15. Relationship between applied moment and end crack opening under monotonic loading for $h_1/h_2 = 1$. The Mode I and Mode II cohesive laws parameters are those listed in Table 3, whereas the steady-state fracture energy vs phase angle equals the fitted curve of Fig. 9, using the parameter given in Table 2.

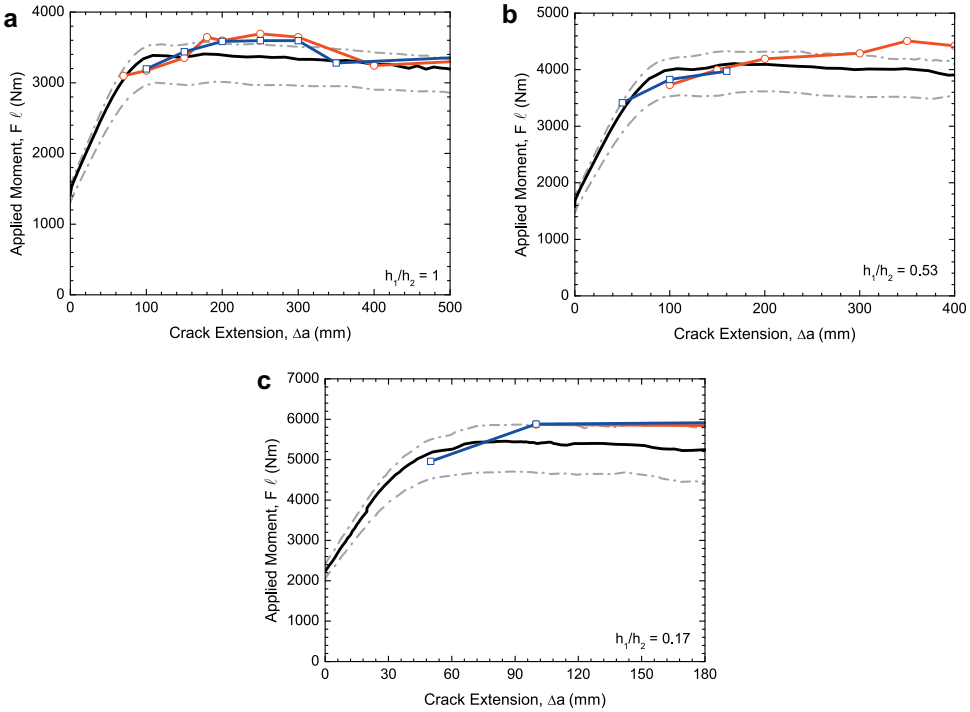

Fig. 16. Predicted relationship between applied moment and crack extension under monotonic loading for various h_1/h_2 ratios: (a) $h_1/h_2 = 1$, (b) $h_1/h_2 = 0.53$ and (c) $h_1/h_2 = 0.17$.

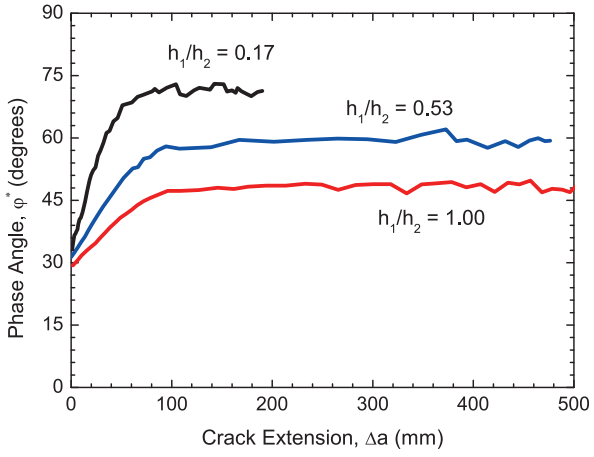

Fig. 17. Predicted phase angle of opening as a function of crack extension for various beam thicknesses.

J_{ss}. For the small-scale bridging solution by Charalambides et al. (1989) we have that $41° < \psi_{nom} < 49°$ for the thickness ratios investigated. However, there are no measured values of J_{ss} for that nominal mode mixity value. Therefore, we use the inter-

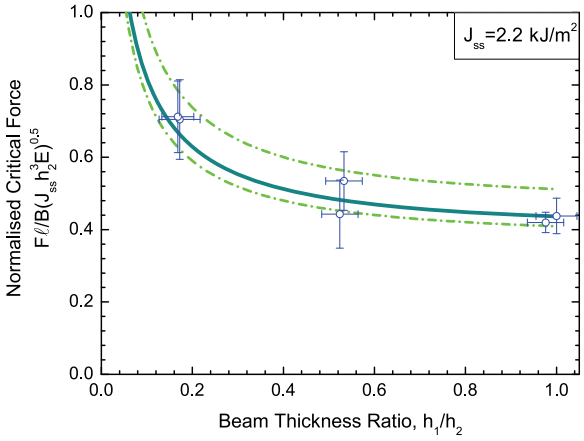

Fig. 18. Predicted (solid line) and measured values (points) of applied force at steady-state crack growth as a function of thickness ratio, h_1/h_2. Dashed lines represent predictions based on upper and lower bounds for the steady-state fracture resistance (J_{ss} = 2.5 kJ/m^2 and J_{ss} = 1.6 kJ/m^2, respectively).

polation function (25) with the parameters given in Table 2. Then, we obtain $J_{ss} \approx 2.2$ kJ/m^2. By inserting this value into (20) we can predict the load carrying capability under steady-state cracking.

The predicted load levels are shown as lines in Fig. 18. The solid line is the prediction based on J_{ss} = 2.2 kJ/m^2; upper and lower bound curves are based on upper and lower bound values of J_{ss} from the DCB-UBM experiments at $\psi_{nom} \approx 45°$.

Fig. 18 also shows the experimental values of the force at crack growth; average values are shown as points. The error bars indicate highest and lowest values. It is seen that there is a good agreement between predictions based on the independent fracture resistance measurements by the DCB-UBM specimens and the experimental results. The trend of h_1/h_2, decreasing normalised force with increasing h_1/h_2, is predicted correctly.

7. Discussion

7.1. The obtained cohesive laws

The shape of the Mode I cohesive law is similar to that found in other studies on cross-over bridging in fibre composites (Sørensen and Jacobsen, 1998; Feih et al., 2005) and predictions by a micromechanical modelling (Spearing and Evans, 1992).

7.2. Comparison between experiments and FE model results

The LEFM solution of the medium-size specimens predicts ψ_{nom} = 41–49° when the adhesive layer is neglected (Charalambides et al., 1989). By (16) we can account for the adhesive layer. We obtain $\psi \approx 30–38°$. Next, by (18) we get for r = 1 mm (the length of ten elements, i.e., approximately the size of the fracture process zone) the phase angle of the openings, $\varphi = \psi - 0.1789$ rad ($\varphi = \psi - 10.25°$) $\approx 20–28°$. We expect the phase angle of the end-opening of the cohesive zone, φ^* to be comparable to the LEFM predictions, φ, for the medium-size specimens as long as the fracture process zones is small. From Fig. 17, we see that $\varphi^* \approx 29–33°$. Thus, the phase angle of openings predicted by LEFM is slightly lower than the phase angle obtained by the use of the cohesive laws. Since the cohesive zone modelling and the LEFM estimate are not directly comparable (no fracture process zone is modelled in the LEFM model), this discrepancy is considered insignificant. This suggests that the FE mesh is sufficiently refined.

The results from the FE simulations agree well with the experiments in terms of load as a function of crack extension. In addition, the change in phase angle with decreasing the h_1/h_2 ratio is also captured (see Figs. 12 and 17). It appears, however, that the predicted values of the steady-state fracture load are slightly lower than the experimental results, see Figs. 15 and 16. This may be the result of the chosen cohesive law parameters.

The phase angle obtained using upper and lower bound parameters gave similar predictions for φ_0^*. However, it should not be concluded that the response is insensitive to the cohesive zone parameters. Larger changes in the cohesive zone parameters can change φ_0^* and thus the steady-state fracture resistance. Examples of this are given in Appendix B, where different peak stresses and critical openings are used while the fracture energy is kept constant. The results in Appendix B show that the choice of cohesive law parameters can cause a change in phase angle, causing a change in the fracture resis-

tance of the fracture process zone, according to (25). This leads to an increase in the predicted fracture load of the medium size specimens.

In the model of the paper, the critical opening for pure Mode I was in all cases less than 1.45 mm. However, as can be seen from Fig. 10, the critical opening found in the fracture experiments is higher than 2.5 mm. This difference is a consequence of approximating a non-linear cohesive law with a linear softening law. Despite that, the current numerical results capture all the interesting behaviour of the experiments.

7.3. Comments regarding numerical and analytical modelling

Both the analytical and numerical models agree well with the load at steady-state cracking of the medium-size specimens. Since we were successful in the prediction of the strength of the medium-size joints from the fracture data determined independently from the DCB-UBM specimens, it is reasonable to expect that the strength of real structures can also be predicted with a good accuracy by the use of the present approach. An analytical solution exists for the medium size specimens investigated in the present study. A real structure, having a more complex geometry, would most likely require a numerical solution.

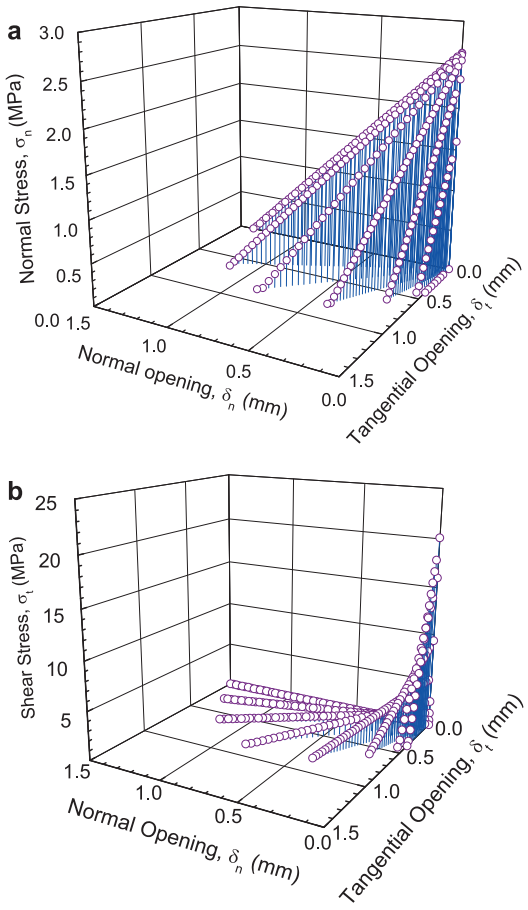

Fig. A1. (a) Mode I cohesive law and (b) Mode II cohesive law as a function of δ_n and δ_t.

8. Conclusion

In the present study, we have attempted to predict the fracture behaviour of 2-m long medium-size specimens experiencing large-scale crack bridging. The approach involves the determination of mixed mode fracture data from tests of smaller (0.3-m long) double cantilever beam specimens subjected to uneven bending moments (DCB-UBM) and comparing the prediction with strength values determined experimentally for medium size specimens. The following conclusions were obtained:

- Due to the stable crack growth of the DCB-UBM tests, fracture resistance parameters for initiation and steady-state crack growth could be obtained. Furthermore, Mode I and Mode II cohesive laws could be obtained using a *J* integral approach.
- The required load to propagate the crack in the medium size specimens, from crack initiation to steady state, predicted by finite element simulations using cohesive laws, was found to be in good agreement with measurements.
- The load-carrying capability (the load under steady-state crack growth) of the medium size specimens were predicted by the use of an analytical model; excellent agreement was found.

Together, these results lend confidence to the suggested approach of obtaining fracture parameters from tests of DCB-UBM specimens and using the fracture parameters for strength predictions of larger structures.

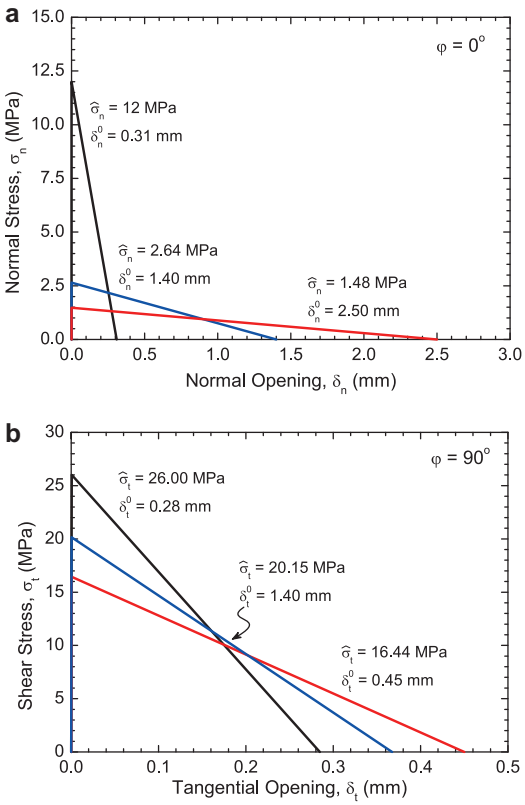

Fig. B1. Schematic illustration of idealised cohesive laws used in the FE model of the present study; the cohesive stresses are shown as a function of opening: (a) pure normal opening and (b) pure tangential opening.

Acknowledgements

This work was supported by an EFP2005 fund (Journal No. 33031-0078) from the Danish Ministry of Environmental and Energy. We thank Kenneth Jørgensen, Jens Olsson, Erik Vogeley and Erling Sørensen for experimental help and Christian P. Debel for useful discussions.

Appendix A

This appendix describes the functioning of the mixed mode cohesive laws in Abaqus. First, at a given load, the phase angle of the openings, φ, is determined by the relative openings of the cohesive element. Under the assumption that $\psi_{\text{nom}} = \varphi$, the relevant fracture energy is determined from Eq. (25). Then, the critical openings, $\delta_n^0(\varphi)$ and $\delta_t^0(\varphi)$, are computed so that the total area under the traction–separation curves (Mode I and Mode II) equals the fracture energy. A constraint in this calculation is that the damage variable (related to the cohesive stiffness) has the same value in Mode I and Mode II components – as a result $\hat{\sigma}_n(\varphi)$ and $\hat{\sigma}_t(\varphi)$ of the element are decreased according to (24).

Fig. A1 shows the idealised Mode I and Mode II cohesive laws for various mode mixities. Since $k_n = k_t$ and $\hat{\sigma}_n < \hat{\sigma}_t$, the peak stress in normal direction decreases slowly from its maximum value (pure Mode I) with increasing the phase angle, φ. How-

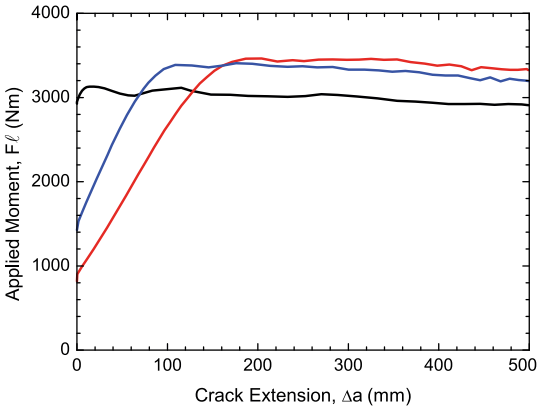

Fig. B2. Predicted relationship between applied moment and crack extension under monotonic loading for $h_1/h_2 = 1$. Line colours refer to the cohesive laws shown in Fig. B1.

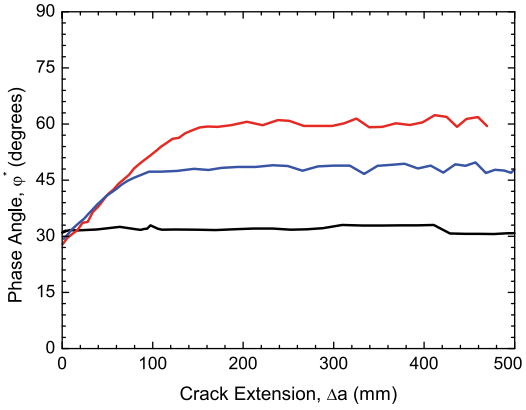

Fig. B3. Predicted phase angle of opening as a function of crack extension for $h_1/h_2 = 1$. Line colours refer to the cohesive laws shown in Fig. B1.

ever, the peak normal stress drops significantly near pure Mode II. The opposite behaviour is observed for the peak shear stress, which is low for a wide range of mode mixities and increases sharply as the pure Mode II situation is approached. As mentioned in Section 4, k_n and k_t are considered as penalty parameters to prevent the crack opening before the failure criterion (Eq. (24)) is satisfied. The experimental results in Fig. 11 suggest that the initial stiffness in the normal direction (corresponding to k_n) is higher than the initial stiffness in the tangential direction ($k_n > k_t$). Then, the cohesive laws (Fig. A1) would be different. Unpublished research shows that this would give higher steady-state cracking load in comparison with the results in Fig. 16. However, the trend regarding the effect of h_1/h_2 ratio would be the same.

Appendix B

Fig. B1a depicts three idealised Mode I cohesive laws. Each of the areas under the Mode I curves is 1850 J/m^2, which the (best fit) steady-state fracture resistance for Mode I (see Fig. 9 and Table 2). The cohesive law (black line) approximates the experimental peak stress best (see Fig. 11), however the critical crack opening is much smaller than the opening found experimentally. The red cohesive law has a critical crack opening much closer to the one found experimentally; as a result, the peak stress is low. The cohesive law in blue colour lies in between the other two case in terms of both the peak stress and critical crack opening. Likewise, Fig. B1b shows three cohesive laws for mode II; they all have a fracture energy corresponding to the (best fit) steady-state fracture resistance for Mode II (Fig. 9). But they have different peak stresses and critical openings.

Simulations were made using the three different cohesive laws. Results are shown in Fig. B2. The moment at cracking is shown as a function of the crack extension for $h_1/h_2 = 1$. When a cohesive law with a higher peak stress and a smaller critical opening is used, the steady-state load is reached at smaller crack extension. Furthermore, the load at steady-state cracking is lower.

The difference in the steady-state fracture resistance under mixed mode cracking can be understood by considering the phase angle of the openings of the fully developed fracture process zone, φ_0^*, see Fig. B3. For the cohesive law with the high peak stress and the small critical opening, the phase angle remains constant as the crack propagates. The steady-state phase angle is higher for the cohesive law having a lower peak stress and a larger critical opening. Then, by Eq. (25) (and Fig. 9), it follows that the mixed-mode steady-state fracture resistance becomes higher. Thus, even if the three cohesive laws have the same fracture energy under pure modes, the change in the phase angle of the openings leads to different steady-state fracture loads.

References

Abaqus Version 6.7. Abaqus Inc, 2007.

Albertsen, H., Ivens, J., Peters, P., Wevers, M., Verpost, I., 1995. Interlaminar fracture toughness of CFRP influenced by fibre surface treatment: part 1. Experimental results. Compos. Sci. Technol. 54, 133–145.

Bao, G., Suo, Z., 1992. Remarks on crack-bridging concepts. Appl. Mech. Rev. 45, 355–361.

Barenblatt, G.I., 1962. The mathematical theory of equilibrium cracks in brittle fracture. Adv. Appl. Mech. 7, 55–129.

Belytschko, T., Liu, W.K., Moran, B., 2000. Nonlinear Finite Elements for Continua and Structures. Wiley, New York.

Camanho, P.P., Davila, C.G., Costa, J., 2003. Numerical simulation of mixed-mode progressive delamination in composite materials. J. Compos. Mater. 37, 1415–1438.

Charalambides, P.G., Lund, J., Evans, A.G., McMeeking, R.M., 1989. A test specimen for determining the fracture resistance of bimaterial interfaces. J. Appl. Mech. 56, 77–82.

Cox, B.N., Marshall, D.B., 1991. The determination of crack bridging forces. Int. J. Fract. 49, 159–176.

Dugdale, D.S., 1960. Yielding of steel sheets containing slits. J. Mech. Phys. Solids 8, 100–104.

Dundurs, J., 1969. Discussion on 'Edge-bonded dissimilar orthogonal elastic wedges under normal and shear loading'. J. Appl. Mech. 36, 650–652.

Feih, S., Wei, J., Kingshott, P., Sørensen, B.F., 2005. The influence of fibre sizing on the strength and fracture toughness of glass fibre composites. Composites A 36, 245–255.

Foote, R.M.L., Mai, Y.-W., Cotterell, B., 1986. Crack growth resistance curves in strain-softening materials. J. Mech. Phys. Solids 34, 593–607.

Hillerborg, A., 1991. Application of the fictitious crack model to different types of materials. Int. J. Fract. 51, 95–102.

Högberg, J.L., Sørensen, B.F., Stigh, U., 2007. Constitutive behaviour of mixed mode loaded adhesive layer. Int. J. Solids Struct. 44, 8335–8354.

Hutchinson, J.W., Suo, Z., 1992. Mixed mode cracking in layered materials. In: Hutchinson, J.W., Wu, T.Y. (Eds.), Advanced in Applied Mechanics, vol. 29. Academic Press, Boston, pp. 63–191.

Jacobsen, T.K., Sørensen, B.F., 2001. Mode I intra-laminar crack growth in composites – modelling of *R*-curves from measured bridging laws. Composites A 32, 1–11.

Kafkalidis, M.S., Thouless, M.D., 2002. The effect of geometry and material properties of the fracture of single lap-shear joints. Int. J. Solids Struct. 39, 4367–4383.

Kinlock, A.J., 1987. Adhesion and Adhesives. Science and Technology. Chapman & Hall, London.

Li, V.C., Ward, R.J., 1989. A novel testing technique for post-peak tensile behaviour of cementitious materials. In: Mihashi, H., Takahashi, H., Wittmann, F.H. (Eds.), Fracture toughness and fracture energy – testing methods for concrete and rocks. Balkema, Rotterdam, pp. 183–195.

Liechti, K.M., Wu, J.-D., 2001. Mixed mode, time-dependent rubber/metal debonding. Mech. Phys. Solids 49, 1039–1072.

Li, S., Thouless, M.D., Waas, A.M., Schroeder, J.A., Zavattieri, P.D., 2005. Use of a cohesive-zone model to analyze the fracture of a fiber-reinforced polymer–matrix composite. Compos. Sci. Technol. 65, 537–549.

Li, S., Thouless, M.D., Waas, A.M., Schroeder, J.A., Zavattieri, P.D., 2006. Mixed-mode cohesive-zone models for fracture of an adhesive bonded polymer–matrix composite. Eng. Fract. Mech. 73, 64–78.

Matthews, F.L. (Ed.), 1987. Joining Fibre-Reinforced Plastics. Elsevier, London.

Mohammad, I., Liechti, K.M., 2000. Cohesive zone modelling of crack nucleation at bimaterial corner. J. Mech. Phys. Solids 48, 735–764.

Olsson, P., Stigh, U., 1989. On the determination of the constitutive properties of thin interphase layers – an exact solution. Int. J. Fract. 41, R71–R76.

Østergaard, R.C., Sørensen, B.F., 2007. Interface crack in sandwich structures. Int. J. Fract. 143, 301–316.

Östlund, S., 1995. Fracture modelling of brittle–matrix composites with spatially dependent crack bridging. Fatigue Frac. Eng. Mater. Struct. 18, 1213–1230.

Plausinis, D., Spelt, J.K., 1995. Application of a new constant *G* load-jig to creep crack growth in adhesive joints. Int. J. Adhes. Adhes. 15, 225–232.
Rice, J.R., 1968. A path independent integral and the approximate analysis of strain concentrations by notches and cracks. J. Appl. Mech. 35, 379–386.
Rice, J.R., 1988. Elastic fracture mechanics concepts for interfacial cracks. J. Appl. Mech. 55, 98–103.
Sørensen, B.F., 2002. Thermally induced delamination of symmetrically graded multilayers. J. Am. Ceram. Soc. 85, 858–864.
Sørensen, B.F., Jacobsen, T.K., 1998. Large scale bridging in composites: R-curve and bridging laws. Composites A 29, 1443–1451.
Sørensen, B.F., Jacobsen, T.K., 2000. Crack growth in composites: applicability of R-curves and bridging laws. Plast. Rubber Compos. Process. Appl. 29, 119–133.
Sørensen, B.F., Jacobsen, T.K., 2008. Characterizing delamination of fibre composites by mixed mode cohesive laws. Composite Science and Technology, accepted for publication.
Sørensen, B.F., Kirkegaard, P., 2006. Determination of mixed mode cohesive laws. Eng. Fract. Mech. 73, 2642–2661.
Sørensen, B.F., Jørgensen, K., Jacobsen, T.K., Østergaard, R.C., 2006. DCB-specimen loaded with uneven bending moments. Int. J. Fract. 141, 159–172.
Spearing, S.M., Evans, A.G., 1992. The role of fiber bridging in the delamination resistance of fiber-reinforced composites. Acta Metall. Mater. 40, 2191–2199.
Suo, Z., 1990. Delamination specimens for orthotropic materials. J. Appl. Mech. 57, 627–634.
Suo, Z., Hutchinson, J.W., 1989. On sandwich test specimen for measuring interface crack toughness. Mater. Sci. Eng. A (107), 135–142.
Suo, Z., Hutchinson, J.W., 1990. Interface crack between two elastic layers. Int. J. Fract. 43, 1–18.
Suo, Z., Bao, G., Fan, B., 1992. Delamination R-curve phenomena due to damage. J. Mech. Phys. Solids 40, 1–16.
Thouless, M.D., Evans, A.G., 1990. Comment on the spalling and edge-cracking of plates. Scr. Metall. Mater. 24, 1507–1510.
Turon, A., Davila, C.G., Camanho, P.P., Costa, J., 2007. An engineering solution for mesh size effects in the simulation of delamination using cohesive zone models. Eng. Fract. Mech. 74, 1665–1682.
Yang, Q.D., Thouless, M.D., 2001. Mixed-mode fracture analysis of plastically-deforming adhesive joints. Int. J. Fracture 110, 175–187.
Yang, Q.D., Thouless, M.D., Ward, S.M., 1999. Numerical simulations of adhesively-bonded beams failing with extensive plastic deformation. J. Mech. Phys. Solids 47, 1337–1353.

Materials Research Division
Risø National Laboratory for Sustainable Energy
Technical University of Denmark
DK-4000 Roskilde, Denmark

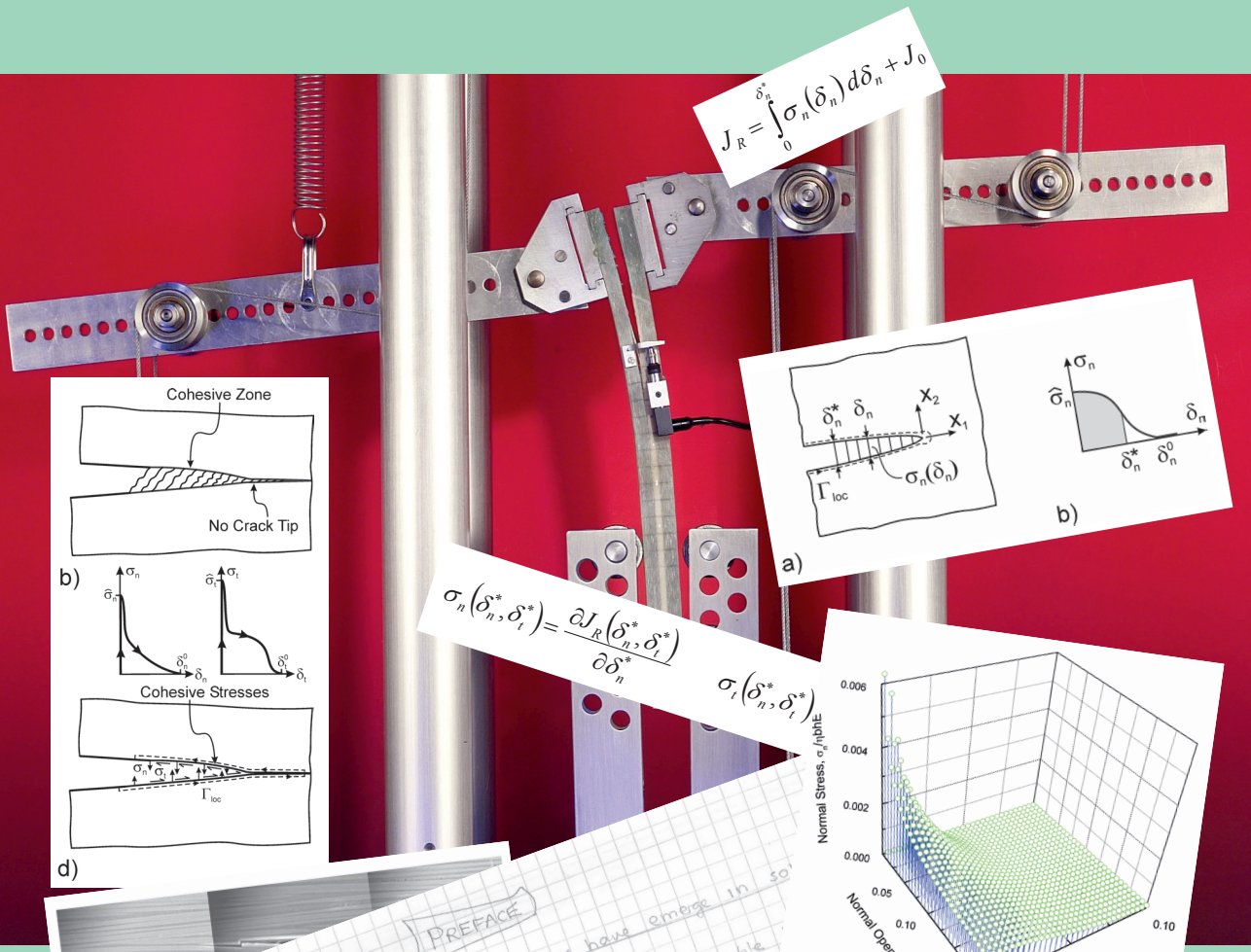

ISBN 978-87-550-3827-1
ISSN 0106-2840